Persistent Spectral Hole Burning in Organic and Inorganic Materials

by

Alexey Turukhin

A dissertation submitted to the Graduate Faculty in Physics
in partial fulfillment of the requirements for the degree of
Doctor of Philosophy
The City University of New York

1999

This manuscript has been read and accepted for the Graduate Faculty in Physics in satisfaction of the dissertation requirements for the degree of Doctor of Philosophy.

6/24/99
Date

Chair of Examining Committee

Dr. Robert R. Alfano (Thesis Co-Advisor), Distinguished Professor of Science and Engineering, Departments of Physics and Electrical Engineering, The City College of The City University of New York, 138th St. and Convent Avenue, New York, NY 10031.

8/31/99
Date

Executive Officer

Dr. Luis Celenza, Executive Officer, Doctoral Program in Physics, The City University of New York and CUNY Graduate Center, Professor,

Dr. Anshel A. Gorokhovsky (Thesis Co-Advisor), Associate Professor, Department of Engineering Science and Physics, College of Staten Island of The City University of New York, 2800 Victory Blvd. Staten Island, NY 10314.

Dr. Norbert Chencinski, Professor, Department of Engineering Science and Physics, College of Staten Island of The City University of New York, 2800 Victory Blvd. Staten Island, NY 10314.

Dr. Yoshi Okamoto, Professor, Department of Chemistry and Polymer Research Institute, Polytechnic University of New York, 6 Matrotech Center, Brooklyn, New York 11201.

Dr. Frederick W. Smith, Professor, Department of Physics, The City College of The City University of New York, 138th St. and Convent Avenue, New York, NY 10031.

The City University of New York

This work is dedicated with respect and love to my parents,

Tamara and Vladimir Turukhin

Acknowledgements

I am extremely indebted to my thesis co-advisor Prof. Robert R. Alfano for his support of this work and for great contribution to my understanding of mechanism of science and life in the United States. His optimism, energy, laughs, and encouragement are always the driven force behind all his students.

I am extremely grateful to my thesis co-advisor Prof. Anshel A. Gorokhovsky for his support, imagination, and knowledge of Physics. Listening to him and working with him over the last six years have provided me with an invaluable opportunity to learn. His friendship, encouragement, criticism, and advice are greatly appreciated.

I would like to acknowledge Prof. Norbert Chencinski for his support and interest in our research during my work at College of Staten Island.

My special thanks to Prof. Yoshi Okamoto and his former student Dr. Ting T. Chu for expert preparation of Tm^{3+} organic complexes, useful discussions of organic chemistry issues, and friendship.

I would like to express my gratitude to Prof. Frederick W. Smith and his research team for their expertise and helpful discussions of diamond materials.

I would like to thank Dr. Joseph Zeilikovich for his help and friendship. I am also grateful to my friends at Institute of Ultrafast Spectroscopy and Lasers: Dr. Bai Guang, Dr. Nick Zhadin, Dr. Yici Guo, Dr. Alexei Bykov, Dr. Dana Calistru, Dr. Yuri Budansky, Dr. Kostas Sutkus, and Mr. Leander Kalpaxis for their friendship and support during my work at the City College of New York. Particularly I would like to thank my coworker Ms. Agnes V. Carpenter for her long-term support and friendship.

I wish to thank faculty staff and all my friends at Moscow Institute of Physics and Technology for the fundamental education in physics and for the six happiest years of my life I spent there.

I would like to acknowledge Prof. Mihael Shainker and Prof. Vladimir Shur who encouraged and supported my first steps in Physics and eventually determined my decision to be a physicist.

Table of Contents

List of Tables

List of Figures

Chapter 1

Introduction

Almost twenty-five years have now elapsed since the first observation of persistent spectral hole burning in inhomogeneously broadened absorption lines in solids. The fact that the spectral shape of an inhomogeneously broadened line can be locally modified for long periods of time has led to a large number of investigations of low-temperature photophysics and photochemistry that would not have been possible otherwise. It was shown that the elimination of inhomogeneous broadening by spectral hole burning technique makes it possible to achieve optical resolution of order kHz - MHz, a resolution increase of 10^4 - 10^6 over conventional spectroscopy. With this resolution come new insights into such questions as hyperfine interactions, energy migration, the structure of defect centers and the nature of homogeneous and inhomogeneous broadening. Using hole burning, important information has been obtained about variety of interactions, including excited-state dephasing processes, host-guest dynamics, proton tunneling, low frequency excitation in amorphous hosts, relaxation mechanisms for vibrational modes, photochemical mechanisms at liquid helium temperatures, and external field perturbations.

At low temperatures the zero-phonon absorption and emission lines of most solid-state systems are inhomogeneously broadened due to distribution of local environments induced by the strains and point defects presented in all real materials[1, 2] (Fig. 1.1).

Spectral hole burning is the selective bleaching of such inhomogeneously broadened absorption line by a narrow band irradiation source (Fig. 1.2, a typical case of photochemical persistent spectral hole burning is shown). In certain experimental

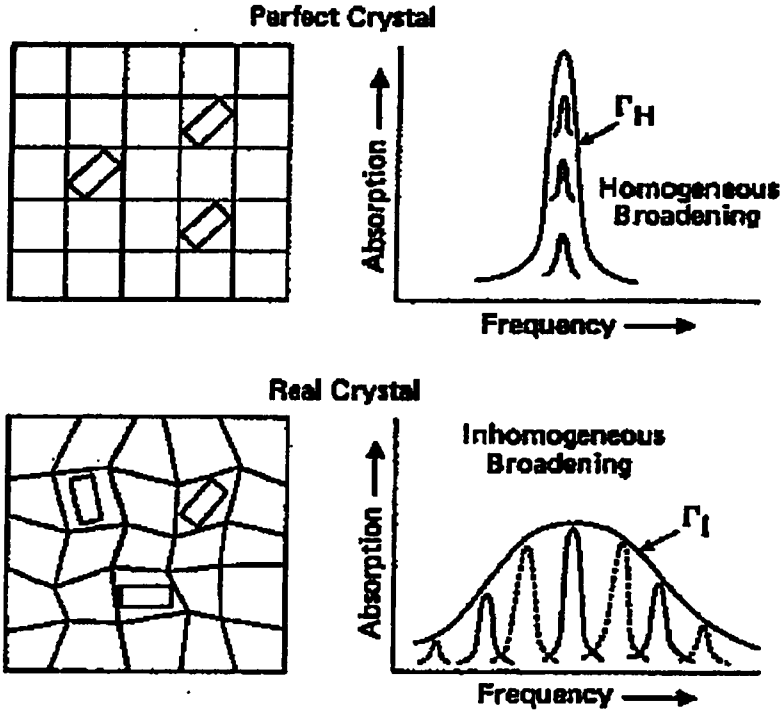

Figure 1.1. If a perfect crystal were possible, all impurity sites would be identical and spectrally non-distinguishable (upper drawing). In real crystal, distribution of parameters of local environments leads to inhomogeneous broadening of spectral lines that enables spectral selectivity (when $\Gamma_{hom} << \Gamma_{inh}$, i.e. at low temperature)

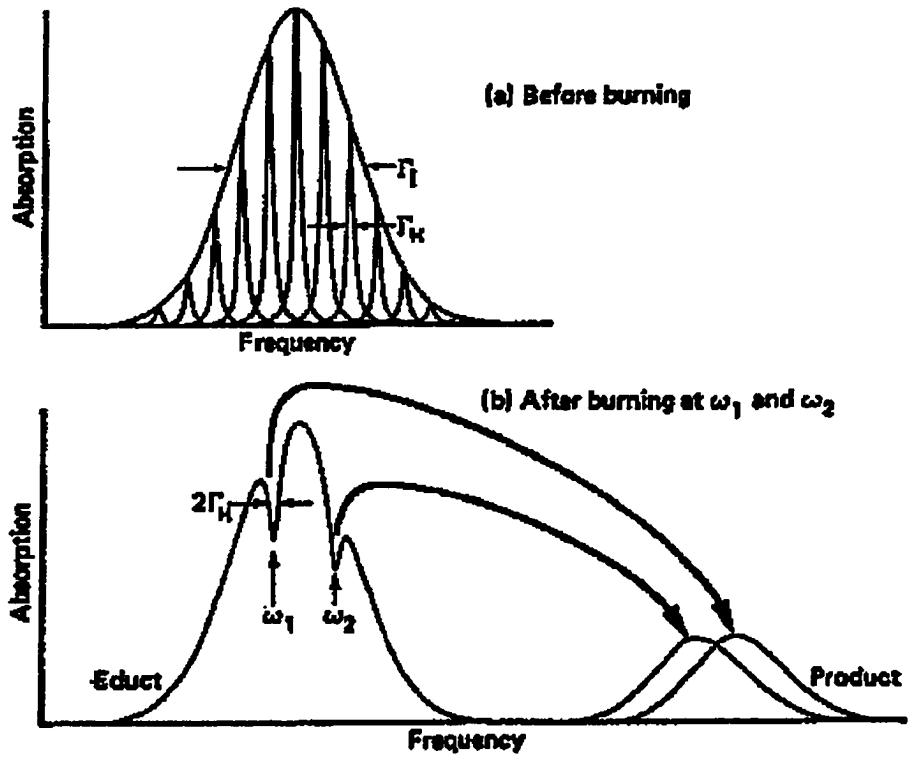

Figure 1.2. An illustration of a photochemical mechanism of hole burning. Narrow band burning laser, selectively interacting with certain subset of absorbing centers, can initiate chemical reaction in these centers. As a result, chemical structure of these centers and position of corresponding absorption lines are changing. Spectral holes indicate the positions of the modified (i.e. spectrally "moved") centers. New absorption bands associated with created chemical structures (product) can be detected in absorption spectrum.

conditions, the minimum holewidth is just twice the homogeneous width of the optical transition (see Section 3.4).

Persistent spectral hole burning (PSHB) has the potential for technological applications to optical data storage, pulse shaping, and optical signal processing. This has resulted in engineering and material research on PSHB at a variety of laboratories around the world. The application that has received the most attention so far is based on the concept of using persistent spectral hole burning to form a frequency-domain optical storage system. In this system, the optical frequency or wavelength at which holes are burned is used to encode digital information, where, for instance, the presence of a hole at particular optical frequency may be used to encode digital "1" and the absence of a hole a digital "0". Fig. 1.3 shows an example of this type of digital encoding in the frequency domain for the case of free-base phthalocyanine in poly(methyl methacrylate) (PMMA)[3].

Due to additional use of the frequency dimension, multiple bits can be stored in one laser focal volume, yielding area densities several orders of magnitude higher than those for conventional optical or magnetic storage. The possibility of data densities of 10^{12} bits/cm^2 is very attractive. This would give 10 Terabytes of information or about 5 billion pages of text in 100 square centimeters. As a comparison, one square foot would be more than enough to store the total information in the Library of Congress[4].

However, the technical problems for hole burning storage are formidable. One of the major drawbacks of these techniques is that the samples are best used at very low temperatures around 2 K, i.e. at liquid helium temperatures. For real world commercial applications, storage systems based on PSHB materials must operate in the environment of the computers: at room temperature. This is substantial challenge, since the

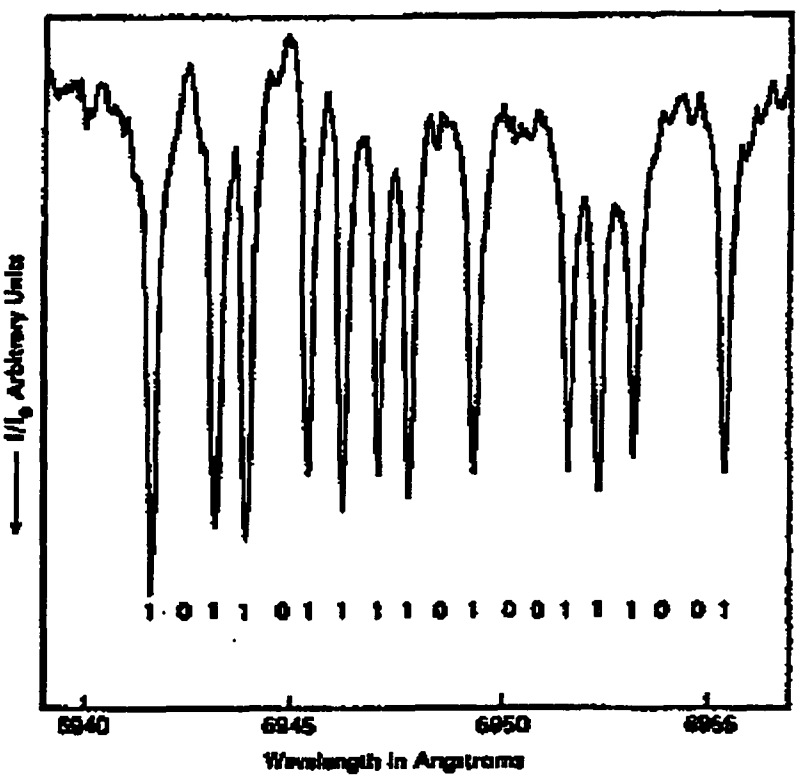

Figure 1.3. An illustration of a frequency domain optical memory based on spectral hole burning. At one spatial spot, thousands of bits can be stored using additional "spectral dimension".

homogeneous band broadens and lifetime of the excited state shortens. The time allotted for reading and writing each bit is another important parameter determining the data rate of the system; 30 ns/bit is chosen to match the data rate of conventional magnetic and optical recording technologies. Materials with high efficiency of hole burning are needed. One more problem arises because lifetime of the alternate (product) state degrades with temperature: storage time becomes shorter.

Despite a lot of research efforts in this field, materials with properties that allow PSHB storage to compete with existing high-volume data storage systems have not yet been found. Much work is still needed to gain a handle on these challenges. Today the field of persistent spectral hole burning is rapidly expanding, with new ideas and novel methods for recording being developed, and new approaches to solving the materials problems being explored. It remains a promising direction for a significant jump in data storage performance.

1.1. Thesis Statement

This Thesis focuses on the experimental and theoretical studies of the persistent spectral hole burning (PSHB) in several organic and inorganic materials. The research was directed towards spectroscopic study of novel perspective materials for PSHB storage at 10 – 77 K temperature range, in particular, for materials with long storage time and high quantum yield of photochemical reactions. The goal of the Thesis was to investigate spectral hole burning and procedures for writing and reading, longtime storage and erasing optical information in selected classes of materials in the temperature range 1.4-300 K in order to evaluate materials as potential storage media[5].

There are two types of materials that have a good potential for commercial applications of PSHB. First, point defects and impurities in diamond and diamond-like amorphous materials with a high degree of structural disorder. These systems have narrow homogeneous lines and high frequency phonon spectra, which enables the detection of informative spectra of defects with well-pronounced zero phonon lines, even at room temperature. Another class of materials is rare-earth ions doped polymer complexes. These systems are characterized by weak electron-phonon interaction and large inhomogeneous broadening that allows to expect ratio $\Gamma_{inh}/\Gamma_{hom}$ even at elevated temperatures to be high enough to create a competitive storage media. A well-determined energy structure of trivalent rare-earth ions is helpful for investigation of various gated mechanisms of hole burning. All of the above-mentioned features make a good basis for the application of these compounds as materials for information storage and processing. The aim of the Thesis is to get information on and to make models for the mechanisms of hole burning and high thermostability of holes in this kind of materials.

In the area of theory expansion, the Thesis concentrates on development of a universal analytical method for the determination of hole burning spectroscopic parameters, particularly quantum efficiency of hole burning and maximal hole depth, of various compounds under investigation.

References for Chapter 1

[1]. W. E. Morerner in: Topics in Current Physics. Persistent spectral hole-burning: science and application, ed. by Morerner (Springer, Berlin, 1987).

[2]. A. M. Stoneham in: Theory of defects in solids Vol. 1,2. Clarendon Press, Oxford, 1975

[3]. A. R. Gutierrez, J. Friedrich, D. Haarer, H. Wolfrum: IBM J. Res. Devel. **26** (1982) 198.

[4]. G. Ashton, Media National Laboratory, Annual Report, 1996.

[5]. Grant proposal by Prof. R.R Alfano and Prof. A. A. Gorokhovsky (1996).

Chapter 2

Background of Spectral Hole Burning

Transient spectral holes were observed as early as 1948 for inhomogeneously broadened magnetic resonance absorption lines in solids[1]. PSHB in optical transitions had to wait at least for the invention of the laser in order to have a tunable, coherent, high brightness source for narrow band excitation. As early as 1961, Nobel laureate A. L. Schawlow remarked at a laser spectroscopy conference that now when lasers had been invented, (transient) spectral hole burning should occur for laser-excited transitions, which are saturated by the exciting light[2]. It took many years, however, before such effects were actually observed. The first hint that PSHB might be possible came from observations of narrowing of fluorescence excitation profiles when laser sources were used to excite the fluorescence of an inhomogeneously broadened system. Such "fluorescence line narrowing" (FLN) effects, first reported by Szabo for ruby, established that narrow packets of centers within inhomogeneously broadened lines could be selectively excited by laser irradiation[3]. Later, Personov *et al.* demonstrated FLN for organic molecules in both polycrystalline and glassy hosts[4]. An important survey of laser spectroscopy of solids with emphasis on FLN was published in 1981[5]. These FLN studies can thus be regarded as forerunners of the direct observation of persistent spectral changes due to PSHB.

Transient spectral hole burning was first observed by Szabo in 1974 for the case of R lines in ruby[6]. Almost at the same time, persistent spectral hole formation was observed by two Russian groups: by Gorokhovskii at al. for free base phthalocyanine in a n-octane

Shpol'skii matrix[7] and by Kharlamov et al. for perylene and 9-aminoacridine molecules in a glassy ethanol matrix[8]. These early observations of PSHB in several organic systems suggested that the process might be fairly widespread in guests with photochemical reactions or in hosts with an amorphous character.

After these pioneering observations, many researches sought to establish the broadest class of mechanisms and materials that undergo PSHB. To date, a number of materials have shown the effect at low temperatures, in organic and inorganic crystals, polymers and glasses.

For the first time, the PSHB has been observed at room temperature for the f-f transitions of the Sm^{2+} ion-doped fluoride single crystals[9]. This room temperature PSHB is a significant scientific breakthrough for new optical memories. As a host material of Sm^{2+} ions, glasses are considered to be more favorable than single crystals because of their large inhomogeneous width of transition, high transparency, and easy mass production[10]. Attractive results for room temperature PSHB have been reported in organic solutions[11] and Sm-doped oxide glasses[12]. An extraordinary high thermostability of spectral holes was observed in case of neutron-colored α-Al_2O_3 where the broad spectral holes burned in the zero-phonon line of color centers at liquid helium temperatures can be observed even after heating the specimen up to 670 K[13]. In a neutron-irradiated type IaB natural diamond, spectral holes burnt at 5 K were partially restored by temperature cycling up to 200 K[14]. However, all of the above mentioned "high temperature" materials are characterized by low efficiency of hole burning, i.e. required high burning intensity (a few W/cm^2) and long exposure time (a few minutes) which are not appropriate for real commercial applications. In addition, multiplicity of demonstrated memory was about 10-

20 bits per laser spot (i.e. ratio of $\Gamma_{inh}/\Gamma_{hom} < 100$, see Chapter 4 for details) which is at least 10 times less than required to create commercially competitive storage.

Currently, spectral hole burning and frequency and time-domain techniques are major area of concentration for many research group around the world. To name a few of them, we should mention groups of Prof. R. Cone, Prof. R. Babbitt and Prof. A. Rebane (Montana State University, Bozeman, MT), Prof. T. Mossberg (University of Oregon, Eugene, OR), Prof. G. Small (Iowa State University), Prof. S. Hasan (Temple University, Philadelphia, PA), Prof. D. Psaltis (California Institute of Technology, Pasadena, CA), Prof. K. Wagner (University of Colorado, Boulder, CO), Dr. S. Shahriar (Research Laboratory of Electronics, MIT, Cambridge, MA), as well as Prof. D. Haarer and Prof. J. Friedrich (Germany), Prof. M. Orrit (France), Prof. R. Personov and Dr. B. Kharlamov (Russia), Prof. S. Kroll (Sweden), Prof. U. Wild (Switzerland). Among research workers at commercial companies, we should mention Dr. R. Macfarlane and Dr. M. Jefferson (IBM, Almaden), Dr. E. Maniloff and Dr. A. Johnson (Templex Technologies, Inc.), R. Equall (Scientific Materials, Inc).

PSHB technology is rapidly expanding beyond the limits of fundamental university research. New spin-off commercial companies such as Templex Technology, Inc, OR, Holoplex, Inc, CA, Call/Recall, Inc, CA, and SPECTRUM Lab, MT are trying to promote new technology into marketplace.

Therefore, today PSHB remains an active, exciting, and promising direction of research and technological development.

References for Chapter 2

[1]. N. Bloembergen, E. M. Purcell, R. V. Pound: Phys. Rev. **71** (1948) 679.

[2]. A. L. Schawlow: in Advances in Quantum Electronics, (Proc. Second Int. Conf. on Quant. Electr.), Ed. by I.R. Singer, (Columbia Univ., New York 1961), pp. 50-64.

[3]. A. Szabo: Phys. Rev. Lett. **25** (1970) 924.

[4]. R. I. Personov, E. I. Al'shits, L. A. Bykovskaya: Opt. Commun. **6** (1972) 169.

[5]. W. M. Yen, P. M. Selzer (eds.): Laser Spectroscopy of Solids, Springer Topics in Applied Physics, Vol. 49 (Springer, Berlin, Heidelberg 1981).

[6]. A. Szabo: Phys. Rev. B **11** (1975) 4512.

[7]. A. A. Gorokhovskii, R. K. Kaarli, L. A. Rebane: JETP Lett. **20** (1974) 216.

[8]. B. M. Kharlamov, R. I. Personov, L. A. Bykovskaya: Opt. Commun. **12** (1974) 191.

[9]. J. Rubio J. Phys. Chem. Solids **52** (1991) 101.

[10]. J. Zhang, S. Huang and J. Yu, Optics Lett. **17**, no. 16 (1992) 1146.

[11]. R. Menzel and P. Witte, J. Chem. Phys. **87** (1987) 6769.

[12]. K. Hirao, S. Todoroki, D. H. Cho, N. Soga, Optics Lett. **13**, no.19 (1993) 1586.

[13]. I. Sildos, M. Aizergendler, I. Dolindo and I. Renge, Opt. Commun. **73** (1989) 223.

[14]. I. Sildos and A. Osvet, Diamond and Related Materials **3** (1994) 725.

Chapter 3

General Theory Behind Spectral Hole Burning

This short theoretical review is intended to provide some basic spectroscopic information on spectral hole burning, which might be useful during discussion of experimental results presented in the Thesis.

3.1. Radiation Induced Saturation and Photochemical Depletion.[1]

The optical two level system is characterized by the probabilities of the system being in the ground state $|0)$ or in the excited state $|1)$, and by their mutual phase relation. In this case the total wave function is given as

$$\Psi_{tot} = C_0 |\Psi_0) + C_1 |\Psi_1) \qquad \text{with} \quad |C_0|^2 + |C_1|^2 = 1 \tag{3.1}$$

The matrix of complex coefficients C_0, C_1 (with C_0^*, C_1^* being the complex conjugates) will therefore describe the evolution of the two level system. For optical transition we have

$$\rho(t) = \begin{bmatrix} |C_0| & C_1 C_0^* \exp\left(-\frac{t}{2T_1} - \frac{t}{T_2^*}\right) \\ C_0 C_1^* \exp\left(-\frac{t}{2T_1} - \frac{t}{T_2^*}\right) & |C_1| \exp\left(-\frac{t}{T_1}\right) \end{bmatrix} \tag{3.2}$$

where T_1 and T_2^* stand for the energy relaxation time and the phase relaxation (pure dephasing) time respectively. When non-radiative decay processes are present, $1/T_1 = 1/T_{1\,opt} + 1/T_{1\,q}$, where the first term describes purely radiative decay and the second one non-radiative decay. Usually the temperature dependence of $T_{1\,opt}$ may be neglected, while $T_{1\,q}$ and T_2^* depend strongly on temperature. For most hole burning experiments at liquid helium temperatures, the non-radiative processes are usually absent or have already reached their low-temperature quantum-tunneling-limited value, and thus dephasing remains the main source of the temperature dependence.

The density matrix $\rho(t)$ can be used to express the radiation induced macroscopic polarization P. In terms of Pauli matrices, any component of polarization can be written as

$$P_i = \langle \sigma_i \rangle = Tr \{ \rho \sigma_i \} \qquad (3.3)$$

By inspecting (3.2) we see that the P_z polarization decays with the decay constant T_1, whereas the transverse polarization P_x and P_y have an additional decay process, which occurs at time scale of T_2^*. The homogeneous width of the spectral line is given by the decay of the transverse polarization P_x and P_y and thus determines the spectral width of a transient hole, as shown in Fig. 3.1.

$$\Delta\omega_h = \frac{1}{2T_1} + \frac{1}{T_2^*} \qquad (3.4)$$

Transient hole burning experiments can be performed in such state of the system, in which the absorption is zero for a certain time window. For instance, it can be shown that after a $\pi/2$ excitation pulse, P_z polarization is zero, i.e. the number of absorbers in the ground state and in the excited state is equal. The system has no net absorption and is therefore transparent to an external probing light beam. Fig. 3.1 shows an example of five two-level systems in which the absorbers, centered at ω_0, are characterized by a polarization $P_z=0$ at frequency ω_0 (saturation). Therefore the "inhomogeneous" absorption line, as characterized by the various frequencies ω_{-2} to ω_{+2}, has a spectral hole in its center at ω_0. The width of the hole is on the order of $\Delta\omega_h$ (see equation (3.4)). Due to strong temperature dependence of T_2^*, the contribution of dephasing to the holewidth increases considerably with temperature. More details on temperature hole broadening and on how to extract information about dephasing processes from hole shape analysis is given in Section 3.5.

It is obvious that after a saturation light beam at ω_0 is removed the excited state of the system will decay to the ground state as defined in (3.2) and the absorption band will return to its original shape.

For transient hole burning, T_1 is the characteristic time with which a fully saturated state returns to its full absorption strength. If we are considering an optical two level system, in which $|0) \rightarrow |1)$ is an allowed transition, T_1 is the order of 10^{-8} s. This is a typical time window for the transient hole burning experiment. To facilitate the experiment, one can use partially forbidden transition with longer T_1.

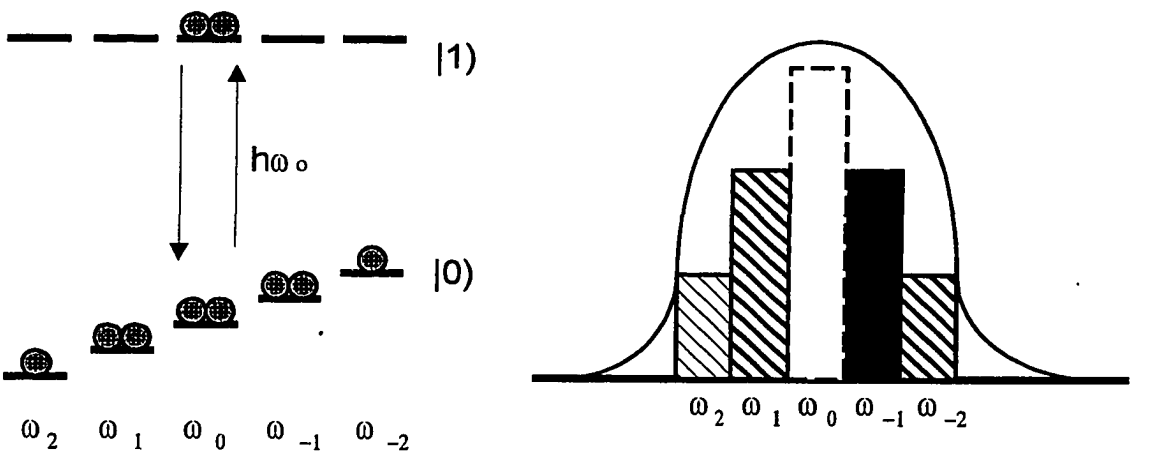

Figure 3.1. Saturation of the two level system by laser irradiation can serve as a hole burning mechanism for transient hole burning. The hole lifetime is limited by the lifetime of the excited state and is on the order of 10^{-9}-10^{-2} seconds.

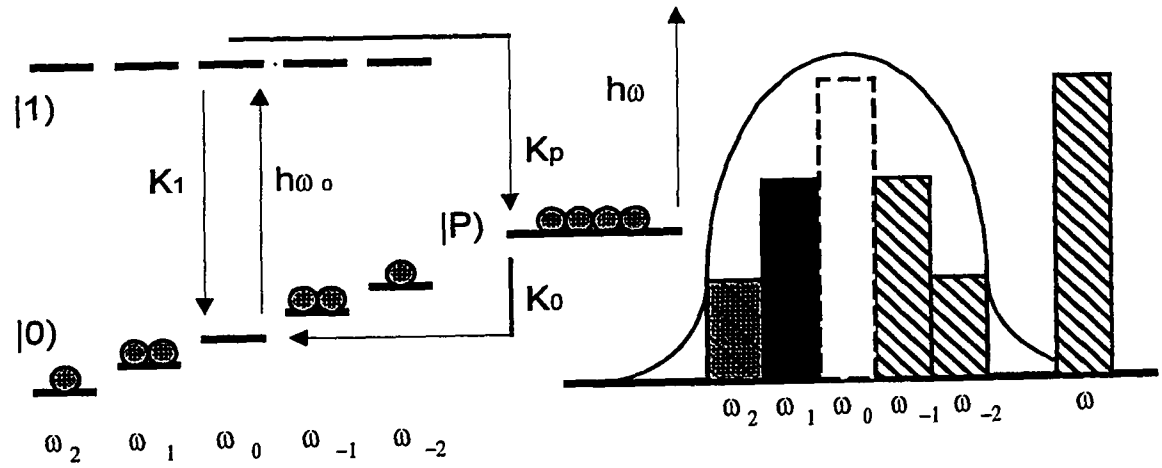

Figure 3.2. A simplified mechanism of persistent hole burning utilizing long-lived "storage" level |P).

A comparatively small variation on the optical two level system, as shown in Fig. 3.2, converts a rather difficult saturation experiment into a simple photochemical depletion experiment.

To implement persistent hole burning, we have to introduce a three level system, in which the |0) and |1) levels are defined as above and where a third level |P) is connected to the |1) state in such a way that it receives a fraction of the optically excited centers which return with a rate $K_1 \cong 1/T_1$ to the ground state |0). The branching ratio $\Phi = K_p/K_1$ is a quantum yield of the hole burning process. Quantum yield is a critical parameter of PSHB for commercial applications, when fast hole recording is needed, and usually obeys the following inequality

$$\Phi = K_p/K_1 < 1 \qquad (3.5)$$

If a depletion rate K_0 of the third level |P) to the original ground state is zero, then we have an ideal long lived hole burning system, in which the laser-induced ground state depletion is permanent. For finite values of K_0, the ground state absorption recovers within a time interval of roughly $t_0 = 1/K_0$.

3.2. Zero-Phonon Lines and Homogeneous Spectrum.[2]

The cornerstone of persistent spectral hole burning is the zero-phonon line (ZPL). Among ZPLs the purely electronic zero-phonon line (PEL) is of special interest because they provide the spectral selectivity that is needed for hole burning or any other site-selective spectroscopic experiments. The majority of the PSHB investigations have been done on PELs.

The general lineshape of an optical transition of the impurity center in host lattice can be described by its zero-phonon part $z(\omega)$ with the linewidth Γ_h and a broad phonon sideband $p(\omega)$ as depicted in Fig.3.3. For the sake of simplicity, we assume $z(\omega-\omega')$ to be a Lorentzian and $p(\omega-\omega')$ to be a Gaussian for the rest of the text. Zero-phonon line corresponds the electronic transition that is not accompanied by any change of phonon population numbers. The shape of the phonon sideband in general reflects electron-lattice interaction and distribution of vibrational modes for given defect.

The zero-phonon line and the phonon sideband can be described by a normalized lineshape function $g(\omega)$, which has the following form

$$g(\omega-\omega') = \alpha\, z(\omega-\omega') + (1-\alpha)\, p(\omega-\omega'-\Delta) \qquad (6)$$

Here the functions $g(\omega-\omega')$, $z(\omega-\omega')$, and $p(\omega-\omega'-\Delta)$ are normalized lineshape functions, α is the Debye-Waller factor (DWF) which characterizes the fraction of oscillator strength belonging to the zero-phonon part of the optical transition, and Δ is the displacement of the phonon sideband; 2Δ is a Stokes shift between the absorption and emission maxima of broad band transition. In hole burning or any site-selective spectroscopy one needs a situation in which α is close to one and, hence, most of line intensity is centered at the frequency ω_0 of the laser, which performs the burning.

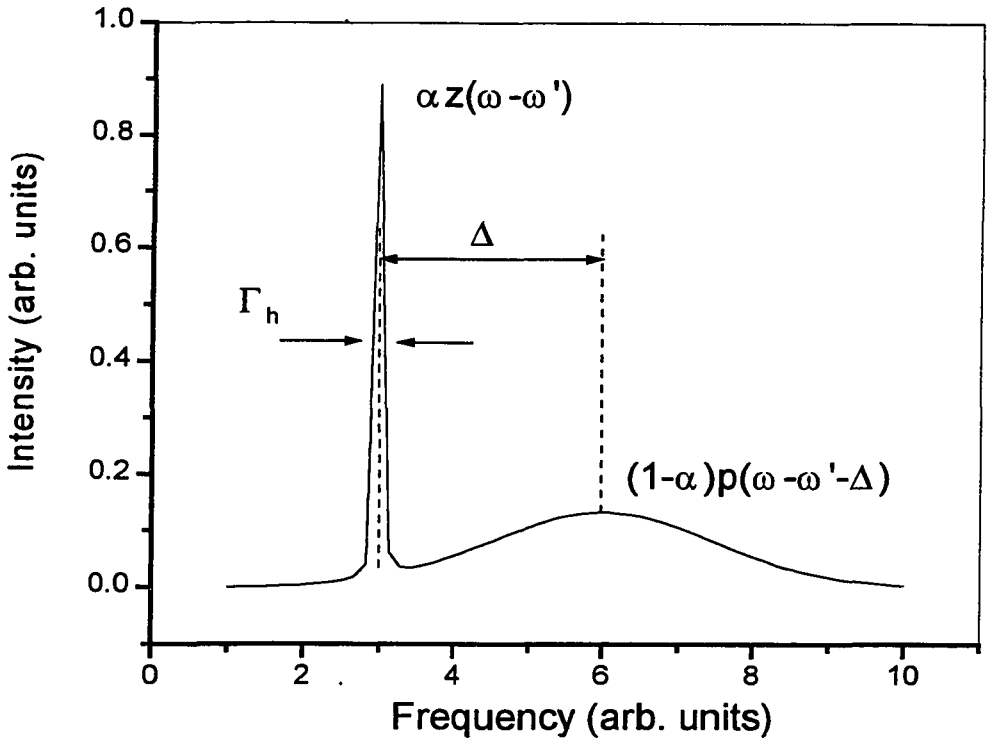

Figure 3.3. Model homogeneous profile for an absorption optical transition of an impurity center in solids. Here Δ is a Stokes shift, α is the Debye-Waller factor, and Γ_h is a homogeneous linewidth of ZPL. Functions $z(\omega-\omega')$ and $p(\omega-\omega'-\Delta)$ describe ZPL and phonon sideband shapes respectively.

The relative integrated intensity of PELs is given by the DWF α(T)

$$\alpha(T) = \frac{S_0}{S_0 + S_p} = \exp\left[-\sum_{s=1}^{N}(2n_s + 1)l_{st}\right] \qquad (3.7)$$

where $l_{st} = P_s/h\omega_s$ is the average dimensionless Stokes' shift for the vibrational mode *s* in the electronic transition under consideration. In terms of basic model[2] we have $2P_S = m_s\omega_s^2 q_{s0}^2$, m_s being the mass, ω_s the frequency, and q_{s0} the change in the equilibrium position of the oscillator; S_0 and S_p are the integrated intensities of the PEL and phonon sideband respectively; and the average number of phonons in the lattice mode *s* at the temperature T is given by

$$\left(n_s + \frac{1}{2}\right) = \frac{1}{2}\coth\left(\frac{\hbar\omega_s}{2k_B T}\right) \qquad (3.8)$$

with k_B being Boltzmann's constant. At high temperatures it increases linearly with T. This leads to an exponential decrease of α(T). The rate of reduction is proportional to the dimensionless Stokes losses in the modes whose phonons are thermally excited at a given temperature. If non-radiative transitions are absent, the sum of the integrated intensities of PEL and the phonon sideband represents the full intensity of the electronic transition (the oscillator strength). The sum of these two strong temperature dependent terms is temperature independent, and the oscillator strength is thus independent of temperature:

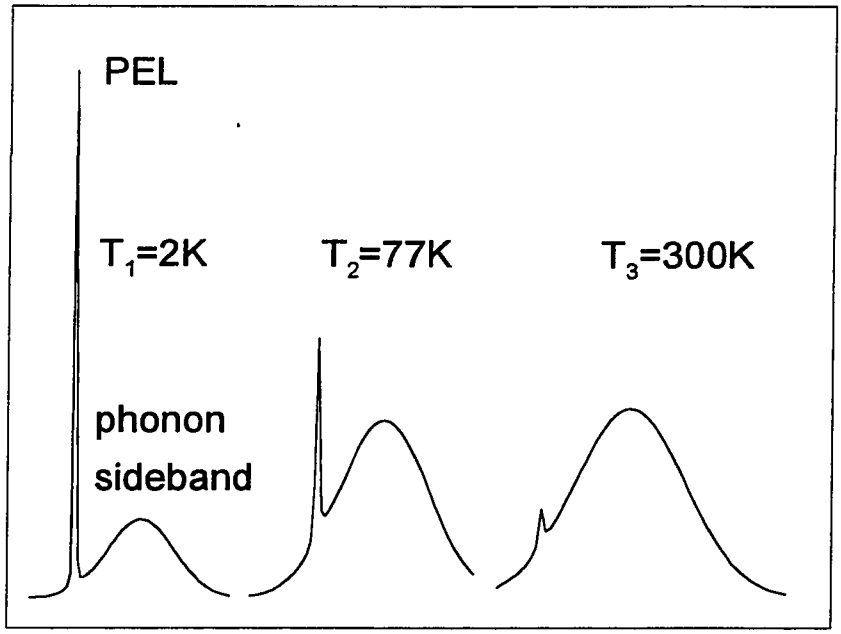

Figure 3.4. Temperature dependence of the Debye-Waller factor results in decreasing of integrated intensity of PEL.

$$S_0(T) + S_p(T) = \text{const} \qquad (9)$$

Thus, (8) tells us that quite often the temperature dependence of the absorption spectrum results in transferring integrated absorption from the PEL to the phonon sideband. Hence, the PEL not only broadens with temperature (see Section 4.5) but also loses its integrated intensity. For many impurity systems the latter is the main reason for the absence of PEL in high temperature homogeneous spectra. Fig. 3.4. shows the dependence of the homogeneous absorption spectra on temperature.

3.3. Selectivity of the Spectral Response of an Inhomogeneous Absorption Band.[2]

In a reasonable approximation, small differences in impurity sites cause shifts of the homogeneous spectrum as a whole in frequency space without any change of the PEL lineshape. In that case, it is convenient to introduce the inhomogeneous distribution function (IDF) $P(\omega)$. For a certain electronic transition $P(\omega)\Delta\omega$ gives the fraction of impurities which have their PELs in the frequency interval $\Delta\omega$ at ω. IDF depends not only on inhomogeneities in the matrix but also on the character of the transition under consideration. The inhomogeneous structure of the matrix has some influence on the frequencies of local modes, on the DWF, and on electronic transition probabilities as well. In general, the unique features of the homogeneous PELs are hidden by inhomogeneity.

An inhomogeneous impurity absorption band is actually a superposition of two distinctly different parts: a continuous band representing the sum of overlapping phonon

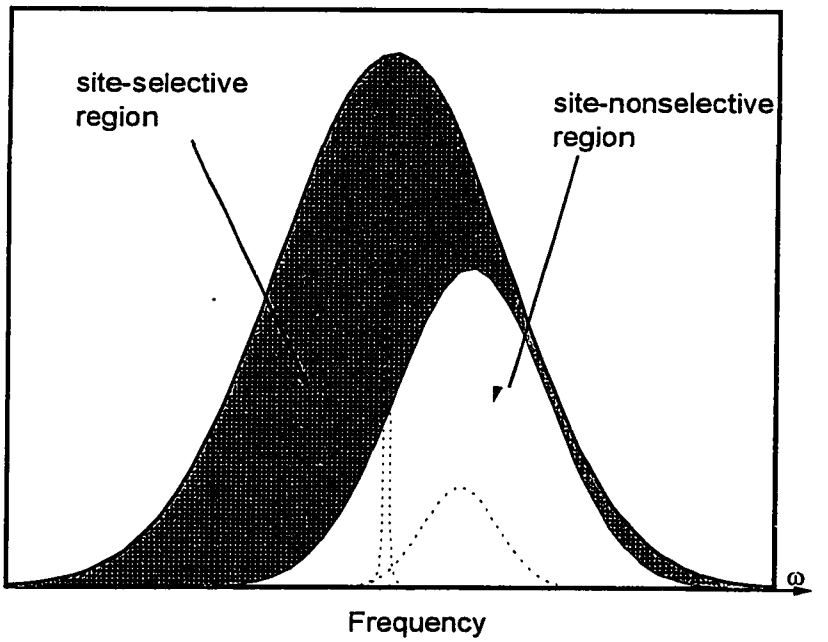

Figure 3.5. Schematic representation of structure of an inhomogeneous band with respect to spectral selectivity. PELs contribute to spectrally selective region (gray), while phonon sidebands form a non-selective region (white).

sidebands and sum of sharp, purely electronic zero-phonon lines. Only the second part leads to spectral selectivity as a result of excitation.

It is clear from Fig. 3.5. that the relative intensities of the two components of the inhomogeneous band depend strongly on the exact excitation frequency: the contribution of the PEL is more pronounced on the long-wavelength side of absorption, while the phonon wings prevail on the short-wavelength side. Following this simple consideration, in the most cases spectral hole burning is easier to observe on the long-wavelength side of the absorption band.

3.4. Spectral Hole Shape Analysis.[3]

The total absorption of a spectral hole is composed of the absorption of the various molecular sites. Each site can be described by a general lineshape function (6). It is important to note that a molecule absorbs laser irradiation at ω_L via two different processes: through its zero-phonon line $z(\omega)$ and through its phonon sideband $p(\omega)$ (see Fig. 9). The transition probability per time unit can therefore be expressed as the sum of two terms

$$W(\omega_L, \omega') = \frac{\sigma I}{h\omega_L}(\alpha z(\omega_L - \omega') + (1-\alpha)\, p(\omega_L - \omega' - \Delta)) \qquad (3.10)$$

where σ is the absorption cross section integrated over the frequency space, and $I/h\omega_L$ is the number of incident photons per unit time per unit area. If Φ is the photochemical quantum yield of the hole burning, the change of the relative number of molecules dP per time unit dt in the absence of reversal processes is given by

$$dP = P(\omega')\Phi W(\omega_L, \omega')dt \qquad (3.11)$$

After integration

$$P(t,\omega') = P(0,\omega')\exp(-W(\omega_L,\omega')\Phi t) \qquad (3.12)$$

where t is a burning time.

A convolution of P(t, ω) and the line profile (3.6) affords the photochemically modified absorption spectrum A(t, ω)

$$A(t,\omega) = \sigma \int_{-\infty}^{\infty} P(t,\omega')[\alpha z(\omega - \omega') + (1-\alpha)p(\omega - \omega' - \Delta)]d\omega' \qquad (3.13)$$

The difference A(0, ω) - A(t, ω) describes the photochemical change in the spectrum, which we refer to as a spectral hole

$$L(t, \omega) = A(0, \omega) - A(t, \omega) \qquad (3.14)$$

Assuming DWF $\alpha \approx 1$, the major term of the integral (3.13) is

$$zz(\omega) = \sigma\alpha P(0,\omega_L)\left\{1 - \int_{-\infty}^{\infty} \exp\left[-\frac{\alpha\sigma I\Phi t}{\hbar\omega_L} z(\omega_L - \omega')\right] z(\omega - \omega')d\omega'\right\} \qquad (3.15)$$

which permits a quite straightforward interpretation: zz(ω) term describes part of the hole formed by PELs burned via excitation of PELs. Other terms include zp(ω), pz(ω), and pp(ω) which are parts formed by phonon sidebands burned via excitation of PELs (direct phonon sidehole), PELs burned via excitation of its phonon wings (pseudo phonon sidehole) and phonon sidebands burned via excitation of phonon wings respectively (Fig. 3.6, for simplicity, only two homogeneous subsets of centers are shown: subset 1 is excited in PEL and subset 2 is excited in its phonon sideband); in our analysis we will consider the first term only. It should be mentioned that equation (3.15) is exact if $\Delta >> \Gamma_{inh}$ when zp(ω) and pz(ω) terms are just out of range of inhomogeneously broadened line and not observable; pp(ω) is usually very weak and can be neglected.

In real life, hole burning spectra are rather complicated: excitation with one single frequency can create holes in several different overlapping IDFs and more then one hole in one IDF, if vibronic ZPLs are involved. One single hole burnt in IDF may give rise to several holes and antiholes in the observed spectra. The frequency separation of the side holes from the central hole directly gives the excited state splittings and their sums. The frequency separation between the central hole and the anti-holes are equal to the ground state splitting and all possible sums and differences of ground state and excited states splittings.

In short time limit, when t is considerably shorter then $h\omega_L\Gamma_h/\alpha\sigma I\Phi$ (where Γ_h is a homogeneous linewidth), the exponent of equation (3.15) can be expanded into a power

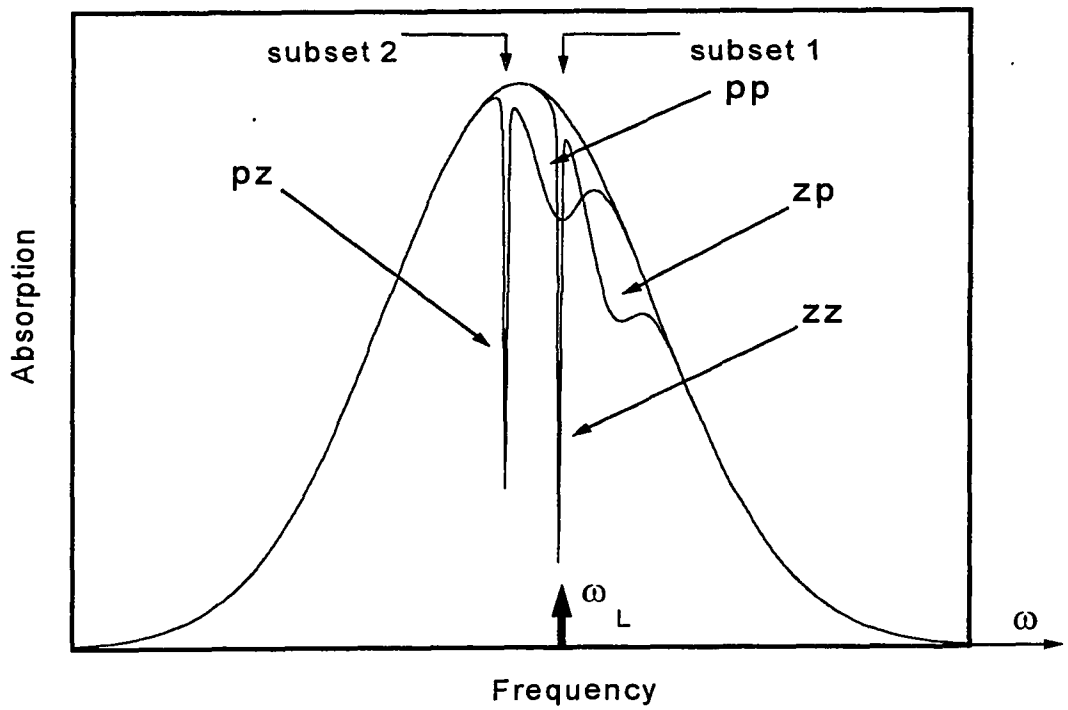

Figure 3.6. An illustration for the analysis of a shape of spectral hole. See text for details.

series. Neglecting higher terms, after integration of (3.15), the line shape of the zero-phonon hole can be then written as

$$zz(\omega) = \frac{It}{\hbar\omega_L}\sigma^2\alpha^2\Phi P(0,\omega_L)\frac{\Gamma_h}{\pi}\frac{1}{(\omega-\omega_L)^2+\Gamma_h^{\ 2}} \qquad (3.16)$$

where Lorentzian form of z(ω) was assumed. Equation (3.16) is also characterized by a Lorentzian line shape with width of $2\Gamma_h$. The short burning time limit enables one to interpret line width in terms of pertinent relaxation times. A lot of unique information on dephasing processes can be extracted from studying temperature dependence of the hole width.

The width of the zero-phonon hole as a function of exposure time or intensity can be calculated analytically only for the limiting cases $t \rightarrow 0$ and $t \rightarrow \infty$ using equation (3.15). As $t \rightarrow 0$, the linewidth approaches $2\Gamma_h$ linearly. For $t \rightarrow \infty$ the exponential factor (3.15) can be omitted from the integral. Using this approximation, the hole width can be calculated as

$$\Delta\omega_h = \sqrt{\frac{\alpha\sigma\Phi\Gamma_h}{\pi \ln 2\hbar\omega_L}It} \qquad (3.17)$$

The hole width increases with the square root of (intensity)×(burning time).

3.5. Homogeneous Broadening of the Spectral Lines.

Homogeneous broadening is experienced equally by all ions in the crystal. It arises from dynamical perturbations on the optical transition frequency, which most commonly are caused by lattice phonons or fluctuating nuclear or electron spins. At liquid helium temperatures, thermally induced phonon contributions are often negligible in inorganic materials, but broadening due to spontaneous phonon emission is significant for all except the lowest components of a J-manifold. Since the separation between J states is often larger than the maximum phonon frequency, multiphonon emission is required to relax the lowest crystal field component. Typically, this multiphonon relaxation results in population decay times (T_1) of the lowest crystal component of a J-manifold of 10^{-8} - 10^{-3} s. For these metastable levels, homogeneous linewidth contributions from phonon coupling, energy transfer, and fluctuating nuclear or electron spins become comparable to, or larger than, the rather small linewidth limits ($\approx$ kHz - MHz) set by T_1. In contrast to this, the upper crystal field components of a given J-manifold are separated from the lowest one by energies of 10's to 100's of wavenumbers, which are typical phonon energies in crystals. This means that spontaneous phonon emission from these levels is much faster than that from the lowest level and they are generally homogeneously broadened by $\approx$ 1 - 100 GHz or more, depending on details of the electron phonon coupling and the phonon density of states at the energy separation in available relaxation pathways (Fig. 3.7). As the temperature increases, two important phonon induced processes occur. One is the single phonon, "direct", process whereby a phonon is

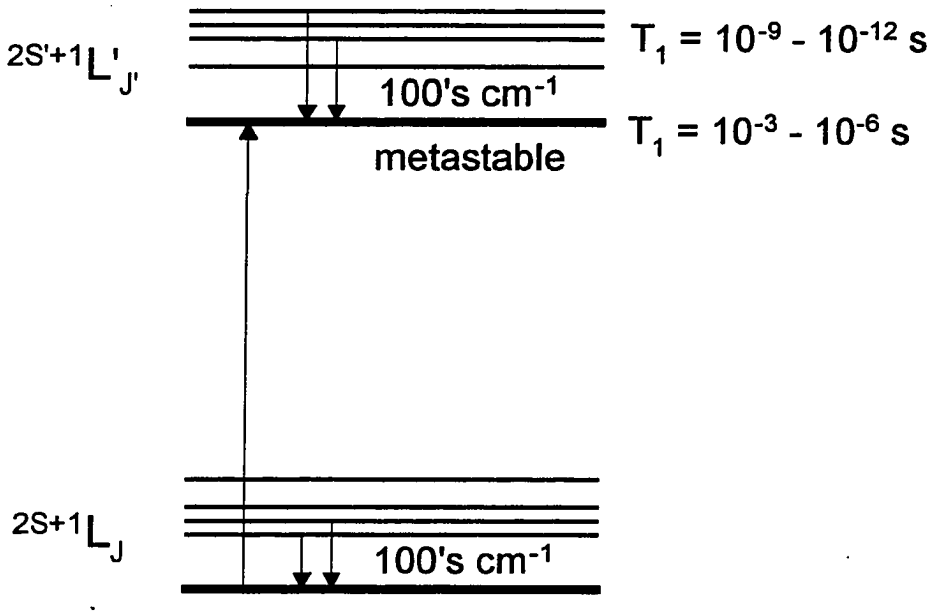

Figure 3.7. A homogeneous linewidth of an optical transition is limited by a lifetime of the corresponding excited level. Accordingly, transitions between Stark or vibronic levels are substantially broader than the transitions between metastable levels.

absorbed taking the system from one electronic state to another. Since crystal field splittings of a few cm^{-1} and higher are common, these direct processes can contribute significantly to the linewidth in the range of 10's degrees Kelvin. For very narrow lines, or with small crystal field splitting, there may be measurable thermal broadening down to about 4 K. The one phonon absorption process is the inverse of spontaneous phonon emission, which occurs from the upper of the two levels as a rate[4]

$$\Delta\omega_h = C[1 + n(\omega)] \qquad \text{with } n(\omega) = \left[\exp\left(\frac{\hbar\omega}{kT}\right) - 1\right]^{-1} \tag{3.18}$$

where $h\omega$ is an energy of crystal field splitting, $n(\omega)$ is the occupation number of phonons of frequency ω at temperature T. Therefore, if C is known from spontaneous emission, $Cn(\omega)$ can be obtained and this gives the thermal broadening of the lower level.

Another mechanism of thermal broadening is the Raman scattering of phonons by the impurity centers[5]. This Raman two-phonon process involves all thermally accessible phonons and hence does not hinge on specific phonon frequencies. The calculations yield a $(T/T_D)^7$ linewidth dependence in the low temperature approximation. In the calculation the phonons are approximated by Debye density of states function and thus the calculation gives also a T^4 dependence for a lineshift (T_D is a Debye temperature). At higher temperatures the Raman process becomes quadratic in temperature.

For organic systems a few models of thermal broadening were proposed. A model involving a single-mode two-phonon process yields following linewidth dependence[6]

$$\Delta\omega_h(T) - \Delta\omega_h(0) \approx n(\omega)[n(\omega)+1] \quad \text{with } n(\omega) = \left[\exp\left(\frac{\hbar\omega}{kT}\right) - 1\right]^{-1} \tag{3.19}$$

where n(ω) is the population and ω is the phonon frequency of the local mode.

In exchange model[7], the optical excitation is coupled to one specific phonon mode. This coupling causes the transition frequency ω_0 to be shifted to $\omega_0 + \delta\omega$ if the phonon state is populated. The theory gives

$$\Delta\omega_k(T) - \Delta\omega_h(0) = \frac{\tau(\delta\omega)^2}{1+(\delta\omega)^2\tau^2}\exp\left(-\frac{\hbar\omega}{kT}\right) \tag{3.20}$$

where τ is a lifetime of the excited phonon state and $\hbar\omega$ is the energy splitting between the purely electronic state and phonon state.

As the temperature decreases, the nuclear spin coupling remains a universally important source of optical coherence loss in solids at temperatures where the phonon contributions have been frozen out. The role of nuclear spin flips as the dominant source of low temperature homogeneous broadening was clearly demonstrated by nuclear spin decoupling experiments: applying external magnetic field allows the system to reach population decay limit for the homogeneous linewidth[8] . The line narrowing observed in magnetic fields greater than the spin-spin coupling is due to quantizing the spin along the field, thus putting part of the dipolar coupling off-diagonal and slowing the mutual flip rate.

Amorphous host-guest systems are very different from crystals. At first, the linewidth in glasses is typically one or two orders of magnitude larger then in comparable crystalline systems. Second, the temperature variation of holewidth is proportional to T^a with a values between 1 and 2 (as compared to a = 7 in crystals).

In a model proposed for explanation of thermal properties of glasses at low temperature, groups of atoms or other structural elements were assumed to be present in amorphous media, which are able to perform tunnel transition between two nearly equivalent equilibrium positions separated by an energy barrier. As a result of tunneling, the levels of vibrational motion near the equilibrium position are split and the spectrum of such system consists of a set of doublets. At low temperature only two levels of the ground vibrational state are important and this is why such tunneling system is often called a two-level system[9] (TLS). A short review of TLS theory can be found in Section 3.8.

3.6. Kinetics of the Spectral Hole Burning.[10]

Spectral hole burning is an inherently time-dependent process, thus the kinetics of hole formation is of central importance. Using equation (3.15), general functional dependence for kinetics of the hole formation can be expected from the time dependent part of zz(ω). For a hole depth we have:

$$A(t,\omega_L) \approx 1 - \int_{-\infty}^{\infty} \exp\left(-\frac{\alpha\sigma I\Phi t}{\hbar\omega_L} z(\omega_L - \omega')\right) z(\omega_L - \omega')d\omega' \qquad (3.21)$$

where a hole depth at infinite time normalized to unity. An analytical evaluation of (3.21) is found to be[11]

$$A(t,\omega_L) \approx B + D\exp\left(-\frac{\alpha\sigma I\Phi t}{\hbar\omega_L}\right) I_0\left(\frac{\alpha\sigma I\Phi t}{\hbar\omega_L}\right) \qquad (3.22)$$

where $I_0(x)$ is modified Bessel function of zero-order, initial absorption normalized to unity, and D is a maximal relative hole depth ($0<D<1$). Hence, $B=1-D$ represents a fraction of non-burnable background.

For illustration, a model curve for hole burning kinetics in transmission is shown in Fig. 3.8. Applying (3.21) for a trace of the time-varying sample transmission T(t) during the (low power) growth of a spectral hole, one can find a convenient way to measure the quantum efficiency for spectral hole burning. If a constant intensity probe beam is both burning and simultaneously detecting the spectral hole as it is burned (usual experimental situation), Φ is given by

$$\Phi = \frac{\left(dT(t)/dt\right)\big|_{t=0}}{\sigma T_0\left(I/\hbar\omega_L\right)\left(1-T_0-R\right)} \qquad (3.23)$$

where T_0 is the initial sample transmission, dT/dt is an initial rate of the hole burning (see Fig. 3.8), R is the total reflection loss and σ is the low temperature peak absorption cross section for molecules within a homogeneous line width of the laser frequency. This equation is exact for systems with the first order kinetics. For other dynamics or for

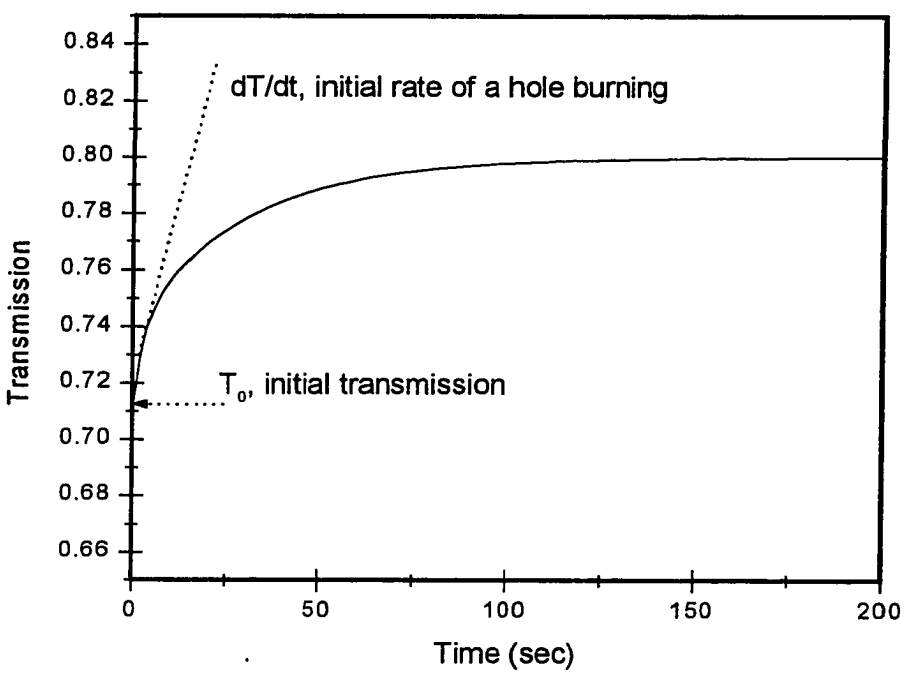

Figure 3.8. A model curve for a hole burning kinetics in transmission (according to equation (3.22)).

situations in which quantum efficiency is not constant for all centers, equation (3.22) can serve as a useful first approximation[12].

A general method of determining the quantum efficiency for persistent hole burning was developed in this Thesis and presented in Chapter 6.

Kinetics of hole burning can provide information on possible mechanisms of photoreaction. Assuming n-step process of a hole burning, kinetics in absorption can be written

$$A(t,\omega_L) \approx 1 - \int_{-\infty}^{\infty} \exp\left(-\left[\frac{I}{\hbar\omega_L}\right]^n \prod_i^n \sigma_i \Phi_i z(\omega_L - \omega) \right) z(\omega_L - \omega) d\omega \qquad (3.24)$$

where σ_i and Φ_i are low temperature homogeneous peak absorption cross section and quantum yield respectively, for the i^{th}- step of a phototransformation.

Then the average initial rate of a hole burning is given by

$$K = \frac{1}{A(t)} \frac{dA(t)}{dt}\bigg|_{t=0} \approx I^n \qquad (3.25)$$

Therefore we can obtain the order of the process by studying the dependence of the initial rate on intensity[13].

Glasses and polymers show very nonexponential kinetics of hole burning. This type of dispersive kinetics is discussed in Section 3.8.

3.7. Mechanisms of the Spectral Hole Burning.[14]

In contrast to the case of transient hole-burning caused by two-level saturation or optical pumping of hyperfine levels (see below), details of the mechanisms involved in PSHB are often not well known and can be very specific to every particular material.

Microscopic mechanisms leading to PSHB can be roughly classified into two categories: photochemical and photophysical (nonphotochemical). Photochemical mechanisms usually involve some internal chemical change in the guest center itself, such as bond breaking, ionization, izomerization, tautomerization, and so forth. Nonphotochemical mechanisms arise from a change in the environment around the center, or perhaps from a reorientation of the center itself with respect to the local environment.

In many crystalline inorganic materials it is believed that photoionization processes are responsible for all the cases of PSHB reported so far. Transformation leading to bleaching most likely occurs directly from the selectively excited energy level or from a metastable level to which it relaxes (Fig. 3.9 a). Assuming that the excited state wave functions are sufficiently extended, tunneling transition to a nearby trap may result in photoionization.

To illustrate typical single-photon mechanism (Fig. 3.9 a), the most important of the hole burning mechanisms for rare earth ions, hyperfine hole burning will be described in some detail. Since the inhomogeneous broadening is usually large compared to the hyperfine splitting, all allowed transitions between ground state and excited state levels are shifted into resonance with the exciting laser for some subsets of ions. The relative strengths of the transitions are determined by the overlap of nuclear spin wave functions

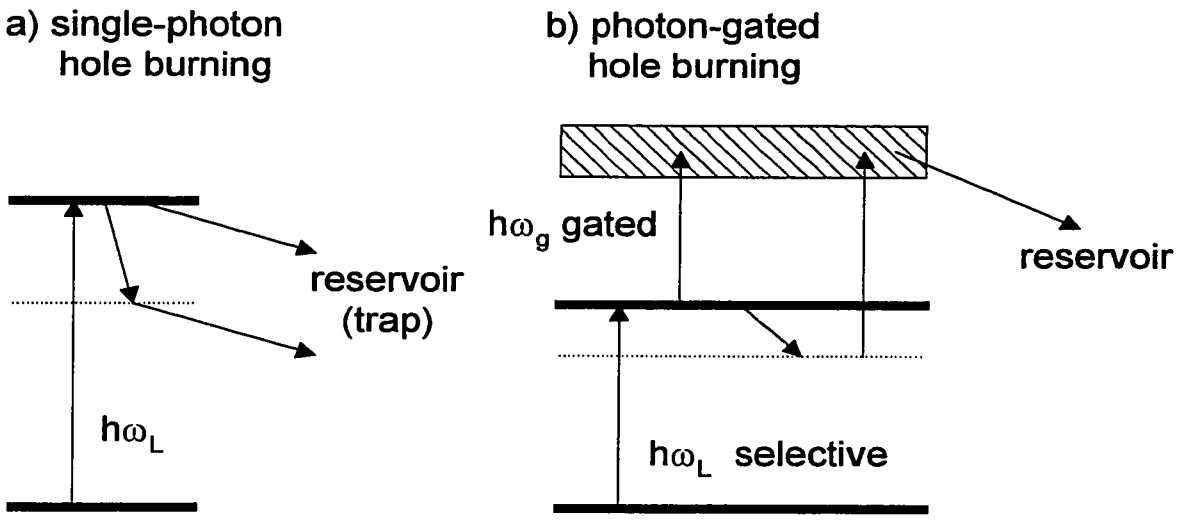

Figure 3.9. Mechanisms of persistent spectral hole burning.

between ground and excited states. A given ion is resonant with the laser on only one of the allowed transitions, but it may relax by another allowed pathway to a ground state level other than that from which it was excited. Thus, levels resonant with the laser are emptied of population, producing a hole at laser frequency. An important feature of this hole burning mechanism is that one expects inhomogeneous broadening to be strongly correlated for optical transitions between different hyperfine levels of a given pair of electronic states. Thus, in addition to the hole at the original irradiation frequency, a pattern of sideholes is expected due to transitions from the ground state levels with depleted population to all of the excited state hyperfine levels. Although in practice the width of these sideholes is often limited by laser frequency jitter, the ultimate limit of their width will be the inhomogeneous broadening of the hyperfine transition. Likewise, the ground state levels with larger than equilibrium populations (i.e. the levels acting as population reservoir) show narrow enhanced absorption features, which are called anti-holes. The overall spectral pattern is then a superposition of holes and anti-holes for each of the subsets of ions corresponding to each of the allowed transitions that were excited.

More recently a new class of materials has been identified in which the ionization is a two-step process leading to so-called "photon-gated' hole burning (Fig. 3.9 b). Here one photon from a narrow band laser source ($h\omega_L$) is used to label a frequency selective subset of the population by exciting it to a metastable level. This can either be the level initially populated by the laser or one to which the system subsequently relaxes. The second step, which may be carried out by a broad band source, takes the excited population produced by the first laser and ionizes some or all of it. Preferably this second photon ($h\omega_g$) should be more energetic than the first so that no hole burning occurs when it is absent, and the

background absorption at the gating wavelength should be broad enough to prevent bleaching.

It is, of course, possible that "self-gating" occurs, i.e. photoionization results from absorption of two photons at $h\omega_L$ from the frequency selective or broad band source. This leads to a greater than a linear dependence of burning rate on laser power (see Section 3.6.).

Photon-gated materials are attractive for a number of reasons. Their characteristic property is the stability of the holes to reading in the absence of gated light, since under these conditions no further bleaching occurs. This is of critical importance in applications to frequency domain storage since reading must be accomplished in a short time ($\approx$ 30 ns) and the photon flux required to do this inevitably leads to erasure of the stored information in single-photon materials (see Chapter 4).

The next class of hole burning mechanisms is where the optical center itself (e.g. impurity ion) is photostable, but where excitation of the center induces a slight rearrangement of the surrounding environment via phonon coupling. This is the mechanism proposed to explain the observation of PSHB in photochemically stable centers such as trivalent rare earth ions in glasses. Theoretical review of this mechanism can be found in Section 3.8.

Qualitatively hole-burning mechanisms at high temperatures are similar to aforementioned mechanisms. Usually, high temperature spectral hole burning involves photophysical mechanisms or photoionization.

High temperature spectral hole burning in neutron-irradiated IaB-type natural diamond[15] and high thermostability of spectral holes in neutron-irradiated sapphire[16] are

assigned to rearrangements in the local surrounding of defect aggregates involving tunneling processes in double well potentials with high (up to 1.17 eV) barriers.

The hole burning mechanisms in Sm^{2+} compounds have been studied[17]. In spite of the interpretation is still not unique, the processes are described as follows: A narrow burning laser line selectively ionizes the Sm^{2+} (A) ions in resonance with the laser to Sm^{2+} (A) ions, then the released electron are probably captured by the Sm^{3+} (B) ions at any sites to form Sm^{2+} (B) ions. That is, Sm^{3+} ions act as electron traps.

3.8. Two-Level System Theory for Amorphous Media.

Whereas crystals are characterized by periodic potentials with well-defined and identical potential wells, glasses are characterized by potentials with variable minimum energies and with variable barrier heights. This randomness is due to the local disorder of the amorphous state and reflects the non-periodic nature of the potential curve.

The only mechanism that has been proposed for nonphotochemical persistent spectral hole burning is based on a so-called two-level systems (TLSs) structural model for glassy state[18]. In this model, the glass is considered to contain a distribution of asymmetric intermolecular double-well potentials (TLSs), see Fig. 3.10, with varying barrier height V, zero-point energy difference e and well separation d. In Fig. 3.10, TLS_G and TLS_F are the potential energy curves for a particular TLS interacting with an impurity molecule in its ground (G) and excited (F) electronic states. TLS is characterized by tunneling parameter W of the form

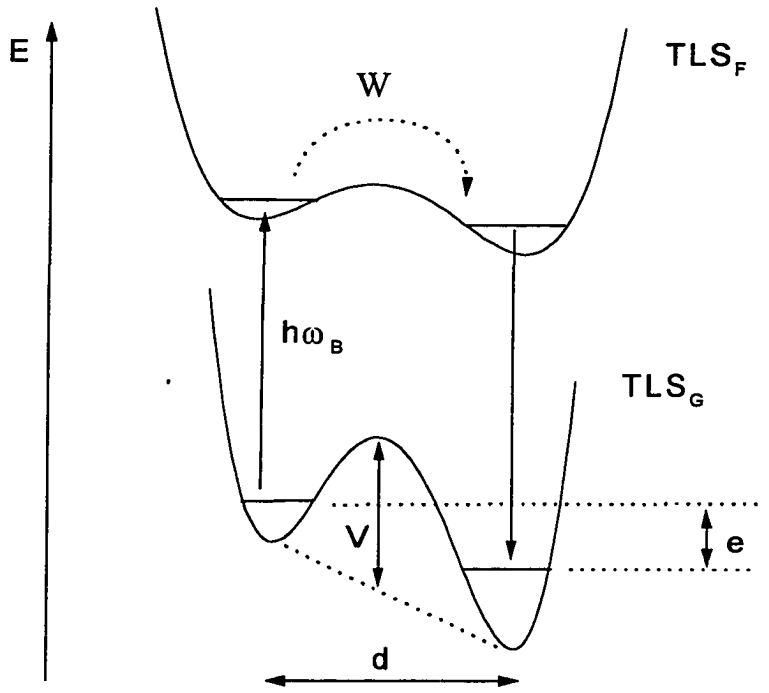

Figure 3.10. An illustration for mechanism of persistent hole burning in an amorphous media. In terms of two level systems, inherent for disordered materials, a hole burning is governed by the tunneling transition to another minima of the excited state with consequent relaxation to alternative metastable ground state.

$$W = \hbar\omega \exp\left(-d\sqrt{\frac{2mV}{\hbar^2}}\right) = \hbar\omega \exp(-\lambda) \qquad (3.26)$$

where m is a mass of tunneling particles or molecular groups. The energy $\hbar\omega$ is on the order of the quantum energy of a harmonic oscillator. The two energy eigenvalues of the TLS system are well know and given by

$$E^2 = e^2 + W^2 \qquad (3.27)$$

where e is a difference in zero-point energies for "left" and "right" wells.

To explain nonphotochemical PSHB at a given burn temperature, T_B, it was proposed[18] that hole formation is due to a subset of the TLSs interacting with impurity molecules which, at the temperature T_B, have the following two properties: (1) Relaxation (either by phonon assisted tunneling or thermal activation) between the two minima of the TLS_G is sufficiently long (i.e. many hours) to account for the hole persistent times; (2) The impurity electron-TLS interaction is sufficiently strong to modify the double-well potential to an extent which makes relaxation between the TLS_F minima competitive with the normal, e.g. radiative, decay processes of the excited electronic state of the impurity. Again, relaxation can occur by phonon assisted tunneling or by a thermally activated process. Typical fluorescence lifetimes for the molecules studied thus far are in the range 1-100 ns.

With these two properties, one can easily see from Fig. 3.10 that if the laser burn frequency ω_B is on resonance with the "left" transition but not with the "right" transition,

hole burning in the persistent type can ensue. A key feature of the above mechanism is the assertion that at a given T_B only a subset of the TLSs interacting with the impurity is involved in hole formation. This was necessary in explaining hole saturation or, in other words, why 100% optical density changes are not generally observed.

The amorphous nature of the material is taken into account by allowing the main parameters e and λ of the two level systems to have broad distribution rather than well-defined values. The glassy system is characterized by dynamical parameters whose distribution is so wide that the slow components characterizing the ensemble of TLS will, within finite times, not reach their equilibrium configuration or energies. In the basic model, the distribution of the pertinent tunneling parameters e and λ is assumed to be flat in the range of the relevance for the low temperature experiments. Therefore, we can write for distribution function P

$$P(e, \lambda) = P_0 = \text{const} \tag{3.28}$$

It is important to know that a flat distribution in the parameters e and λ leads to a distribution which is close to being flat in energy space. A straightforward calculation shows that the density of states as a function of energy can be written as

$$\rho(E)dE \rightarrow P(e,\lambda)\ln\left(\frac{2E}{W_{\min}}\right)dE \tag{3.29}$$

The above energy dependence is only logarithmic and can, for systems with high barriers and with reasonable energy values, be considered as a quasi-flat.

It is important to note that two classes of TLS are usually considered: extrinsic TLS_{ext} and intrinsic TLS_{int}. Intrinsic TLSs have low barriers, so that even at very low temperatures phonon-assisted tunneling occurs producing a rapidly time-varying environment and hence broadening. Usually, TLS_{int} are associated with internal structure of the host media and considered to be a major contributor to the dephasing. Hole burning process, on the other hand, involves extrinsic TLSs with higher barriers because hole lifetimes are very long so that once the barrier surmounted, the system remains in that configuration until it is warmed up to a temperature comparable to the barrier height. Therefore, TLS_{ext} are strongly associated with the impurity. Again, dephasing occurs due to the interaction of the impurity with a "sea" of weakly interacting TLS_{int}. For a large sea, each and every impurity should undergo phase-memory loss with the same characteristic time constant. Hole burning occurs due to strong interaction with one or a small number of nearby TLS_{ext}.

The next section deals mostly with intrinsic TLS, while the section devoted to hole burning kinetics deals with extrinsic TLS.

3.8.1. The Optical Linewidth and Dephasing.

Temperature dependence of a holewidth is experimentally found to be proportional to $T^{1.1\text{-}1.6}$ which is very different from one in crystals (see Section 3.5).

Trying to explain these anomalous dependencies, a number of models has been worked out, taking into account the interaction of the impurity with TLS and the vibrations of the skeleton of glass. Theoretical models differ by the consideration of

various interactions on calculating the spectrum in one center and by the methods of the subsequent averaging over the inhomogeneous parameters of the matrix. It is supposed that the impurity and TLS may interact via electrical or elastic forces of various multiplicity. The vibrations of the matrix interact with the impurity through phonon-induced transitions in TLS. The direct interaction of the impurity with the impurity-induced quisilocal vibration as well as with the intrinsic quisilocal vibrations of the disordered matrix are also taken into account (see summary in Ref. 9).

The TLS states seem to have a high spectral density at very low energies and this is responsible for so-called thermal anomalies: at low temperatures below 1 K the specific heat increases linearly with temperature[19] (while $\sim T^3$ for crystal). Using a general function $\rho(E) \propto E^{\mu}$ for a density of states and s for multipolar form of interaction $U \sim r^{-s}$, the temperature dependence of a linewidth is given by $T^{\mu+4-9/s}$. Thus, theoretical models predict a broad spectrum of possible temperature dependence of the ZPL linewidth on T^0 up to T^4 and exponential similar to equation (3.19). Since the density of elementary excitations of the matrix depends on temperature, the study of holewidth as a function of temperature can provide information on mechanisms and relative contributions of actual interactions. Temperature dependence $T^{1.3}$ experimentally found for the most amorphous compounds can be explained by μ=0.3 and dipolar-dipolar interaction between TLSs (s=3). Rigorous physical justification for such a universal "power law" has not yet been found.

But not only dephasing contributes to the experimentally observed holewidth in a traditional hole burning experiment.

3.8.2. Spectral Diffusion in Glasses.

In equilibrium, the tunneling dynamics do not change the total number of molecules absorbing at the given frequency and, hence, the inhomogeneous line profile does not change with time and temperature. The site population is in a stationary state.

This situation changes if, by light irradiation, a hole is burnt into a inhomogeneous distribution. The equilibrium is then perturbed and more particles tunnel into the hole relative to those tunneling out of it. This process leads to a change in a line width by spectral diffusion. Processes of this kind are always present and can be detected with high sensitivity in hole burning experiments at low temperatures and by subsequently cycling the temperature. At high temperatures the rates determining spectral diffusion increase via thermally assisted processes. The glassy state moves towards a state of new quasi equilibrium. If the temperature is recycled to the low value again, the new state is frozen in and can be evaluated spectroscopically. The hole width changes irreversibly with temperature; it becomes dependent on the sample history, a characteristic feature of non-equilibrium systems[1].

Because of these irreversible diffusion processes, one has to proceed with extreme care if it is desired to measure a homogeneous line width and its temperature dependence: after a long time interval the hole does not reflect the true "homogeneous" linewidth but rather a sum of the homogeneous linewidth and a width due to spectral diffusion.

Hole burning offers a means of investigation the time scale of such diffusion processes. It should be mentioned, however, that spectral diffusion in photochemical hole burning can be due to two different processes: it can be caused by the reorientation of molecules in the ground state (physical dark process) and can also be caused by a back

reaction from product state to original ground state (chemical back reaction). Both processes may change the hole width in a different way[3].

Comparison of results of spectral hole burning and photon echo experiments can provide valuable information on spectral diffusion. The photon echo method[20] is quite different from the spectral hole burning in that the sample is excited by short pulses whose spectral widths are large compared to the homogeneous width of the optical transition. No significant spectral selection by laser occurs. Rather, the effect of inhomogeneous broadening is removed by the pulse sequence itself. The two-pulsed echo experiment is carried out by exciting the sample with the two laser pulses, separated by delay τ (Fig. 3.11 a. Phase as a function of time is shown for three different dipoles. b. Timing of the photon echo experiment). The first pulse creates a coherent superposition of the ground and excited state wave functions. This coherence is detectable because it leads to microscopic oscillating dipole, which is capable of emitting coherent radiation, and it rapidly decays on a timescale given by the inverse of the broad portion of the inhomogeneous line that was excited. The second pulse has the effect of exchanging to some degree the amplitudes of the ground and excited states in the coherent superposition, i.e. the sign of this accumulated phase is reversed for each given ion. Following the additional evolution period of time τ, the net phase shift is canceled for every ion, leading to a rephasing of the coherence and emission of a burst of coherent radiation.

This burst of light is the photon echo. The intensity or amplitude of the echo reflects the decay of coherence due to homogeneous relaxation processes during the time 2τ. It can be shown that with increasing delay time between the first $\pi/2$-pulse and the second π-pulse the echo intensity I_e decreases exponentially[21] as

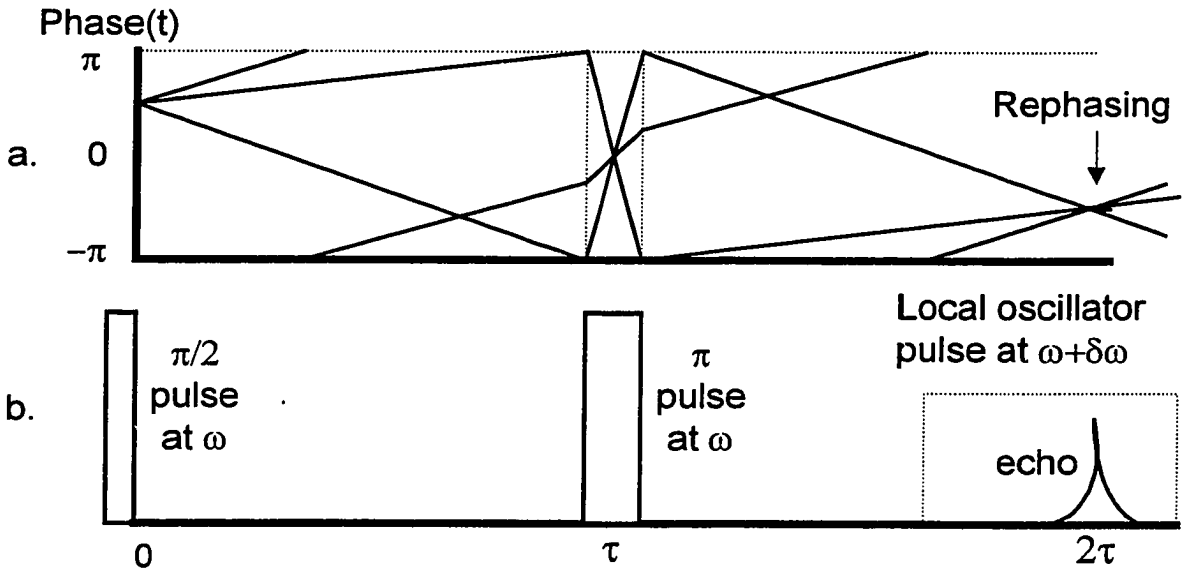

Figure 3.11. Phase (a) and intensity (b) time dependencies for photon echo experiment.

$$I_e(2\tau) = I_e(0)\exp\left(\frac{-2\tau}{T_2}\right) \qquad (3.30)$$

where as usual $1/T_2 = 1/(2T_1) + 1/T_2^*$.

A plot of echo amplitude versus 2τ, yields a dephasing time T^{hom}. Ideally, one wants to excite the sample to a coherent superposition state with equal amplitudes for being in the ground and excited states, i.e. $\pi/2$ pulse. The second pulse should be π pulse, to perfectly interchange the amplitudes and phase factors for the ground and excited states. However, echoes can be observed with nonoptimal pulse area.

The echo is only sensitive to the fast fluctuations of the glassy structure. Hole burning experiment operates on a time scale which is 11 to 12 orders of magnitude longer than the echo. Its sensitivity to very slow evolution also causes dephasing - spectral diffusion. The hole burning dephasing time temperature dependence should include an additional term which accounts for the temperature dependence of the spectral diffusion. Studying temperature dependence of the dephasing time (holewidth) in both experiments, temperature dependence of the spectral diffusion can be obtained by subtracting the echo data from the hole burning data[21].

3.8.3. Dispersive Hole-Growth Kinetics and Spontaneous Hole Filling.

Inherent disorder of glasses precludes the observation of pure exponential decay in many relaxation processes since the rate determining parameters are governed by distributions. Using phenomenological distribution (28) which leads to $\rho(E) \sim \rho_0$, one can find the distribution function for tunneling rates[1]

$$P(R)dR = \frac{1}{2} P_0 \frac{dR}{R\sqrt{1-\frac{R}{R_{min}}}} \tag{3.31}$$

where it is necessary to introduce a maximum and minimum value for R. Singularities at $R=R_{min}$ and $R=R_{max}$ have no physical justification but still equation (3.31) leads to logarithmic decay of the hole area (spontaneous hole filling) as a function of observation time due to physical dark back reaction: the number of molecules which have returned to the educt state after a time t can be calculated by integrating the rate distribution function (3.31)

$$\frac{n}{n_1} = N_0 \int_{R}^{R_1} P(R)dR \tag{3.32}$$

where n_1 is the number of molecules in the photoproduct state after a time t_1 has elapsed between hole burning and the first probing (detection) experiment; $R_1=1/t_1$ is the fastest rate which can be observed in the experiment.

After integrating (3.32), one obtains an expression for the relative hole area which shows a logarithmic time dependence[1]

$$\frac{A}{A_1} = 1 - \ln\left(\frac{R_1}{R_{min}}\right)^{-1} \ln\left(\frac{t}{t_1}\right) \tag{3.33}$$

At the same time, a lot of experimental hole growth kinetics are so dispersive and so non-exponential that they can not be described by the model based on simple distribution function (3.28). However, instead of using a fixed P_0 value one can assume a Gaussian distribution function of λ, which leads to following distribution of tunneling rates[22]

$$P(R)dR \propto R^{-\alpha} \exp[\beta \ln^2(R)]dR \qquad (3.34)$$

where α and β are collections of constants, including parameters of the λ distribution. Using distribution (3.34) in the equation (3.32) one can obtain the final expression for dispersive hole burning kinetics

$$D(I,t) = 1 - \frac{F(b_2) - F(b_1)}{F(b_2) + 0.5}, \quad F(\sqrt{2}x) = \frac{1}{2} erf(x) \qquad (3.35)$$

where $b_1 = \frac{\ln\left(\frac{k}{I\sigma\omega_0 t}\right)}{2s} + \frac{\lambda_0}{s}$ and $b_2 = \frac{\ln\left(\frac{k}{\omega_0}\right)}{2s} + \frac{\lambda_0}{s}$, σ stands for a homogeneous low temperature peak absorption cross section, I is an intensity of burning laser, ω_0 is a frequency of a harmonic oscillator (see Fig. 3.10), k is a rate of spontaneous decay (i.e. $k=1/\tau$); λ_0 and s are the center and width of the distribution of the tunneling parameter λ.

In terms of the model presented, we can discuss the distribution of quantum yields for the hole burning process (assuming that normally k>>R):

$$\Phi(R) = \frac{R}{R+k} \approx \frac{R}{k} \qquad (3.36)$$

and introduce the average value $\langle\Phi\rangle$

$$\langle\Phi\rangle = \frac{\langle R\rangle}{k} = \frac{I\sigma\omega_0}{k^2}\exp(-2\lambda_0)\exp(2s^2) \qquad (3.37)$$

Sometimes it is useful to introduce an average quantum yield $\langle\Phi\rangle_\varsigma$ that corresponds to the initial fraction ς (say, 0.05) of the hole burning[23].

Being employed for many years for description of dispersive kinetics and calculation of quantum efficiency of a hole burning process, the presented above approach often fails to explain experimental data. In this Thesis, substantially modified universal approach for determination of quantum efficiency is proposed and applied to hole burning studies of several phthalocyanines (see Chapter 6).

References for Chapter 3

[1]. D. Haarer in: Topics in Current Physics. Persistent spectral hole burning: science and application, ed. by Morerner (Springer, Berlin, 1987).

[2]. K. K. Rebane: Impurity spectra of solids (Plenum Press, New York, 1970).

[3]. J. Friedrich and D. Haarer, Angewandte Chemie, vol. **23**, 2, February 1984, 113-140.

[4]. R. M. Macfarlane and R. M. Shelby in: Spectroscopy of solids containing rare earth ions. (Ed. by A. A. Kaplyanskii and R. M. Macfarlane) Elsevier Science Publishers, 1987.

[5]. D. E. McCumber, M. D. Sturge, J. Appl. Phys. **34** (1963) 1682.

[6]. A. A. Gorokhovskii, R. K. Kaarli, L. A. Rebane: JETP Lett. **20** (1974) 216.

[7]. S. Volker, R. M. Macfarlane, J. H. van der Waals: Chem. Phys. Lett. **53** (1978) 8.

[8]. R. M. Macfarlane, Solid State Physics, RJ IBM **5612** (1987) 56922.

[9]. A. A. Gorokhovskii in: Zero-phonon lines and spectral hole burning in spectroscopy and photochemistry, ed. by O. Sild and K. Haller, Springer-Verlag, 1988.

[10]. K. K. Rebane in: Topics in Current Physics. Persistent spectral hole burning: science and application, ed. by Morerner (Springer, Berlin, 1987).

[11]. M. Drobizhev and M. Sapozhnikov, Chem. Phys. Lett. **236** (1995) 438.

[12]. W. E. Morerner, M. Gehrtz, A. L. Huston, J. Chem. Phys, **88** (1984) 6459-6460.

[13]. L. A. Rebane, A. A. Gorokhovskii, J. V. Kikas, Appl. Phys. B **29** (1982) 235-250.

[14]. R. M. Macfarlane in: Topics in Current Physics. Persistent spectral hole burning: science and application, ed. by Morerner (Springer, Berlin, 1987).

[15]. I. Sildos and A. Osvet, Diamond and Related Materials **3** (1994) 725.

[16]. I. Sildos, M. Aizergendler, I. Dolindo and I. Renge, Opt. Commun. **73** (1989) 223.

[17]. J. Zhang, S. Huang and J. Yu, Optics Lett. **17**, no. 16, (1992) 1146.

[18]. G. Small in: Spectroscopy and excitation dynamics of condensed molecular systems, ed. by A.V. Agranovich and R.M. Horchstrasser, North-Holland, 1983.

[19]. S. K. Lyo, Phys. Rev. Lett. **48**, no. 10, (1982) 688.

[20]. R. M. Macfarlane and R. M. Shelby in: Spectroscopy and excitation dynamics of condensed molecular systems, ed. by A.V. Agranovich and R.M. Horchstrasser, North-Holland, 1983.

[21]. L. R. Narasimhan, D. W. Pack, M. D. Fayer, Chem. Phys. Lett. **152**, no. 4-5, (1988) 287.

[22]. R. Jankowiak, L. Shu, M. J. Kinney and G. J. Small, J. Lum. **36** (1987) 293.

[23]. R. Jankowiak and G. J. Small, Science **237** (1987) 618.

Chapter 4

Applications of Persistent Spectral Hole Burning

Persistent spectral hole burning has the potential for technological applications to optical storage, pulse shaping, and optical signal processing. This has resulted in engineering and material research on PSHB at a variety of laboratories around the world. This chapter concerns several engineering issues and basic materials requirements for commercial applications of PSHB[1] with particular emphasis on optical high-density data storage. To understand the real perspective of the PSHB storage products on marketplace, a short review of existing data storage techniques is presented below.

4.1. Overview of Existing Data Storage Technologies. [2]

Magnetic recording and optical recording are the major technologies used to provide long-term storage of information in today's computer systems. Magnetic recording has been used for data storage in computer systems for over 40 years, and the advances in technology that have occurred in that time frame are nothing short of phenomenal. Magnetic recording is now advancing at faster rate than at any time in the past. Magnetic hard drives represent the largest segment of the data storage business, and the number of hard-disk drives sold is increasing at about 20% per year.

The original hard-disk drive, which was known as the RAMAC was built by IBM in 1956, had an areal density of 2,000 bits/in^2, a data rate of 10 kbytes/s, and used 50 24-in. disks to store 5 Mbytes of information. It was considerably larger than a refrigerator and though mostly were leased, the cost was of the order of $100,000 ($20/Mbyte). By

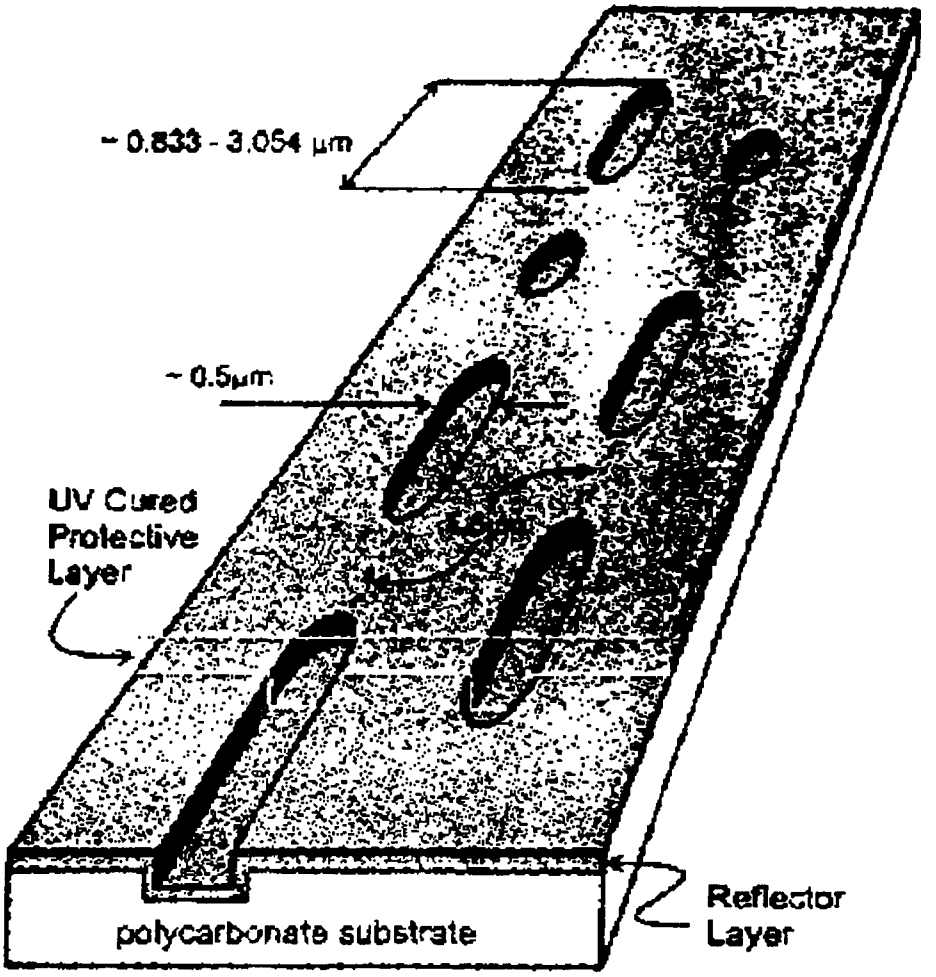

Figure 4.1. A fragment of a conventional optical disk[3].

comparison the most recent (March 1999) disk drive announced by IBM has an area density of 2.7 Gbits/in^2, a data rate of 19.7 Mbytes/s, and uses three 2.5-inch disks to store 36.7 Gbytes of information.

Key to achieving higher areal densities in magnetic disk hard drives is lower head-disk spacing, higher coercivity, and lower noise magnetic coatings on the disks, and both higher magnetization write heads and higher sensitivity read heads.

A fundamental problem for magnetic hard disk recording that has been recognized for many years and that must be eventually overcome in hard-disk drives is the fact that as the bit and the grain sizes are being reduced, the magnetic anisotropy energy K_uV, which keeps the magnetization stable (where K_u is the magnetic-anisotropy-energy density and V is the volume of the magnetic switching unit), is becoming smaller and approaching thermal energy k_BT (where k_B is Boltzmann's constant and T is the absolute temperature). Calculations suggest that with continued liner scaling of magnetic recording, somewhere between 10 and 100 Gbits/in^2, the grain size will become so small that thermal instabilities will become a problem. At today's rate of progress, this will occur some time between 2001 and 2006[2].

Optical recording was introduced into marketplace in 1982 (by SONY and Philips) and has secured a significant market. However, thus far, optical recording has primarily found new market niches, rather than being directly competitive with magnetic recording. CD-ROMs are widely used for the distribution of the prerecorded information – a business that is now comparable in size to the magnetic drive business. New DVD technologies are expected to enjoy larger markets than previous optical recording technologies, but they are not expected to impact upon the hard disk drive business. They

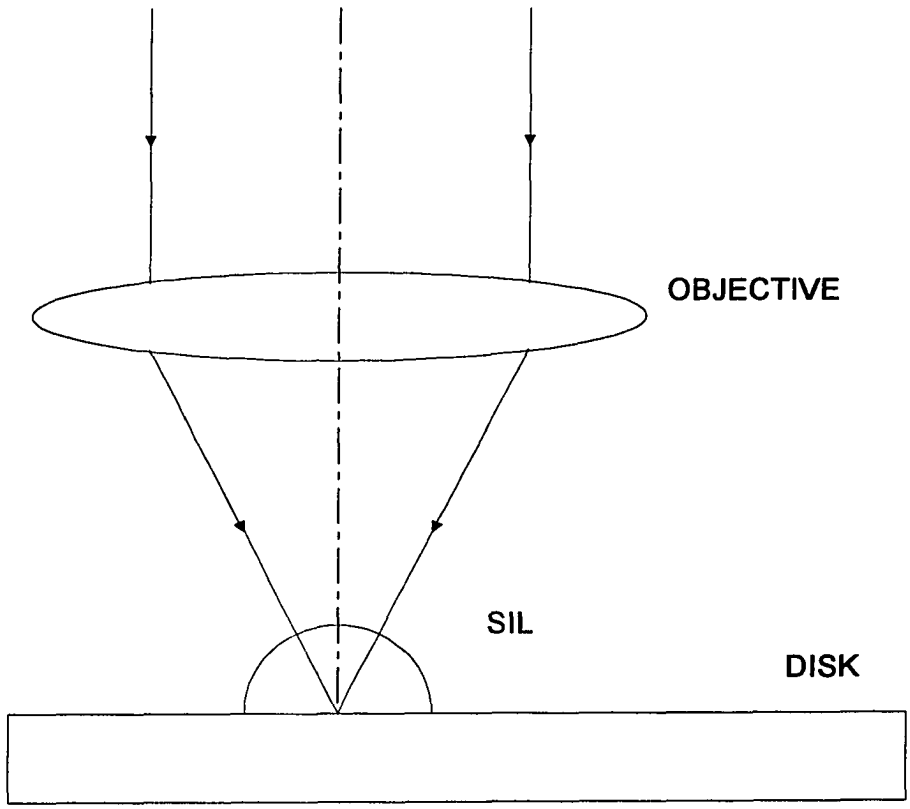

Figure 4.2. A simplified configuration for Near-Field Storage optical system with solid-immersion lens (SIL)[3].

are likely to compete for some of the same markets as type drives and flexible disk drives, but it looks like all of these technologies will continue to enjoy significant markets for at least the next 5-10 years.

Approximately 90% of all personal computers shipped today contain a CD-ROM or DVD drive. This large installed base, plus the low cost of the disk ($0.005/Mbyte for a "one-off" recorded CD, and even less for mass replicated CD) makes CD the ideal format for distributing or sharing digital data[3].

Initially, the optical disk family consisted only of ROM disks. Information is first laser-recorded in photoresist on a high-quality disk substrate, which is a process called mastering. The photoresist is then developed and coated with a metal layer. The coated substrate is called a stamper and it has protrusions where photoresist was exposed by the laser. The stamper is used as one face of a mold that is injected with molten polycarbonate plastic. The plastic creates disc substrate, which now contains depressions where the photoresist was exposed. These depressions or "pits" form a continuous spiral. The side of the substrate with the pits is coated with aluminum or aluminum alloy. The reflective layer is protected by coating, which is generally a UV cured acrylate.

During reading, light from a laser is focused through the substrate onto the reflective layer, forming a spot with diameter of 1 μm. Since disks consist of transparent plastic and aluminum alloy reflector, the reflectivity of the pits and the surrounding region (the "land") is the same; interference effects, not reflectivity variations, form the basis for the detection of the pits. Since the pits are narrower than the diameter of the focused laser spot, as a pit is rotated under the spot, both the pit and the surrounding land are illuminated. As the pits are approximately $\lambda/4$ deep, the light reflected from the bottom of

the pit is shifted in phase by $\lambda/2$ relative to light reflected from the land. As a result, light reflected from the two areas destructively interfere, making a pit appear dark (see Fig. 4.1).

The digital information is actually stored in the position of the edges of the pits. A transition from light to dark or dark to light (corresponding to a pit edge) during a clock cycle corresponds to a "1", the lack of transition corresponds to "0".

In conventional recordable/rewritable laser-disk drives optical recording is performed by a focusing a laser beam to a diffraction-limited spot $\approx 1\mu m$ in diameter on a recording material and modulating the light according to the information. For example, in recordable CD-ROM, the light is absorbed by the dye, causing it to reach a temperature of several $100\ ^0C$. For the cyanine dye recording layers, this causes the dye to bleach, which greatly reduces both the real and imaginery parts of the index of refraction. For the phthalocyanine dye recording layers, a chemical reaction produces a physical vesicle in the recording layer. In either case, the optical properties of the exposed region are changed in a way that reduces the light reflected by an amount similar to that caused by the pits in a molded CD.

For common optical storage, areal storage densities can approach 1 Gbits/in^2, and are fundamentally limited by optical diffraction. Recently developed near-field optical storage is using solid immersion lens (SIL) that is essentially in contact with recording layer. The simplest form of SIL is a semisphere of glass (see Fig. 4.2). Because the effective wavelength inside the SIL is reduced by the refractive index n, the spot size is

	Magnetic Hard Disk	*Laser Disk*	*Holographic Disk*	*Hole-Burning Storage*
Today's Density	3 Gbits/in^2	1 Gbits/in^2	0.5* Gbits/in^2	8* Gbits/in^2
Cost	5 c/MB	0.5 c/MB	?	?
Density Limit	10-100 Gbits/in^2	1 Gbits/in^2	10-100 Gbits/in^2	1000 Gbits/in^2
Limited By	Thermal instability	Diffraction	Material and diffraction	Material

* laboratory demonstration

Table 4.1. Comparison of today's and future data storage technologies.

reduced by factor *1/n* compared to focusing in air. For typical glasses, this implies that the spot size can be reduced by a factor of two. The corresponding increase in areal density is a factor of four over the 1 Gbites/in^2 density of a CD.

Holographic data storage offers the potential of storing pages of information optically in three-dimensional material and accessing it a page a time. Hence it potentially offers large, volumetric storage density, high data rate, and short access time. Holographic memories, first investigated in the late-1960s and early-70s, have made a remarkable comeback in the 1990s. Rewritable holographic memories are typically demonstrated with photorefractive crystals. Such memories have high storage density due to 3-D recording, fast read-out rate due to the parallel retrieval of entire pages, and potentially faster random access than magnetic disks. More than 1,000 holograms can be superimposed at one location, each hologram containing 1 Mbyte of data. So, approximately 1 Gbyte is stored in 1 cm^3 crystal[3]. The maximum read-out rate that has been demonstrated is 1,000 holograms per second corresponding to an impressive 1 Gbyte/s read out rate with each hologram storing 1 Mbyte. The demonstration of fast read-out is important because rewritable holographic memory products can find a place in the market only if they can be made faster than magnetic disks and at the same time cheaper than dynamic random access memory (DRAM). The main remaining problem to be solved is the development of a reliable, erasable, optical material for this application. The most serous shortcoming of photorefractive materials is volatility: holograms decay when they are read-out. The availability of recording materials will dictate if and when holographic memory products will be introduced in the next few years. While the theoretical storage density of

holography is $1/\lambda^3$, one must take a more conservative view for the near term and assume the real storage density to be about 10 Gbits/in^2.

4.2. Engineering Issues for Frequency Domain Optical Storage. [4]

Compared to conventional optical storage techniques, which areal density is fundamentally restricted by diffraction-limited laser spot, the phenomenon of persistent hole burning in solids at low temperatures (4 K) allows the use of the laser frequency as an extra dimension. When the presence or absence of a spectral hole at designated frequencies corresponds to a "0" or "1", the frequency domain can be used for information storage with the storage density increased approximately by the factor of $\Gamma_{inh}/\Gamma_{hom}$ over conventional techniques. This ratio can be as high as 10^8, depending on the specific properties of the active center and host used, and is highly temperature dependent. Therefore, thousands of bits can, in principle, be stored in the frequency domain in the volume illuminated by a focused laser beam, offering the potential for storage densities as high[51] as 1000 Gbits/in^2. The cost per megabyte is expected to be very low because of the relatively low cost of the materials and the very high data density which can be stored using this technique. Work is being carried out at many location throughout the world and competition is high. It is estimated that the time to the working prototype is in the range of 5-10 years.[2]

Today PSHB storage remains promising direction among known types of storage with respect to possible storage density and cost per megabyte stored information. The properties of the recording materials naturally place certain constraints on the system

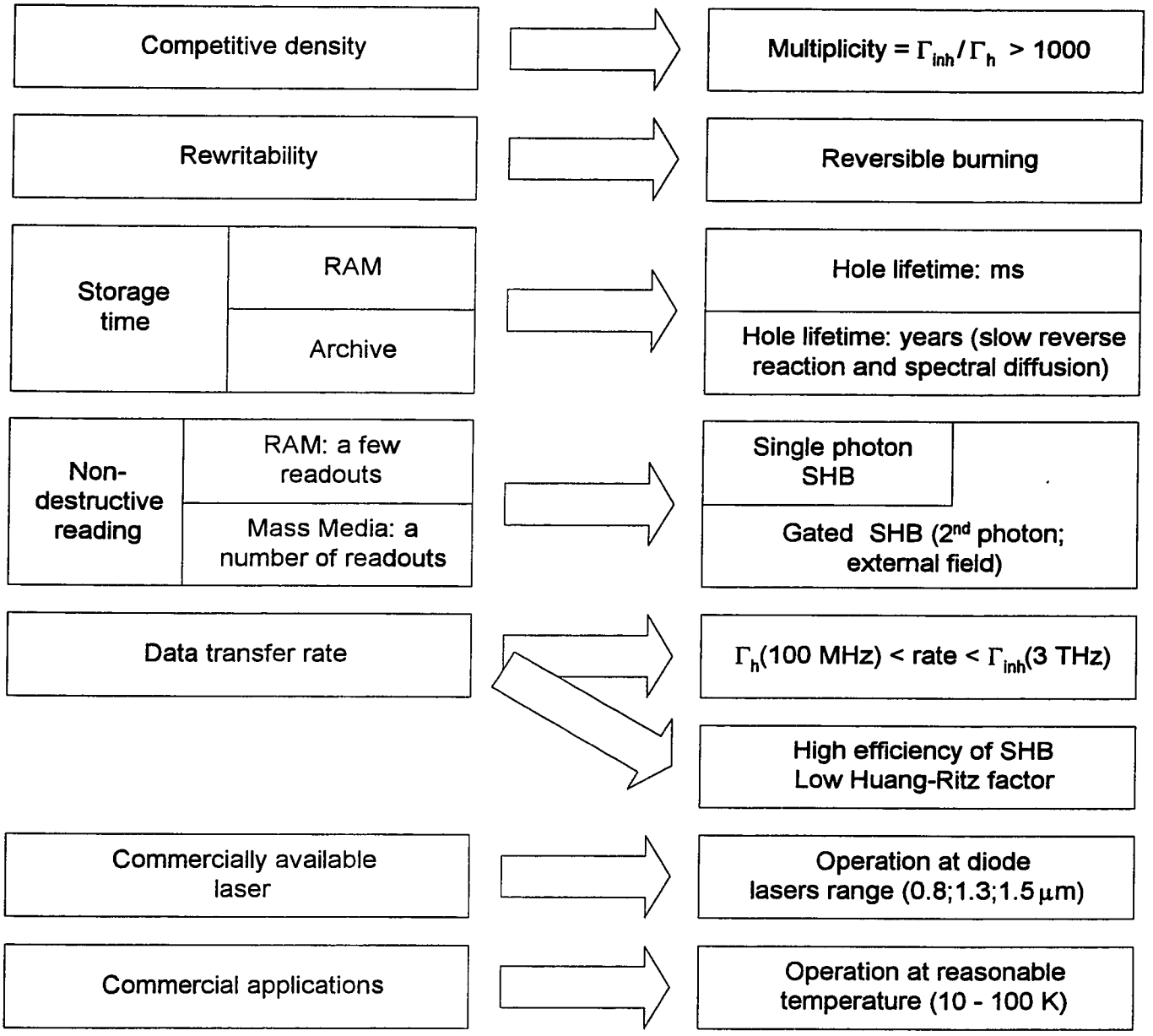

Figure 4.3. Engineering issues and material requirements for frequency domain PSHB storage systems.

configuration for frequency domain optical storage. At the same time, the system configuration places certain requirements on the recording material, and it must be capable of delivering the required signal-to-noise ratio in an appropriate bandwidth for practical data storage and retrieval. There are several critical for frequency domain memory engineering issues that have to be considered:

- The demands on laser performance are much more stringent in frequency domain optical stirage than in laser optical disk recording. Tunable laser with high tuning rate and wide tuning range is required. A suitable diode laser should operate in a single transverse and longitudinal mode and exhibit narrow (a few MHz) linewidth.
- Hole detection is a crucial requirement. Hole must be detected at a rate on the order of 30 ns/bit (to match modern data exchange rates) with signal-to-noise ratio (SNR) adequate for digital data retrieval, i.e. 26 dB in the 16 MHz detection bandwidth (the detection bandwidth is chosen to be in agreement with reading/writing rate 30 ns/bit, and SNR = 26 dB is chosen to be consistent with conventional optical memory standards).
- Low temperatures are necessary for reading and writing of the spectral holes (This is essential to keep the absorption line inhomogeneously broadened). Therefore, configuration of focusing optics and beam positioning system (x-y access) must provide remote operation to keep major electro-optical components outside the cryostat with liquid helium.
- Simultaneous spectral and high density spatial recording with low crosstalk places extra constraints on a whole optical system.

Operation at elevated temperatures is a problem for any type of storage systems. Temperature is a substantial destructive factor for all existing memories. Table 2 shows time periods of full degradation for today's memories as a function of temperature and relative humidity. However, for PSHB memory, operation at reasonable temperature appears to be a pressing problem. At the present moment, there are no indications that it is possible to keep spectral line inhomogeneously broadened at room temperature. Still, a temperature range 10-77 K can be considered acceptable for modern refrigeration systems. Therefore, search for novel materials should be directed to compounds which exhibit high quantum efficiency and high multiplicity (i.e. inhomogeneous-to-homogeneous linewidth ratio) in the temperature range accessible by commercial refrigeration systems. In this connection, closed cycle refrigeration (CCR) systems are very attractive for temperatures above 8 K due to their immediate advantages of a compact size, operation in any orientation, lack of liquid helium, and ability to achieve low temperatures in relatively short time.

4.3. Material Requirements for Frequency Domain Optical Storage.

Any reasonable system design also places demands on the properties of the photoactive hole-burning materials. It is important to note that implementation of different types of memory, i.e. archival memory, RAM memory etc., requires substantially different physical properties of recording material (see Figure 17). However, several basic materials requirements for the frequency domain optical storage have to be satisfied for any commercial system:

Temperature	RH	Magnetic storage		CD-ROM	Newspaper	Silver Microfilm
		Hard Disk	Tape			
50^0F (10^0C)	25%	30-50 years	15-50 years	30-200 years	200 years	500 years
68^0F (20^0C)	40%	10-15 years	5-10 years	10-50 years	15-20 years	200 years
104^0F (40^0C)	80%	3-6 months	3 months	1-2 years	3 months	10-20 years

Table 4.2. Temperature as a destructive factor for today's storage systems (based on data from Ref. 5).

- Holewidth 100-500 MHz. Holes much narrower than 100 MHz would be broadened by Fourier transform limitations during the required reading time of 30 ns/bit. If a hole is very broad, excessive demands will be placed on the tuning range of the diode laser.
- Operation at diode laser wavelengths. Since fast reading and writing must be achieved with a compact, low cost tunable laser, the ultimate PSHB mechanism must be active at tunable single-mode diode laser wavelengths.
- Reversible burning. The problem of reversal of the hole formation process is very important because an archival, write-once low-temperature storage system would not be practical.
- Long hole lifetime at low temperatures for archival storage and transient hole burning for RAM and associated applications.
- Thin-film compatibility. Since the laser spot for reading and writing must be on the order of 10 μm in diameter, the recording material must be fabricated in a thin film of thickness on the order of the Rayleigh range of the beam waist. This is to prevent overlap of the written information in adjacent spatial regions.
- Fast burning (30 ns/bit). It is chosen to match the data rate of conventional magnetic and optical recording technologies.

Therefore, a material, in order to be useful in a practical storage system, must simultaneously show several required properties: the ability to form deep holes in short burning times (30 ns/bit) and yet allow fast reading (30 ns/bit) at high SNR with focused reading beams. More detailed analysis of material requirements for PSHB storage should take into account if a single-photon recording mechanism or photon-gated mechanism of hole burning is used

4.4. Limitations of a Single-Photon Mechanism.[6]

The essential problem with such mechanisms is that there is no threshold in the hole formation process. To illustrate the central issue, a material with low hole-burning efficiency would be quite easy to read without serious destruction of the written holes, but such a system would be difficult to write with high contrast in short burning times. Conversely, a system that allows fast burning due to high quantum efficiency for hole production would be difficult to read without burning of the unburned centers by the tightly focused laser beam. The thorough analysis[45] of the coupled fast reading and fast writing problem in small spots shows that useful single-photon material must have low absorption cross section and high quantum efficiency. Optimal region for these parameters can be roughly determined between 10^{-2} 10^{-1} for quantum yield and between 10^{-15} and 10^{-14} cm^2 for low temperature peak homogeneous absorption cross section (see Fig. 4.4). High solubility 10^{19} - 10^{20} cm^{-3} is also important. Major constraints can be understood qualitatively: arbitrarily small cross section cannot be used, because the resulting concentration of centers (which is needed to maintain reasonable signal to noise ratio) would become large enough to cause hole broadening owing to spectral diffusion. A good rule of thumb is to require that relative molar concentration of absorbing centers be kept below 1 mol. %. In addition, extremely large quantum efficiencies near 1 result in hole broadening owing to the reduction in excited state lifetime that occurs when the photochemical reaction occurs too readily. The other constraint for large cross section and low quantum efficiency comes from power broadening during reading (see Section 3.4).

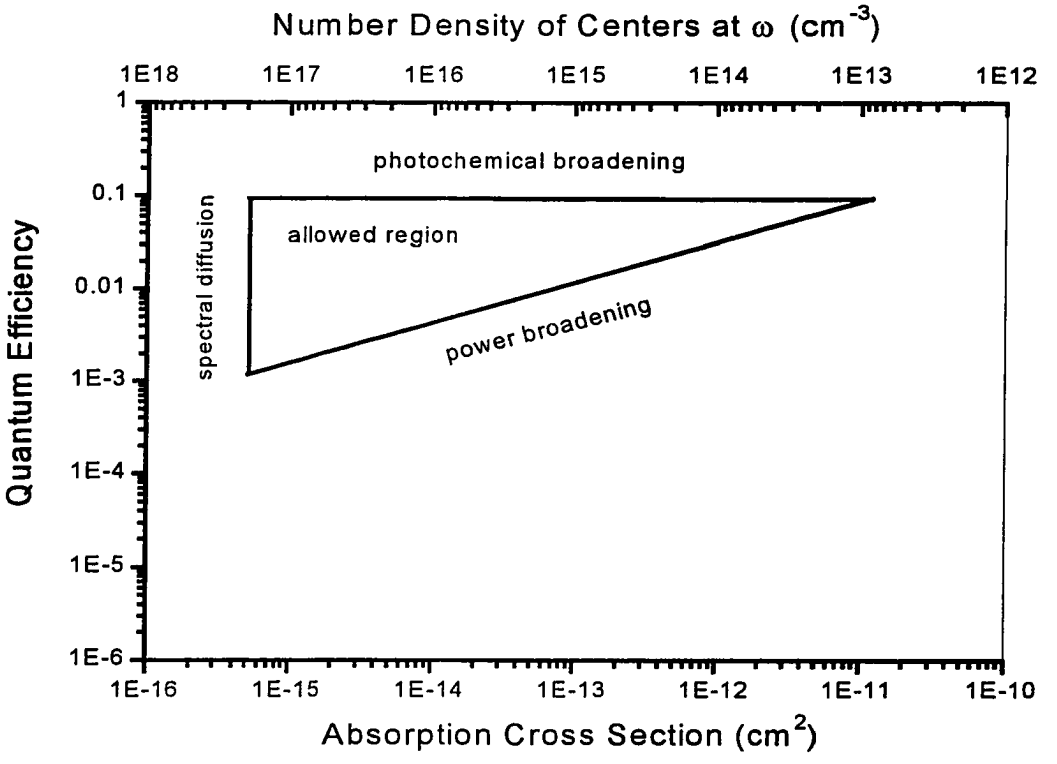

Figure 4.4. Allowed region of quantum efficiency, number density of centers at ω, and peak low temperature absorption cross section in order for the first read to yield acceptable SNR[6]. Optimization performed for 30 ns read/write time per bit, 10 μm diameter laser spot, 100 μm thick sample, and 10 mW maximum reading power.

4.5. Material Requirements for Photon-Gated Mechanisms.

To provide fast burning, high signal to noise ratio, fast reading and focused spot, gated hole burning mechanism is essential. Gated mechanisms add a threshold to the writing process, which allows the reading process to be nondestructive. The performed analysis[7] was looking for appropriate values for the absorption cross section (for frequency selective transition), the density of centers within a homogeneous width of the laser frequency, sample length, and quantum yield that result in SNR > 26 dB in a 16 MHz bandwidth. Result of the optimization procedure is presented in Fig. 4.5. Materials within the shown boundaries for quantum efficiency 0.1 permit data readout with SNR equal to or greater than the required value with a maximum of 10 mW reading power. For high cross sections and large values of (concentration)x(thickness) the optical absorption becomes so strong as to prevent sufficient light from reaching the detector. For high cross sections and low values (concentration)x(thickness) the achievable SNR is limited by power broadening of the detected holes. For cross sections less than 10^{-15} cm^2 the avalable laser power of 10 mW is lower than the saturation power, thus the available reading power defines the SNR limit. At the top of the figure, undesirable interactions between the optically active centers, e.g. energy migration and cooperative excited-state quenching, can restrict the usable concentration of centers; this limit is highly material dependent.

4.6. Storage Density Limit.

The theoretical recording-density limit of PSHB memory has to be considered as a function of readout time, required SNR, and recording material parameters such as absorption cross section, concentration, hole depth multiplicity, and

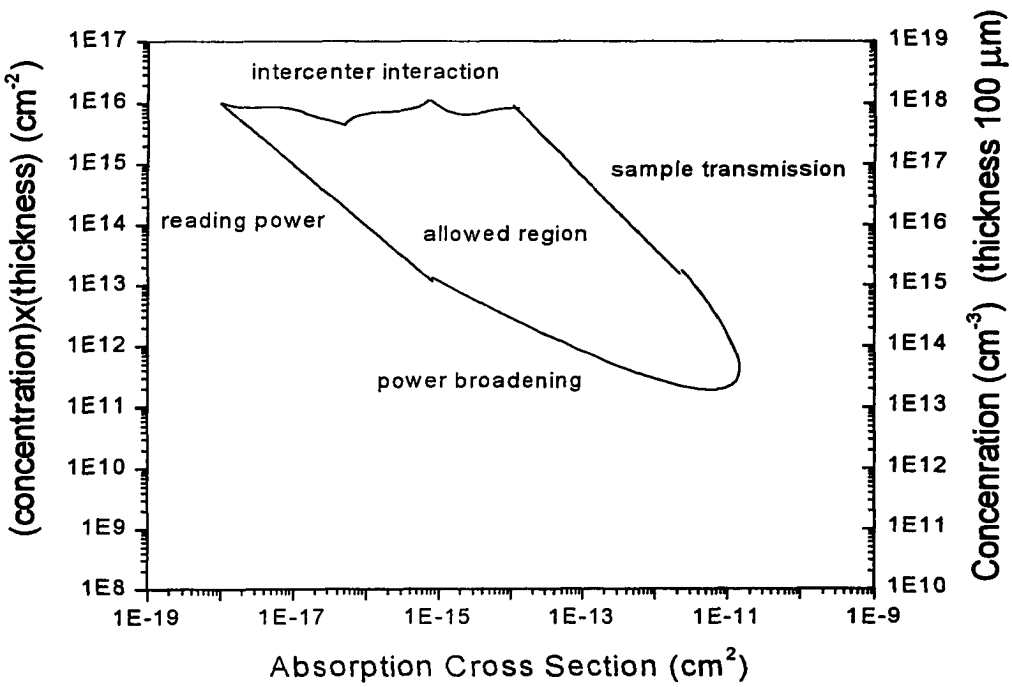

Figure 4.5. Materials constraints for gated PSHB materials in order to achieve practical SNR[7].

excited state lifetime of active centers. Shot noise and material noise have to be considered as a principal noises. These two noises originate in the fluctuation of the number of generated electrons in photodetector and the active center concentration respectively. For traditional PSHB system configuration, shot noise is about 90% of the total noise[8]. Nevertheless, material noise can impose a limit on the achievable storage density for a given concentration of storage centers. A tightly focused laser spot may interact with such a small ensemble of centers that statistical number fluctuations on the inhomogeneously line become noticeable.

The result of theoretical analysis for storage density limit is presented in Fig. 4.6. It was found that the limit for areal storage density of PSHB memory with realistic multiplicity $\Gamma_{inh}/\Gamma_{hom}$ is impressively high. Operating with 10^6 color channels and reasonable signal efficiency, this technology can achieve a 10^3-fold increase in areal storage density over that available with traditional optical memories.

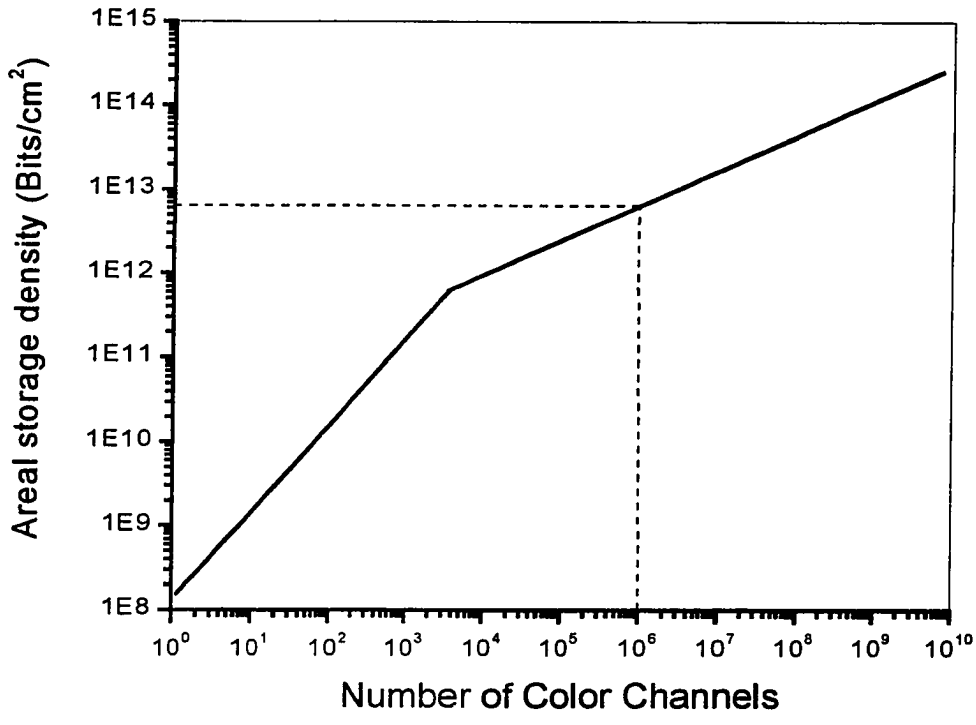

Figure 4.6. Maximized areal storage density for PSHB memory[9]. Optimization performed for the following parameters: the number of active atoms per bit necessary to produce reliable signals is 10^4, the operational wavelength is 780 nm, the maximum concentration of the active centers is 10^{20} cm^{-3}.

References for Chapter 4

[1]. W. E. Moerner in: Topics in Current Physics. Persistent spectral hole-burning: science and application, ed. by Morerner (Springer, Berlin, 1987).

[2]. M. Kryder in: MRS Bulletin, September 1996, Vol. 21, No. 9.

[3] D. Psaltis, D. Stinson, and G. Kino in: Optics and Photonics News, November 1997 and references therein.

[4]. W. E. Moerner, W. Lenth, and G. C. Bjorklund in: Topics in Current Physics. Persistent spectral hole-burning: science and application, ed. by Morerner (Springer, Berlin, 1987).

[5]. G. Ashton, Media National Laboratory, Annual Report, 1996.

[6]. W. E. Moerner and M. D. Levenson, J. Opt. Soc. Am. B, Vol. 2, No. 6 (1985) 915.

[7]. W. Lenth and W. E. Moerner, Opt. Commun. **58** (1986) 249.

[8]. N. Murase, K. Horie, M. Terao, and M. Ojima, J. Opt. Soc. Am. B, Vol. 9, No. 6 (1992) 998.

[9]. W. R. Babbitt and T. W. Mossberg, J. Opt. Soc. Am. B **11** (1994) 1948.

Chapter 5

Experimental Methods, Setup and Instruments

This chapter contains a short review of experimental methods widely used in persistent spectral hole burning. Some unique components of the experimental setup and instruments used during Thesis research are described in detail.

5.1. Introductory Remarks on Experimental Methods of PSHB.

To detect a spectral hole or/and hole burning kinetics, one should find a way to observe a population redistribution or/and dynamics in the ground state of the studied inhomogeneously broadened transition. Hence, fine measurement of change in absorption is required. There are two quite straightforward methods can be proposed to measure absorption. First method is a measurement of direct transmission. Second one is a measurement of the luminescence excitation spectrum. In both cases the detected signal is proportional to the absorption, i.e. the population of the ground state. Obviously, the transmission measurements can not be applied for non-transparent or highly scattered samples, while measurement of the luminescence excitation spectrum requires noticeable phonon sideband of the studied zero-phonon line.

Considering very small widths of the homogeneous lines involved in the hole burning experiment at low temperatures, ultra-high resolution spectral technique is needed. Therefore, the narrow band single mode tunable laser becomes the primary element of any hole burning setup. Narrow spectral line of laser irradiation enables site-

selective excitation of particular sub-set of absorbing centers within the inhomogeneously broadened band. Continuous tuning of the laser frequency gives an opportunity to scan over particular spectral range and detect photoinduced changes in the absorption spectrum, i.e. spectral holes.

Any hole burning experiment includes two major steps: (i) burning and (ii) detection (scanning) of the hole. Actual phototransformations in the sample under investigation are taking place during burning of a hole. Monitoring a time varying signal, one can follow dynamics of a hole burning process. Analyzing hole growth kinetics, quantum efficiency of a hole burning and information on hole-burning mechanism for a particular compound can be obtained (see Chapter 6). To measure a hole shape, a substantially decreased intensity of a laser beam is used to prevent undesirable burning. Scanning a tunable laser over particular spectral range (usually in the vicinity of burning frequency), a hole spectrum can be recorded.

5.2. Experimental Setup and Instruments.

Our current setup for the site-selective spectroscopy consists of a single frequency tunable Ti:Sapphire/Dye laser (COHERENT 899-29) pumped by Argon laser (COHERENT INNOVA 310), spatial filter (SF), optical power stabilizer (PS), OXFORD variable temperature optical helium cryostat with helium pump line, GaAs thermocooled photomutiplier HAMAMATSU (P), photodiodes (PD), McPherson monochromator, STANFORD RESEARCH lock-in amplifier, wavelength meter (WM) and computers for laser control and data acquisition, and the graduate student (see Figure 5.1).

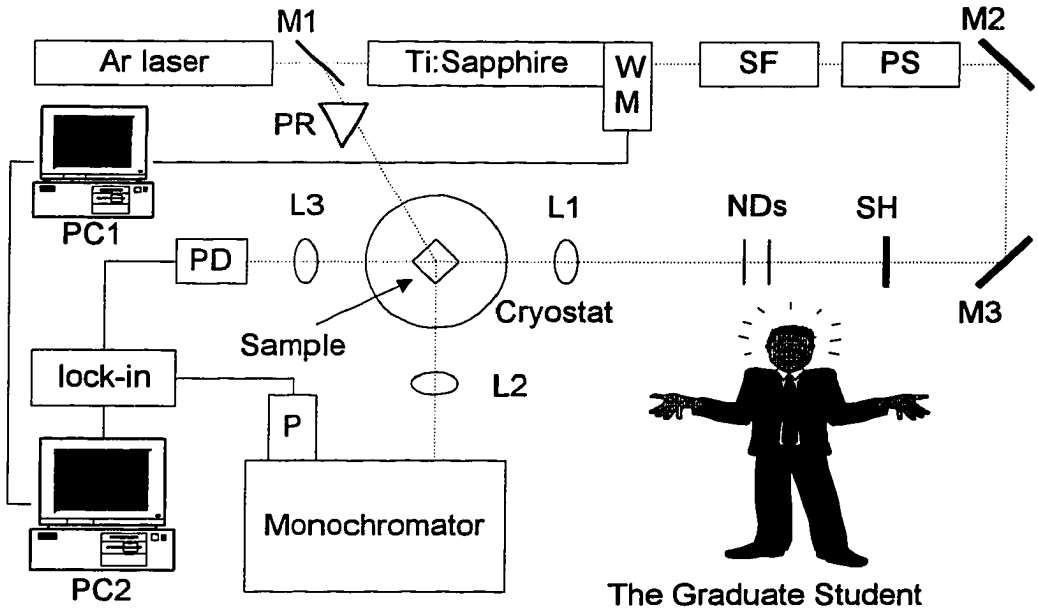

Figure 5.1. Configuration of the current experimental setup used during the Thesis research.

Present experimental configuration allows various types of PSHB related measurements, including high resolution (1 MHz, limited by laser jitter) hole-burning absorption and (or) fluorescence excitation spectra with relative hole depth down to 0.1% in the temperature range 1.3-300 K. The following experiments are possible with minimal restructuring of the experimental setup shown in Fig. 5.1:

- Spectral hole burning in photoluminescence excitation spectrum. Spectral selective excitation is provided by Ti:Sapphire laser with luminescence detection of a phonon sideband by photomultiplier via monochromator. For detection of very weak signals the monochromator can be replaced by suitable narrow band filter.
- Spectral hole burning in absorption spectrum. Signal detection in direct transmission is provided by photodiode.
- Luminescence Line Narrowing measurements with selective excitation by Ti:Sapphire laser into ZPL and detection via phonon sideband by photomultiplier with scanning monochromator.
- Photoluminescence measurements with excitation by Argon laser. Additional mirror M1 and prism PR have to be installed. Simple combination of the prism and aperture allows selection of any Argon laser line. Detection is provided by the monochromator and photomultiplier.
- Time resolved measurements using Argon laser, Ti:Sapphire laser or external laser excitation with acousto-optical modulator (not shown) or mechanical shutter (SH). Detection by photomultiplier (resolution up to 1 ns) or photodiode.

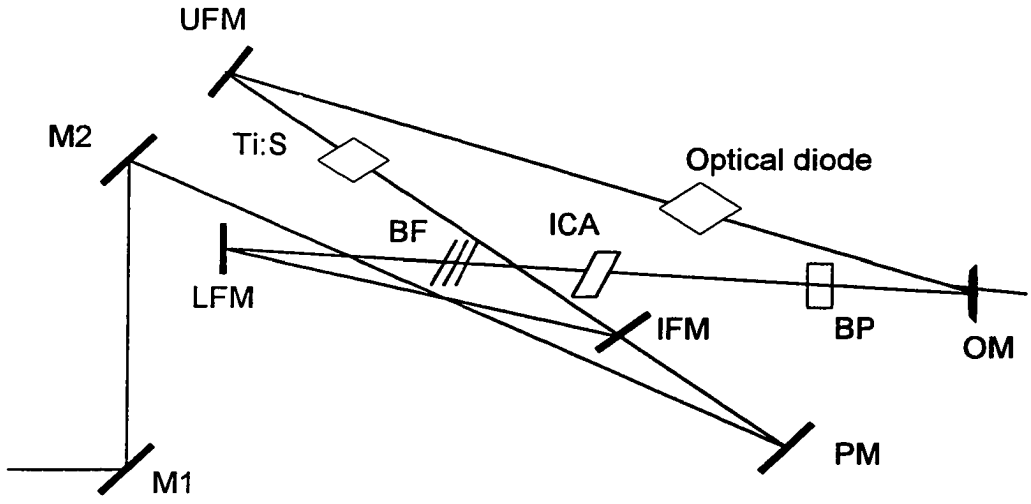

Figure 5.2. Optical diagram of the COHERENT 899-29 laser[2]. PM, LFM, IFM, UFM and OM stand for pump, lower fold, intermediate fold, upper fold and output mirrors respectively; Ti:S is a titanium:sapphire crystal; see text for further explanations.

5.3. Major Elements and Components. [1]

The central component of the PSHB experimental setup is *a tunable single-mode narrow band laser*. The model 899-29 Ring laser is a convertible ring laser that can operate as a conventional dye ring laser, or it can operate as a solid state ring laser using titanium:sapphire as a gain medium. It is tunable from 680 to 1025 nm in titanium:sapphire operation (the effective tuning range is limited by the reflectivity curve of the resonator mirrors, and for an optimum output power over the whole spectral range three different sets of mirrors are used). A medium power pump laser Innova 310 10W argon ion laser is used as the pump source. The 899-29 incorporates passive and active frequency control in order to obtaine stable operation in a single longitudinal cavity mode. The system may also be scanned without loss of frequency stability. An optical diagram of titanium:sapphire laser configuration is shown in Fig. 5.2.

All components and stages are mounted directly or indirectly to a 2-inch Invar bar that provides mechanical strength and length stability due to low coefficient of thermal expansion. This results in passive cavity length thermal stabilization of less than 1 μm/K.

Unidirectional lasing is achieved with *an optical diode* which is a device that has low losses for light passing into one direction but sufficiently high losses to prevent laser oscillations for light travelling into the opposite direction. It consists of a Faraday rotator which turns the plane of polarization by the angle $\pm\alpha$ (Fig. 5.3), a birefringent crystal which also turns the plane of polarization by α, and elements with a polarization-dependent transmission such as Brewster windows. For the wanted direction the turning angles $-\alpha+\alpha=0$ just cancel while the other direction results in reflection losses at the Brewster windows.

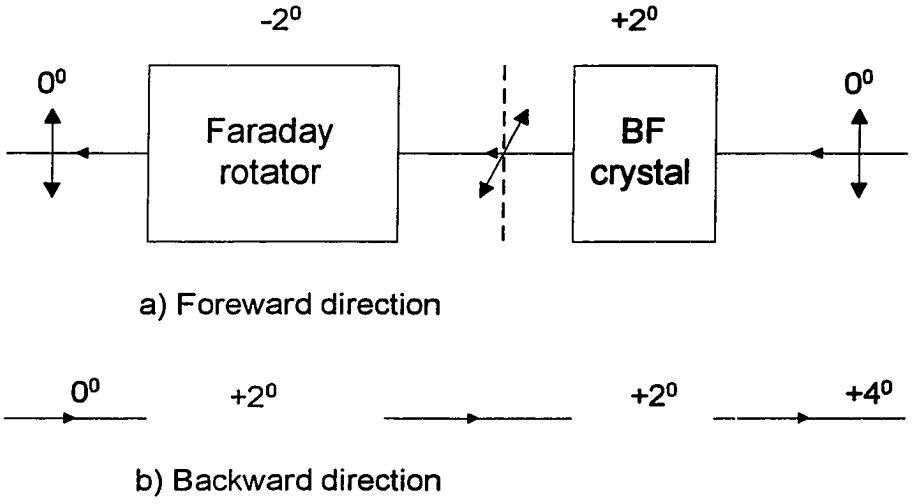

Figure 5.3. Simplified illustration for a principle of operation of optical diode. Tilting of the polarization vector for the forward (a) and backward (b) directions are shown.

Passive frequency control is achieved with a series of intracavity frequency filters. The three plate birefrinngent filters (BF) allows broadband operation with a bandwidth of 2 GHz. This filter is uncoated and mounted at Brewster angle to ensure maximum tuning range. The elementary birefringent filter (*Lyot filter*) consists of a birefringent crystal placed between two linear polarizers. Assuming that the two polarizers are both parallel to the electric vector of the incoming wave, the transmission of the BF filter is a function of the phase retardation between an ordinary and an extraordinary beams:

$$T(\lambda) = T_0 \cos^2\left(\frac{\pi \Delta n L}{\lambda}\right) \tag{5.1}$$

where $\Delta n = n_0 - n_e$ is a difference in ordinary and extraordinary indexes of refraction, and L is a thickness of the BF crystal. The free spectral range $\delta\nu$ can be obtained:

$$\delta\nu = \frac{c}{\Delta n L} \tag{5.2}$$

If N elementary BF filters with different lengths L_m are placed in series, the total transmission T is the product of the individual transmissions T_m:

$$T(\lambda) = \prod_{m=1}^{N} T_{0m} \cos^2\left(\frac{\pi \Delta n L_m}{\lambda}\right) \tag{5.3}$$

The free spectral range $\delta\nu$ of this filter equals that of the shortest component. The halfwidth $\Delta\nu$ of the transmission peaks is, however, mainly determined by the longest component. The wavelength of the transmission peak can be tuned by changing the difference Δn. It can be realized by changing the angle between the optical axis and the wave vector, which alters the index n_e. The difference $\Delta n=n_0-n_e$ therefore has an angular dependence. Turning the crystal around the axis of laser wave propagation results in a continuos change of Δn and a corresponding tuning of the peak transmission wavelength.

With the insertion of the intracavity etalon assembly (ICA), which consists of a *thick and thin etalons*, the operational bandwidth may be narrowed to 10 MHz. The coated etalons are of low finesse to allow broadband coverage. In order to implement continuos tuning, the transmission maxima of the wavelength selectors have to be tuned synchronously with the tuning of the resonator length. Then a tilted etalon with thickness t and refractive index n is employed, the transmission maximum λ_m which is given by

$$m\lambda_m = 2nt\cos\theta \qquad (5.4)$$

can be continuously tuned by changing the tilting angle θ. In all practical cases, including ours, θ is very small, and we can use the approximation for wavelength shift $\Delta\lambda=\lambda_0-\lambda$

$$\Delta\lambda = \frac{2nt}{m}(1-\cos\theta) \approx \frac{1}{2}\lambda_0\theta^2 \qquad (5.5)$$

where $\lambda_0=\lambda(\theta=0)$. Equation reveals that $\Delta\lambda$ is proportional θ^2, but is independent of the thickness *t*. Two etalons with different thicknesses t_1 and t_2 can be mounted on the same tilting device. The motor simultaneously drives a potentiometer which provides a voltage proportional to the tilting angle θ. This voltage is electronically squared, amplified, and fed into the piezo element of the resonator mirror. An exact synchronization of the resonator wavelength shift $\Delta\lambda_L=\lambda_L\Delta d/d$ with the shift $\Delta\lambda$ of etalon transmission maximum is realized with computer control. The continuous change of the resonator length *d* is limited to about 5-10 μm if small piezo cylinders are used (5-10 nm/V). Large tuning ranges are obtained by tilting *a plane-parallel glass plate* around the Brewster angle inside the laser resonator. The additional optical length through the plate at an incident angle α is:

$$s = d\left[\sqrt{n^2 - \sin^2\alpha} - \cos\alpha\right] \tag{5.6}$$

If the plate is tilted by the angle $\Delta\alpha$, the optical path length changes by:

$$\delta s = \frac{ds}{d\alpha}\Delta\alpha = d\sin\alpha\left(1 - \frac{\cos\alpha}{\sqrt{n^2 - \sin^2\alpha}}\right)\Delta\alpha \tag{5.7}$$

The Brewster plate is tilted in a controllable way by a galvo-drive, where the tilting angle is determined by the strength of the magnetic filed.

Active frequency control is achieved with an electronic servo loop and reference cavity (not shown in Fig. 5.2). The servo loop uses an error signal derived from the reference cavity when the laser frequency drifts. Part of the error signal is applied to the

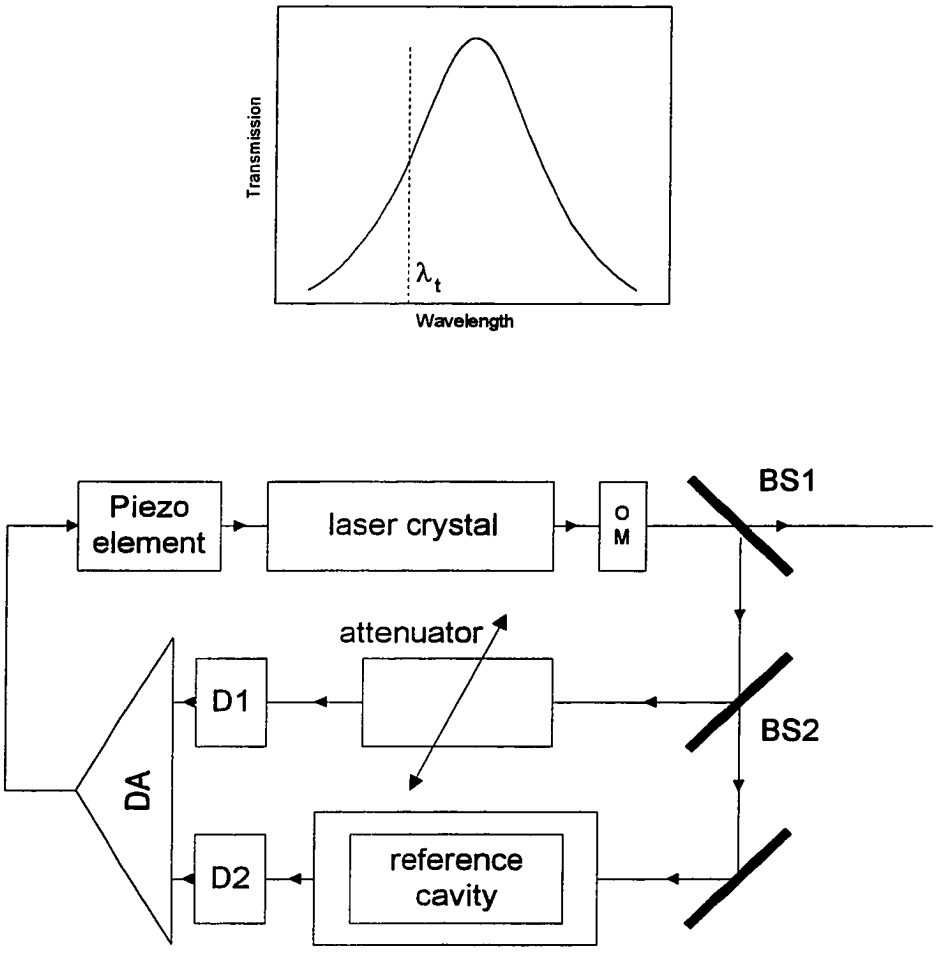

Figure 5.4. Wavelength stabilization onto the slope of the transmission of a stable reference cavity. DA stands for a difference amplifier, OM stands for an output mirror of a laser resonator.

tweeter (LFM) to correct for fast cavity length variation. The other part is used to drive the rotating Brewster's plate (BP) to compensate for the slower cavity length changes. With active frequency control, line width may be narrowed to 1 MHz. The detailed diagram of *wavelength stabilization system* in presented in Fig. 5.4. The wavelength λ_t at the turning point of the reference cavity's transmission peak $I_T(\lambda)$ (i.e. where the slope $dI_T(\lambda)/d\lambda$ has its maximum) is chosen as a reference point. The laser intensity $I_T(\lambda)$ transmitted through the reference cavity is compared with a reference intensity I_R split by BS2 from the same partial beam. The output signals from the two photodiodes D1 and D2 are fed into a difference amplifier, which is adjusted so that its output voltage becomes zero for $\lambda_L=\lambda_t$. If the laser wavelength λ_L deviates from $\lambda_L=\lambda_t$, signal from D1 becomes smaller or larger, depending on the sign of $\lambda_L-\lambda_t$, and the output of the difference amplifier is proportional to the deviation. The output signal passes PID control (see below) and a high-voltage amplifier, and is fed into the piezo-element of the resonator mirror.

Single mode frequency scanning in ranges up to 30 GHz is possible by continuously varying the cavity length with the rotating galvanometer driven Brewster plate. The Brewster plate is mounted at the vertex of the optical beam path. This design minimizes displacement of the intra-cavity beam while maintaining a constant reflection loss of about 0.4% during a scan. The thickness of the thick etalon may be varied with the piezoelectric transducer in order to track the laser frequency as it is scanned. The thin etalon is tuned by a galvanometer drive which controls the tip angle.

Laser system can be controlled by computer Autoscan system. The most prominent feature of Autoscan is the on-board wavelength meter (WM, Fig. 5.1), a device capable of determining the laser wavelength to an absolute accuracy of $\pm$ 200 MHz ($\pm$ 7×10^{-3} cm^{-1}).

Interfaced to a PC (PC1, Fig. 5.1) with special hardware and software, Autoscan can automatically tune to any desired wavelength within the bandwidth of the laser gain medium. The overall alignment of BF filter and ICA is controlled by Autoscan via signals from sensors placed in laser head which monitor reflections.

An additional feature is the incorporation of data collection capability into the system electronics. With three data input channels available, Autoscan can automatically sweep wavelength calibrated data from external instrumentation (i.e. from lock-in amplifier or photodiode, in the current configuration of the experimental setup).

Wavelength meter is a core of the Autoscan system. Wavelength meter includes Optical Activity Monochromator (used for course wavelength determination) and Vernier Etalon (used for fine wavelength determination). An etalon is used as a primary component of wavemeter besause of its high resolution wavelength selecting capability. With an etalon, laser frequency is given by the expression:

$$\nu_{LASER} = n_{etalon}\frac{c}{2d} + \Delta\nu \qquad (5.8)$$

where c/2d is a free spectral range of the etalon. In a scanning laser like COHERENT 899-21 $\Delta\nu$ is determined by measuring the difference between the laser frequency and the frequency of the nearest peak with a short scan and retrace back to ν_{LASER} that can be easily performed. The hard part of wavelength determination is finding the order n_{etalon}. The etalon transmission is a periodic function spanning all wavelength, so there is an ambiguity as to which peak ν_{LASER} located next to. One more etalon with slightly different

length is added to the system. The resulting etalon pair is called a Vernier Etalon (VET). In the VET the spacing between a peak in etalon 1 and the closest peak in etalon 2 increases until the peaks overlap and the pattern repeats. The VET order spacing is given by $c/2(d_2-d_1)$ and is equal to 150 GHz. This repetition period is much greater than the periods associated with the individual etalons (6.78 and 6.47 GHz). This increased repetition period helps to determine the laser frequency. It is important to note a fact that due to mechanical limitations of laser elements, which prevent system from repeatedly reproducing a desired configuration, the inherent error in a reading of an etalon is 1% of the free spectral range (FSR). The FSR of the etalons in the VET is chosen to be about 6.5 GHz; that is sufficient to achieve the necessary precision (±50 MHz). FSR can not be much smaller since it makes determination of the n_{etalon} more complicated. To complete wavelength determination using VET, it is necessary to measure the wavelength within the resolution of the one VET order (150 GHz). This is accomplished by Optical Activity Monochromator (OAM). The physical basis for the operation of the OAM is the rotation linearly polarized light in optically active crystalline quartz. The optical activity which is responsible for the polarization rotation is dispersive, i.e. each wavelength receives a different amount of polarization rotation. Employing differential measurement of rotation for two long pieces of quartz (111 and 107 mm), OAM is able to reach accuracy of rotation of polarization sufficient for spectral resolution of 150 GHz.

The intensity of a CW laser is not completely constant but shows periodic and random fluctuations and also, in general, long term drifts. Since these intensity fluctuations lower the signal-to-noise ratio, they may become very troublesome in detection of spectral holes with relative depth of less that 1%. Intensity stabilization system, incorporated in our

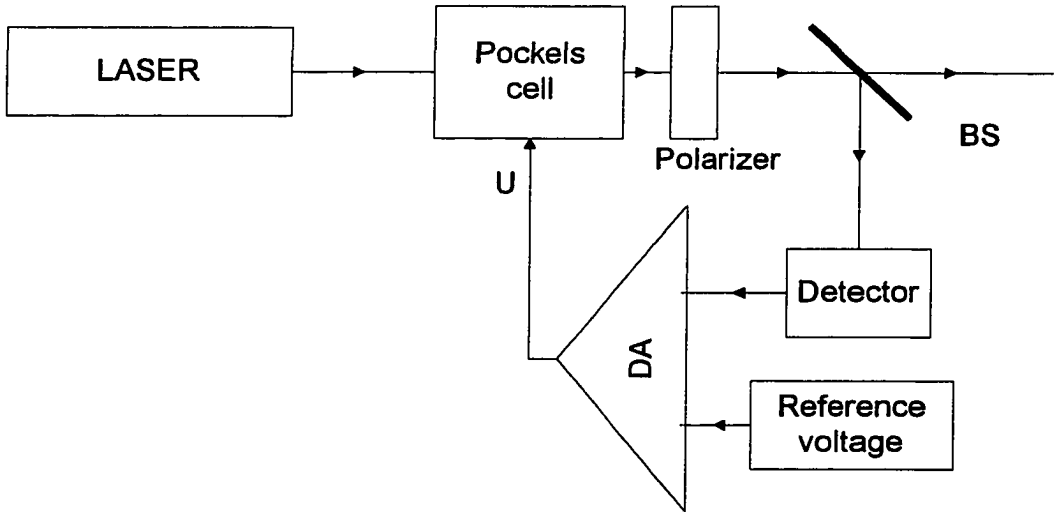

Figure 5.5. Intensity stabilization of laser by controlling the transmission of a Pockels cell. DA is a differential amplifier, BS is a beam splitter.

tunable laser, was proved to be non-adequate to our requirements. Some additional stabilizing elements had to be introduced. Currently, we are using spatial filter and optical power stabilizer. The LASS-II (Laser Amplitude Stabilization System) (PS, Fig. 5.1) by Conoptics, Inc. is an electro-optic feedback loop designed to reduce amplitude variations commonly associated with most lasers. The system allows to reduce optical noise up to 0.3%. Power stabilazer performance is affected by the quality of the input laser beam linearity and mode structure. Custom-built traditional spatial filter was installed before stabilization system to "clean up" laser output beam. The fundamentals of our *intensity stabilization system* operation are illustrated at Fig. 5.5. The output from the laser is sent through a Pockels cell, which consists of an optically anisotropic crystal (KDP, Potassium Dideuterium Phosphate), placed between two linear polarizer. An external voltage applied to the electrodes of the crystal causes optical birefringence which rotates the polarization plane of the transmitted light and therefore changes the transmittance throughout the second polarizer. If part of the transmitted light is detected, the amplified detector signal can be used to control voltage at the Pockels cell. Any change of the transmitted intensity can be compensated by an opposite transmission change of the Pockels cell. In principle, this stabilization control works up to frequencies in the megahertz range if the feedback-control electronics are sufficiently fast. Electronic system of feedback control includes three operational amplifiers with a different frequency response that are put in parallel. The first is a common *proportional* amplifier, with an upper frequency determined by the resonance frequency of the mirror piezo system. The second is *integral* amplifier. This amplifier is necessary to bring the signal, which is proportional to the intensity deviation, really back to zero. This can not be performed with a proportional amplifier. The third

amplifier is a *differentiating* device that takes care of fast peaks in the perturbations. All three functions can be combined in a system called *PID control.*

Detection system for regular hole burning measurements contained two Si photodiodes (Electro-Optical Systems), DSP Lock-In Amplifier SR830 (Stanford Research Systems), Optical Chopper 3501 (New Focus), Data Acquisition Board Lab-PC+, and a computer. During hole burning measurements in direct transmission, one photodiode was used for monitoring laser intensity to assure normal operation of the intensity stabilization system. And was connected directly to DAQ Board. Another photodiode was used to measure intensity transmitted through sample, and was connected to Lock-in Amplifier. Both photodiodes were dual gain photoreceivers with DC coupling, therefore, both modulated light signals and DC light levels were measured. Special care was taken to shield the units from any stray or room light during operation to prevent saturation of the incorporated preamplifiers.

Lock-in amplifiers are commonly used to detect and measure very small AC signals. Accurate measurements may be made even when the small signal is obscured by noise sources many thousands of times larger. Lock-in amplifiers use a technique known as phase-sensitive detection to single out the component of the signal at a specific reference frequency and phase. Noise signals at frequencies other than the reference frequency are rejected and do not affect the measurements. Hence, lock-in measurements require a frequency reference. In our case experiment was excited at a fixed frequency 2 kHz produced by optical chopper designed to interrupt light path; the lock-in amplifier detected the response from the experiment at the reference frequency. The chopper has a crystal controlled frequency synthesizer that serves as an internal frequency reference for locking

the chopper to a particular chopping frequency. Several measures ensure that jitter and drift of the chopping frequency is reduced to a minimum. Precision photo-etched wheels are mounted on a high quality DC motor. The motor head has a photo-sensor for monitoring the chopping frequency of the outer part of the wheel. The chopper controller then actively stabilizes the motor speed to match the desired chopping frequency. This technique minimazes phase noise at the chopping frequency and provides for long term stable chopping with a minimum frequency drift.

Computerized data acquisition system is based on multifunction analog, digital and timing I/O board. The Lab-PC+ contains a 12-bit A/D converter with eight analog inputs, two 12-bit D/A converters with voltage outputs, 24 lines of TTL logic compatible digital I/O, and three 16-bit counter/timer channels for timing I/O. Integrated user friendly software package enables control of the experimental setup and efficient real-time data acquisition, analysis, and visualization.

To provide low temperatures needed for spectral hole burning experiments, Optistat Bath by Oxford Instruments, Inc. was used. The cryostat contains a liquid helium reservoir, a liquid nitrogen reservoir, and a variable temperature insert. Four sealed windows allow performing any optical measurements with samples directly immersed in superfluid helium at 1.3K or in helium vapor at higher temperatures. Sample temperature is continuously variable between 1.3K and 300K and controlled by the ITC502 microprocessor based temperature controller. Temperature was measured by two sensors, one of them being mounted directly on the sample holder. In general, for use in cryogenic applications, ITC502 can accept a wide range of different temperature sensors and can

provide up to 80W heating power. In addition it contains internal logic to drive a motorized valve as a means of controlling sample cooling in a continuous flow cryostat.

For regular absorption measurements, Perkin-Elmer Lambda 900 spectrograph was used. For low temperature experiments, a cold head of closed cycle refrigeration (CCR) system CRYO Model 396-022 based on CTI CRYODYNE Model 22 refrigerator was inserted into one of the optical channels of the spectrograph. In general, CCR systems are very attractive for temperatures above 8 K due to their immediate advantages of a compact size, operation in any orientation, lack of liquid helium, and ability to achieve low temperatures in relatively short time. This CRYODYNE system is comprised of a water cooled compressor unit with oil separation system and refrigerator unit (cold head) located remotely from the compressor. Temperature is controlled by digital cryogenic temperature controller CONDUCTUS Model LTC-10. Helium gas is used as a refrigerant.

The cold head includes vacuumed chamber with four quartz windows and a sample holder attached to the cold finger. This allows the CCR system to be used for various optical and spectroscopic measurements. The minimal temperature was found to be 8 K. The system was able to reach this temperature in approximately 1.5 hour. Reverse process (with the compressor and the cold head turned off) takes approximately 20 minutes to warm up to 50 K, and about 4 hours to reach the initial room temperature.

The main disadvantage of low priced commercial CCR systems is vibration, which might substantially affect experimental results if not taken into consideration. A simple optical technique for studying mechanical vibration and the application of this technique for investigating the vibration of our CCR system is presented in Appendix A. This method utilizes an amplitude modulation of a laser beam by the knife-edge attached to the

cold finger of the CCR system. The sensitivity of the proposed optical technique is determined by the diameter of the focused laser beam and a displacement of 1 μm is readily detectable. For the system CRYO Model 396-022 based on CTI CRYODYNE Model 22 refrigerator, experimental studies were conducted for different cold finger temperatures, cold head orientations, and mechanical holders. The total amplitude of the displacement was on the order of 50 μm for a cold head fixed into rigid mechanical holder placed on the optical table and 30 μm for the same holder placed on a special stand decoupled from the optical table. Three main frequency components at 3 Hz, 60 Hz, and 120 Hz have been observed.

During photoluminescence measurements, a standard set of 0.35 m McPherson Monochromator and cooled Hamamatsu Photomultiplier Tube R943-02 were used. For time-resolved measurements, the laser beam was modulated by the acousto-optic modulator Isomet 1206C with frequency 1000 Hz. The signal of photoluminescence was detected by the photomultiplier and averaged by Tektronix Digital Storage Oscilloscope TDS 724A. The time resolution of 0.7 μs was determined by the response time of the photomultiplier.

Excitation by single pulses of the second harmonic of a mode-locked Nd:YAG (yttrium aluminum garnet) laser at 532 nm with repetition rate of 10 Hz and pulse duration of 30 ps was used for ultrafast time resolved measurements (see Chapter 7). The photoluminescence was detected by streak camera the resolution of 0.7 ps. The basic principle of a streak-camera is schematically depicted in Fig. 5.6. The optical pulse is focused onto a photocathode where it produces a pulse of photoelectrons. The

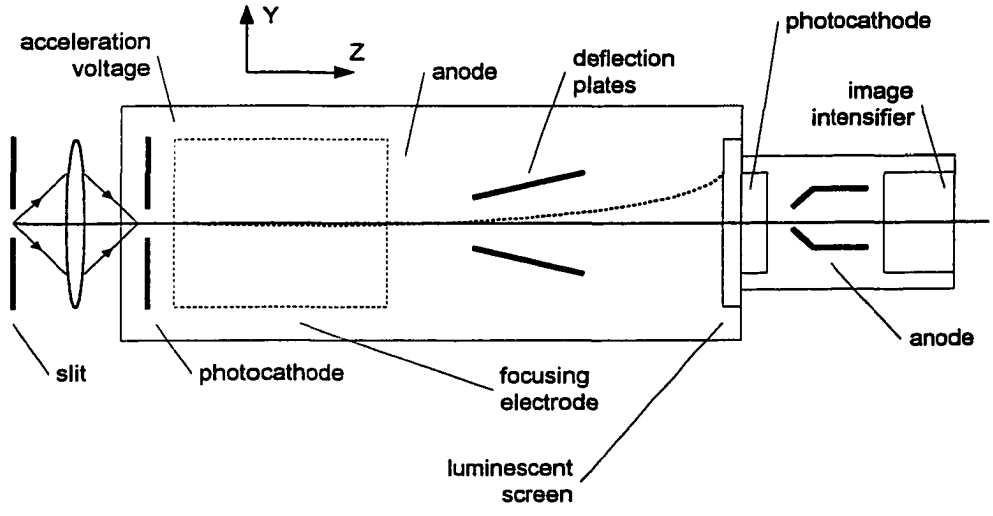

Figure 5.6. Principle of operation of streak-camera.

photoelectrons are extracted into the z-direction by a plane grid at the high voltage. They are further accelerated and imaged onto a luminescent screen. A pair of deflection plates can deflect the electrons into the y-direction. If a linear voltage ramp is applied to the deflection plates, the focal point of the electron pulse at the screen depends on the time t when electrons enter the deflecting electric field. The spatial distribution of the photoelectrons in y-direction therefore reflects the time profile of the incident light pulse.

References for Chapter 5

[1]. W. Demtroder, Laser Spectroscopy, Springer, 1996.

[2]. COHERENT documentation for 899-29 Ring-Laser System.

Chapter 6

Determination of Quantum Efficiency for Persistent Spectral Hole Burning Using Dispersive Kinetics

Introduction.

Persistent spectral hole burning (PSHB) has been proved to be a powerful method for scientific studies of the local environments of absorbing centers in solids[1]. Advances of PSHB for information storage and related applications have led to extensive study of a number of various materials in the laboratories around the world. In order to effectively continue search for the materials suitable for commercial applications, it is useful to have a rather general method of comparison of major PSHB characteristics and parameters, particularly quantum efficiency, for compounds under investigation.

Quantum efficiency of PSHB can be regarded as the probability for one act of photoinduced change per center per absorbed photon. This parameter appears to be one of the most critical parameters of PSHB for practical applications. Higher values of quantum efficiency are desired for fast PSHB used in dynamic memory applications and optical signal processing. In contrast, the low quantum efficiency of a single photon hole burning allows to avoid the destructive reading in applications based on gated two-photon mechanisms of PSHB. A universal method for obtaining reliable values of quantum efficiency would be extremely helpful in the process of research and development of new materials.

Early attempts to develop a method for determination of quantum efficiency have been undertaken by Gorokhovsky *at al.*[2] Later, a standard method for the computation of quantum efficiency has been presented in Ref. 3 by Morerner *at al.* Both methods are based on measurements of an initial slope of PSHB kinetics and applicable for situations in which the quantum efficiency is constant for all centers. Though any type of possible dispersion inherent to hole burning kinetics was neglected, both methods work relatively well for estimation of the quantum efficiency in crystals and can serve as a useful first approximation for calculation of quantum efficiency in amorphous solids. Dispersive character of the hole burning kinetics in amorphous solids requires special consideration. Difficulties associated with phenomenological description of hole burning kinetics in disordered materials were pointed out by Friedrich and Blumen[4]. They showed that depending on the experimental conditions and on the distribution of relaxation rates, mathematically distinct decay forms (such as logarithmic, stretch exponential or algebraic decays) may describe the same set of experimental data. To create a correct method for determination of quantum efficiency, a physically justified model for a hole-burning process in amorphous media is needed. Many models have been worked out to explain the observed dispersion[5-8]. Considering two-level systems (TLS) inherent to glasses[9], these models are based on distribution of the tunneling parameter λ (or underlying λ parameters) which defines the relaxation rate between two TLS metastable states. There are few possible distributions proposed. The classical model of Philips[10] and Anderson[11] with uniform distribution for the λ was successfully used to explain low-temperature behaviors of ultrasonic, dielectric, specific heat and thermal conductivity in glasses. However, this model often fails to describe experimentally observed hole-

burning kinetics[12,13]. On the other hand, there are evidences[12] that the tunneling parameter λ is subject to Gaussian distribution rather than a uniform distribution. Gaussian distribution of λ was successfully used by Jankowiak *at al.*[6] and Elschner *at al.*[5] to describe dispersive hole burning kinetics in various amorphous hosts. However, it should be admitted that other distribution functions of tunneling rates, even distribution based on rather exotic gamma function[8], still can be used for qualitative discussion of major features of hole burning kinetics in desordered media.

Despite a lot of work done in this area, a universal method for determination of quantum efficiency in crystalline and glassy materials is not available. Many values of quantum efficiency reported in the literature are based on specific mechanisms of PSHB appropriate for a narrow class of materials only. It makes comparison of different materials extremely difficult if not impossible. A systematic approach for determination of quantum efficiency for PSHB is described below. The proposed method can be applied to photochemical and photophysical hole burning in crystalline and amorphous solids and allows an extraction of the quantum efficiency of the hole burning from experimental kinetics of hole formation. The Section 6.1. contains a short theoretical consideration of dispersive PSHB kinetics. A few examples of analysis of experimental hole burning kinetics based on proposed approach can be found in Section 6.2.

6.1. Analysis of Dispersive PSHB kinetics.

There are a few primary mechanisms of dispersion for hole burning kinetics. First, there is an inherent dispersion due to difference in absorption at laser frequency for individual centers distributed within the inhomogeneously broadened absorption band. As a result of this difference, the burning rate of an individual center is strongly dependent

on detuning of its homogeneous ZPL relative to the laser frequency. Second, there is dispersion due to random orientation of the absorbing centers with respect to polarization of a burning laser. Third, there is dispersion due to distribution of quantum efficiency or other spectroscopic parameters involved in the hole burning process. Often, a combination of all mentioned above mechanisms is observed. Since different dispersion mechanisms might result in similar kinetics patterns, analysis of the experimental kinetics becomes difficult and distinction between mechanisms is not always possible. All mechanisms must be taken into account for proper determination of the quantum efficiency, even though the latter mechanism of dispersion is often considered to be the strongest one and usually dominates over the former two mechanisms.

Within the inhomogeneous absorption band, an impurity with homogeneous line centered at ω' absorbs at the laser frequency ω_L through its zero-phonon line and through its photon sideband. The probability of optical transition as a function of frequency ω_L is:

$$W(\omega_L, \omega') = \sigma I p(\omega_L - \omega') \qquad (6.1)$$

Here, I is a photon flux of burning irradiation, σ is a peak homogeneous absorption cross section [see Ref. 3 for methods of determination of σ at low temperatures], and function p(ω-ω') describes homogeneous spectrum centered at ω'. The change in the relative number of centers *dn* at frequency *ω'* during burning by laser irradiation at ω_L per time unit *dt* is given by:

$$dn = -n(\omega')\varphi W(\omega_L, \omega')dt \qquad (6.2)$$

where φ is a quantum efficiency of spectral hole burning and $n(\omega')$ is the fraction of centers that absorb in the frequency interval $d\omega$ centered at ω'. After integration:

$$n_t(\omega',t) = n_0(\omega')\exp(-W(\omega_L,\omega')\varphi t) \qquad (6.3)$$

where t is a burning time. A convolution of (6.3) and the homogeneous line profile p(ω-ω') gives a hole spectrum in absorption:

$$A(\omega,t) = \sigma\int_{-\infty}^{\infty} n_0(\omega')p(\omega-\omega')\exp(-W(\omega_L,\omega')\varphi t)d\omega' \qquad (6.4)$$

Neglecting contribution from the phonon side band of the homogeneous line to the hole spectrum and considering homogeneous line to be narrow (compared to inhomogeneous line) Lorentzian, the hole shape spectrum comes to[14]:

$$A(\omega,t) = \sigma\alpha n_0(\omega_L)\int_{-\infty}^{\infty} L(\omega-\omega')\exp(-\alpha\sigma I\varphi t L(\omega_L-\omega'))d\omega' \qquad (6.5)$$

where $L(\omega-\omega')=\Gamma^2/[(\omega-\omega')^2+\Gamma^2]$, Γ is a homogeneous line half-width, and α stands for a Debye-Waller factor.

The crucial implicit assumptions contained in equation (6.5) and in the rest of the text are: (i) the spectral linewidth of the burning laser is much smaller than the

homogeneous line width Γ of the absorbing center, (ii) hole refilling processes are neglected on the time scale of the experiment, and (iii) burning flux is weak enough to prevent power broadening of the spectral hole. Considering time dependence of absorption at $\omega = \omega_L$, an analytical solution for the hole burning kinetics can be obtained for a Lorentzian shaped ZPL. Though at later stages of the hole development, the rate of hole burning via excitation in the phonon sideband becomes comparable with the rate of hole burning via excitation of the ZPL[14, 15], we assume this rate to be small enough to warrant our analytical results. Non-Lorentzian ZPL shape requires the numerical calculation of (4) with a particular function of the homogeneous spectrum $p(\omega-\omega')$.

A time dependence of absorption at laser frequency (i.e. at the peak of the hole) is obtained from integral (6.5) analytically and resultant kinetics allows comparison with the experimental data[8]:

$$H(t) = B + D\exp\left(-\frac{\alpha I\sigma\varphi t}{2}\right)I_0\left(\frac{\alpha I\sigma\varphi t}{2}\right) \qquad (6.6)$$

where $I_0(x)$ is modified Bessel function of zero-order, initial absorption is normalized to unity, and D is a maximal relative hole depth ($0<D<1$). Hence, $B=1-D$ represents a fraction of non-burnable background.

With photon flux of burning irradiation I, low temperature peak homogeneous absorption cross section[3] σ, and Debye-Waller factor α easily obtainable from the experiment, equation (6.6) can be used to fit experimental data with only two free fitting parameters: quantum efficiency of PSHB φ and maximal relative hole depth D. Both

parameters φ and D can be unambiguously determined by the fitting procedure. It should be emphasized that function (6.6) shall be considered as an "elementary" kinetics function for a hole burning process. This function reflects the minimal degree of dispersion that is inherent to hole burning in any inhomogeneous band, whether crystalline or amorphous solids are considered. Equation (6.6) is directly applicable for hole-burning in systems with a unique orientation of absorbing centers and constant quantum efficiency of hole burning determined, for example, by the well defined quantum yield of photochemical reaction.

For isotropic solids such as glasses and polymers, kinetics of PSHB is getting more complicated and other mechanisms of dispersion should be taken into account. Random orientation of absorbing centers lead to the angular distribution of molecular transition moments relative to the polarization of the burning laser irradiation[5]. The angular distribution on the angle θ between molecular transition moment and the direction of polarization of the burning laser is accounted by setting $\sigma(\theta) = \sigma \cos^2 \theta$. Assuming an isotropic angular distribution, the kinetics of the hole burning process in disordered solids results from integration of (6.6) over all possible angles:

$$H(t) = B + \frac{3}{2} D \int_0^{\pi} \exp\left(-\frac{\alpha I \varphi t \sigma \cos^2\theta}{2}\right) I_0\left(\frac{\alpha I \varphi t \sigma \cos^2\theta}{2}\right) \cos^2\theta \sin\theta d\theta \qquad (6.7)$$

Again, both fitting parameters, namely quantum efficiency φ and maximal relative hole depth D, can be unequivocally extracted from the fitting procedure.

Photophysical mechanism of hole burning, observed for many glasses and polymers, involves the photoinduced change in local environment of the absorbing center[16]. The mechanism often is considered in the frame of two-level systems (TLS) theory[9] (Section 3.8). Due to random nature of the amorphous media, the TLS parameters are subject to distributions. Distribution of underlying the quantum efficiency parameters leads to distribution of the quantum efficiency itself. The hole burning kinetics appears to be strongly dispersive and has to be characterized by the average value of the quantum efficiency.

To understand dispersive kinetics, preliminary consideration of a photophysical hole burning mechanism is required. Our approach to the problem is based on Jankowiak *at al.*[6] and Elschner *at al.*[5] mathematical descriptions of dispersive kinetics. Jankowiak's model description suggested that the interwell tunneling transition in the TLS excited state is the process responsible for hole burning. The tunneling parameter λ is assumed to subject to Gaussian distribution. Detailed description and major mathematical results of this approach can be found in Section 3.8 (equation (3.35) and (3.37)). However, our analysis of experimental dispersive kinetics demonstrated that the fitting procedure based on equation (3.35) often results in ambiguity of obtainable fitting parameters. Therefore, we suggested a few modifications of Jankowiak's model to assure unambiguous determination of the quantum efficiency of PSHB. First, the dispersion inherent to any inhomogeneous band and reflected by the equation (6.6) should be added. It is important for proper calculation of quantum efficiency even if this dispersion mechanism is dominated by the TLS related dispersion. Second, the saturated hole depth assumed to be 100% (i.e. no non-burnable background is present). Later it will be shown

that a fraction of non-burnable background is a critical parameter for correct calculation of the quantum efficiency. Some fraction of the non-burnable background is always present due to overlapping of zero-phonon lines with phonon-side bands[17], non-resonant absorption, and possible photoinduced and spontaneous hole refilling processes. In any experimental configuration, the non-burnable background also includes unavoidable intensity losses, like scattering and reflections, associated with particular experimental setup. Therefore, setting this parameter to zero can be hardly justified. Third, an analytical expression used for calculation of the average quantum efficiency based on distribution parameters was obtained by integration over λ in infinite limits, including negative values. Due to exponential dependence of the quantum efficiency on λ, it can substantially increase average quantum efficiency. To avoid nonphysical negative values of λ, some artificial constrains on fitting parameters are required [see, for example, Ref. 20]. Presented in Ref. 6 fitting curves fail to describe the intensity dependence of the experimental kinetics, which are argued to be consequences of laser induced hole filling. Thus, at the present form substantial corrections are needed to use the model as a general tool for reliable calculation of average quantum efficiency.

Bassler's group model description of dispersive kinetics[5,12], closely associated with Richert results[18,20], involves substantially less *a priori* assumptions on specific mechanism of PSHB and, consequently, possesses a wider applicability for practical determination of quantum efficiency. The model takes into account all three mechanisms of dispersion. Still, integration over negative values of tunneling parameter may require additional analysis of the obtained fitting parameters[20]. Maximal relative hole depth was assumed to be about 0.5 for all materials. Nevertheless, this mathematical model can

serve as a cornerstone for building a general method for determination of quantum efficiency of PSHB.

Having combined appropriate features of the both model descriptions of dispersive PSHB kinetics mentioned above, the following approach to determination of the quantum efficiency has been developed. To avoid unnecessary association with any particular mechanism of PSHB and its parameters, which are frequently unknown, we set quantum efficiency in the parameterized form $\varphi = exp(-a)$. Possible pre-exponential factor considered to be automatically taken into account by proper choosing of the parameter a. Therefore, the principal parameter a alone defines entirely the value of the quantum efficiency. Physical interpretation of the principal parameter a depends on particular mechanism of phototransformation and is discussed below. Following Bassler *at al.*[12] argumentation, we assume that parameter a is subject to Gaussian distribution. The hole forming kinetics can be found by introduction of $\varphi = exp(-a)$ and the Gaussian distribution function of parameters a into integral (6.7):

$$H(t) = B + \frac{3}{2}\frac{D}{w}\sqrt{\frac{4\ln(2)}{\pi}}\int_0^{\infty}\int_0^{\pi}\exp\left(-\frac{I\exp(-a)t\sigma\cos^2\theta}{2}\right)I_0\left(\frac{I\exp(-a)t\sigma\cos^2\theta}{2}\right)\cos^2\theta\sin\theta d\theta\exp\left(-4\ln(2)\frac{(a-a_c)^2}{w^2}\right)da \quad (6.8)$$

where a_c and w are the center and width of the principal parameter distribution respectively. In contrast with the above mentioned models, integration over positive values of λ only is dictated by the requirement to have quantum efficiency $\varphi < 1$ for all centers.

At initial stages of hole development, when hole burning through the phonon sidebands may be neglected, the experimental kinetics cannot be fitted by the three parameters a_c, w and D unambiguously due to the detection noise and the limited range of exposure, It, for this measurements. Furthermore, performing the fitting procedure for long kinetics with the extended exposure range will not give the correct parameters either due to kinetics distortion caused by hole burning via excitation of the phonon sidebands. In Ref. 5 and 6, the maximal relative hole depth D was chosen *a priori* to be 100% and 50%, respectively. Though the two remaining parameters could be determined unambiguously, the choice of D may lead to a systematic error in the obtained results. To avoid this problem, one may fit an initial segment of the PSHB kinetics with the parameter D fixed by the independent measurement of the maximal saturated hole depth at the highest experimentally achievable exposures. An alternative approach to increase the exposure range and the number of datapoints in the initial stage of recorded kinetics, is to reduce the burning intensity. Then, the fitting procedure has to be performed simultaneously for initial segments of several kinetics recorded at different low burning intensities with fitting parameters a_c, w and D shared for all datasets. Due to these additional datasets, a single set of parameters a_c, w and D can be found. The two outlined procedures imply that the maximal relative hole depth is independent on intensity that may be not true if resonant photoinduced hole refilling processes are involved. It should be pointed out that any reverse to hole burning processes make calculation of quantum efficiency strongly dependent on nature of this particular refilling process. Analytical description of the hole burning kinetics becomes highly material dependent and must include intensity dependence of the rate of the refilling process.

With distribution parameters obtained, one can calculate the average quantum efficiency, which will characterize hole burning ability of this particular system:

$$\langle\varphi\rangle = \frac{\int_0^\infty \exp(-a)\exp\left(-\frac{(a-a_c)^2}{w^2}\right)da}{\int_0^\infty \exp\left(-\frac{(a-a_c)^2}{w^2}\right)da} \qquad (6.9)$$

It has to be emphasized that in the proposed approach no specific hole burning mechanism is suggested to calculate the average quantum efficiency. However, physical interpretation of parameter a depends on specific mechanism of PSHB. For PSHB determined by tunneling transition in TLS excited state[5,6], quantum efficiency is defined by the rate competition between the interwell transition in the TLS excited state $R=\omega_0\exp(-\lambda)$ (ω_0 is an attempt frequency; λ is a tunneling parameter) and the relaxation from the TLS excited state to the ground state K, so that $\varphi=R/K=(\omega_0/K)\exp(-\lambda)$. Then our principal parameter a is easily related to λ by:

$$a = \lambda - \ln\left(\frac{\omega_0}{K}\right) \qquad (6.10)$$

so that any scalar pre-exponential factor might be accounted by the shift of the center of the distribution. The proposed approach will work for an activation mechanism of the interwell transition as well. In this case, for the center of the distribution we have (U_c is a center of barrier's heights distribution):

$$a_c = \frac{U_c}{kT} - \ln\left(\frac{\omega_0}{K}\right) \qquad (6.11)$$

A comparison between (6.10) and (6.11) shows that temperature dependence of the parameter a_c can help to differentiate between tunneling and activation mechanisms of the transition, and in some cases to find ratio ω_0/K[20]. However, possible reverse processes at higher temperatures can substantially deform the observable dependence and must be properly accounted.

6.2. An experimental illustration.

A usual way to observe the hole forming kinetics is to record a trace of the time-varying sample transmission (absorption) during the low burning intensity growth of a spectral hole. Obtained transmission (absorption) kinetics can be compared with theoretical results presented in the previous section.

During investigation of several free-base- and metallo- phthalocyanines for holographic storage applications[22], the proposed method enabled us not only to obtain reliable values of quantum efficiencies and maximal hole depths for these materials, but also enabled discrimination between photochemical and photophysical mechanisms of hole burning. All samples were provided by Prof. Psaltis group, California Institute of Technology. Representative results for persistent spectral hole burning in 2,11,20,29-tetra-tert-butyl-2,3-naphthalocyanine (H_2-TBNP) and zinc 2,11,20,29-tetra-tert-butyl-2,3-naphthalocyanine (Zn-TBNP) embedded in polyvinilbutyrate (PVB) with molar concentrations 2×10^{-4} mol/l and 5×10^{-5} mol/l respectively are presented below. Both

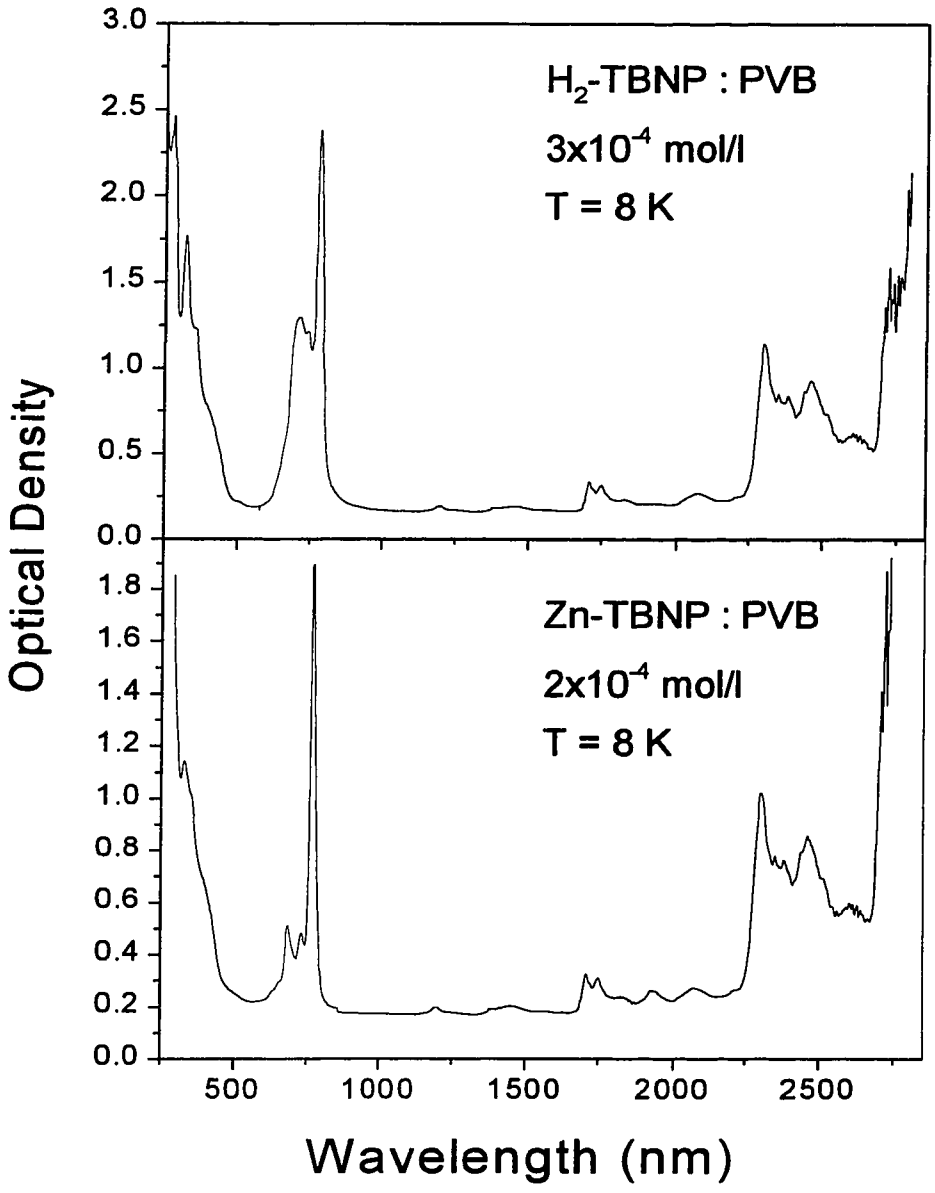

Figure 6.1. Absorption spectra of H_2-TBNP and Zn-TBNP embedded in PVB detected at 8 K.

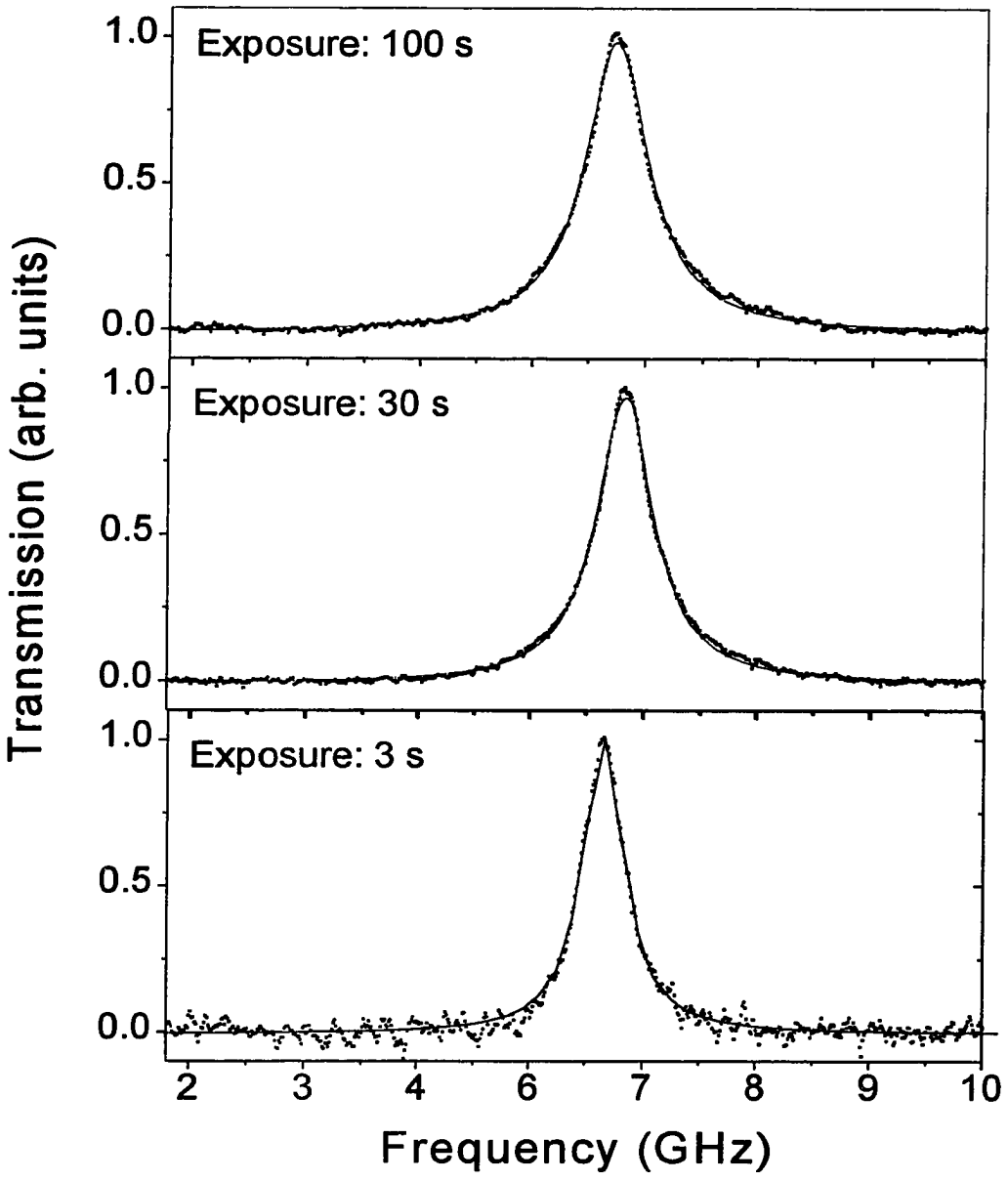

Figure 6.2. Spectral hole profiles detected in Zn-TBNP embedded in PVB at different stages of hole development. Intensity of hole burning was 192 $\mu W/cm^2$. Dots and solid lines represent experimental spectra and fit by Lorentzians respectively.

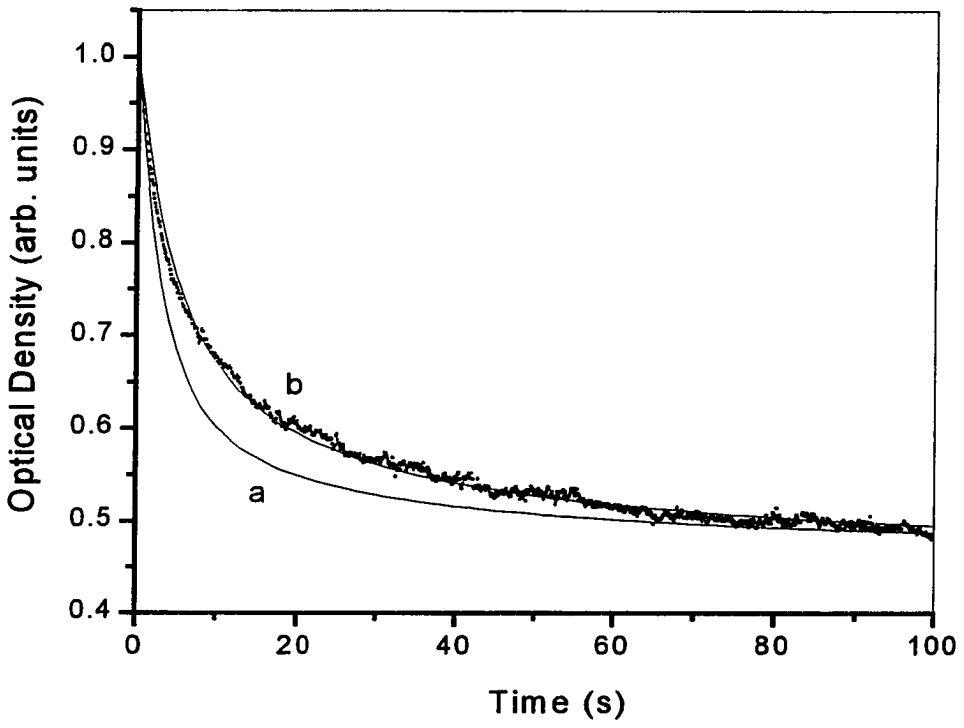

Figure 6.3. Data on hole burning kinetics in H_2-TBNP embedded in PVB. Experimental kinetics recorded at 1.5 K with burning intensity of 192 $\mu W/cm^2$. Traces (a) and (b) are fitting curves by equations (6.6) and (6.7) respectively. All fitting curves used $\sigma_h=2.6\times10^{-11}$ cm^2 as a peak low temperature homogeneous absorption cross section.

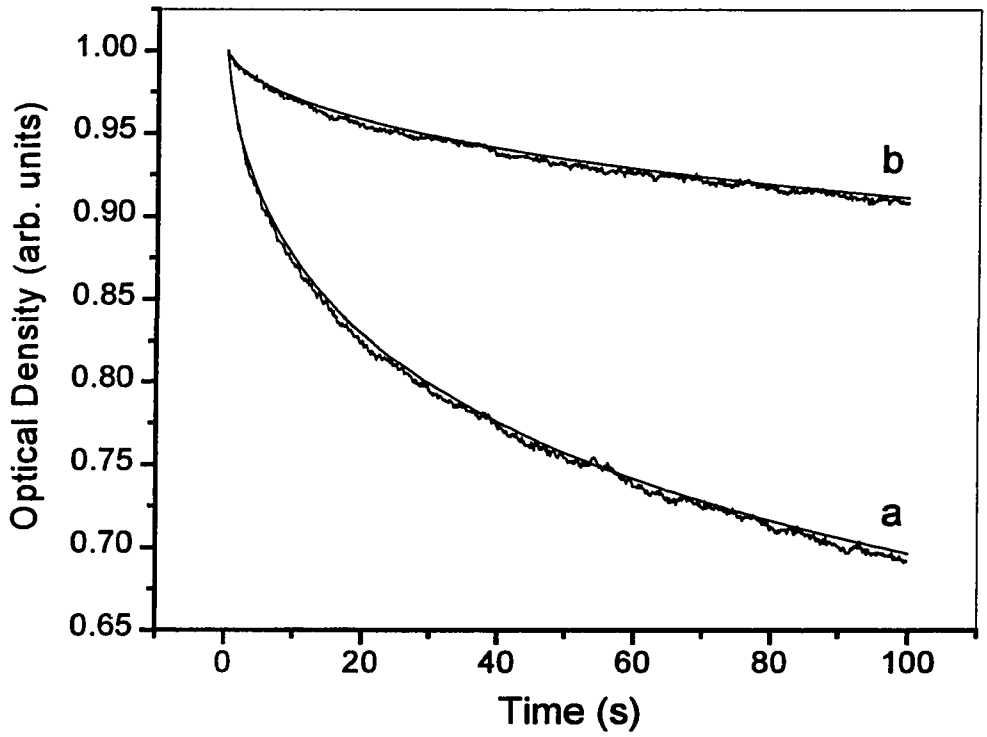

Figure 6.4. Data on hole burning kinetics in Zn-TBNP embedded in PVB. Upper and lower experimental kinetics recorded at 1.5 K with burning intensities 12 $\mu W/cm^2$ and 192 $\mu W/cm^2$ respectively. Traces (a) and (b) are obtained by fitting simultaneously both experimental datasets by equation (6.8) with the same values of a_c, w, and D, and proper burning intensity for each dataset. Both fitting curves used $\sigma_h=1.7\times10^{-11}$ cm^2 as a peak low temperature homogeneous absorption cross section.

samples appear to be slightly colored films with thickness of about 0.5 mm. Low temperature absorption spectra of both samples between 400 nm and 3000 nm are displayed in Fig. 6.1. Absorption peak at 800 nm related to singlet-singlet molecular transition is clearly visible. Spectral holes were burned into these inhomogeneously broadened bands by the Ti:Sapphire laser with linewidth less than 1 MHz. Spectral holes burnt in all samples demonstrated long life-time and absence of photoinduced hole refilling.

Hole forming processes were recorded in transmission at temperature 1.5 K with burning intensities range 10-200 $\mu W/cm^2$. The measured kinetics were analyzed according to the approach presented in the previous section to determine the quantum efficiency of PSHB. Initial optical densities in all cases were about 0.7. Representative spectral hole profiles detected in Zn-TBNP embedded in PVD are presented in Fig. 6.2 and correspond to the highest level of burning intensity used. Lorentzian hole shape is proving that an approximation of the ZPL to Lorentzian is valid at this exposure range.

The two material parameters α and σ required for the fitting procedure were obtained by independent spectroscopic measurements as follows: (i) the Debye-Waller factor α was estimated from the decomposition analysis of the low temperature absorption band, (ii) the peak homogeneous absorption cross section σ was calculated using the integral absorption cross section σ_{int}, which was determined from the absorption and concentration data, as $\sigma=(\Gamma_{inh}/\Gamma_h)\ \sigma_{int}$, (iii) the inhomogeneous broadening Γ_{inh}, was determined from the width of the Gaussian corresponding to the 0-0 electronic transition in the decomposition fit, (iv) the homogeneous linewidth Γ_h is half of the found minimal holewidth since no spectral diffusion was observed in the time range of 10 - 10^5 seconds.

The minimal holewidth was found by extrapolation of the holewidth dependency on burning intensity and on burning time to the zero-intensity zero-exposure limit (see Fig. 6.2 for a representative hole spectrum). The ratio of noise-to-signal for our experimental kinetics is at most 1% and permits discrimination between Gaussian and uniform distribution of the parameter α in favor of a Gaussian distribution [16], proving our initial assumption. Due to this low noise, the accuracy of the obtained results was mostly determined by the accuracy of the experimental values of α and σ and was estimated to be $\pm 15\%$.

Fig. 6.3 shows the PSHB kinetics for H_2-TBNP in PVB. The experimental kinetics is satisfactorily described by Eq. (6.7) with a single value of quantum efficiency and does not require the introduction of a distribution. This result is a clear sign of the photochemical reaction with a constant (non-distributed) value for the quantum efficiency, most likely proton phototautomerization. At the same time, the fit by Eq. (6.7) is far superior than the fit by Eq. (6.6), where the angular dependence was not taken into account. The quantum efficiency and maximal relative hole depth were found from the fitting procedure to be $(8.4\pm1.2)\times10^{-3}$ and 0.58 ± 0.05, respectively. The observed quantum efficiency is about one order of magnitude higher than that found in H_2-pthalocyanine using the initial rate of hole broadening [18].

The experimental hole burning kinetics in Zn-TBNP measured with two substantially different intensities are presented in Fig. 6.4. Eqs. (6.6) and (6.7) clearly failed to fit the dispersive kinetics (not shown). Both shown datasets were fitted simultaneously by Eq. (6.8) satisfactorily. This result supports the assumption of the single photon hole burning mechanism for Zn-TBNP.

Sample	Concentration cm^{-3}	Holewidth MHz	Inhom. width MHz	σ_b cm^2	Efficiency of PSHB	Distribution parameters		
						center	width	B
H_2-TBNP(PVB)	6.0×10^{15}	150	1.0×10^{7}	8.7×10^{-11}	2.8×10^{-3}	4.69	0	0.57
H_2-TBNP(PVB)	4.2×10^{17}	100	1.5×10^{7}	6.2×10^{-11}	1.3×10^{-3}	6.92	3.5	0.58
H_2-TBNP(PS)	3.0×10^{16}	1150	0.9×10^{7}	3.2×10^{-12}	3.2×10^{-2}	3.27	0	0.43
H_2-OBP(PVB)	1.8×10^{17}	200	1.6×10^{7}	4.5×10^{-12}	1.1×10^{-2}	6.38	0	0.57
Zn-TBNP(PVB)	1.2×10^{17}	380	1.0×10^{7}	1.7×10^{-11}	1.1×10^{-3}	9.55	6.0	0.28
Zn-TBNP(PS)	1.1×10^{17}	≈1000	1.2×10^{7}	$\approx4.6\times10^{-12}$	$\approx1.4\times10^{-3}$	9.16	6.7	0.48
Ni-TBNP(PVB)	3.6×10^{17}	100	1.5×10^{7}	2.1×10^{-11}	6.7×10^{-3}	5.00	0	0.67
Si-NPDO)PVB)	1.2×10^{17}	400	2.0×10^{7}	8.7×10^{-11}	8.1×10^{-4}	10.06	4.7	0

Table 6.1. Preliminary results on spectroscopic parameters for a set of commercial free-base and metallo- phthalocyanines for holographic storage applications.

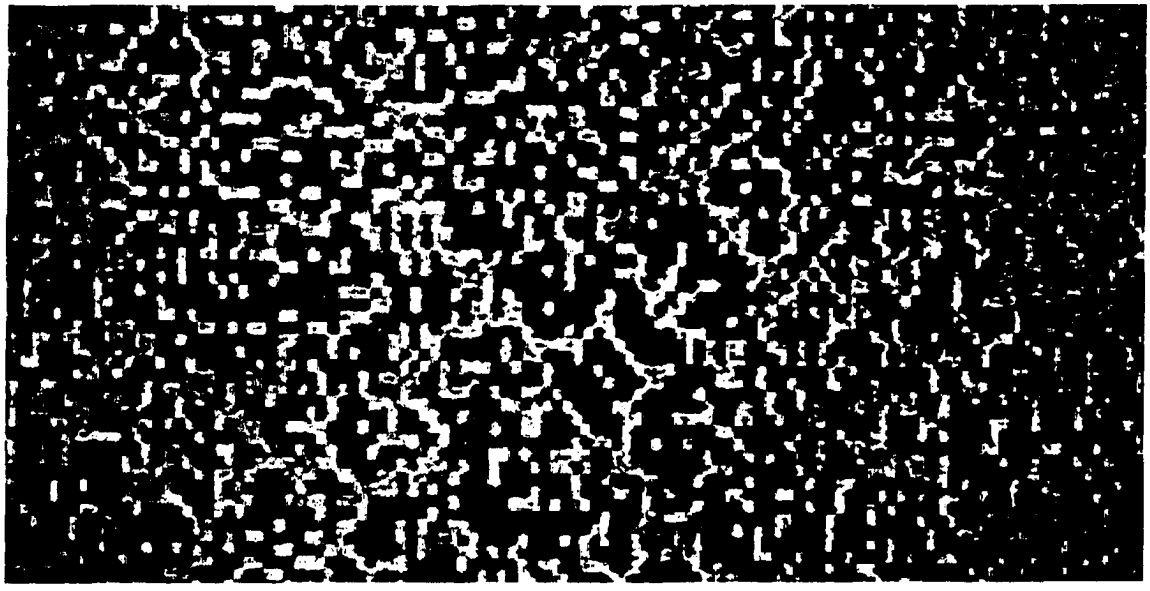

Figure 6.5. Reconstruction of data page recorded in H_2-TBNP (PVB) sample on spot of 400 microns with diode laser at 788 nm (optical density 5.5). The absorption hologram was recorded by Mr. C. Moser, California Institute of Technology.

Parameters a_c, w, and D were found to be 9.15, 6.0 and 0.72, respectively. The value obtained for D is in good agreement with the limit for hole depth of D = 0.74 obtained from long 10^5 s kinetics. The average quantum efficiency according to (6.9) was calculated to be $(1.2\pm0.2)\times10^{-3}$. A similar calculation with the chosen *a priori* maximal hole depth of 100% gives an indistinguishable fitting curve for kinetics (a) and a substantially lower value of quantum efficiency of $(7.4\pm1.1)\times10^{-4}$. The observed distribution of the quantum yields suggests that Zn-TBNP possess a nonphotochemical mechanism that is likely related to the rotation of small molecular groups attached to either a relatively rigid phthalocyanine ring the host structure. The distribution of TLS parameters is manifested in the dispersion of the hole burning kinetics.

Table 6.1 summarizes spectroscopic parameters obtained to date for eight molecules studied. Table 6.1 demonstrates that major part of free-base phthalocyanines exhibits photochemical mechanism of PSHB with non-distributed values of quantum efficiency, while metallo-phthalocyanines mostly reveal photophysical mechanism of PSHB with wide distributions of quantum efficiency. Obtained values of quantum efficiency and maximal relative hole depth allow development of recommendations on appropriate usage and optimization of these novel materials for holographic storage applications. Fig. 6.5 presents reconstruction of the data page recorded in H_2-TBNP (PVB) sample.

6.3 Summary of results.

A practical approach for the determination of the quantum efficiency of PSHB from the experimental hole burning kinetics has been proposed and experimentally verified. The hole burning quantum efficiency was determined to be 8.4×10^{-3} for H_2-

TBNP and 1.2×10^{-3} (average value) for Zn-TBNP in polyvinilbutyrate. The single photon nature of the hole burning process and the Gaussian distribution of the principal parameter *a* were verified from the experimental kinetics analysis. The obtained distribution parameters demonstrated clear correlation with different mechanisms of PSHB: photochemical hole burning in H_2-TBNP is described by a single value of quantum efficiency, while the distribution of the quantum efficiency observed in Zn-TBNP implies a photophysical mechanism of PSHB.

References for Chapter 6.

[1]. W. E. Morerner in: Topics in Current Physics. Persistent spectral hole burning: science and application, ed. by Morerner (Springer, Berlin, 1987).

[2]. A. A. Gorokhovsky, Y. V. Kikas, V. V. Palm and L. A. Rebane, Solid State Physics **23** (1981) 1040 (in Russian).

[3]. W.E. Morerner, M. Gehrtz, A. L. Huston, J. Chem. Phys. **88** (1984) 6459-6460.

[4]. J. Friedrich and A. Blumen, Phys. Rev. B **32** (1985) 1434.

[5]. A. Elschner and H. Bassler, Chem. Phys. **123** (1988) 305-315.

[6]. R. Jankowiak, L. Shu, M.J. Kinney and G.J. Small, J. Lum. **36** (1987) 293.

[7]. H. Talon, M. Orrit, and J. Bernard, Chem. Phys. **140** (1990) 177.

[8]. M. Drobizhev and M. Sapozhnikov, Chem. Phys. Lett. **236** (1995) 438.

[9]. W. A. Phillips, J. Low Temp. Phys. 7 (1972) 351.

[10]. W. A. Phillips, Rep. Prog. Phys. **50** (1987) 1657-1708.

[11]. P. W. Anderson, B. I. Haperin and C. M. Varma, Phil. Mag. **25** (1972) 1.

[12]. A. Elschner, R. Richert and H. Bassler, Proceedings of the Academy of Sciences of the Estonian SSR, **37** (1988) 154.

[13]. A. V. Carpenter, A. V. Turukhin, A. A. Gorokhovsky, T. Chu, and Y. Okamoto in: Proceedings of Persistent Spectral Holeburning Workshop, February 14-16, 1997, Bozeman, MT.

[14]. J. Friedrich and D. Haarer, Angew. Chem. Int. Ed. Engl. **23** (1984) 113-140.

[15]. A. A. Gorokhovsky and Ya. V. Kikas, Zhurnal Prikladnoi Spectroskopii, Vol. 28, No. 5, (1978) 566.

[16]. G. Small in: Spectroscopy and excitation dynamics of condensed molecular systems, ed. by A.V. Agranovich and R.M. Horchstrasser, North-Holland, 1983.

[17] K. K. Rebane: Impurity spectra of solids (Plenum Press, New York, 1970).

[18]. R. Richert, Chem. Phys. Lett. **118** (1985) 534.

[19]. M. A. Krivoglaz in: Zero-phonon lines and spectral hole burning in spectroscopy and photochemistry, ed. by O. Sild and K. Haller, Springer-Verlag, 1988.

[20]. R. Richert, J. Chem. Phys. **86** (1987) 1743.

[21]. E. S. Maniloff, F. R. Graf, H. Gygax, S. B. Atner, S. Bernet, A. Renn, U. P. Wild, Chem. Phys. **193** (1995) 173.

[22]. A. V. Turukhin, A. A. Gorokhovsky, T. Chu, Y. Okamoto, C. Moser, I. V. Solomatin and D. Psaltis in: Proceedings of Persistent Spectral Holeburning Workshop, March 7-10, 1999, Bozeman, MT.

Chapter 7

Diamond and Diamond-like Materials

Introduction.

Of all crystalline solids, diamond holds a special position. Its name is derived from the Greek *adamas*, meaning "unconquerable, invincible". The diamond-cubic lattice consists of two interpenetrating face-centered cubic lattices, displaced by one quarter of the cube diagonal. Each carbon atom is tetrahedrally coordinated, making strong, directed σ bonds to its neighbors using hybrid sp^3 atomic orbital. The great interest in diamond stems from its extreme properties. Diamond has the highest atom number density of any material at terrestrial pressures[1]. As a result of its high atom-number density and strong covalent bonding, diamond has the highest hardness and elastic modules of any material and is the least compressible substance known. The thermal conductivity of diamond at 300 K is higher than that of any other material and its thermal expansion coefficient is 8×10^{-5}, lower than that of Invar. Diamond is a very wide band gap semiconductor (E_g = 5.5 eV) and has a high breakdown voltage 10^7 V cm^{-1}.

Many outstanding optical properties of diamond make it an attractive material for optical and opto-electronic applications. Diamond has a very wide optical transparency band raging from 0.22 μm (fundamental absorption edge) to far infrared. Only a moderate intrinsic absorption band between 2.5 and 7 μm disturbs the perfection of diamond transparency in the infrared region. Being transparent in the ultraviolet, visible and infrared

spectral regions, diamond offers a great opportunity for lattice defects to reveal optical activity of their electronic and vibrational transitions. The large energy band gap is a favorable condition particularly in the case of luminescence, because effective radiative electronic transitions require the ground and excited electronic states to be lying within the band gap. By now more than 100 vibrational and more than 400 electronic optically active centers have been known in diamond in a spectral range from 20 to 0.17 μm, that is from the vacuum ultraviolet till the middle infrared region. To fill up this large spectral range diamond possesses many optically active defects of different origin[2], including intrinsic and impurity related, point and extended ones. Both types of the intrinsic point defects (vacancy and interstitial related) in diamond are optically active. Many impurities are known to form optically active defects in diamond, they are: H, He, Li, B, N, O, Ne, Si, Ti, Cr, Ni, Zn, Zr, Ag, Xe, and Tl.

An important optically related feature of diamond is its high Debye temperature (almost 2000 K). This value is the highest one among all known solids. Owing to the high Debye temperature, a substantial excitation of phonons in diamond, and, consequently, electron phonon coupling in optically active centers, occurs at relatively high temperatures. As a result many optical centers in diamond retain their spectral structure and transition probabilities to relatively high temperatures. It is important for spectral hole burning because phonon scattering processes cause temperature broadening of homogeneous linewidth Γ_h that is determined by the number and frequencies of the participating phonons. It was shown that for acoustic phonons $\Gamma_h \sim (T/T_D)^7$ at low temperature (see Section 3.5) where T_D is the Debye temperature. Considering that for diamond $T_D \cong 1850$ K, temperatures of 77 K, or even 300 K, appear to be not very high in

terms of phonon population for this material. Therefore, there is a possibility to avoid rapid homogeneous line broadening with temperature due to phonon scattering mechanism. It makes diamond an attractive material for high temperature PSHB[3]. Indeed, promising results were obtained for hole burning in the lines at 649.5 nm, 655 nm, and 681 nm, where the holes burnt at 5 K were partially restored by temperature cycling up to 200 K.[4] Room temperature PSHB in neutron-irradiated diamond was also reported[5]. However, obtained very low multiplicity ratio ($\Gamma_{inh}/\Gamma_{hom}$ = 2-5) and required high burning intensities (dozens of MW/cm^2) in these measurements are not adequate for technological applications.

To maximize storage density for a PSHB storage system, it is advantageous to use materials with very high inhomogeneous-to-homogeneous linewidth ratio (see Chapter 4). Disordered (amorphous) solids usually exhibit relatively large inhomogeneous broadening of spectral lines. Trying to combine perspective high temperature features of natural diamond and high multiplicity of disordered media, it is interesting to investigate amorphous carbon and diamond films. In general, disordered carbon phase covers a wide range of materials, such as amorphous carbon, hydrogenated amorphous carbon, and "diamond-like" carbon that have properties very similar to those of a natural diamond. The disordered carbon films can be produced by the well-developed technology of chemical vapor deposition (CVD) growth. The inhomogeneous broadening of ZPLs was found to be almost an order of magnitude higher in chemical-vapor deposited diamond (i.e. polycrystalline CVD diamond) than in natural diamond or in high pressure synthesized diamond single crystals. The large ratio of the inhomogeneous ZPL width (>1000 GHz) to the holewidth in chemical-vapor deposited diamond films suggests that a large number of

holes can be formed within inhomogeneously broadened absorption band. Therefore, the high strains present in CVD diamond may be advantageous for optical memory[3] application at elevated temperatures.

To summarize, these materials are expected to have broad inhomogeneous lines, narrow homogeneous lines, and temperature stable spectral holes. All of these properties are very important for high temperature hole burning and for high storage density of the future memory systems.

Si-doped Chemical-Vapor-Deposited Diamond Films

7.1. Samples.

During the past years, significant progress has been made on experimental techniques for synthesizing diamond by the decomposition of hydrocarbon gases[6]. Using chemical-vapor-deposited methods, diamond can be grown from a methane-hydrogen mixed gas on various substrates. In the microwave-assisted plasma CVD method, which was used for making the samples under investigation, a substrate is placed in a quartz tube that penetrates perpendicularly to a rectangular waveguide, and microwaves generated by a magnetron are guided to the quartz tube producing a plasma. The position of the plunger is adjusted so that the substrate is entirely immersed in the plasma (Fig. 7.1).

Two samples studied were free-standing polycrystalline diamond films approximately 60 μm thick. Sample #1 was gray and semitransparent, while sample #2 was black and not transparent, most likely due to high concentration of disordered carbon phase. The morphologies of both films are characterized by well-defined square {100} crystal facets with sizes of 5-10 μm (see Fig 7.2). Samples were grown at Crystallume on a silicon substrate at 860 ^{0}C and were provided by Dr. W. Phillips. As the Si substrate was used, it is very naturally to assume that Si from the substrate was transferred in trace amounts to the diamond microcrystals to form the optical center. In addition, diamond film might incorporate some Si impurities derived from the etching of the silica walls of the reaction chamber by the plasma during CVD growth.

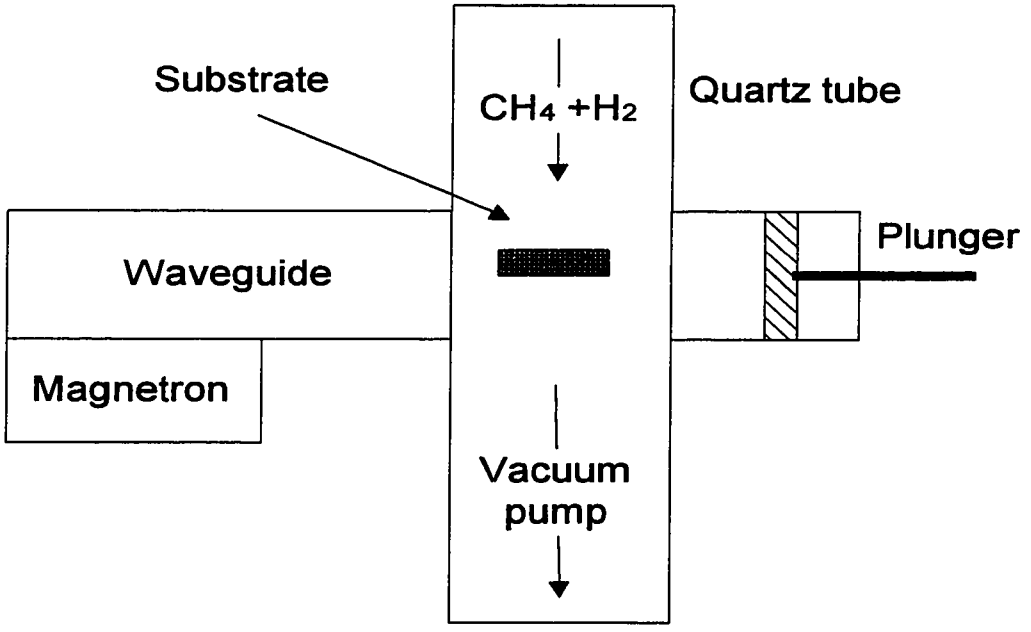

Figure 7.1. Microwave-assisted plasma chemical-vapor deposition (CVD) method[6] for diamond synthesis.

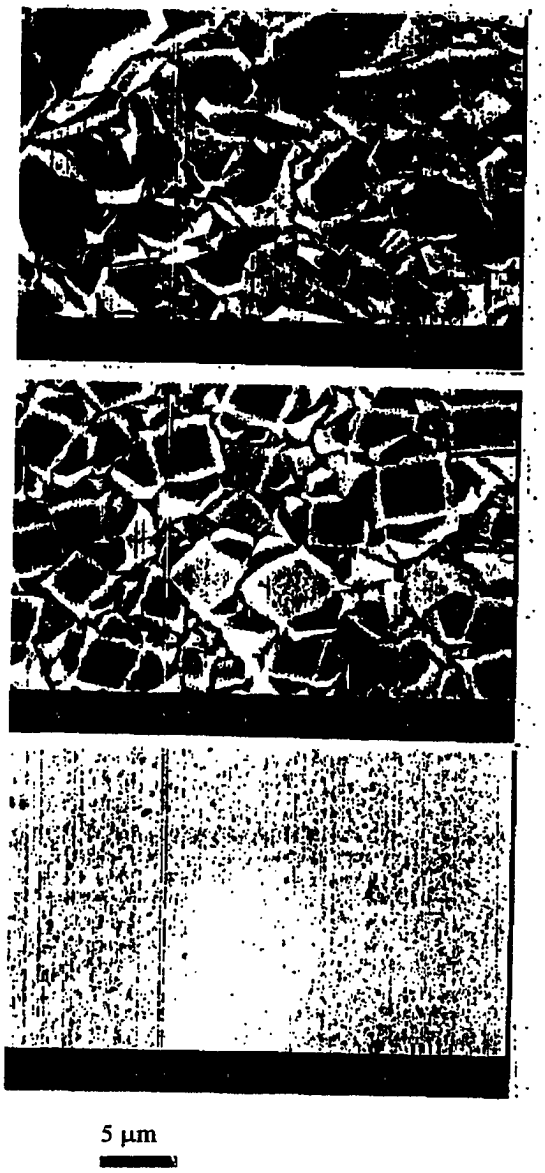

Figure 7.2. Free standing polycrystalline diamond films grown on silicon substrate at 860^0C. Various spots of the surface of sample #2 are presented. Major part of the work was done on the spot in the middle picture. Samples and photo were provided by Dr. W. Phillips, Crystallume, Inc.

7.2. Absorption and Photoluminescence Spectroscopy.

In cathodoluminescence spectra of ion-implanted epitaxial diamond films[7] and natural diamonds[8] a line was observed at 737 nm (1.682 eV). This line was assigned to a defect containing interstitial Si atoms (sometimes referred as "1.682 eV center" in literature). On the basis of the observed square law dependence of the luminescence intensity on the implantation dose, it was proposed that this defect contains two Si atoms[8]. Such a square law dependence may be explained in a different manner, related to a defect containing one implanted Si and one vacancy, both produced by ion implantation. Consequently, this proposal of a two Si structure[8] is questionable. Recent studies of cathodoluminescence[9] and photoluminescence[10] of CVD diamond films (performed at 77 K) determined that Si impurities are due to the Si substrate widely used in CVD techniques and confirmed that they are responsible for the 737 nm line. In Ref. 11 a 12-line fine structure is observed close to 737 nm (1.682 eV) in a single diamond crystal. The observed spectral pattern can be divided into three similar groups, each containing four components. The relative strength of the optical absorption for the three groups of lines are found to be the same as the ratio of the abundancies of the natural isotopes of silicon, ^{28}Si, ^{29}Si, and ^{30}Si, thus proving that the 1.682 eV center is related to silicon impurity. A four energy level scheme, with two sublevels of separation 0.20 meV (1.61 cm^{-1} or 48 GHz) in the ground state, together with two levels of separation 1.07 meV (8.63 cm^{-1} or 258 GHz) in the excited state, has been found to adequately account for the temperature dependence (between 10 K and 60 K) of the relative intensities of the lines in absorption and photoluminescence. It is established that the occupancies of the two excited-state levels tend to reach thermal equilibrium after optical excitation and before luminescence takes place. According to Ref. 11, optical transitions between the upper sublevels of the ground and excited

states of the center have the same transition probability as transition between the lower sublevels of the ground and excited states. On the other hand, transition from an upper to lower sublevel (or vice versa) between ground and excited states have a much lower transition probability. This suggests the existence of a defect which has two similar configurations available to it, causing a doubling of the ground and excited states of the center, in turn leading to a spectral fine structure of very sharp lines. These features are rather similar to those exhibited by two-level systems (TLS) in amorphous media where the level doubling is due to a tunneling behavior between the two metastable states of a TLS. A similar tunneling process may be associated with the silicon center in diamond.

The defect was studied in homoepitaxial CVD diamond films by applying uniaxial stress and external magnetic fields[12]. In a homoepitaxial diamond film, the defect exhibits narrow ZPL with linewidth of 0.2 meV as there is substantially no strain in the film. Owing to the narrow linewidth, spectra reveal a complex fine structure of the ZPL transition. The splitting pattern at external fields and uniaxial stress was combined with thermalization measurements. The electronic energy level scheme similar to the one in Ref. 11 was deduced from the experimental data. It is concluded that the symmetry of the center is tetragonal, possibly slightly distorted toward lower symmetry. Energy separation in excited and ground states are reported to be 2.10 meV (16.93 cm^{-1} or 507 GHz) and 1.17 meV (9.43 cm^{-1} or 282 GHz) respectively. Comparable energy splitting of 0.8 meV (6.45 cm^{-1} or 193 GHz) was reported in Ref. 13 for the excited state of the center in CVD diamond film.

Despite these studies, the defect structure is not known at the present time and, in addition, no data are provided on the vibrational frequencies of the Si defect.

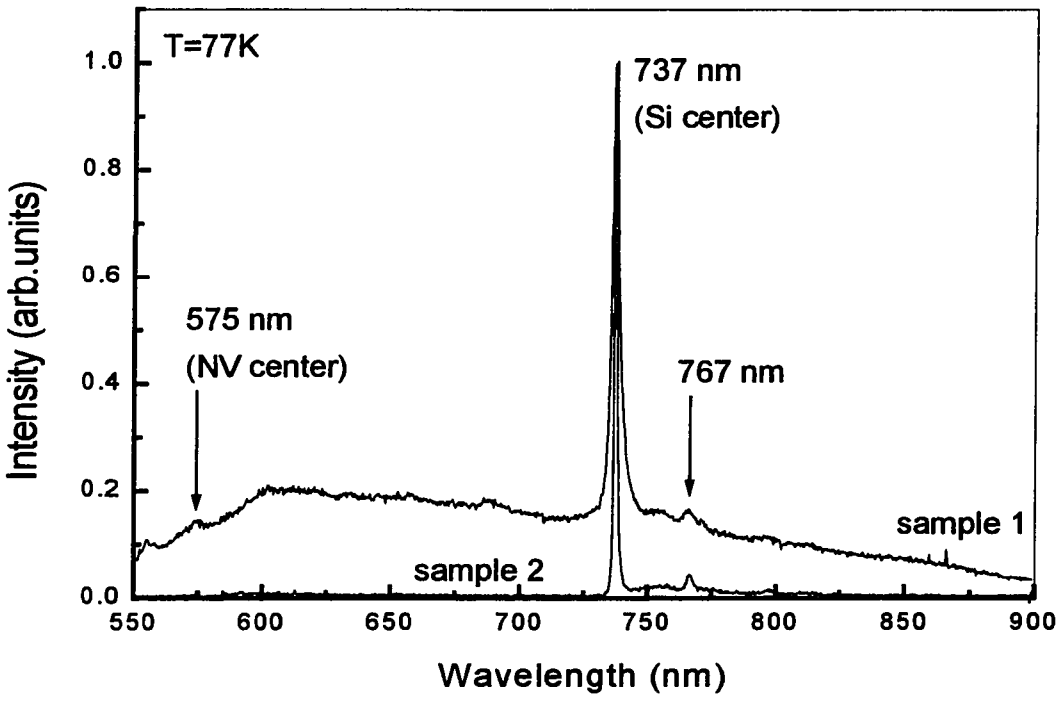

Figure 7.3. Photoluminescence spectra of CVD diamond films under excitation with 514.5-nm 50 mW/mm^2 CW Argon laser at 77 K.

At low temperatures, the luminescence from CVD diamond was excited by Argon laser at 514.5 nm (see Fig. 7.3). The spectrum of sample #1 consists of a weak line at 575 nm attributed to a nitrogen-vacancy complex, a strong line at 737 nm of the Si center, a line at 767 nm, will be assigned to a quasilocal mode of 515 cm^{-1} of the Si center, and a few weaker lines. The very broad band between 550 and 900 nm, which is related to the sp^2 carbon phase, can be clearly seen as well. In the spectrum of sample #2, the Si-center line at 737 nm and its vibrational structure are much more prominent, the line at 575 nm is absent, and the broad band sp^2 photoluminescence is much weaker than for sample #1.

The line at 737 nm was observed in absorption spectrum as well which proves its pure electronic character. A transparent grease with index of refraction n = 1.5 was used for absorption measurements at 78 K. Though the grease does not match the diamond refraction index n = 2.42, it removes diamond-vacuum interface and dramatically reduces scattering. Obtained absorption spectrum is presented in Fig. 7.4.

With decreasing temperature, the luminescent line narrows due to the decrease of the phonon dependent homogeneous part of the linewidth, and its intensity increases (see Section 3.2 and Fig. 7.5 for experimental dependence observed in sample #1). For the Si-center line at 737 nm, linewidths of 40 cm^{-1} (5 meV) and 18 cm^{-1} (2.2 meV) which are mostly caused by inhomogeneous broadening at 77 K, were observed for samples #1 and #2 respectively. The fine structure of this ZPL reported in Ref. 11-13 was not resolved in our samples due to large inhomogeneous broadening of spectral lines in CVD diamond films. The broadening phenomenon of the ZPL of CVD diamond originates from large inhomogeneous strain caused by various reasons, such as the polycrystalline structure, high concentration of crystal lattice defects, or different thermal expansion between the

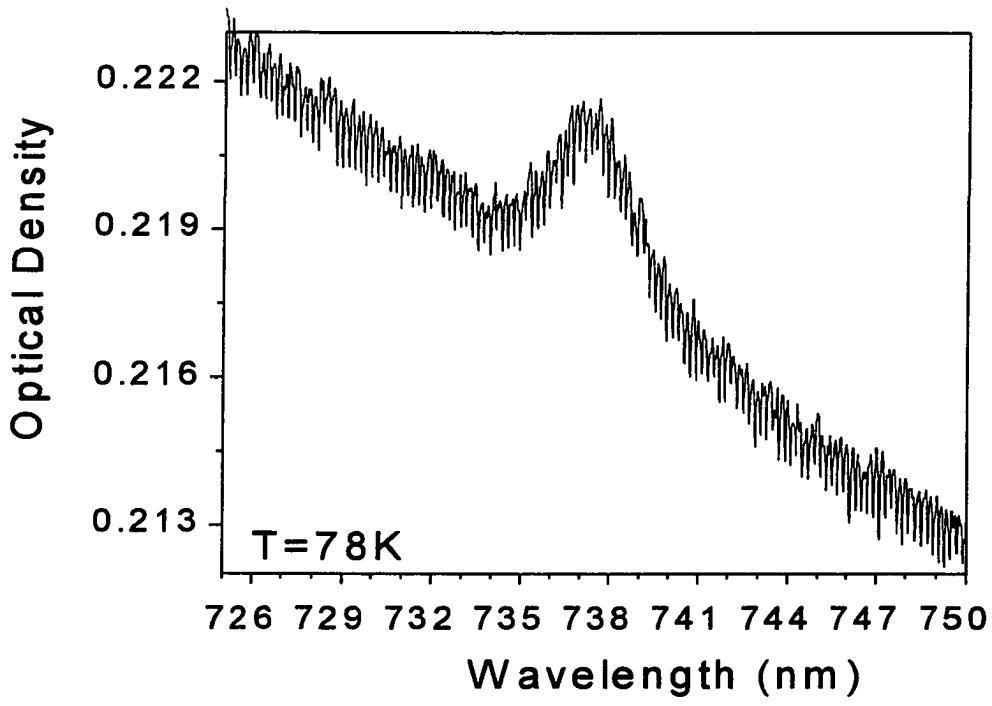

Figure 7.4. Absorption spectrum of the Si defect in CVD diamond sample #1.

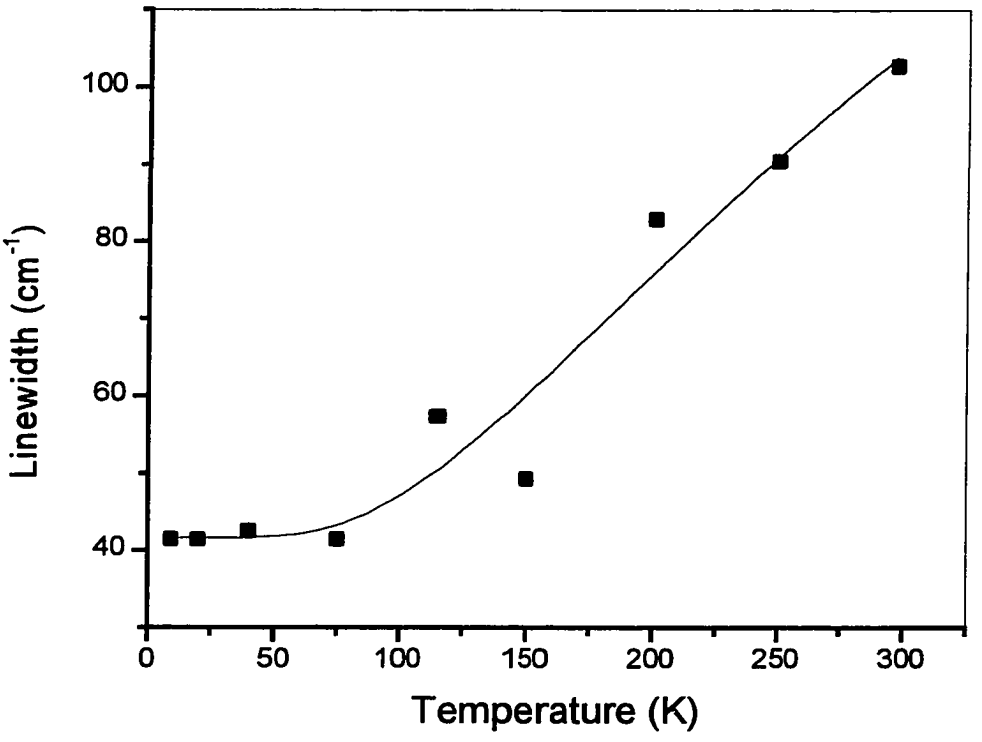

Figure 7.5. Temperature dependence of the inhomogeneously broadened line width of the Si defect peak at 737 nm in photoluminescence for sample #1. A flat portion of the curve at low temperatures allows determination of the inhomogeneous broadening of the spectral line. (Solid curve is a guide for the eye).

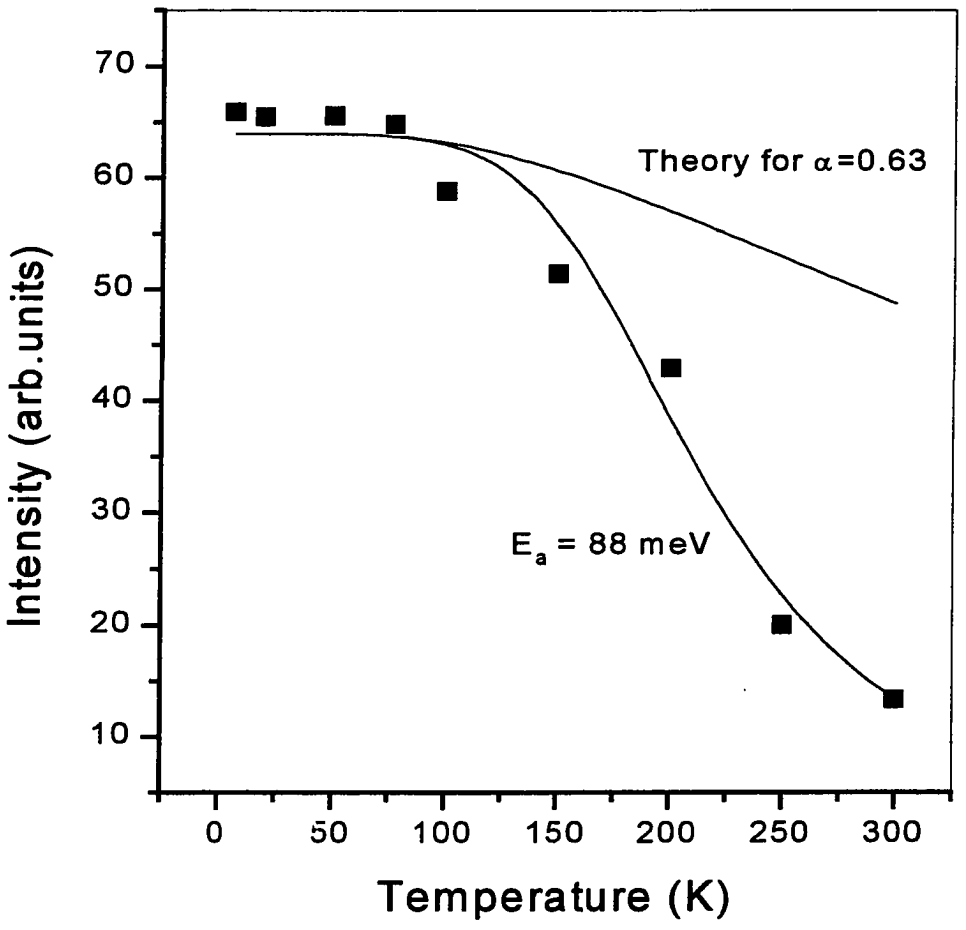

Figure 7.6. Experimental temperature dependence of the integrated intensity of the Si defect ZPL at 737 nm in CVD diamond sample #1 (squares). Solid lines represent theoretical curve according to equation (3.7) (Section 3.2) (upper line) and fitting curve with introducing of nonradiative transition according to equation (7.2) (lower line) with activation energy of 88 meV.

film and substrate. Therefore, this result shows that the quality of film #2 in terms of stress gradients, dislocations, and point defects is substantially better than that of film #1. Linewidth values between 32 and 80 cm^{-1} were observed for a few CVD diamonds at 77 K[9].

Taking into account the areas of ZPL and phonon sideband, the Debye-Waller factor was determined to be α=0.63±0.1 at T=9 K. Assuming quasilocal vibration at 514 cm^{-1} (see Section 7.3) to be the primary contributor to temperature dependence of the Debye-Waller factor, we can calculate the expected variation of the ZPL integrated intensity with temperature (Section 3.2). The calculated curve is shown in Fig. 7.6 together with the experimental data. It can be seen that the decrease in intensity is far greater than that predicted by the linear electron-phonon coupling. Clearly, we have a thermally activated process that leads to a reduction in the luminescence intensity.

The experimental dependence can be explained by a simple model involving competition between the radiative transition responsible for the photoluminescence emission and nonradiative transition[13]. The quantum efficiency for emission η can be expressed by

$$\eta = \frac{P_r}{P_{nr} + P_r} \tag{7.1}$$

where P_r is the probability for radiative transition and is independent of temperature, and P_{nr} is the sum of all nonradiative recombination processes. Assuming a single nonradiative process and that a barrier with an activation energy E_a is involved, equation (7.1) becomes

$$\eta(T) = \frac{P_r}{P_r + P_{nr} \exp\left(-\frac{E_a}{k_B T}\right)} \qquad (7.2)$$

where T is the absolute temperature, k_B is a Boltzmann constant, and P_{nr} is a the maximal rate of the nonradiative process. With this additional mechanism of decreasing of integrated intensity of ZPL, we were able to fit our experimental data well. The fitting curve is shown in Fig. 7.6. Using independently measured value of $P_r = 5.3\times10^7$ s^{-1} (Section 7.4), the activation energy E_a and the maximal rate P_{nr} were found to be 88±5 meV and $(4.3\pm0.5)\times10^9$ s^{-1} respectively. The activation energy 88 meV is the energy needed to channel the Si center from the excited state to the additional nonradiative path. The activation energy values of 56-70 meV are reported in the literature.[13,14] The exact mechanism of this thermally activated process is not known at the present time.

7.3. Luminescence Line Narrowing. [15]

The luminescence spectrum dramatically changes under resonance excitation of 0-0 ZPL at 737.3 nm of the Si defect (see Fig. 7.7). A few narrow peaks are now observed on the broad phonon sideband background in the one-phonon region (0-1332 cm^{-1})[16] of the lattice spectrum of diamond at temperatures between 10 and 200 K. In addition to the 767 nm line, a set of weaker lines between 790 and 820 nm appeared. Since all of these lines have excitation spectra resembling the 737 nm ZPL, these lines can be attributed to a Si center and, apparently, represent phonon replicas for the centers excited at 737.3 nm. The observed vibrational energies are 340 cm^{-1} for the 756 nm (1.640 eV) line, 515 cm^{-1} for the 767 nm (1.6165 eV) line, 1010 cm^{-1} for the 797 nm (1.556 eV) line and the barely resolved complex band centered at 1250 cm^{-1} for the 814 nm (1.523 eV) line. The observed behavior arises from the following

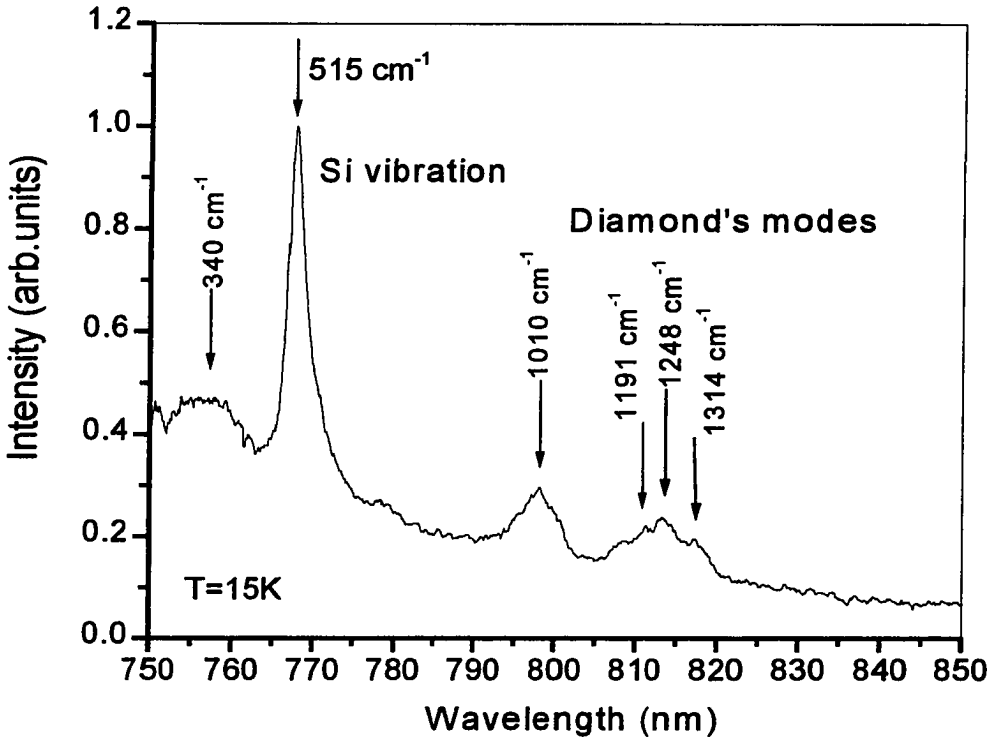

Figure 7.7. Photoluminescence spectra of CVD diamond film #1. Excitation wavelength is 737.3 nm and intensity is 4 mW/mm^2.

processes. First, the absorption cross-section at the excitation wavelength of 737.3 nm, near the maximum of ZPL at 737.0 nm, is much larger than at 514.5 nm. According to our measurements, it is about 2500 times larger at 10 K. Second, the narrowband laser excites only a selected part of the centers at 737.3 nm, within the inhomogeneously broadened absorption line of the pure electronic transition, which causes fluorescence line to be narrowed[17]. In our case, the vibronic line at 767 nm becomes 2.5 times narrower in comparison with the condition of nonselective 514.5 nm excitation.

At low temperatures, the phonon sideband structure of ZPL reflects the phonon density of states of an imperfect crystal, weighted by the extent to which the electronic transition of the defect center interacts with different lattice mode[18]. The density of states of natural and CVD grown diamonds have no sharp features[19] in the acoustic region around 515 cm^{-1}. Thus, the presence of the phonon replica at 767 nm indicates a significant modification of the lattice dynamics of diamond in the acoustic region by the Si impurity. A prominent resonance vibration at 515 cm^{-1} appears, which is close to the TO mode in crystalline Si (522 cm^{-1}), to the Si-Si bond in amorphous SiC (508 cm^{-1})[20], and to the vibration of the free molecule Si_2 (509 cm^{-1})[21]. On this basis we may ascribe this resonance mode to Si-Si vibration of our impurity. Appearance of such a vibration confirms the diatomic structure hypotheses for the Si defect[8]. Moreover, it points to the cluster quasi-molecular structure Si_2 for this defect. As the vibrational frequencies of the neutral cluster Si_2 and the negatively charged cluster Si_2^- are comparable (509 ± 10 and 528 ± 10 cm^{-1}, respectively[21]), the anion Si_2^- is not excluded as a possible defect on the basis of only the vibrational data. One should note, that there is no optical transition matching the observed ZPL at 737 nm for free Si_2 and Si_2^-. This leads to the

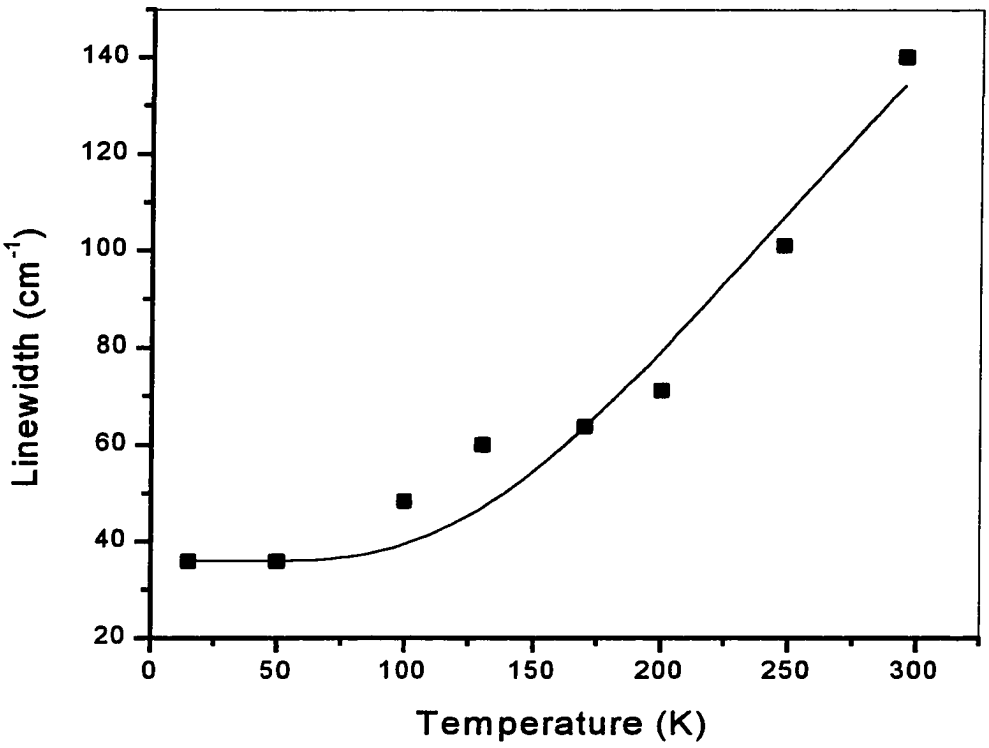

Figure 7.8. Temperature dependence of the linewidth of the quasilocal vibration peak at 767 nm in photoluminescence for sample #1. The minimal linewidth is defined by the lifetime of vibrational state and inhomogeneous distribution of vibration frequencies (Solid curve is a guide for the eye).

more complex Si defect configuration, possibly including vacancy and dangling bonds in addition to the cluster Si_2.

For the temperature range between 9 and 50 K, the linewidth of the 767 nm peak is 36±2 cm^{-1} (4.5 meV) and is temperature independent. As the temperature increases, the line broadens and reaches 140 cm^{-1} (17.4 meV) (see Fig. 7.8). At low temperatures, one may identify two temperature independent (or weakly dependent) parts contributing to the observed linewidth of 36 cm^{-1}: homogeneous broadening related to the 515 cm^{-1} vibrational state lifetime and inhomogeneous distribution of this vibrational frequency[22]. At higher temperatures, the major contributions in the observed linewidth are due to the temperature dependent phonon parts of the homogeneous linewidths occurring from both pure electronic and vibronic transitions.

The phonon replica at 1010 cm^{-1} may be assigned to the second overtone of 515 cm^{-1} Si-Si bond vibration, or to the LA phonons at the L critical points in the Brillouin zone with frequency 1006 cm^{-1}, or other critical point phonons of similar energy[19]. The dependence of the phonon frequencies of these vibronic lines on the energy of the laser excitation across the 0 - 0 band has been studied in order to choose between the above-mentioned assignments. The replica at 515 cm^{-1} increases almost linearly in energy from 508 to 527 cm^{-1} with decreasing wavelength of optical excitation from 739 to 736 nm. This frequency increase means that defects with higher electronic energy have stiffer Si-Si bonds, which results in good correlation between the inhomogeneous distributions of the 0 - 0 electronic and 0 - 1 vibronic transitions. One can expect a similar dependence on wavelength but with double the slope for the replica at 1010 cm^{-1} if this line were an overtone of the 515 cm^{-1} mode. However, a totally different

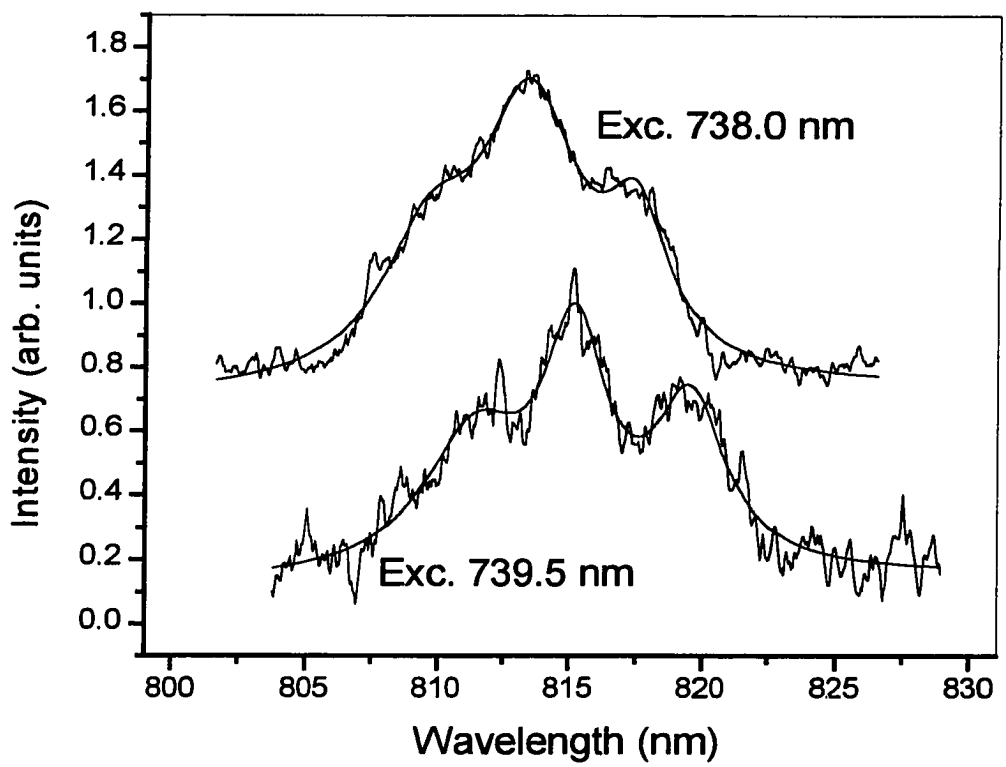

Figure 7.9. Photoluminescent spectra and the fitting curves of the triplet structure at 814 nm under excitation with different wavelengths. Spectra are shifted vertically for clarity.

behavior was observed. Therefore, the replica at 1010 cm^{-1} originates from a phonon spectrum of diamond.

In addition to the phonon replica frequencies, the linewidths are also found to be dependent on the energy of optical excitation. For the 1250 cm^{-1} replica the narrowest linewidth appears at 739.5 nm excitation. In this case a triplet structure is clearly resolved (see Fig. 7.9). Most likely, the observed linewidth dependence on excitation energy is related to correlation between the vibrational inhomogeneity for phonon replicas and electronic frequency of pure electronic transition. Comparing the observed frequencies with the energy of critical-point phonons, the line at 1191(±3) cm^{-1} is ascribed to TO(L) (1206±5 cm^{-1} according to Ref. 19), the line at 1248(±4) cm^{-1} is ascribed to LO(L) (1252±5), and the line 1314(±12) cm^{-1} is ascribed to O(Γ) (1332.5±1). The error in our results is ± 2 cm^{-1}. The uncertainty shown in brackets is determined by the dependence of phonon structure on the energy of optical excitation between 738.0 and 739.5 nm, where the triplet structure is resolved. Due to this uncertainty, the proposed assignments are tentative. Nevertheless, we would like to indicate the high activity of the L point phonons in the observed luminescence spectra that leads to a suggested orientation of the Si_2 defect along the <001> axis of the diamond lattice.

7.4. Ultrafast Time-Resolved Photoluminescence Measurements. [23]

As indicated above, the photoluminescence spectrum of a typical CVD diamond consists of a few zero-phonon lines (ZPL) attributed to different point defects and a broad band peaked at ≈ 600 nm (2.05 eV). Recent analyses attribute this band to sp^2-bonded carbon clusters[23] or to an sp^2 disordered amorphous carbon phase[25]. The prominent ZPL at 737 nm (1.6823 eV) belongs to the Si optical center. Some studies, including ours[14], point to a diatomic quasimolecular Si_2 structure[8] with participation of a vacancy[4].

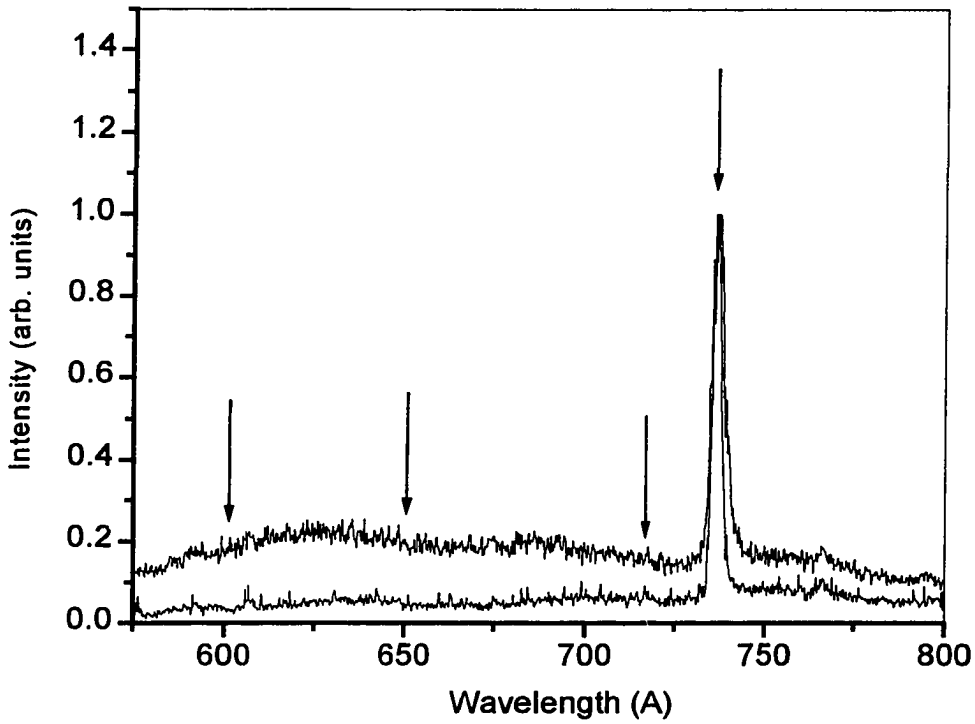

Figure 7.10. Photoluminescence spectra of CVD diamond films (film #1 is the upper spectrum and film #2 is the lower one) under 532-nm 1 MW/mm^2 30 ps pulse excitation at 77 K. Arrows show the wavelengths where photoluminescence decay was measured in bandwidth of 12 nm.

The decay time of the Si-center in diamond films was measured recently in catodoluminescence[26] and photoluminescence[11] spectra. The complex catodoluminescence decay with a slow initial portion followed after 3 ns by a more rapid exponential decay with a time of 2.4 ns was observed for the microwave CVD grown film at 77 K[26]. The photoluminescence monoexponential decay with decay time vary between 4 ns (5 K) and 2.7 ns (300 K) was observed for the homoepitaxial film, and close to 1 ns for the polycrystalline film[11]. This discrepancy was ascribed either to a non-radiative recombination, or to the presence of high strain in polycrystalline film. The decay time of 1.5 ns for Si-center, and of 0.65 ns and 9.6 ns for broadband photoluminescence were measured for polycrystalline film at 20 K[27]. No luminescence quantum yield was determined.

For the time-resolved measurements, the photoluminescence from CVD diamond was excited by single pulses of the second harmonic of a mode-locked Nd:YAG laser at 532 nm (2.33 eV) with repetition rate of 10 Hz and pulse duration of 30 ps. Photoluminescence was collected with the back reflection scheme, passed through a wavelength selection filter and focused onto the slit of a streak camera (Hamamatsu) with time resolution of 10 ps. The signal from the streak camera was accumulated and averaged up to 3000 times for each curve by an OMA III system. During measurements, samples were kept in liquid nitrogen at temperature 77 K. Quantum yields of luminescence were determined by comparison of steady state photoluminescence spectra of the diamond films and Styryl 7 dye solution in ethylene glycol with a known luminescence yield of 0.7.

High intensity of the pulsed laser could bring out some new features in the photoluminescence spectrum due to multiphoton absorption or other nonlinear mechanisms. To check such a possibility, the photoluminescence spectra were measured at the same

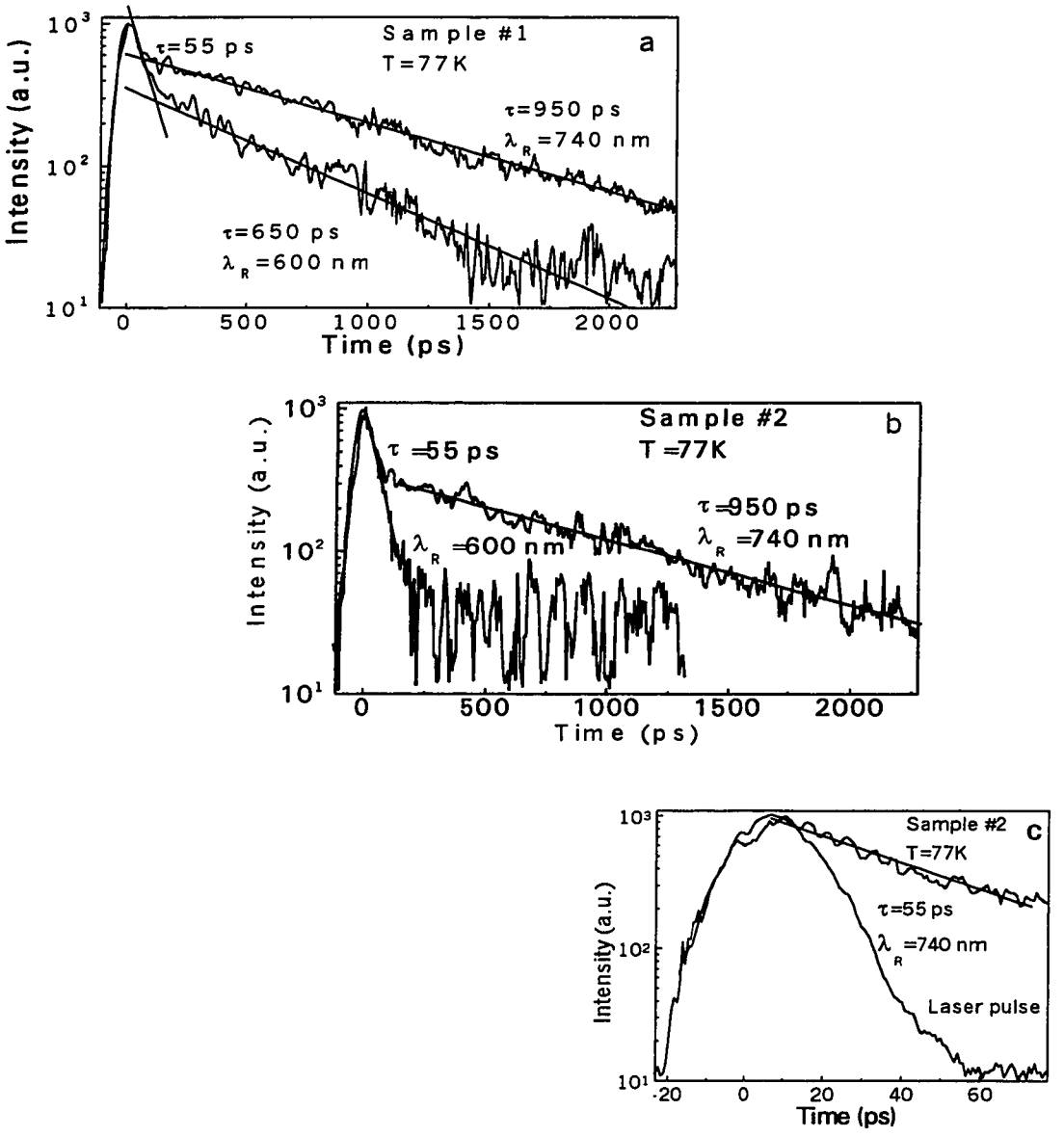

Figure 7.11. Decay curves of the photoluminescence of the two CVD diamond films at different wavelengths with low (a, b) and high (c) streak camera scan speed. Straight lines represent simple exponential decay. Laser pulse (c) shows the time resolution of the registration system. The zero time was set at maximal amplitude of excitation pulses. Excitation wavelength is 532 nm and intensity is 1 MW/mm^2.

conditions of excitation using high intensity pulses which were used for photoluminescence decay detection. The time integrated spectra (Fig. 7.10) are very similar to those of the steady state conditions (Fig. 7.3) for both samples. These results indicate that the origin of the photoluminescence is essentially the same for CW and pulse excitation. The photoluminescence decay was measured at four different wavelengths of 600 nm, 650 nm, 720 nm and 740 nm, as marked by arrows on Fig 7.10, in a bandwidth of 12 nm. The decay curves for both samples at 740 and 600 nm are displayed in Fig. 7.11 on a semilogarithmic scale. The photoluminescence decay of either sample at a wavelength of 740 nm is nearly biexponential with a short time constant of 55 ps and a long one of 950 ps. At the wavelength of 600 nm sample #1 shows biexponential decay with the same short constant of 55 ps but with a different long constant of 650 ps (Fig. 7.11 a), while sample #2 shows a fast single exponential decay with a constant of 55 ps (Fig. 7.11 b). Measurements at 650 and 720 nm give similar time constants as at 600 nm, but with a different amplitude ratio between short and long components. We do not observe any decay dependence on intensity of laser excitations in the range between 0.06 and 2 MW/mm^2. The results of fitting of the decay curves using laser pulse deconvolution are presented in Table 7.1.

To make the interpretation clearer, we have marked the photoluminescence spectrum of sample #1 by points showing the relative amplitude of each exponential decay from Table 7.1 (Fig. 7.12). Corresponding to the three observed decay constants we can define three spectral sub-bands. The first sub-band α and adjacent vibrational band, which decay with a time constant of 950 ps, are due to the Si optical center with a ZPL at 737 nm. The second sub-band β, the broad band between 550 nm and 900 nm, has a very fast decay of 55 ps. The

	600 nm	650 nm	720 nm	740 nm
$A_1(\tau_1=55$ ps)	0.6±0.15	0.6±0.15	0.8±0.15	0.3±0.1
$A_2(\tau_2=650$ ps)	0.4±0.1	0.4±0.1	0.2±0.1	---
$A_3(\tau_3=950$ ps)	---	---	---	0.7±0.15

Table 7.1. Relative amplitudes of the luminescence decay multiexponential $\sum_{i=1}^{3} A_i \exp\left(-\frac{t}{\tau_i}\right)$ fitting for sample #1.

third sub-band σ covers the range between 550 and 700 nm and has a decay of 650 ps. The sub- band σ does not appear in sample #2. We will discuss the origins of the broad sub-bands β and σ later.

To understand the mechanisms of the observed picosecond decays, the photoluminescence yields were determined for sample #1 at two excitation wavelengths of 514.5 nm and 737 nm. In the case of 514.5 nm excitation our estimate is $8x10^{-4}$ and 10^{-4} for the broad photoluminescence band and for the Si-center spectrum respectively. The yield of 0.05±0.01 was determined for the Si-center photoluminescence for excitation in the ZPL at 737 nm. Consequently, the major reason for the fast luminescence decays is the large probability of non-radiative recombination in our CVD diamond films. The values for the yield are based on the amount of the absorbed photoexcitation energy. The absorption spectrum was measured at 78 K (see Fig. 7.4), and the value of 1.4 ± 0.1 cm^{-1} was obtained for a Si-related absorption at 737 nm.

The 950 ps photoluminescence decay time for the Si-center is the same for both films and similar to decay times measured for different polycrystalline diamond films[11,27]. This result shows that the photoluminescence quenching most likely is not related to the disordered carbon phase and that other defects, such as dislocations, are responsible for non-radiative recombination. The photoluminescence yield of 0.05 leads to a calculated radiative transition time of τ_r = 19 ns which is close to that of an allowed transition with unit oscillator strength. Assuming equal degeneracies of the excited and ground states of the transition and using radiative time τ_{RAD} =19 ns, linewidth Γ_{inh} = 40 cm^{-1} at 77 K, absorption integral cross section of 10^{-15} cm^2 was estimated according to Ref. 28

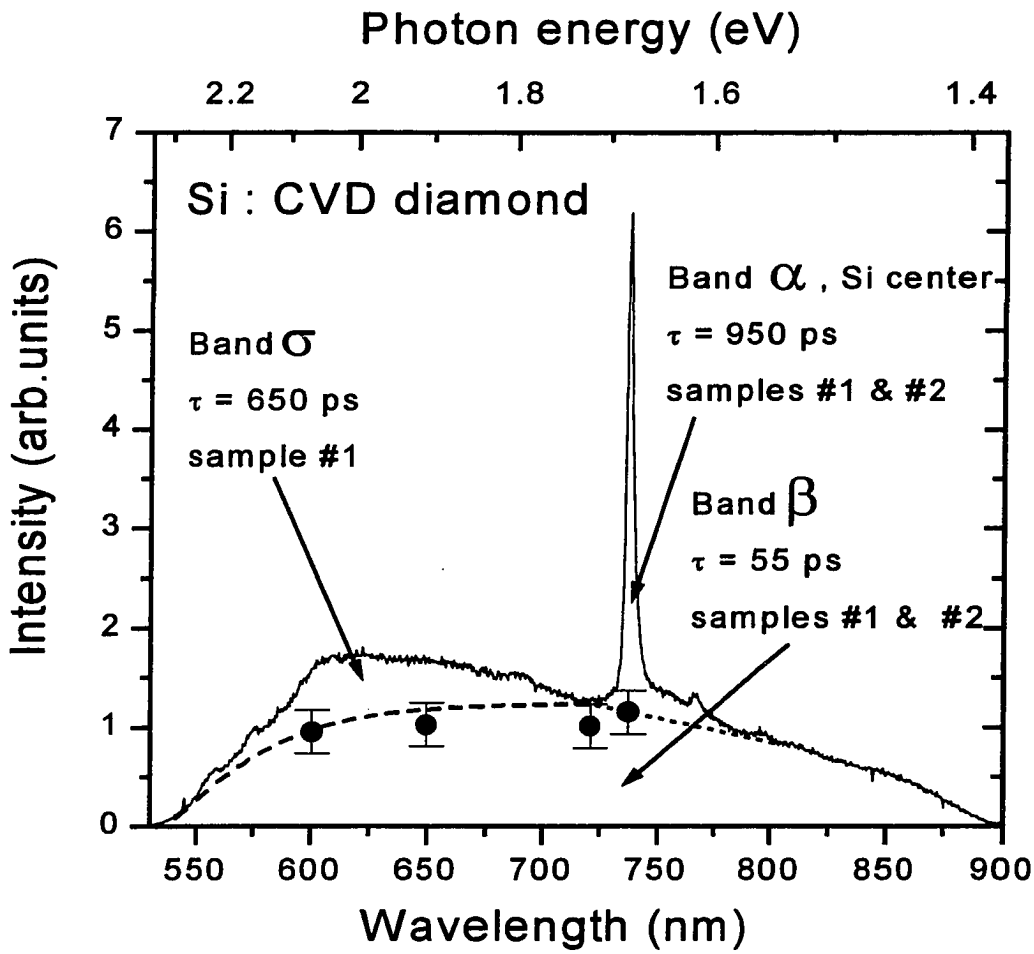

Figure 7.12. Luminescence spectrum of diamond film #1 (solid line) and normalized contributions of each exponential photoluminescence decay component (points). Dashed and dotted lines are hand drawn to illustrate the complex photoluminescence spectrum structure.

$$\int \sigma(\upsilon) d\nu = \frac{\lambda^2}{8\pi} \frac{1}{\tau_{RAD}} \qquad (7.3)$$

where $\lambda = c/n_0\upsilon$, $n_0 = 2.4$ is a coefficient of refraction for diamond, and $\sigma(\upsilon)=\alpha(\upsilon)/n$ where n is a density of absorbing centers, and $\alpha(\upsilon)$ is an absorption coefficient at frequency υ, which was obtained from the observed line profile in absorption A(ν) and thickness of the sample. The calculated absorption cross section allows estimation of a concentration of the Si centers in sample #1 to be 2×10^{15} cm^{-3}. Such a low concentration is the same order of magnitude as that for Si ion implanted diamonds[7] and reflects very low solubility of Si in the diamond host.

The photoluminescence sub-band β between 550 and 900 nm with decay time of 55 ps was observed in both samples and in accordance with the results of Ref. 24 and 25 may be ascribed to luminescence of an sp^2 carbon phase in CVD diamond. The lower intensity of the sub-band β in sample #2 may be explained by the effective quenching in this disordered carbon-rich film. The structure and location of this sp^2 - bonded phase and the mechanism of photoluminescence are under discussion. Our observation of a fast monoexponential photoluminescence decay and low quantum yield contradicts the interpretation[25] based on the model for optical transitions between localized band-tail states of a disordered semiconductor[29]. This model predicts a broad distribution of the radiative and non-radiative transition probabilities due to tunneling over different separations of the electron and hole (or trap). More likely, the excited electrons relax to the radiative state, which is efficiently quenched by the non-radiative recombination with a single or narrow distribution of transition rates. Surface states and (or) dangling bonds could be responsible for such a mechanism. The

spectral position of the other sub-band, σ, matches the vibronic band of the 575 nm (2.154 eV) optical center, with the maximum near 600 nm[24,29]. However, we cannot ascribe this band to the 575 nm center which has a 29 ns lifetime[27,31] much longer than the 650 ps observed for sub-band σ. We suggest that the σ sub-band represents the second component of sp^2-related photoluminescence which has the relatively long decay of 650 ps, close to the decay time observed in Ref. 26. This sub-band is completely quenched in carbon-rich film #2.

7.5. Persistent Spectral Hole Burning.

PSHB in diamond has been studied in different ZPLs at low temperatures[32-34]. The first investigation of PSHB in diamond concerned four well-known centers, i.e. the N3 center (containing three nitrogen atoms) with ZPL at 415 nm, the H4 center (formed by a vacancy and an aggregate of nitrogen atoms) with ZPL at 496 nm, the nitrogen-vacancy center (N-V) at 637 nm, and the GR1 center (consisting of single vacancy) with ZPL at 741 nm[31]. In case of the nitrogen-vacancy center, a short-lived hole burning spectrum, which caused by a redistribution of spin levels[33] is studied. PSHB in neutron-irradiated and annealed diamond was investigated at helium temperatures for several ZPLs in the red spectral range; in one of these ZPLs (at 655 nm) PSHB could be observed up to 200 K[34]. Room temperature PSHB in this material was also reported for lines at 774 nm and 813 nm[5].

In our investigation, for the first time persistent spectral hole burning in the 737 nm Si defect line was observed at temperatures of 2-17 K. A holewidth of ~300 MHz and a hole lifetime more then 10^3 seconds were detected at the lowest temperature. Detection of the spectral hole burning has been performed in the photoluminescence excitation spectrum at 767 nm replica (Fig. 7.13, spectrum of sample #1 is shown). This

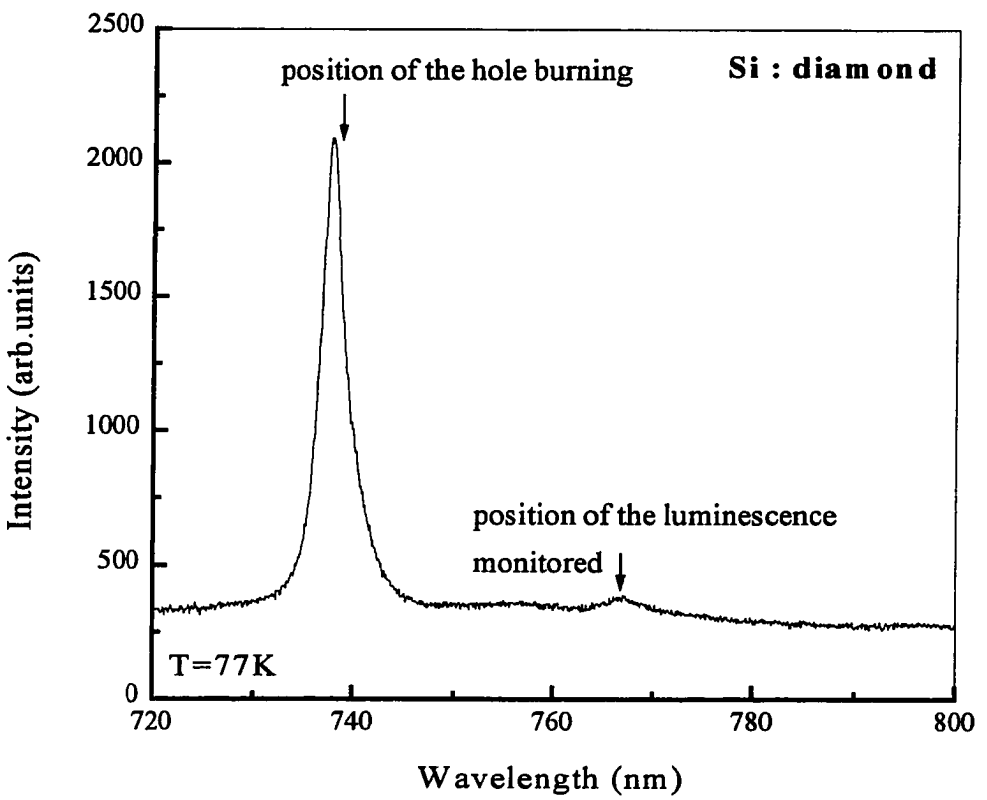

Figure 7.13. Luminescence spectrum of CVD diamond film #1. PSHB was performed in ZPL at 737 nm and detected in photoluminescence excitation spectrum of the quasilocal vibration peak at 767 nm.

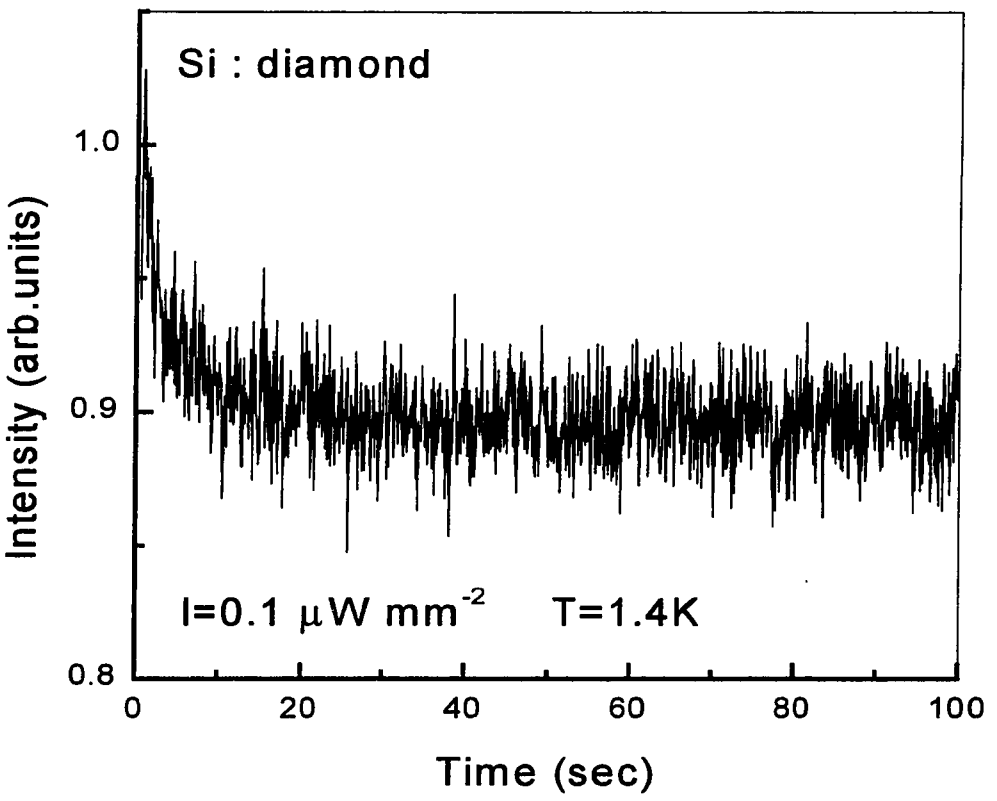

Figure 7.14. An experimental hole burning kinetics observed in CVD diamond sample #1 at 1.4 K at 738.2 nm. Burning laser intensity was 0.1 $\mu W/mm^2$.

detection method is useful for CVD diamond films especially because it is difficult to observe transmission spectra for opaque films.

Persistent spectral holes were burnt in the inhomogeneously broadened ZPL of the Si defect at 737 nm with laser intensity of 0.1 $\mu W/mm^2$ and detected in photoluminescence excitation spectrum of the quasilocal vibration peak at 767 nm with substantially reduced intensity of 0.001 $\mu W/mm^2$. The lower limit of detection intensity was set by the signal-to-noise ratio of the detected photoluminescence. Because of this, the detection was slightly destructive for the burnt hole spectra and allowed only a single scan of the hole.

To evaluate suitability of this material for practical application, quantum efficiency of PSHB was determined using hole burning kinetics shown in Fig. 7.14. The low temperature peak homogeneous absorption cross section was found according to Ref. 35 from integral absorption cross section of 10^{-15} cm^2 and multiplicity ratio $\Gamma_{inh}/\Gamma_{hom} = 2500$ and was shown to be 4×10^{-12} cm^2. Using value of burning intensity of 0.1 $\mu W/mm^2$, low temperature peak homogeneous absorption cross section of 4×10^{-12} cm^2, and Debye-Waller factor of α=0.63, experimental kinetics was fitted by equation (6.6) (see Chapter 6 for the method of determination of the quantum efficiency of PSHB developed in this Thesis). The quantum efficiency of the hole burning process was obtained to be 10^{-4}, with maximal relative hole depth 0.2. Limited maximal hole depth can indicate existence of substantial non-resonance absorption and/or unknown photoinduced reverse processes that counteract the hole burning.

The linear character of the hole burning process was determined by studying the intensity dependence of the initial rate of hole burning according to equation (3.25) (Section 3.5) (Fig. 7.15). A single-photon persistent hole burning mechanism must be

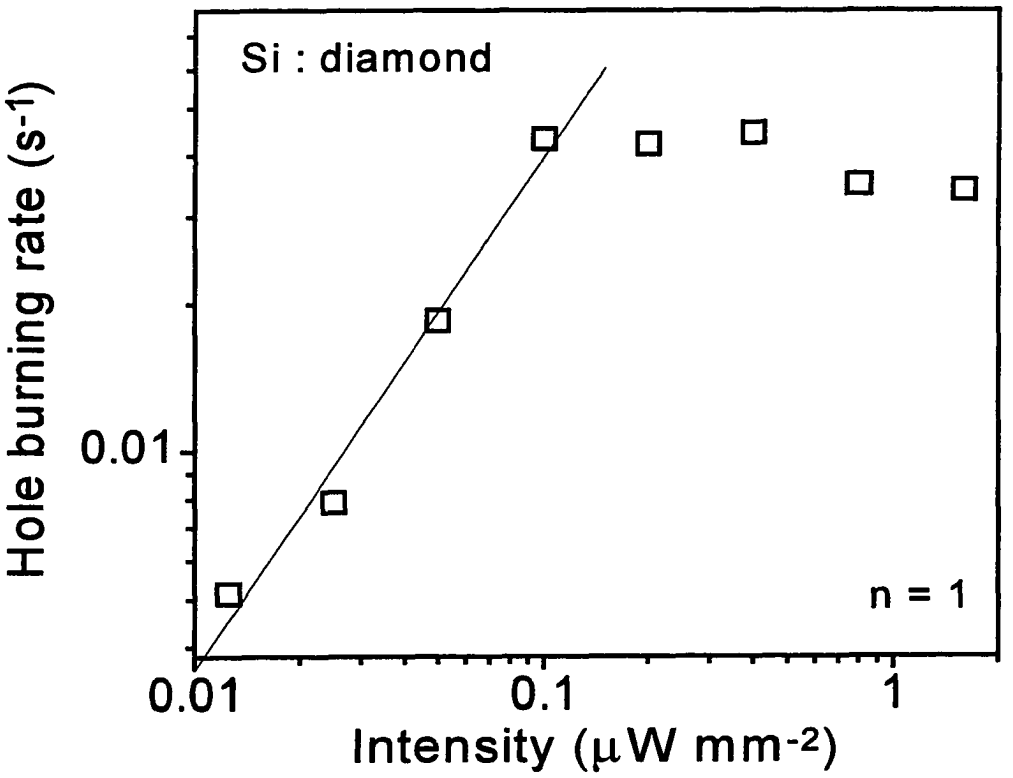

Figure 7.15. Dependence of an initial rate of hole burning on burning laser intensity.

concluded. Flat portion of the experimental dependence at higher burning intensities may be explained by population saturation effects.

For GR1 color center in an electron-irradiated type IIa diamond, a non-linear dependence of PSHB efficiency (which is proportional to an initial rate of hole burning) was reported and thereby a multiphoton mechanism of hole burning was introduced[32]. Such a multiphoton process can be due to an excitation in a higher level, and for the GR1 center these excitations are described in literature in connection with photoionization[31]. A corresponding process can be eliminated in our case because we did not observe such a nonlinear dependence.

Typical holeshape was fitted well by a Lorentzian and at the achieved signal-to-noise ratio did not show any specific features (Fig. 7.16). Presented profile was measured at 1.4 K, after 3 seconds of burning exposure. Observed holewidth for these conditions is 360 MHz and relative holedepth is about 15%.

We made an attempt to search for anti-hole lines and satellite holes to confirm energy level structure presented in Ref. 11,12, and 14. This search was extremely difficult due to poor signal-to-noise ratio (limited by the low intensity of the reading laser which is in its turn limited by the high photosensitivity of the samples studied), large spectral shift, and unknown inhomogeneous distributions of these spectral lines. At the present time, no anti-hole lines or satellite holes were found.

To understand relaxation processes for the Si center, it is important to determine the low intensity zero-exposure limiting holewidth. The usual way to do that is to study a holewidth as a function of the intensity and exposure. Taking linear extrapolation to $I \rightarrow 0$ and $t \rightarrow 0$, the minimal holewidth was obtained to be 330 MHz at 1.4 K, which is in an

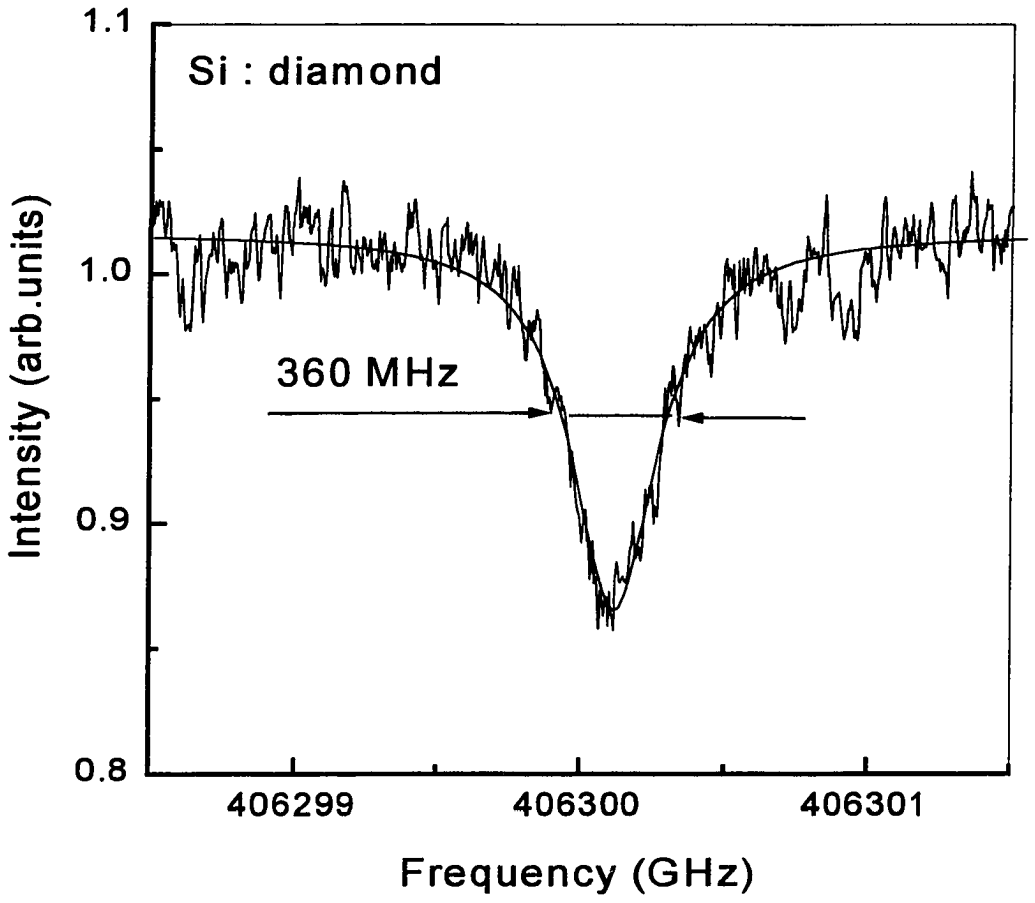

Figure 7.16. A representative spectral hole profile detected at 1.4 K after 3 s exposure time with burning intensity of 0.1 $\mu W/mm^2$.

excellent agreement with our lifetime measurements for this optical transition. This correlation shows that a spectral diffusion and other dephasing mechanisms are essentially absent at this low temperature. The experimental dependencies of hole depth and hole width on exposure time for burning intensity of 1 $\mu W/mm^2$ are presented in Fig. 7.17. In the frame of standard PSHB models (see Chapter 3), both relative hole depth and hole width are expected to increase with burning time. Taking into account normal behavior of PSHB kinetics (Fig. 7.14) recorded at burning intensity of 0.1 $\mu W/mm^2$, experimental dependencies presented in Fig. 7.17 might be explained by the unknown opposite to hole burning photoinduced processes activated at higher burning intensities.

The holewidth of persistent holes in the Si center depends strongly upon temperature (see Fig. 7.18). The rapid broadening is observed for the spectral holes between 1.4 and 20 K ($\Gamma_h \propto T^5$) and suggests a coupling to a low frequency vibrational mode. Unfortunately, the experimental temperature range is too restricted to unambiguously determine the mechanism from its temperature dependence. Though the possibility of direct phonon absorption (emission) process (Section 3.5) or Orbach process[28] can hardly be ruled out completely, considering high frequency phonon spectrum inherent for diamond, we argue for the mechanism involving quasielastic scattering of a vibrational mode. Off resonance scattering for a Debye spectrum of diamond would give a T^7 dependence. However, if we approximate the density of the states by a delta function at frequency ω, the temperature dependence of the linewidth is given by equation (3.19) from Section 3.5. Observed experimental dependence was fitted by equation (3.19) with energy of quasilocal vibration equal to 19 cm^{-1}. Fig. 7.18 displays both experimental data and corresponding fitting curve.

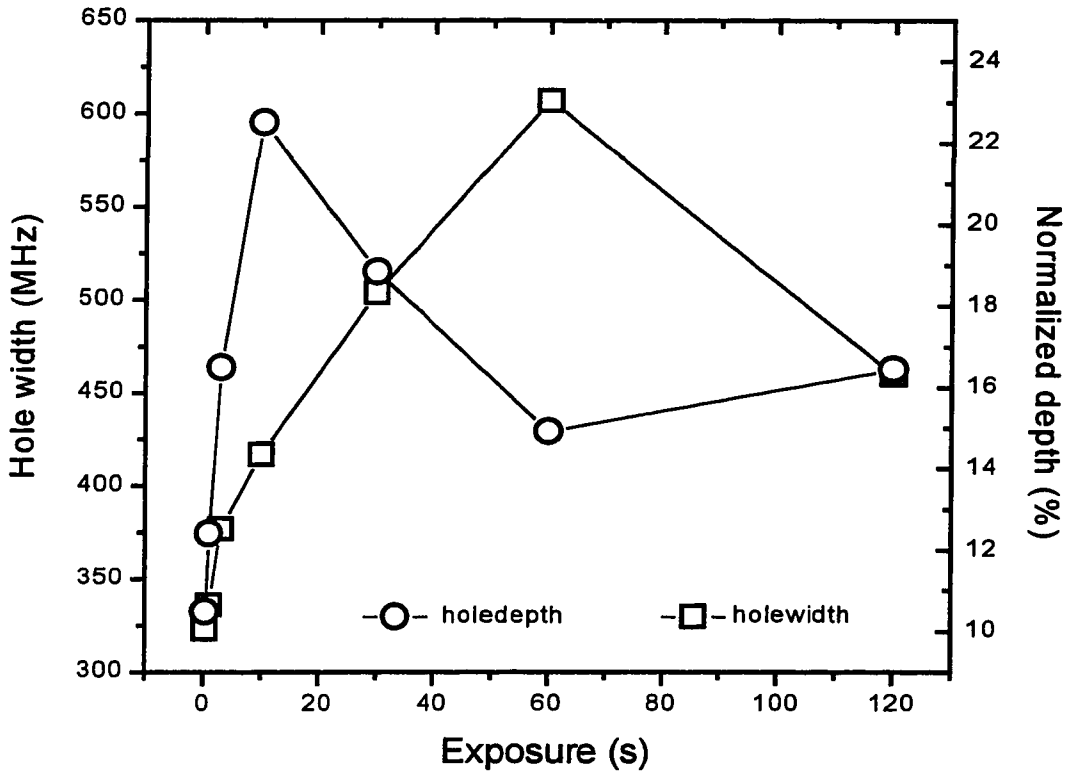

Figure 7.17. Experimental dependencies of the hole width and hole depth on the exposure time. Burning intensity is 1 $\mu W/mm^2$.

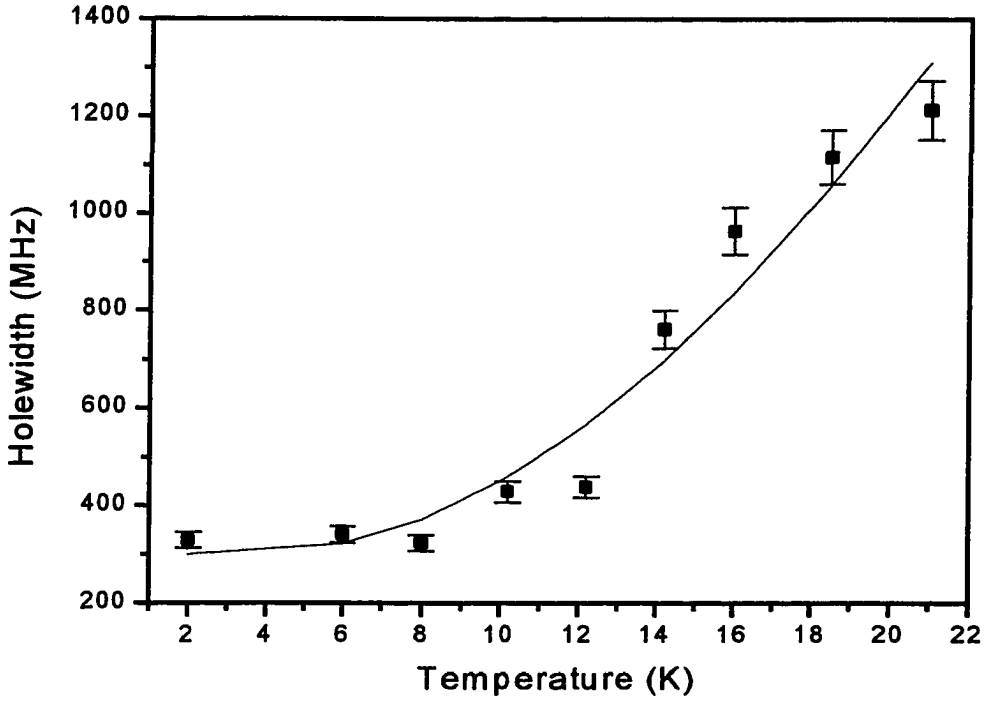

Figure 7.18. Experimental temperature dependence of the holewidth and fitting curve according to equation (3.19) with energy of quasilocal vibration of 19 cm^{-1}.

Our studies of the persistent spectral hole burning for Si center show a clear hole interaction effect, in which the apparent size of a spectral hole decreases after a second hole is burned nearby in frequency space (see Fig. 7.19). Spectrally nonselective heat induced mechanism of a hole refilling has to be ruled out due to absence of such effect under non-resonance excitation (i.e. excitation spectrally positioned out of the 737 nm peak) with comparable laser intensity and absorption. Observed photoinduced hole refilling shows that photoproducts are accumulated at wavelengths within the ZPL. Since the "old" hole is not fully filled up with the photoproducts of the "new" one, the photoproducts are still spread throughout a relatively wide wavelength range.

Holes burnt in the Si center are quite stable at low temperature: no observable degradation in hole shape at 1.4 K was detected for dark times on the order of hours. Furthermore, holes can withstand a certain amount of temperature cycling without complete annealing of the hole and reversal of the photophysical process. After allowing the cryostat to warm up to temperature 120 K for dozen of minutes, previously burnt holes could regularly be observed, although with reduced area and increased width (Fig. 7.20). Fig. 7.21 displays experimental dependencies of a relative hole width and a relative hole area on annealing temperature. Observed dependencies show that both spectral diffusion (responsible for the hole broadening) and hole refilling process (responsible for decrease in the hole area) are present.

Summarizing the analysis of the presented experimental data, we made a conclusion that a single-photon photophysical process is responsible for persistent spectral hole burning in Si defect in CVD diamond film. This mechanism is likely to involve rearrangement of the local environment of the Si center. Particularly, Clark *et al.* results[11]

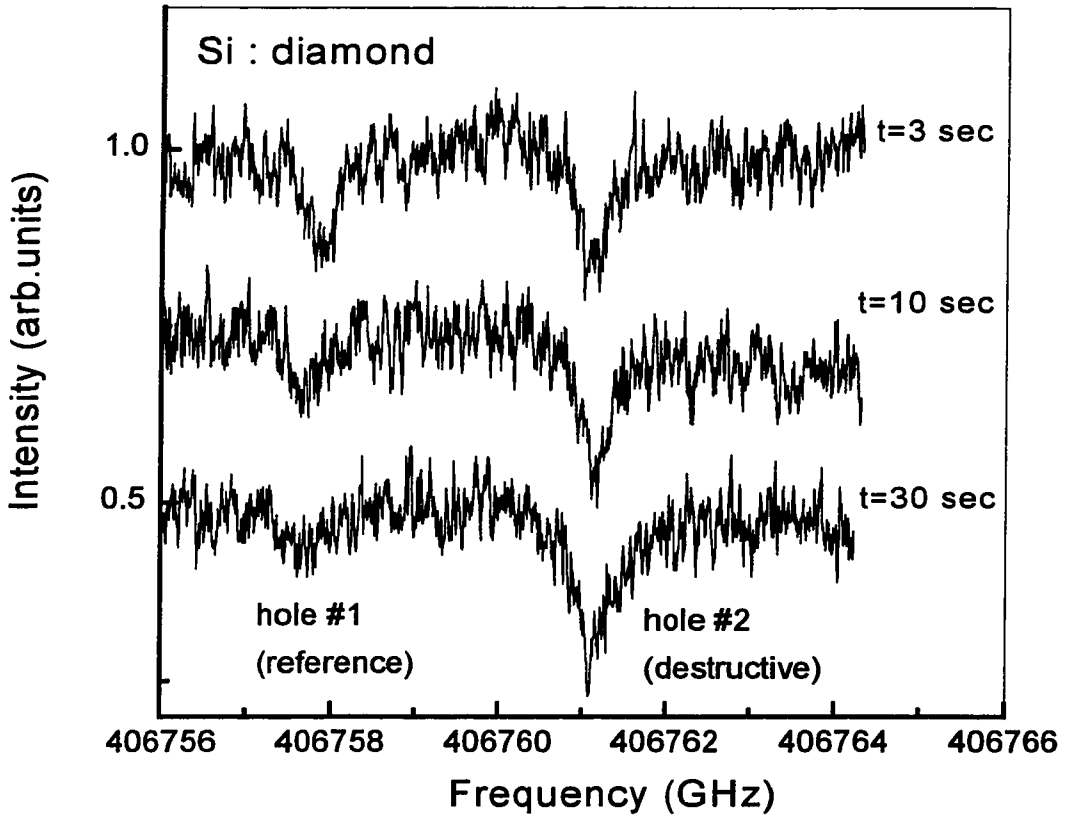

Figure 7.19. Photoinduced hole refilling. Spectra show that hole #1 is partially destroyed by the burning of hole #2 in the spectral vicinity of hole #1. Exposure times for hole #2 are marked. Exposure time for hole #1 was 30 s. Burning intensity was 0.1 $\mu W/mm^2$ for both holes.

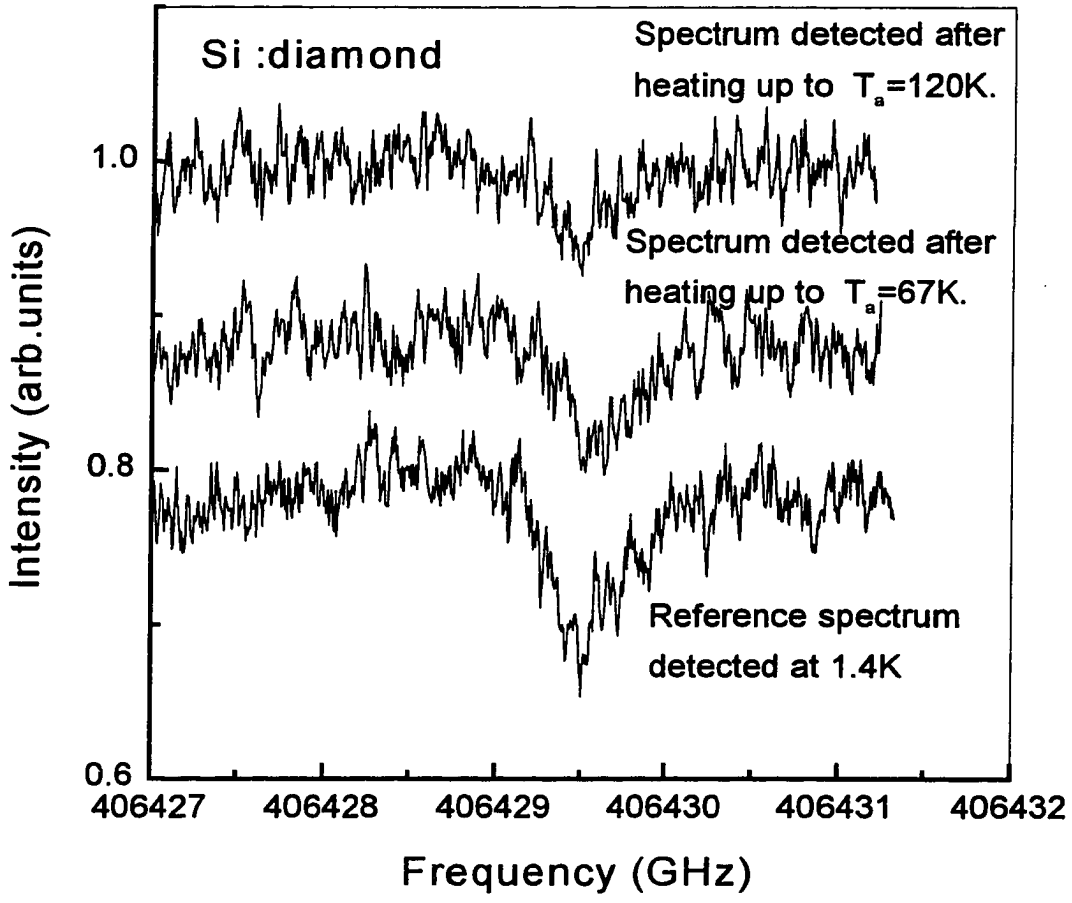

Figure 7.20. Spectral hole profiles after temperature cycling experiment. Spectral holes were able to withstand temperature cycle with annealing temperature up to 120 K.

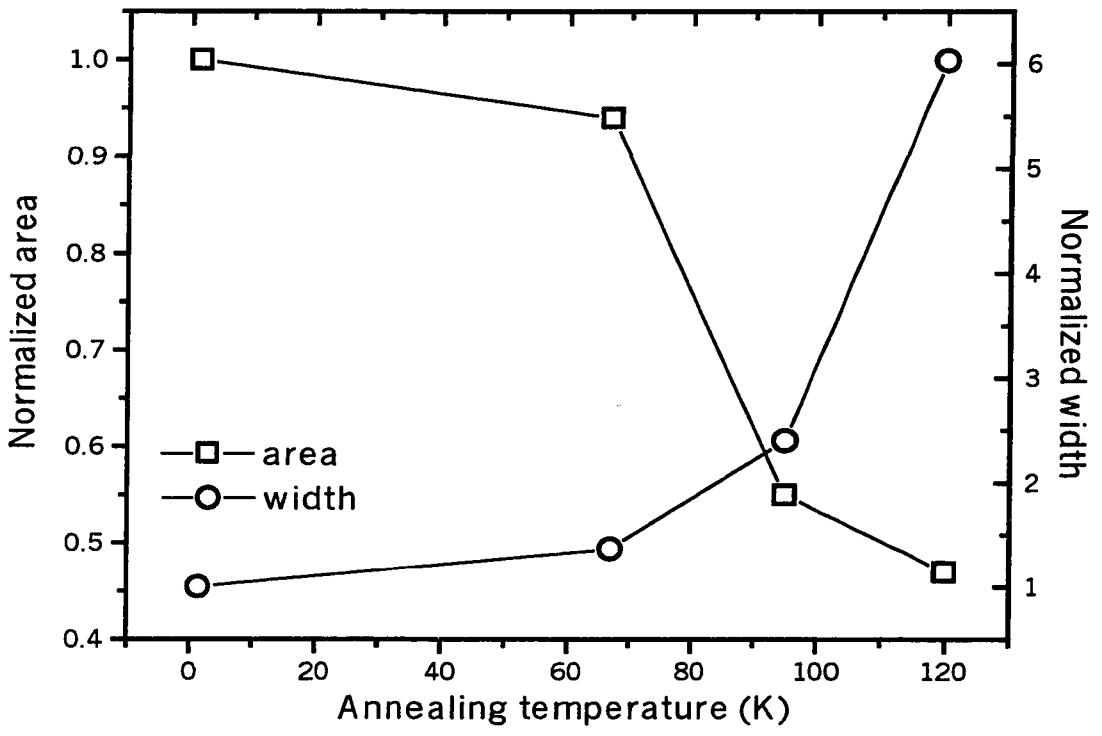

Figure 7.21. Temperature dependence of the relative hole area and width on annealing temperature in the temperature cycling experiment.

suggest the structure of Si defect, which has two similar configurations available to it. Though the spectral fine structure for Si defect usually is not observed in polycrystalline CVD diamond, a tunneling between two similar configurations in the excited state of the Si defect might lead to PSHB. In terms of this mechanism of PSHB, hole refilling (Fig. 7.19) might be explained by photoinduced redistribution of ground state population between metastable energy levels with separation on the order of hundreds of megahertz caused by tunneling behavior. This splitting proved to be highly sample dependent and, consequently, hole refilling processes can be eliminated by increasing this energy difference up to values exceeding the inhomogeneous broadening. Assuming thermally assisted tunneling in the ground state to be responsible for decrease in relative hole area during temperature cycling experiments, we may estimate primary parameters of the ground state potential. The energy levels splitting, tunneling rate, and potential barrier height were found to be 300 K, 10^{-2} s^{-1}, and 1700 K respectively (see Chapter 8 for details on thermally assisted tunneling).

7.6. Summary of results.

For the first time, PSHB in Si center in CVD diamond film was demonstrated in temperature range 1.4 – 21 K. Photoluminescence, fluorescence line narrowing, and spectral-hole burning of the Si impurity center at 737 nm in CVD diamond were studied. Di-atomic quasi-molecular Si_2 structure of the defect has been proved. A set of important spectroscopic parameters such as lifetime, absorption low temperature integral and peak homogeneous cross sections, quantum yields of photoluminescence at different excitations, and quantum efficiency of hole burning were obtained. A single-photon photophysical mechanism of persistent hole burning was proposed. There are some

indications that an unknown opposite to hole burning photoinduced process is operating at higher burning intensities. Mechanism of the temperature broadening of homogeneous ZPL involving local vibration with energy 19 cm^{-1} has been established. High thermostabily (up to 120 K) of spectral holes and high multiplicity ratio in CVD diamond show a good potential of this sort of materials for high temperature high density hole burning.

References for Chapter 6

[1]. J. Angus and C. Hayman: Science **241**, (1988) 913-921.

[2]. A. M. Zaitsev in: Optical Properties of Diamond, FernUniversitat GHS in Hagen, 1995.

[3]. Grant proposal by Prof. R. R Alfano and Prof. A. A. Gorokhovsky (1996).

[4]. I. Sildos, U. Bogner and A. Osvet in: Pnonon scattering in condensed matter, VII, Eds. M. Meissner and R. O. Pohl, Springer Series in Solid-State Sciences, Vol. **112** (1993) 515.

[5]. R. Bauer, A. Osvet, I. Sildos and U. Bogner: J. Lum. **56** (1993) 57.

[6]. K. Kobashi, K. Nashimura, Y. Kawate, T. Horiuchi: Phys. Rev. B **36** (1988) 4067-4083.

[7]. V. S. Vavilov, A. A. Gippius, A. M. Zaitsev, B. V. Deryagin, B. V. Spitsyn, and A. E. Aleksenko, Sov. Phys. Semicond. **14**, (1980) 1078.

[8]. A. M. Zaitsev, V. S. Vavilov, and A. A. Gippius, Sov. Phys. Lebedev Inst. Rep. **10**, (1981) 15.

[9]. J. Ruan, W. J. Choyke, and W. D. Partlow, Appl. Phys. Lett. **58**, (1990) 295.

[10]. L. Bergman, B. R. Stoner, K.F. Turner, J. T. Glass, and R. J. Nemanich, J. Appl. Phys., **73**, (1993) 3951.

[11]. C. D. Clark, H. Kanda, I. Kiflawi, and G. Sittas, Phys. Rev. B **51**, (1995) 16681.

[12]. H. Sternschulte, K. Thonke, R. Sauer, P. C. Munzinger, and P. Michler, Phys. Rev. B, **50**, (1994) 14554; H. Sternschulte, K. Thonke, J. Gerster, W. Limmer, R. Sauer, J. Spitzer, and P. C. Munzinger, Diamond and Related Materials **4** (1995) 1189-1192.

[13]. T. Feng and D. Schwartz: J. Appl. Phys. **73** (1993) 1415.

[14]. A. T. Collins, L. Allers, C. J. H. Wort, and G. A. Scarsbrook, Diamond and Related Materials, **3**, (1994) 932.

[15]. A. A. Gorokhovsky, A. V. Turukhin, R. R. Alfano, W. Phillips: Appl. Phys. Lett. **66** (1), (1995) 43.

[16]. G. Devies, in *The Optical Properties of Diamond*, in *Chemistry and Physics of Carbon* vol. 13, edited by P. L. Walker, Jr. and P.A. Thrower (Marcel Dekker, New York, Basel, 1977), pp. 1-143.

[17]. A. Szabo, Phys. Rev. Lett. **25**, (1970) 924.

[18]. K. K. Rebane, *Impurity Spectra of Solids*, (Plenum Press, New York, 1970).

[19]. C. A. Klein, T. M. Hartnett, and C. J. Robinson, Phys. Rev. B **45**, (1992) 12854.

[20]. M. Gorman and S. A. Solin, Solid State Commun. **15**, (1974) 761.

[21]. T. N. Kitsopoulos, C. J. Chick, Y. Zhao, and D. M. Neumark, J. Chem. Phys. **95**, (1991) 1441; C. C. Arnold, T. N. Kitsopoulos, and D. M. Neumark, J. Chem. Phys. **99**, (1993) 766.

[22]. A. A. Gorokhovsky and J. Kikas, Opt. Commun. **21**, (1977) 272.

[23]. A. V. Turukhin, C.-H. Liu, A. A. Gorokhovsky, R. R. Alfano, W. Phillips: Phys. Rev. B **54** (23), (1996) 16448.

[24]. L. H. Robins, E. N. Farabaugh, A. Feldman, and L. P. Cook, Phys. Rev. B **43**, (1991) 9102.

[25]. L. Bergman, M. T. McClure, J. T. Glass, and R. J. Nemanich, J. Appl. Phys. **76**, (1994) 3020.

[26]. Y. L. Khong, A. T. Collins, and L. Allers, Diamond and Related Materials, **3**, (1994) 1023.

[27]. T. Dallas, S. Gangopadhyay, S Yi, and M Holtz, in *Applications of Diamond Films and Related Materials: Third International Conference, 1995*, NIST special publication SP 885, p. 449.

[28]. B. Di Bartolo: Optical Interactions in Solids (Wiley, 1989).

[29]. R. A. Street, in *Semiconductors and Semimetals,* edited by J. I. Pankove (Academic, New York, 1984), Vol. 21, p. 197.

[30]. A. T. Collins, and S. C. Lawson, J. Phys. Condens. Matter **1,** (1989) 6929.

[31]. G. Davies, in *The Optical Properties of Diamond*, in *Chemistry and Physics of Carbon* vol. 13, edited by P. L. Walker, Jr. and P. A. Thrower (Marcel Dekker, New York, Basel, 1977), pp. 1-143.

[32]. R. T. Harley, M. J. Henderson, R. M. Macfarlane, J. Phys. C, Solid State Phys. **17**, (1984) L233-L236.

[33]. N. R. S. Reddy, N. B. Manson, and E. R. Krausz: J. Lum. **38**, (1987) 46-47.

[34]. A. Osvet, A. Suisalu and I. Sildos, Proc. Estonian Acad. Sci. Phys. Mater. **41** (1992) 222.

[35]. W. E. Morerner, M. Gehrtz, A. L. Huston, J. Chem. Phys, **88** (1984) 6459-6460.

Chapter 8

Tm^{3+} Chelates in PMMA Matrix

Introduction.

Spectral hole-burning is a powerful scientific method of high-resolution spectroscopy for fundamental research of solids, particularly local environments of absorbing centers[1]. At the same time, spectral hole-burning has the potential to advance optical high-density information storage, coherent signal processing, quantum computing, and similar state-of-the-art technological applications. The possibilities of commercial applications mostly depend on performance of materials involved in a technological project. Therefore, the search for suitable materials has become a key issue in translating spectral hole-burning technique into commercial products. The material performance is determined by quite large array of spectroscopic and other parameters. Among the most important ones, there are the homogeneous and inhomogeneous linewidths of the optical transition, the hole life time, and the hole-burning efficiency. Many commercial applications require maximal inhomogeneous-to-homogeneous linewidth ratio that, for example, defines the areal storage density of the frequency domain based storage systems. It is not surprising that considerable work has been carried out on compounds containing rare-earth ions. Interest in rare-earth ion doped materials is based on the fact that the optical 4f electrons of the rare-earth ions are shielded by the outer 5s and 5p electrons. As a result, the optical 4f electrons are not strongly affected by motion of neighboring atoms. The phonon-electron interaction is weak and the optical transition

exhibits small homogeneous vibrational broadening. In addition, rare-earth ions with even number of 4f electrons have nonmagnetic singlet electronic states, and consequently have small homogeneous broadening caused by the magnetic interaction with neighboring spin magnetic moments. Among rare-earth ions with even number of 4f electrons, trivalent ion of thulium, Tm^{3+} holds a special place due to $^3H_6(I) \rightarrow {}^3H_4(I)$ transition absorbing near 800 nm, i.e. in a wavelength range extremely convenient for commercial GaAlAs diode lasers.

To be used in commercial products, materials must possess an efficient mechanism of hole-burning. Many of the rare-earth ions in crystalline solids reveal quite universal mechanism of persistent hole-burning via optical pumping of hyperfine levels with long storage lifetimes[2]. This well-known mechanism is efficient only at low temperatures, generally less than 10 K, where the hyperfine splitting exceeds the homogeneous linewidth. Hyperfine splitting is absent in Tm^{3+} ions and consequently, the above mentioned mechanism can not be employed even at low temperatures. The other possible hole-burning mechanism for Tm^{3+} doped crystals that involves optical pumping in long lived electronic level was successfully used for a set of impressive demonstrations of time domain hole-burning technique[3]. Nevertheless, the hole life spans were limited to $10^{-6} - 10^{-2}$ seconds due to relatively short lifetime of the storage electronic levels[4].

The motivation for investigation of Tm^{3+} organic complexes in polymer matrix as prospective materials for frequency domain optical storage was twofold. First, disordered polymer host allows to obtain large inhomogeneous linewidths. Combined with relatively small homogeneous linewidth, it results in high inhomogeneous-to-homogeneous linewidth ratio. Second, many disordered amorphous solids exhibit quite common

mechanism of persistent hole-burning due to photoinduced rearrangements of the local environment of the ion[5]. Thus, long lived spectral holes in these materials could be anticipated.

Typical rare-earth ion containing organic system consists of trivalent ion La^{3+} bound with surrounding ligands predominately via ionic interaction and embedded in polymer host. Lanthanide complexes exhibit a coordination number from six to twelve, with eighth and nine being the most common. The geometric configurations found for lanthanide complexes are quite varied, being determined by ligand conformation, competition between ligand donor group and solvent (polymer) molecules, crystal packing forces, and size of rare-earth ion.

In this Chapter, we present results on the persistent hole-burning studies and optical properties of four Tm^{3+} - organic ligand complexes in a polymer matrix. The samples under investigation are Tm^{3+} chelates, specifically β-diketone tris chelates of thulium, blended in a poly(methyl methacrylate) (PMMA) matrix as a host. Optical absorption, steady state and time-resolved photoluminescence, and spectral hole burning at the transition between the $^3H_6$ and the $^3H_4$ manifolds were studied at temperature range of 1.4 - 300 K.

8.1. Samples

Chelates were prepared by the technique described in Ref. 6 using thulium chloride ($TmCl_3 \bullet 6H_2O$) with thenoyltrifluoroacetylacetone (TTFA), 1,1,1-trifluoro-2,4-pentanedione (TFD), 1-phenyl-1,3-butanedione (PBD), and 1,3-diphenyl-1,3-propanedione (DBM) ligands. The molecular structure of these β-diketone tris chelates of

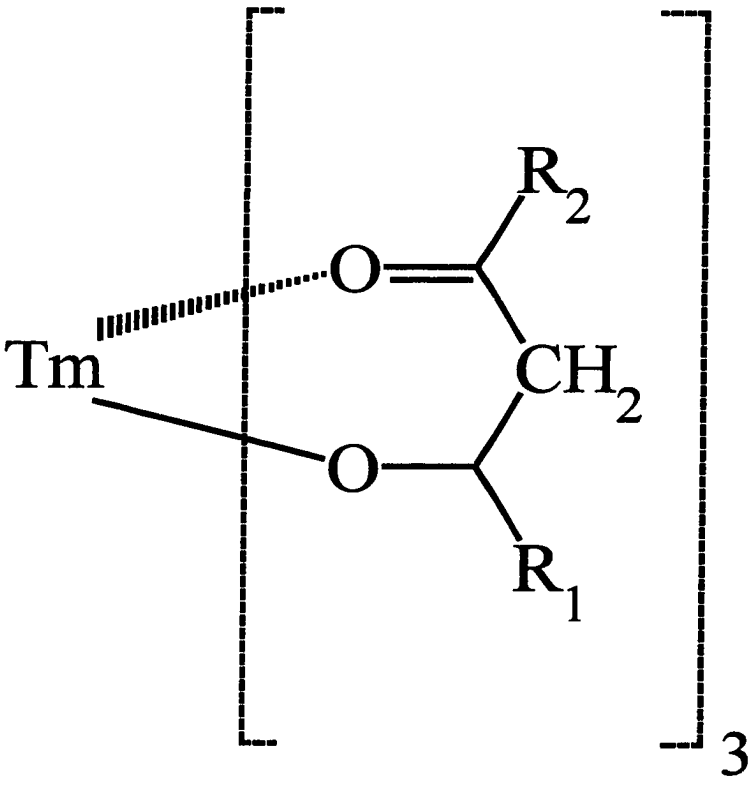

Figure 8.1. Chemical structure of β-diketone tris chelates of thulium. Substituent groups R_1 and R_2 for the studied ligands are presented in Table 8.1.

Name of the ligand		Structure of the substituent groups	
Full name	Abbreviation	R_1	R_2
1,1,1-trifluoro-2,4-pentanedione	TFD	$-CH_3$	$-CF_3$
1-phenyl-1,3-butanedione	PBD	$-CH_3$	
thenoyltrifluoroacetylcetone	TTFA	$-CF_3$	
1,3-diphenyl-1,3-propanedione	DBM		

Table 8.1. Substituent groups R_1 and R_2 associated with ligands of Tm^{3+} complexes studied.

thulium is shown in Fig. 8.1, and the symbols assigned to each ligand are listed in Table 8.1. The chosen structures allow overcoming solubility problem inherent in these types of compounds and obtaining relatively large samples with good optical quality. Six oxygen atoms are available for coordination to the Tm^{3+} ion. There is, however, evidence[7] that between one and three additional oxygen atoms may be delivered by coordination water molecules. Thus, the samples consist of Tm^{3+} ligand complexes with some water molecules blended with PMMA. There is no indication of chemical bonding between polymer and Tm^{3+} ligand complexes. The concentration of Tm^{3+} ion in the samples was determined on the basis of input chemical concentrations and found to be 0.35, 0.14, 0.32, and 0.2 mol % for $Tm(TFD)_3$, $Tm(TTFA)_3$, $Tm(PBD)_3$, and $Tm(DBM)_3$ complexes respectively. Physically, the samples appeared to be transparent slightly yellow colored cylinders, having diameters of 8 -10 mm and lengths of 15-20 mm.

All samples were synthesized and provided by Prof. Y. Okamoto group, Department of Chemistry and Polymer Research Institute, New York Polytechnic University, New York.

8.2. Absorption Spectroscopy.

Solid state spectroscopy of trivalent rare earth ions has long been characterized by a remarkable richness of the spectral structure arising from the $4f^n \rightarrow 4f^n$ transition. The spectra generally consist of groups of lines that arise from crystal filed splitting of J multiplets of the three ion, since the spin-orbit interaction is larger than the effect of the crystal field. The electronic configuration of Tm^{3+} in the ground state is sometimes

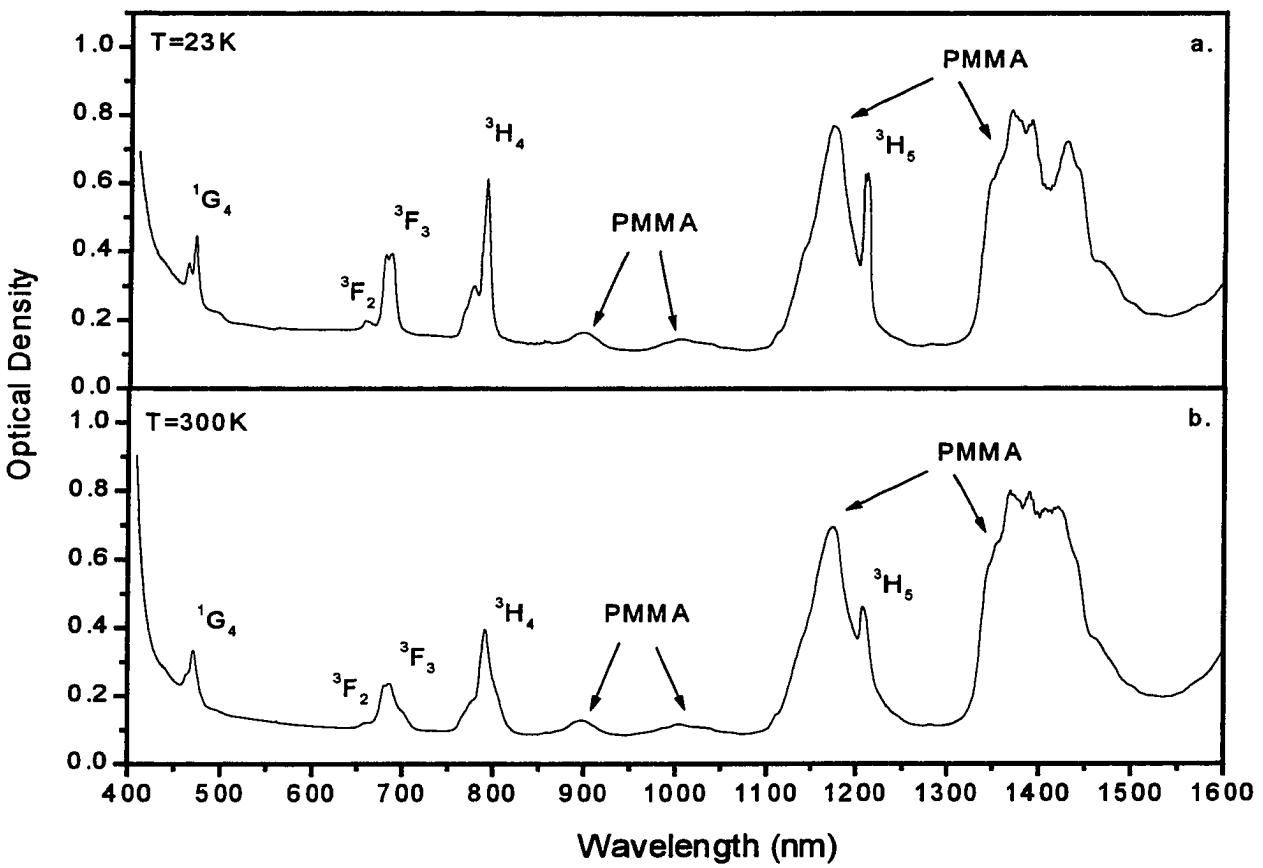

Figure 8.2. Absorption spectra of $Tm(TTFA)_3$ in PMMA at (a) 23 K and (b) 300 K. The sample thickness was 15 mm.

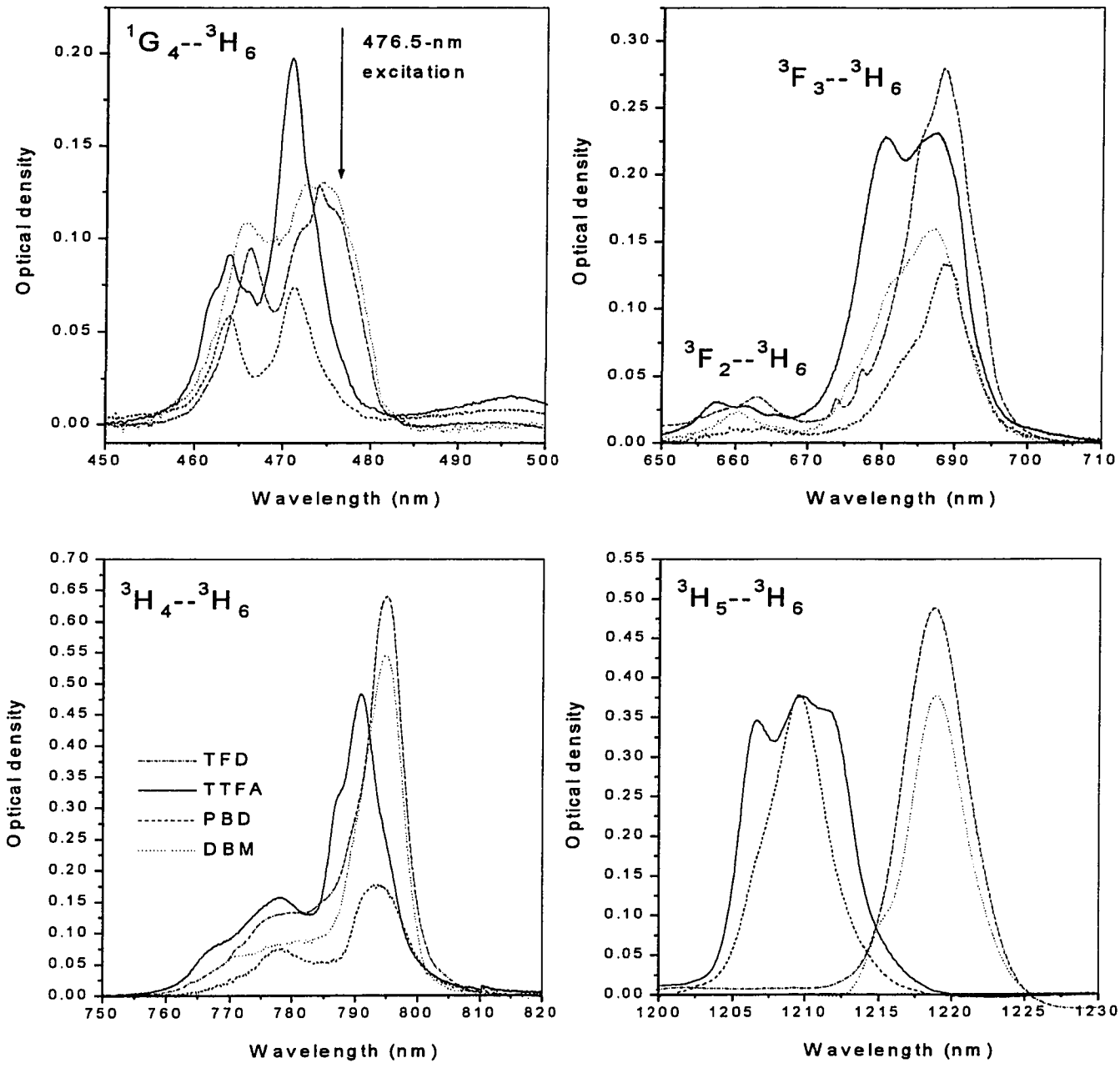

Figure 8.3. Absorption spectra of Tm^{3+} ion transitions of studied organic complexes at 10-23 K. Arrow in $^1G_4 \leftarrow {}^3H_6$ transition spectrum indicates a spectral position of the laser excitation used for luminescence measurements.

written as [Xe core] $4f^{12}$ shell where there are essentially two "holes" in the 4f shell. Electric-dipole transitions within a pure f^n configuration are strictly parity forbidden. However, weak, induced electric-dipole transition can occur as a result of the interaction of the central ion with the surrounding ligand-field mixing into the f^n configuration states from configurations of opposite parity and thus relaxing the parity restriction. Electric-dipole transitions may also be induced as a result of the asymmetries produced by means of the vibronic coupling of the central ion with ligands.

The absorption spectra for the four Tm^{3+} organic complexes in PMMA were measured at low temperature (typical range 12 – 23 K) and room temperature. Fig. 8.2 displays the absorption spectra for $Tm(TTFA)_3$ complex in PMMA at 23 K and room temperature as an example. The similarity between the low and high temperature spectra observed for all systems demonstrates weakness of the interaction of the Tm^{3+} ions with the vibrational excitations of the surrounding ligands and the polymer matrix.

Individual absorption bands on the spectra can be assigned with confidence to the transitions in Tm^{3+} ion, ligand, and the host matrix. Absorption bands due to transitions from the $^3H_6$ ground states of Tm^{3+} ion to the exited electronic states $^3H_5$ at 1210 nm, $^3H_4$ at 795 nm, $^3F_{3,\,2}$ near 690 nm, and $^1G_4$ at 470 nm are clearly visible[8]. Comparison of the absorption spectra of doped and pure PMMA samples shows that the broad complex bands in the near infrared at 1400, 1170, 1000, and 900 nm belong to vibrational transitions of the host PMMA. The steep increase in the absorption at 400 nm is explained by a singlet-singlet transition in the TTFA ligand. The other three complexes show quite similar absorption spectra between 400 and 1600 nm. However, the individual structure of the separate Tm^{3+} ion related absorption bands appears to be different.

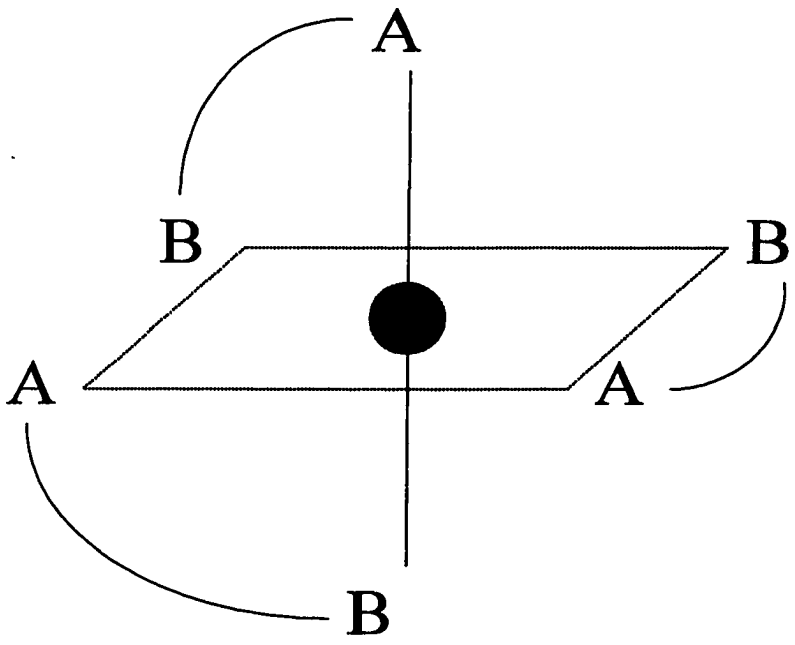

Figure 8.4. Model for local structure of the $Tm(ligand)_3$ absorbing center. Tm^{3+} ion is presented by gray sphere, oxygen atoms associated with different substituent groups R_1 and R_2 are presented by letters "A" and "B" respectively.

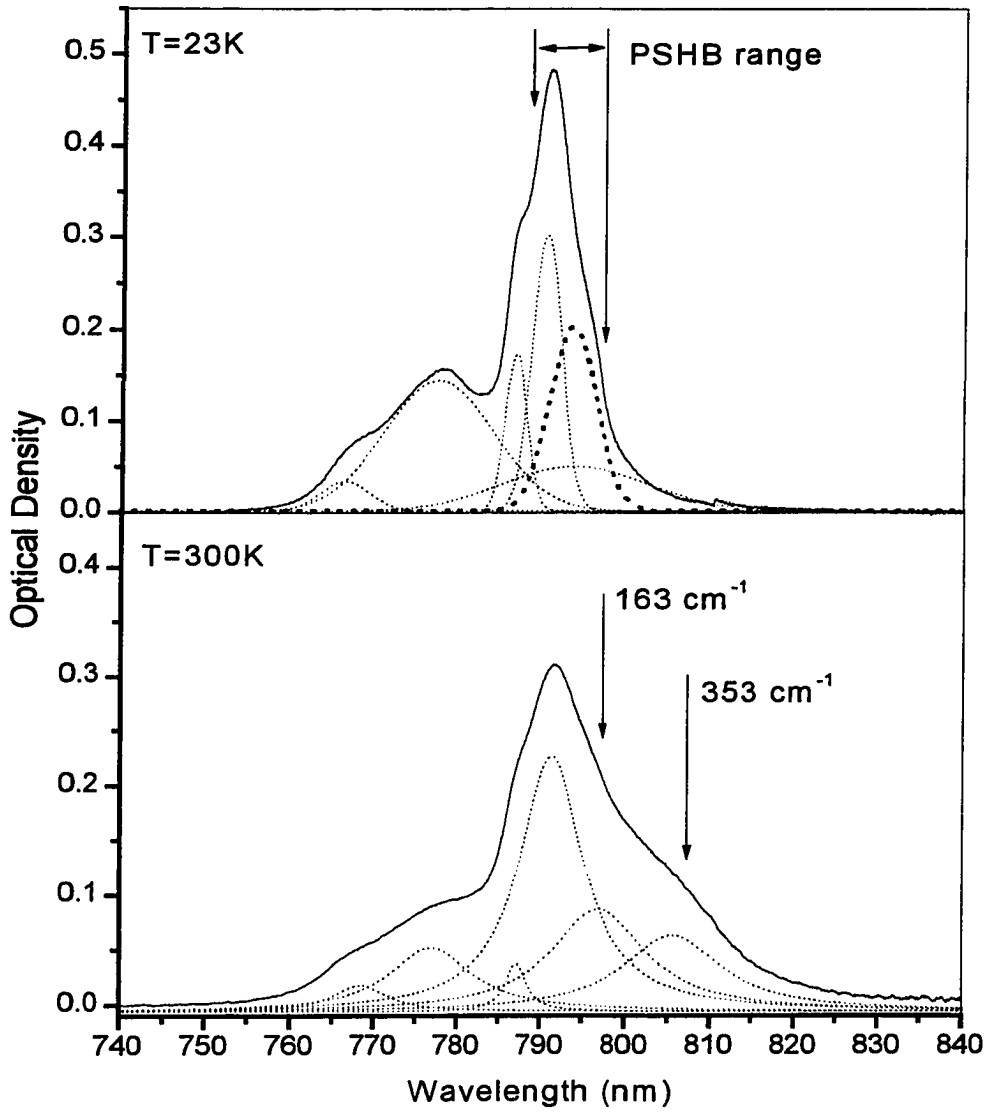

Figure 8.5. Absorption spectra of $Tm(TTFA)_3$ complex at low (upper graph) and high (lower graph) temperature (solid lines). The result of decomposition on elementary Gaussian components is shown by dotted lines. Thick dotted line at upper graph represents an elementary band involved in PSHB. Arrows at lower graph mark "hot" absorption bands.

Comparative picture of the low temperature spectra of Tm^{3+} ion transitions for the four complexes is presented in Fig. 8.3. Different internal structure of these absorption bands reflects distinctions in site symmetry and structure of the complexes inside the polymer host. Each absorption band combines several overlapping elementary bands. Elementary absorption bands represent transitions between separate Stark components of involved electronic levels as well as might originate from the different coordination structures (sites) of the Tm^{3+} complexes in the polymer matrix.

A detailed understanding of the relation of the optical properties and local symmetry of the absorbing center in amorphous media represents one of the significant challenges remaining in solid state spectroscopy. Because an amorphous solid does not have the ordered structure inherent to crystals, the local environment of the absorbing ion is not defined sufficiently well to permit a simple concatenation with its optical properties[8]. In disordered matrix, the absorption observed from rare-earth ions consists of a superposition of contributions from individual ions distributed among the entire ensemble of local environments. As a result, a broad statistical distribution of Stark components can significantly increase inhomogeneous broadening of the absorption bands that makes structure derivation extremely difficult if not impossible (see Ref. 10 and 11 for a few successful attempts of such kind of studies). Nevertheless, preliminary qualitative analysis of the observed spectra was undertaken. Assuming that the only one dominating site for each complex exists in the polymer matrix and that most of the Stark components are resolved in spite of large inhomogeneous linewidths, we tentatively propose the following model for the local structure of the Tm^{3+} organic complexes in PMMA. Considering the number of components in each absorption band presented in

Fig. 8.3, the absorbing centers most likely possess C_{3V} symmetry with different degree of distortion. Other possible types of symmetry would result in substantially larger number of elementary components[12-14] for Tm^{3+} ion electronic transitions considered. Though some of these components might not be resolved in our measurements, such complex hidden structure is not justified by our absorption and photoluminescence spectra. Similar symmetry of β-diketon chelates complexes was considered in Ref. 15 and 16. The local structure of the complex seems to depend dramatically on the extent of hydration of the compound[17]. For example, for $Y(acac)_3 \bullet 3H_2O$ complex similar to ours, each yttrium ion is surrounded by eight oxygen atoms, contributed by three acac groups and two water molecules. Thus, the polyhedron formed about the yttrium ion by the eight coordinated oxygen atoms is a distorted square-antiprism. The third water molecule, associated with each β-diketonate unit, links the β-diketonates, in pairs, by hydrogen bonding. Similarly, structure of $Y(bza)_3 \bullet H_2O$ indicates that the molecules are monomeric, with yttrium ion being at the center of a distorted monocapped octahedron of chelate oxygen atoms capped on one face by the water molecule. The X-ray analysis of $Er(thd)_3$ indicates that the Er^{3+} ion is coordinated by six oxygen atoms and the coordination geometry is almost trigonal prismatic. The structure of $Dy(thd)_3 \bullet H_2O$ has revealed that the oxygen polyhedron around the Dy has pure 7-coordination geometry, the seventh ligand being the water molecule. Since the exact number of water molecules associated with each $Tm(ligand)_3$ complex is not known at the present time, we can assume the most common type of these complexes based on an octohedral disposition of the six oxygen atoms (Fig. 8.4). Note that complexes with more symmetrical ligands such as TFD and DBM, appear to possess less distorted C_{3V} symmetry, which manifests itself in a simpler structure of

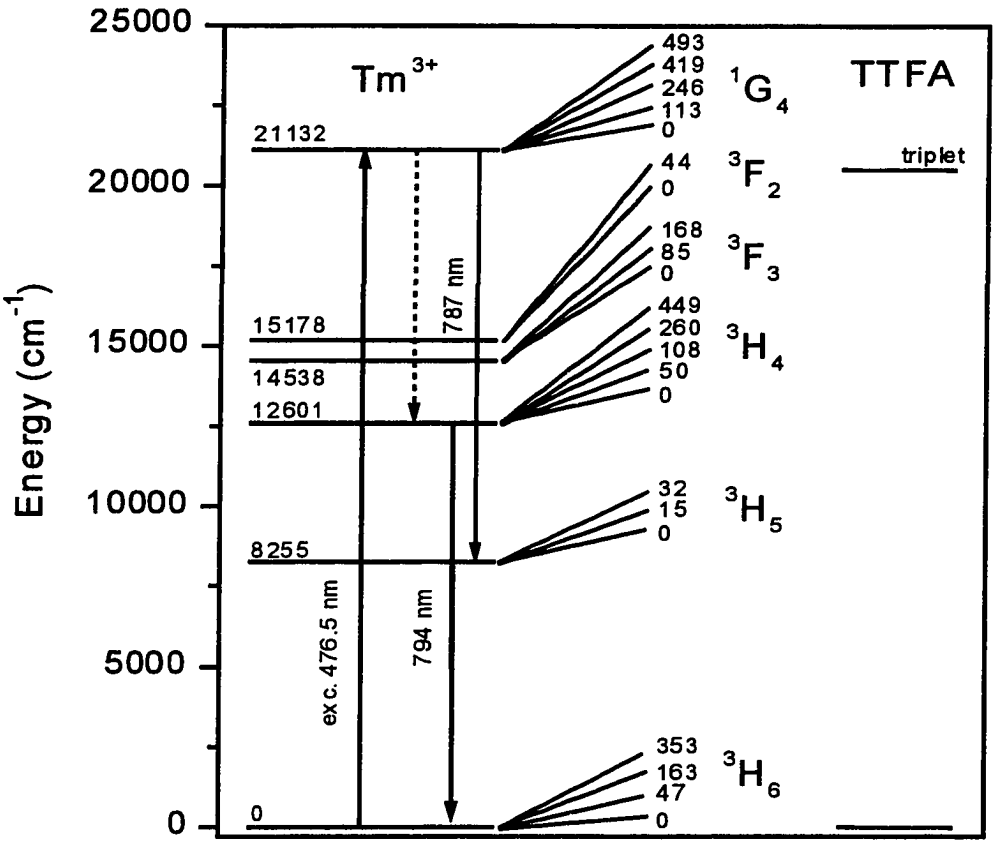

Figure 8.6. Energy level diagram of the Tm^{3+} $(TTFA)_3$ complex in PMMA. Paths of laser excitation and radiative transition (solid arrows) as well as non-radiative relaxation (dotted arrows) are shown. Position of the TTFA triplet state is shown according to Ref. 15 and 16.

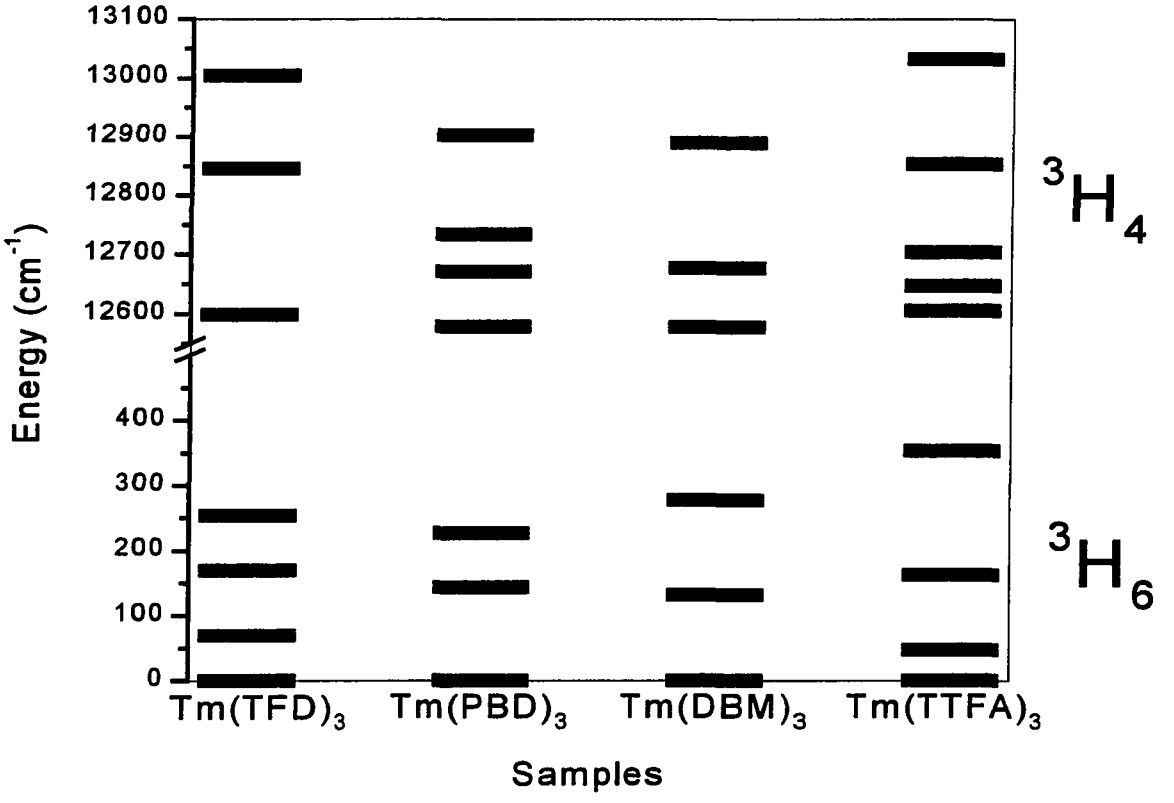

Figure 8.7. Energy level diagram for $^3H_4$ and $^3H_6$ manifolds of samples studied.

the absorption bands. In contrast, less symmetrical complexes with TTFA and PBD ligands exhibit correspondingly more complex spectra (Fig. 8.3). This tentative model may be subjected to refinement upon completion of scheduled fluorescence line narrowing measurements.

Inhomogeneous broadening of the Tm^{3+} ion zero-phonon lines was found to be quite large as predicted. To determine the magnitude of inhomogeneous broadening, an absorption band was fitted by the superposition of several Gaussians. The width of the Gaussian centered at the transition between the lowest Stark components, $^3H_4(1) \leftarrow {}^3H_6(1)$ gives the inhomogeneous broadening of this transition (the homogeneous broadening can be neglected) and was found to be between 90 and 140 cm^{-1} for different complexes (see Table 8.3). In addition, the fitting allowed determination of the Stark component splitting of the $^3H_4$ state and the other observed excited states. The same procedure applied to high temperature spectra allowed determination of the transitions originating from the thermally populated $^3H_6$ ground state levels. Fig. 8.5 presents an example of described analysis for $^3H_5 \leftarrow {}^3H_6$ transition in $Tm(TTFA)_3$ complex. Low temperature absorption spectrum demonstrates that an absorption band near 800 nm contains at least six elementary Gaussian bands. Peak centered at 793.2 nm represents an absorption transition between lowest Stark components of $^3H_5$ and $^3H_6$ manifolds with inhomogeneous broadening of 3000 GHz (presented by thick doted line). Spectral range observed persistent hole burning matches this elementary band. Room temperature absorption spectrum of the same manifold exhibits two extra "hot" absorption bands at 798 and 807 nm originated from upper Stark energy levels of the $^3H_6$ state. The energy splitting between these excited levels and ground level was found to be 163 and 353 cm^{-1}

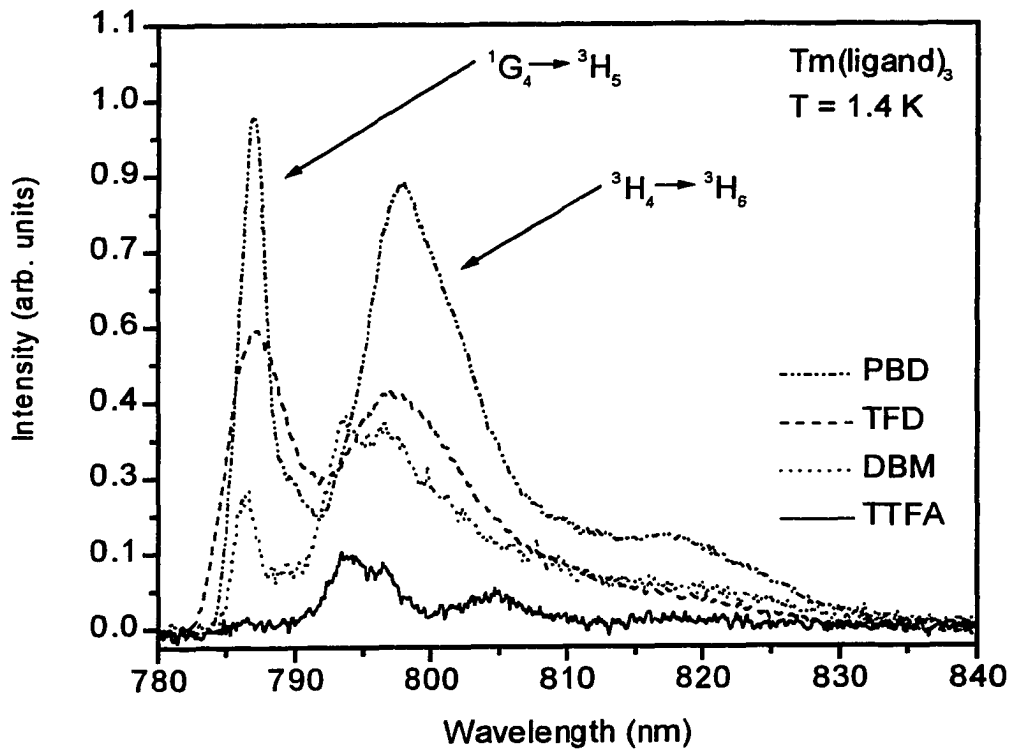

Figure 8.8. Photoluminescence spectra of Tm^{3+} chelates in PMMA at 1.4 K upon 476.5 nm excitation by Argon laser.

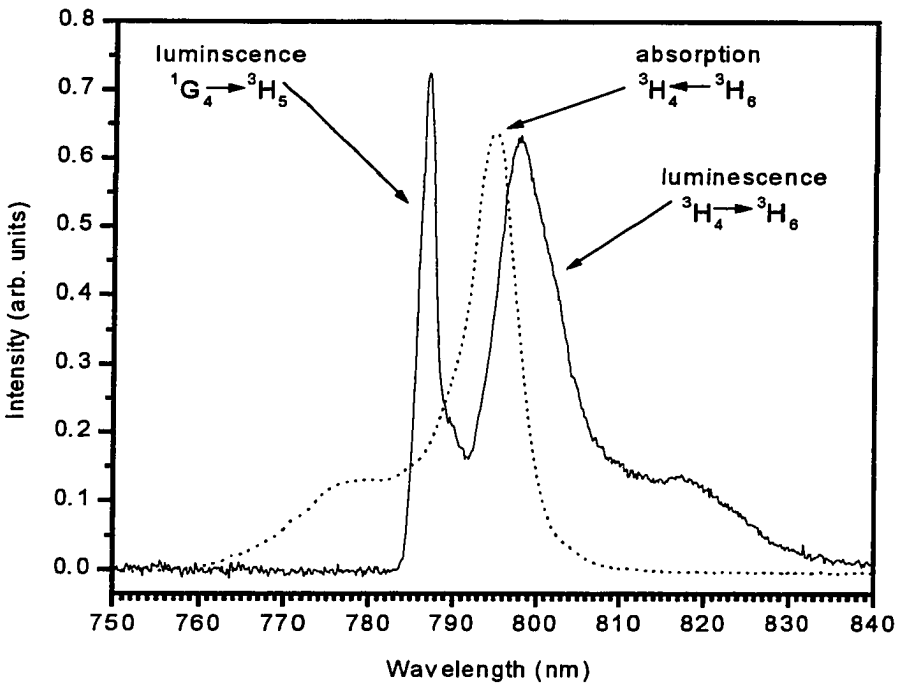

Figure 8.9. Absorption (dotted line) and photoluminescence (solid line) of the $Tm(PBD)_3$ in PMMA. The absorption spectrum was measured at 12 K. The photoluminescence spectrum was measured using the conditions indicated in caption for Fig. 8.8.

respectively. Along with analysis of luminescence spectra, it permits the ground state energy splitting for each complex to be found. These results were used to find the energy level diagrams for each compound. The full energy diagram for the $Tm(TTFA)_3$ complex is shown in Fig. 8.6 as an example. Energy level diagram for $^3H_4$ and $^3H_6$ manifolds where PSHB was observed for all samples studied, is presented in Fig. 8.7.

8.3. Photoluminescence Spectroscopy.

Luminescence spectra of the Tm^{3+} chelates were investigated in the region of the $^3H_4 \rightarrow {}^3H_6$ transition near 795 nm. The emission spectra upon excitation by CW Ar laser lines 457.9 nm and 476.5 nm into the $^1G_4$ manifold consist of a few relatively narrow bands and a strong broad background. The emission upon 488.0 nm excitation, which is out of resonance with Tm^{3+} ion absorption, shows the background only. Thus, this broadband background emission, which is likely related to ligands or unknown impurities, may be separated from the Tm^{3+} luminescence by subtraction. The photoluminescence spectra for studied materials are displayed in Fig. 8.8. Though the relative intensities are different, the spectrum structure is similar for all materials. It consists of a relatively narrow band with width 2 - 5 nm at 787 nm and a much broader band centered around 798 nm. To find the origin of these bands, we overlapped the absorption and luminescence spectra as shown in Fig. 8.9 in the case of $Tm(PBD)_3$. The broad luminescence band has mirror-like symmetry with the $^3H_4 \leftarrow {}^3H_6$ absorption band. Thus, this luminescence corresponds to the $^3H_4 \rightarrow {}^3H_6$ transition and originates from the lowest Stark component of the $^3H_4$ state and terminates in the $^3H_6$ state manifold. The shoulder in each spectrum corresponds to the Stark splitting of about 250 cm^{-1} for both the ground $^3H_6$ and the excited $^3H_4$ states. After careful analysis based on level positions

Transition	Tm:ligand complexes	Lifetime (μs) ±15%	Relative Quantum Yield
$^1G_4 \rightarrow {}^3H_5$	$Tm(TFD)_3$	13.9	0.88
	$Tm(PBD)_3$	9.2	0.17
	$Tm(TTFA)_3$	25.4*	0.015
	$Tm(DBM)_3$	3.1	0.013
$^3H_4 \rightarrow {}^3H_6$	$Tm(TFD)_3$	19.5	1.0
	$Tm(PBD)_3$	13.7	0.20
	$Tm(TTFA)_3$	25.4*	0.16
	$Tm(DBM)_3$	5.1	0.034

*Luminescence components were not resolved due to low level of signal of photoluminescence.

Table 8.2. Photoluminescence lifetimes and relative quantum yields.

and the temperature dependence of the spectra, the narrow peak at 787 nm was assigned to the luminescence corresponding the $^1G_4 \rightarrow {}^3H_5$ transition (see Fig. 8.6). The smaller width of the peak at 787 nm in comparison with the width of the peak at 798 nm is a result of laser-induced line narrowing of the $^1G_4 \rightarrow {}^3H_5$ luminescence at the laser excitation at $^1G_4 \leftarrow {}^3H_6$ transition, i.e. only a given subset of sites absorbing at excitation wavelength radiates within the inhomogeneously broadened $^1G_4 \leftarrow {}^3H_6$ absorption band. This effect is absent for the $^3H_4 \rightarrow {}^3H_6$ luminescence, apparently due to the loss of correlation with site distribution of the $^1G_4 \leftarrow {}^3H_6$ transition after nonradiative relaxation from $^1G_4$ to $^3H_4$ state. Similar interpretation of the Tm^{3+} ion luminescence was reported in Ref. 19 for indium-based fluoride glasses.

The $^3H_4 \rightarrow {}^3H_6$ and $^1G_4 \rightarrow {}^3H_5$ luminescence decays, as well as the background emission decays, were also measured in all materials after $^1G_4 \leftarrow {}^3H_6$ pulsed excitation at 476.5 nm for T = 1.4 K. For these measurements, the laser beam was modulated by the acousto-optic modulator Isomet 1206C with frequency 1000 Hz. The signal of photoluminescence was detected by the photomultiplier and averaged by Tektronix Digital Storage Oscilloscope TDS 724A. The time resolution of 0.7 μs was determined by the response time of the photomultiplier.

The decay curves were successfully fitted by single exponents. The results are reported in Table 8.2 together with the relative quantum yields of luminescence. The quantum yields were estimated on the basis of relative luminescence intensities, absorption coefficients at the wavelength of laser excitation (see Fig. 8.3, upper-left spectrum), and lifetimes of irradiating levels. The decay times of the narrow band at 787 nm and the broad band at 797 nm were found to be different for all samples, in agreement

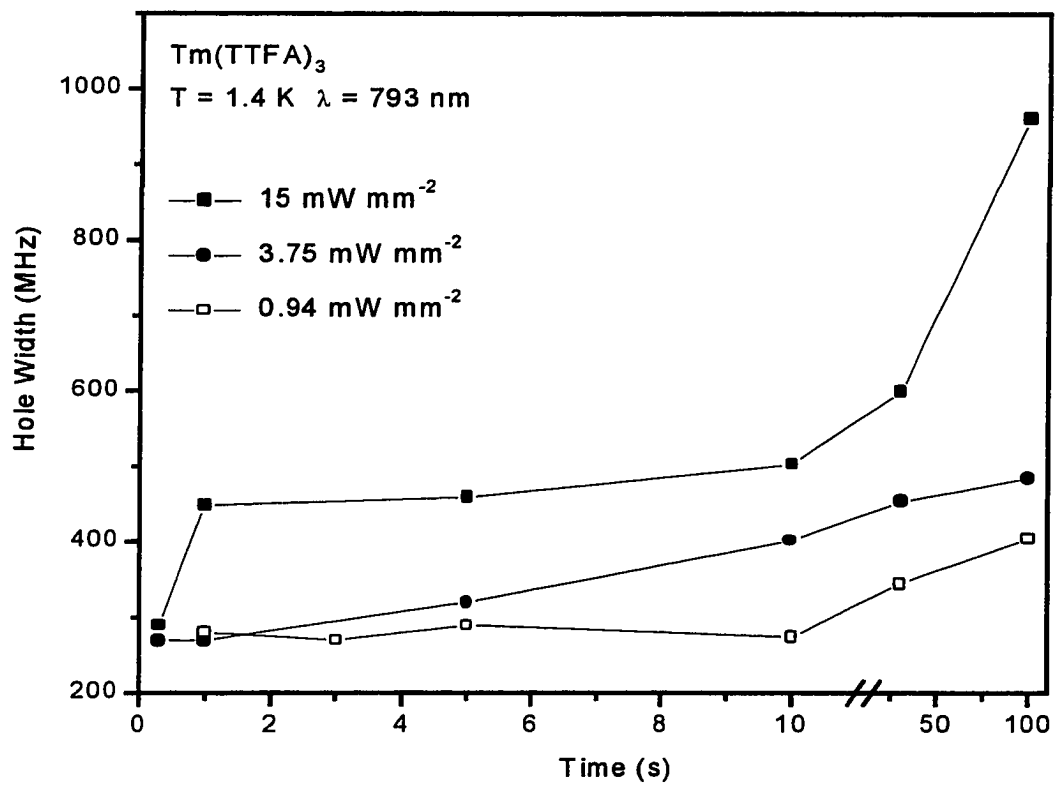

Figure 8.10. Dependence of the holewidth on exposure time at different burning intensities for $Tm(TFFA)_3$ in PMMA.

Parameters	$Tm(TTFA)_3$	$Tm(TFD)_3$	$Tm(PBD)_3$	$Tm(DBM)_3$
ZPL center (nm)	793.2	793.6	794.8	795.3
Γ_{inh} (GHz)	3000	4300	2800	2500
PSHB range (nm)	789-797	789-796	790-797	789-798
Γ_{hole} (MHz)	220	230	360	180
$\Gamma_{inh} / \Gamma_{hole}$	1.4×10^4	1.9×10^4	0.8×10^4	1.4×10^4

Table 8.3. Parameters of inhomogeneous and homogeneous lines of the $^3H_4(1) \leftarrow {}^3H_6(1)$ transition of Tm^{3+} chelates in PMMA.

with our assignment of their respective origins. The decay times are about two orders of magnitude shorter than reported for the same transitions in inorganic indium based fluoride glasses[19] with comparable Tm^{3+} concentration. This is most likely related to specific features governing nonradiative relaxation in the organic matrix, e.g. additional vibrational frequencies of the polymer matrix, presence of O-H vibrations of coordinated water[20], and an additional deexcitation path through the triplet states of ligand due to its close proximity to the $^1G_4$ level[18] of Tm^{3+} (see Fig. 8.6).

8.4. Persistent Spectral Hole-Burning

For the first time, persistent spectral hole burning has been performed in Tm^{3+} ion contained organic compounds. Long lived stable spectral holes were observed for all four systems listed in Table 8.1. Persistent hole burning was studied in the $^3H_6(I) \rightarrow {}^3H_4(I)$ transition of Tm^{3+} ion for temperature range 1.4 – 30 K. Table 8.3, the first and the second row, summarizes the positions of the center and inhomogeneous widths of the optical transition between the lowest Stark components for the four samples under investigation. These data are resulted from the decomposition of the absorption bands on elementary Gaussians. The third row of the Table 8.3 provides wavelength ranges where persistent holes were detected for each system. Spectral holes demonstrated high stability at temperature 1.4 K. No changes in holeshape were detected over the experimental time of 10 hours. To understand relaxation processes for Tm^{3+} organic complexes, it was important to determine the low-intensity limiting holewidth. The minimal holewidth was obtained by extrapolation of the holewidth dependency on burning intensity and burning time to zero-intensity zero-exposure limit. The example of the experimental dependency on burning time at different burning intensities is shown in Fig. 8.10 for $Tm(TTFA)_3$

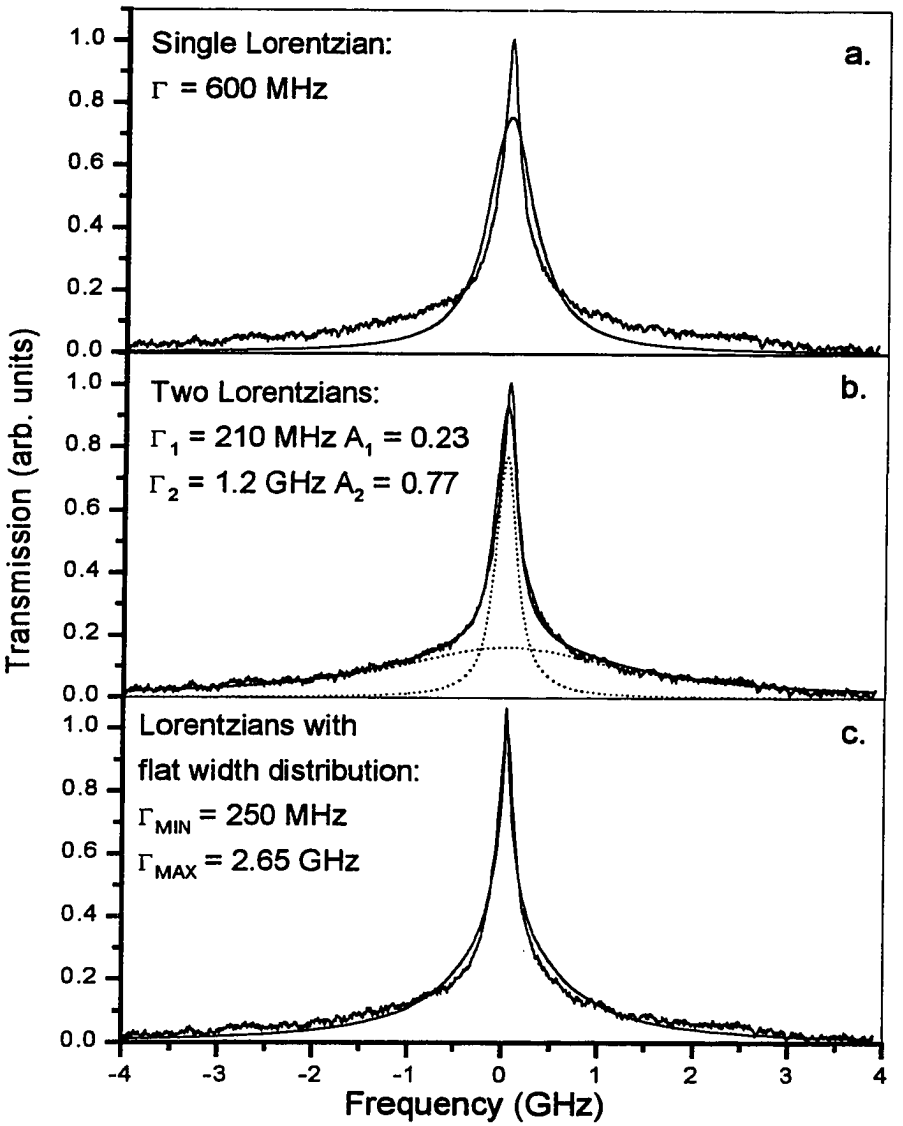

Figure 8.11. An experimental spectral hole profile fitted by different models: (a) a single Lorentzian, (b) a superposition of two Lorentzians (widths and relative amplitudes are marked), and (c) superposition of Lorentzians with continuous uniform distribution of widths between Γ_{MIN} and Γ_{MAX}. Spectrum measured in $Tm(TTFA)_3$ at 1.4 K near 794 nm after 30 seconds of hole burning with intensity of 1 mW/mm^2.

complex. A linear portion of these dependencies at short burning exposures proves the absence of power broadening at low intensity measurements of the holewidth and assures that parameters of the burning regime were chosen correctly to avoid saturation effects. Obtained minimal holewidths are shown at Table 8.3, fourth row. The obtained holewidths are significantly larger than holewidth limit defined by the lifetime of the corresponding electronic levels (see Table 8.2). It can be explained by unresolved fine structure of the hole or by additional dephasing effects that are operating to broaden the hole beyond the lifetime-limited value. In addition, spectral diffusion effects might be responsible for the observed widths. In the latter case, the characteristic time of the spectral diffusion effects must be substantially shorter then experimental "waiting" time between burning and detection of the spectral hole which was about 30 seconds for our experimental conditions. The last fifth row of Table 8.3 presents inhomogeneous-to-homogeneous linewidths ratio for studied materials. These values allow estimation of the achievable areal memory density for this group of compounds. Applying the method described in Section 4.3, the maximal areal density was estimated to be on the order of 10^{12} Bits/cm^2.

A typical hole shape observed for all complexes is found to be non-Lorentzian (Fig. 8.11 a). Comprehensive analysis of the good quality hole profile spectra demonstrated that the hole profiles were best described by superposition of two Lorentzians (Fig. 8.11 b). Attempts to describe the observed holeshape by combination of Lorenzians with continuous distribution of widths (either uniform[5] (Fig. 8.11 c) or Gaussian) or by holeshape originating from the fracton theory[21] were unsuccessful. Dependence of the holeshape spectrum upon frequency position within the

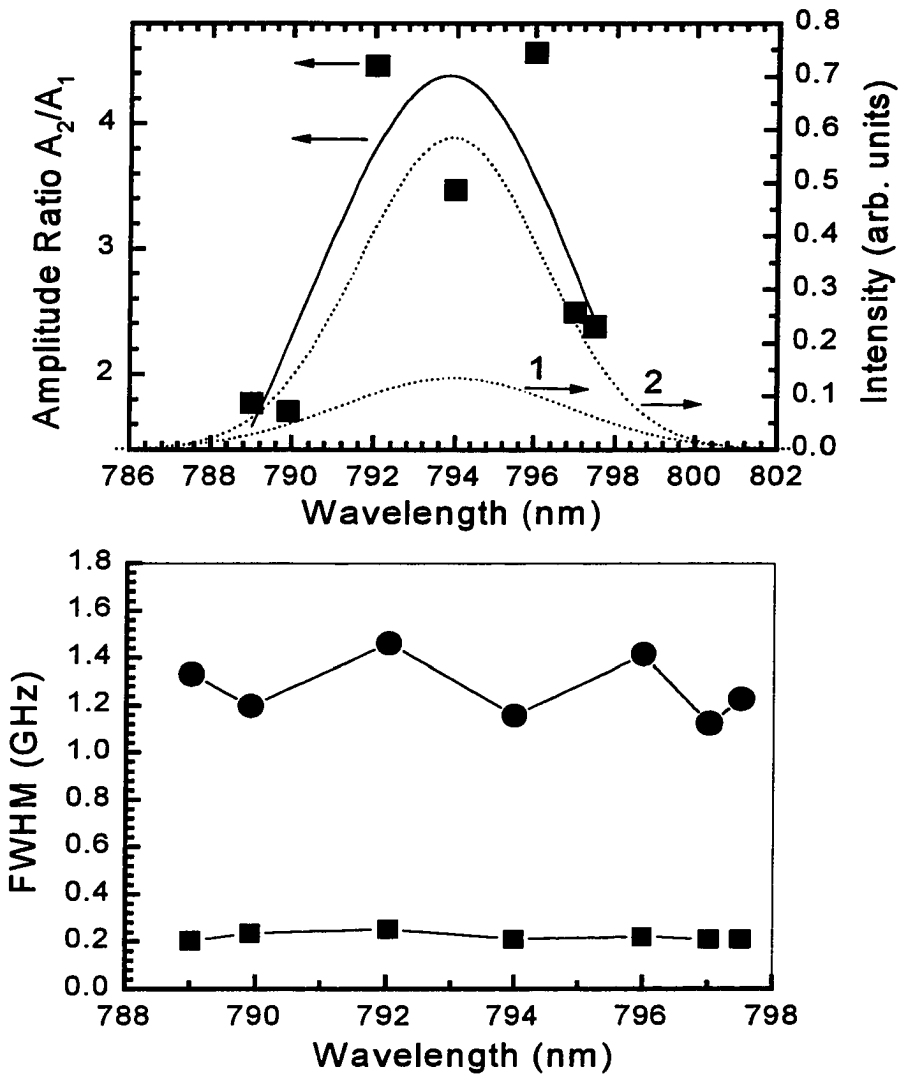

Figure 8.12. The amplitude ratio of the constituted Lorentzians (upper graph, squares) as a function of hole position within inhomogeneous absorption band. Solid line is a fitting curve of this experimental dependence by the model described in the text. Extracted from the fitting procedure two hidden components are represented by dotted lines. Lower graph shows that widths of the Lorentzians remain constants across the inhomogeneous band. Experimental conditions for all analyzed spectra are given in caption for Fig. 8.11.

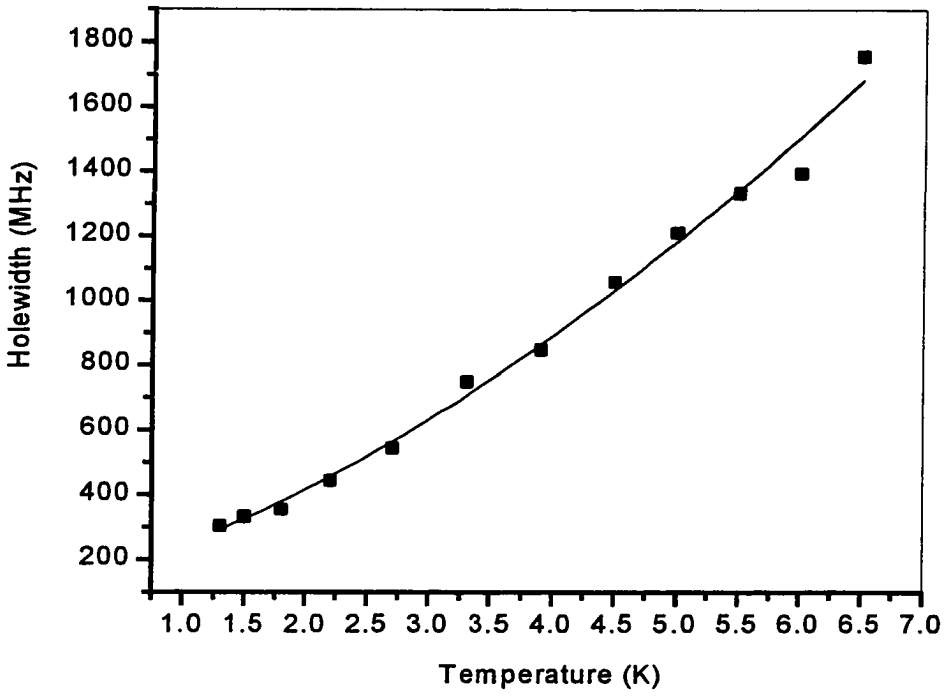

Figure 8.13. Experimental temperature dependence of a holewidth for $Tm(DBM)_3$ (squares). Solid line represents a fit by equation $\Gamma(T)-\Gamma(0)=aT^n$ with $\Gamma(0)=160$ MHz, $a=90$, and $n=1.5$.

inhomogeneous line demonstrated an interesting trend: while widths of the constituted Lorentians remain practically constant, the ratio of their amplitudes was changing. The obtained dependencies are presented in Fig. 8.12. Widths of the constituted Lorenzians were found to be 230±20 MHz and 1.3±0.2 GHz. The observed holeshape behavior may be explained by the existence of two unresolved overlapped spectral components inside the inhomogeneous absorption band where spectral holes were burned. In this case, the observed spectral hole is a superposition of two independent holes burnt in these two components. Proposed model allows explanation of the experimental dependencies in Fig. 8.12. Because a width of the constituted hole depends only on dephasing and/or spectral diffusion processes associated with corresponding inhomogeneously broadened component, the holewidths remain approximately constant across the range of the measurable spectral hole burning. The amplitude ratio of the constituted holes depends on the relative position of the inhomogeneous components and their inhomogeneous widths. Performing the fitting of the experimental dependencies in Fig. 8.12 according to the outlined model, the widths of the hidden components were found to be 4.6 nm and 5.6 nm. The center wavelength was found to be 793.9 nm for both components. These components most likely originate from two different sites of the Tm^{3+} complex in PMMA host. The possibility that two Stark components of the same site are involved has to be ruled out for the following reasons: first, two close Stark components would have substantially higher difference in the homogeneous linewidths; second, the amplitude ratio of the constituted holes would be expected to be practically independent upon spectral position within the inhomogeneous absorption band unless some additional forms of inhomogeneity (for

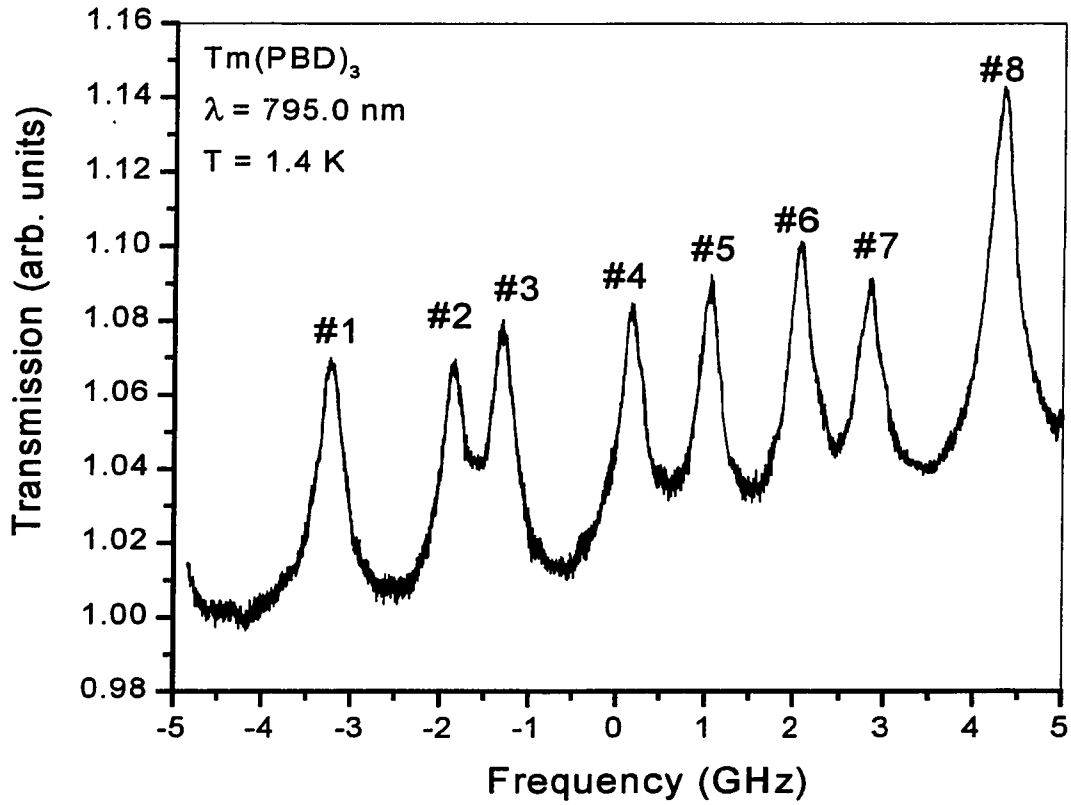

Figure 8.14. Spectra of eight spectral holes consecutively burnt in $Tm(PBD)_3$ complex in PMMA at 1.4 K near 794.0 nm. Burning intensity was 1 mW/mm^2 with 30 s exposure for each hole.

example, inhomogeneity of the quantum efficiency of hole burning) are present. Due to complex shapes of the spectral holes, the holewidths reported elsewhere in the text refer to holewidths measured at the half of amplitude of the actual hole and should be considered as "effective values".

Holewidths were measured over 1.4 – 16 K temperature range. The maximal temperature of detectable spectral hole-burning was found to be substantially different for all four systems under investigation (see Table 8.5, the seventh row). This observation is discussed further in the section devoted to the mechanism of hole burning. The representative experimental temperature dependence of holewidth for $Tm(DBM)_3$ complex is shown in Fig. 8.13. Similar holewidth dependencies are observed for all compounds and found to be governed by a temperature weak power law $\Gamma_{hole} \propto T^n$ with n = 1 – 1.6 (see Table 8.5, the sixth row). A similar dependence of the homogeneous line broadening with n = 1 - 2 was observed in many doped glasses and polymers[22] and explained by the interaction between the optical transition in the impurity ion and the low frequency excitations (quasilocal vibrations and tunneling systems) of the amorphous matrix.

Having pursued our major goal to evaluate these new systems as prospective materials for high density frequency domain storage, the capability for storage of a number of spectral holes was tested experimentally. We performed persistent spectral hole burning at sufficiently close frequencies over the inhomogeneously broadened absorption band. No hole interaction effects such as laser-induced refilling or broadening were detected within current experimental accuracy. Fig. 8.14 displays a set of eight consecutive holes burned across a region of 8 GHz. All holes remained stable over

experimental time of a few hours. Since major properties of spectral hole demonstrated independence on position within the inhomogeneous band, we expect the same stable behavior of the multiple holes across the full inhomogeneously broadened absorption band. Therefore, the studied materials possess sufficiently high capabilities to be used in multicolor optical storage systems.

8.4.1. Determination of Quantum Efficiency of PSHB.

To understand a mechanism of hole-burning, quantum efficiencies of hole-forming process were determined and compared for all samples. Detailed discussion of the method for determination of quantum efficiency developed in this Thesis can be found in Chapter 6.

Strong dispersive character of the hole burning kinetics also suggests a photophysical mechanism of hole burning that involves the photoinduced change in local environment of the absorbing center. The mechanism is often considered in the frame of two-level systems (TLS) theory (see Section 3.8.). Due to random nature of the amorphous media, the TLS parameters are subject to distributions. Distribution of underlying the quantum efficiency parameters leads to distribution of the quantum efficiency itself. The hole burning kinetics appears to be strongly dispersive and has to be characterized by the average value of the quantum efficiency. It was shown by model calculations that for dispersive kinetics based on uniform or Gaussian distributions of tunneling parameter, the difference in amplitude of detectable time-varying signal does not exceed 3% along the full time range of kinetics[24]. Signal-to-noise ratio of our experimental kinetics is better then of 0.1% and permits discrimination between these model distributions in favor of Gaussian one.

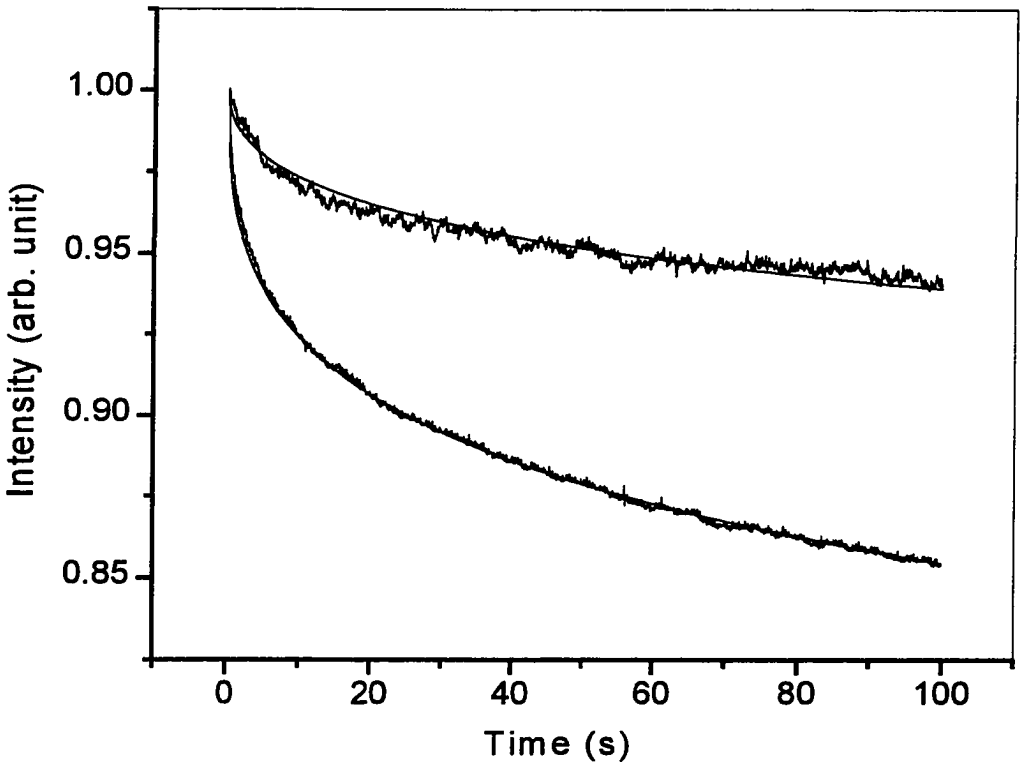

Figure 8.15. Experimental hole burning kinetics detected in $Tm(TTFA)_3$ complex at 1.4 K near 795 nm and fitting curves according to equation (6.8), Chapter 6. The upper and lower experimental kinetics were recorded at 0.25 and 4 mW/mm^2 respectively.

Sample	Tunneling Rate (s^{-1}) (Path A)	Average Efficiency of PSHB	Distribution parameters		
			a_c center	w width	D depth
$Tm(TFD)_3$	5.641	1.1×10^{-4}	9.99	4.7	0.38
$Tm(PBD)_3$	6.642	9.1×10^{-5}	10.46	3.8	0.17
$Tm(TTFA)_3$	0.102	2.6×10^{-6}	14.69	9.2	0.42
$Tm(DBM)_3$	1.961	1.0×10^{-5}	12.58	6.68	0.27

Table 8.4. Average quantum efficiencies of hole burning, tunneling rates and distribution parameters at 1.4 K for Tm^{3+} complexes under investigation.

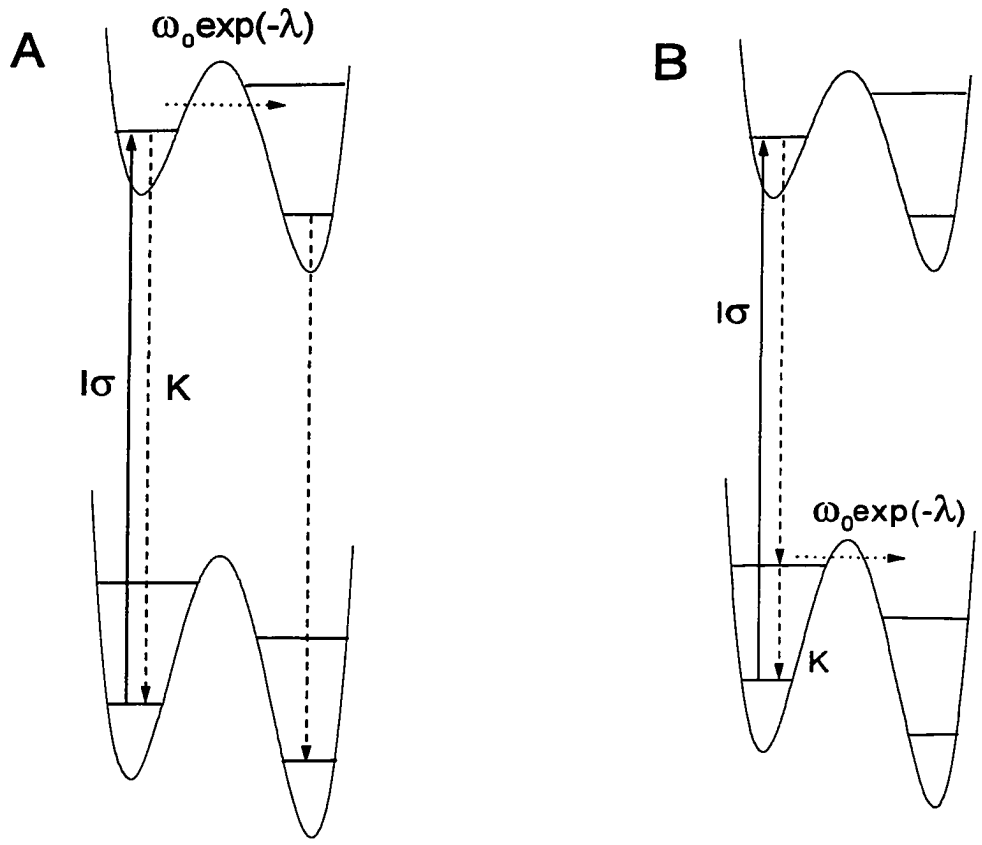

Figure 8.16. Two possible paths of hole burning acceptable in terms of TLS model. Laser excitation Iσ (solid arrows), spontaneous decays K (dashed arrows), and possible tunneling interwell transitions $\omega_0 exp(-\lambda)$ (dotted arrows) are shown.

Thus, the hole growth kinetics were fitted by the integral (6.8) from Chapter 6. To unambiguously determine fitting parameters, dynamic range of recorded kinetics was extended. The fitting procedure has been performed simultaneously for two kinetics recorded at 4 and 0.25 mW/mm^2 and the unique set of parameters was determined for each system. Fig. 8.15 displays experimental kinetics and fitting curves for $Tm(TTFA)_3$ complex. The average quantum efficiency was found according to equation (6.9) in Chapter 6:

$$\langle \varphi \rangle = \frac{\int_0^\infty \exp(-a)\exp\left(-\frac{(a-a_c)^2}{w^2}\right)da}{\int_0^\infty \exp\left(-\frac{(a-a_c)^2}{w^2}\right)da} \qquad (6.9)$$

A summary of obtained parameters is presented in Table 8.4.

Standard TLS model permits two possible paths for persistent hole burning, Path A and Path B, presented in Fig. 8.16. As can be seen, the Path A involves interwell tunneling transition in the excited state, while the Path B employs only interwell transitions in ground state double-well potential. Accordingly, parameters of distribution obtained from a hole burning kinetics can belong to double-well potentials either in ground or in excited state. The Path A is conventionally considered to be responsible for hole burning[5].

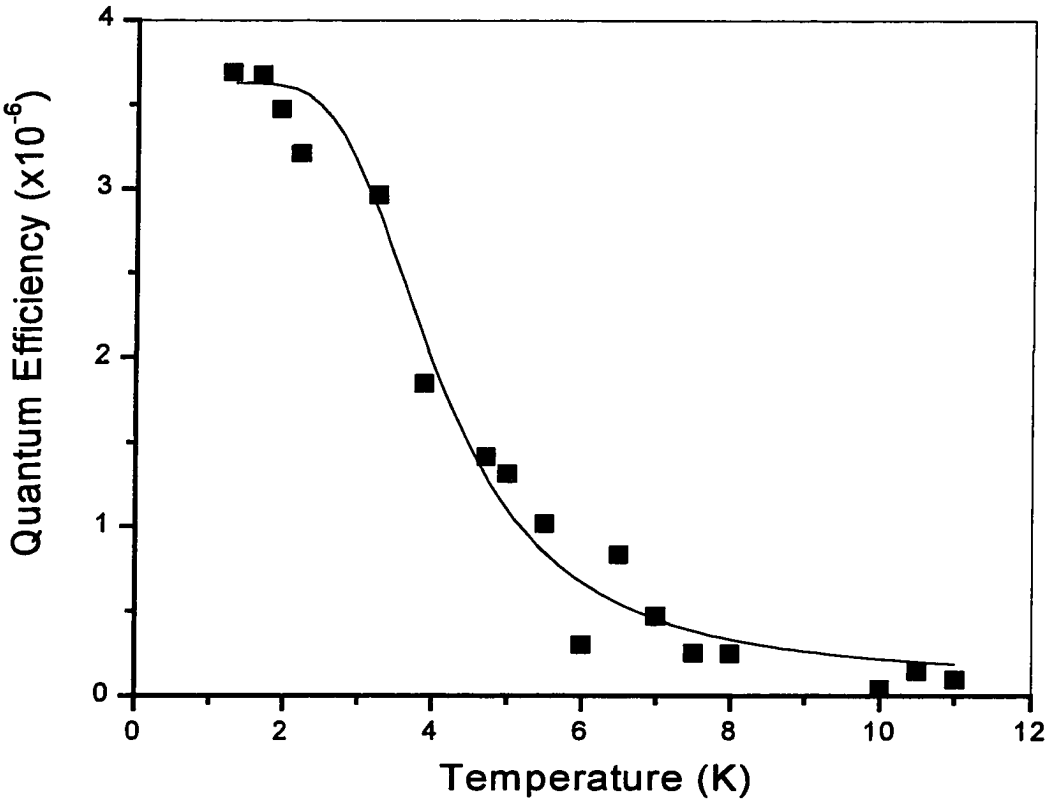

Figure 8.17. Experimental temperature dependence of the quantum efficiency of hole burning in $Tm(TTFA)_3$ (squares) and fitting curve by equation (8.4) (solid line). See text for further details.

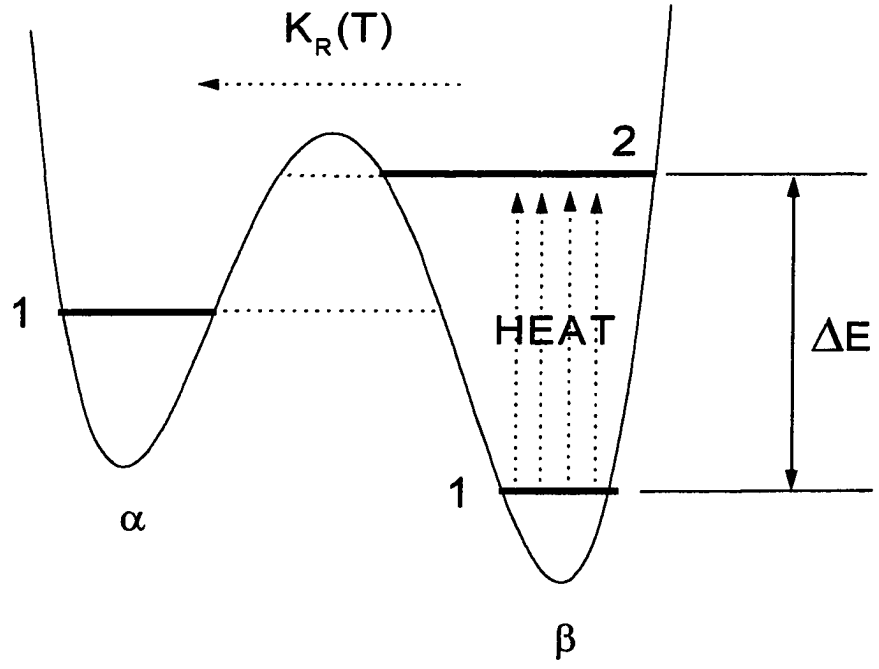

Figure 8.18. An illustration for thermally assisted tunneling process.

For the Path A, quantum efficiency of PSHB is defined by the rate competition between interwell transition in the excited state $R=\omega_0 exp(-\lambda)$ and the relaxation from the

excited state to the ground state K, so that $\varphi=R/K=(\omega_0/K)exp(-\lambda)$ (Fig. 8.16). From this equation we estimated average tunneling rates for our materials to be on the order of 10-10^{-1} s^{-1} (Table 8.4).

8.4.2. Temperature dependence of quantum efficiency of PSHB.

To facilitate further understanding of a hole burning mechanism for our compounds, temperature dependence of quantum efficiency of hole burning was measured. Hole burning kinetics were detected at temperature range between 1.4 K and 12 K and analyzed according to the outlined above procedure. Temperature broadening of the homogeneous line and related reduction in homogeneous peak absorption cross section were taken into account during this analysis. Maximal hole depth D was found to be a constant along the entire temperature range for each material.

Quantum efficiency of hole burning demonstrated dramatic dependence on temperature (see Fig. 8.17). The observed behavior can be explained by decreasing of the rate of the direct interwell tunneling with temperature or by occurring of the reversal process at higher temperatures. Following Bassler's results[25], we used the latter approach for explanation of the obtained experimental dependence, assuming that some unknown thermally induced process opposite to hole burning is responsible for sharp decrease of quantum efficiency at higher temperatures, while the direct tunneling process is not dependent on temperature. Taking into account this reversal process, the equation for quantum efficiency has to be modified:

$$\varphi(T) = \frac{\omega_0 \exp(-\lambda)}{K + K_R(T)} \qquad (8.1)$$

where $K_R(T)$ is a temperature dependent rate of the reversal process, K is a decay rate of the energy level involved. There are a few possibilities for reversal process $K_R(T)$ that have to be considered: it could be either activation or tunneling process, and it could take place either in ground or excited state. In addition, the possibility that some intermediate state is involved can not be ruled out completely.

Gaussian distribution of the parameters of the double-well potentials was proved to be the only model distribution able to explain the observed hole burning kinetics, no matter which of the two Paths -- A or B -- were employed in PSHB mechanism (see Section 8.4.1). Therefore, we shall consider that parameters of both TLS excited and ground state potentials are subject to this type of distribution. Though parameters of the distributions might be different for the excited and ground states, there is no apparent reason to expect qualitative distinctions. Substantial scattering of the experimental data on temperature dependence of quantum efficiency does not allow determination of the distribution parameters, so that in our analysis we shall imply single "effective values" for involved TLS parameters.

An attempt frequency on the order of a few megahertz is required to describe experimental temperature dependence of quantum efficiency of PSHB by reversal process with activation mechanism. The possibility of existence of such low vibrational frequency appears to be very remote for these types of organic materials. Thus, the reversal process has to be attributed to thermally assisted tunneling. To clarify the nature of thermally assisted reversal tunneling process, we consider two well potential presented in Fig. 8.18. The potential can belong to either excited or ground TLS electronic state. In

both cases we consider that $\alpha \rightarrow \beta$ direct transition is leading to hole burning, and $\beta \rightarrow \alpha$ transition is a reversal process. At zero temperature, the probability of $1\beta \rightarrow 1\alpha$ transition is very low and can be neglected. Following Osad'ko's results[26], at finite temperature the rate of thermally assisted tunneling reversal transition is defined by the equation:

$$K_R(T) = \gamma \exp\left(-\frac{\Delta E}{kT}\right) \qquad (8.2)$$

where γ determines the probability of interwell $2\beta \rightarrow 1\alpha$ transition and $\exp(-\Delta E/kT)$ is a Boltzman factor. It will be shown that our experimental dependence does not justify introduction more than one excited vibrational level. Therefore, temperature dependence of the quantum efficiency of hole burning was fitted by the equation:

$$\varphi(T) = \frac{\varphi_0}{1 + \dfrac{\gamma \exp\left(-\dfrac{\Delta E}{kT}\right)}{K}} \qquad (8.3)$$

where φ_0 is a quantum efficiency at low temperature. The resultant fitting curve describes the experimental data with two fitting parameters γ/K and ΔE found to be 132 and 20 K respectively (Fig. 8.17). Obtained values demonstrated that temperature enables effective interwell transition with tunneling rate about two orders of magnitude higher[26] than rate

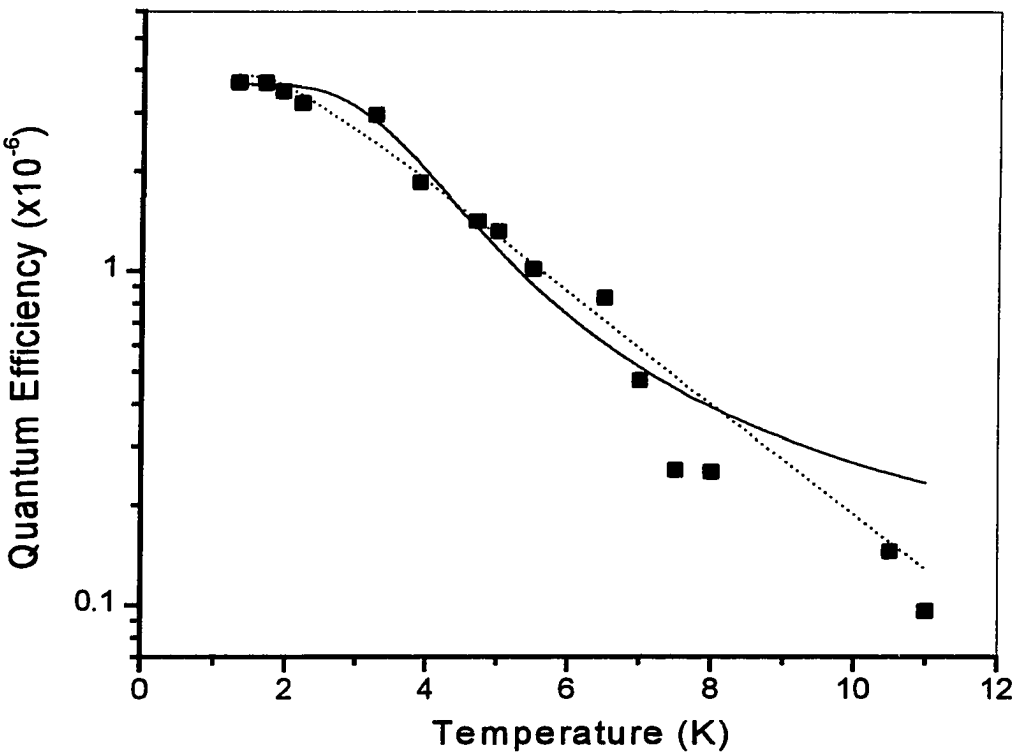

Figure 8.19. Experimental temperature dependence of the quantum efficiency (squares), fitting curves according to models involving reversal process (equation (8.3), solid line) and tunneling with dissipation (equation (8.4), dotted line).

of spontaneous decay from the excited state to the ground state measured to be 4×10^4 s^{-1} for $Tm(TTFA)_3$ complex. Following that, γ can be calculated to be 5.3×10^6 s^{-1}. However, the obtained result can not provide information whether the reversal process operates at ground or excited TLS states.

As mentioned above, alternative approach to explanation of the observed temperature dependence of quantum efficiency of PSHB could be based on decreasing of the probability of the direct tunneling process with temperature. Because relatively large molecular groups might be involved in tunneling process during hole burning, the interaction between these groups and the environment could have a strong influence on tunneling probability. In this connection, the quantum tunneling with dissipation deserves more attention. The investigation of how dissipation affects the microscopic quantum tunneling in a double-well potential was initiated by Caldeira and Laggett[27]. They described dissipation by an interaction with the environmental degrees of freedom and concluded that the quantum tunneling is suppressed in general by dissipation. Bray and Moor[28] analyzed the Caldeira-Laggett model more closely and found a dissipative phase transition for a strong dissipative interaction. According to Larkin's results[29] on tunneling with dissipation, the transition from tunneling regime of barrier crossing at low temperature to the classical regime involving an activation energy may be either a first-order transition or second-order transition. Assuming the latter, in the vicinity of critical temperature T_0 tunneling probability depends on temperature as follows:

$$R(t) = R_0 \exp\left(-\frac{A}{T} + B(T - T_0)^2\right) \qquad (T < T_0)$$
$$R(t) = R_0 \exp\left(-\frac{A}{T}\right) \qquad (T \geq T_0) \qquad (8.4)$$

where A and B are some phenomenological parameters. Experimental dependence of quantum efficiency of hole burning was fitted by equations (8.5) with parameters A, B and T_0 found to be 0.97, 0.005 and 50 K respectively. Though Larkin's approach offers better fit at high temperatures (Fig. 8.19), the quality of fitting curves alone does not enable discrimination between two proposed models. Some studies of tunneling with dissipation showed that the ground state is mixed with excited states by dissipative interaction and that this effect tends to enhance the ground state quantum tunneling[30]. For some cases, this enhancement factor can exceed the Caldeira-Laggett suppression factor. Therefore, more research work is needed to take into account interplay of tunneling, resonance, and dissipation in quantum barrier crossing and to study possible influence of these effects on PSHB.

In our present discussion, we continue to consider reversal process as a primary reason for the reduction in the quantum efficiency of PSHB with temperature.

8.4.3. Temperature cycling experiments.

To associate the reversal process with TLS potentials in excited or ground state, temperature cycling experiments were performed. During each temperature cycle, a spectral hole was burnt and hole spectrum was detected at lowest available temperature T_B. Then temperature was raised up to annealing temperature T_A and maintained at this level for about 600 seconds. Next, temperature was lowered back to T_B and hole

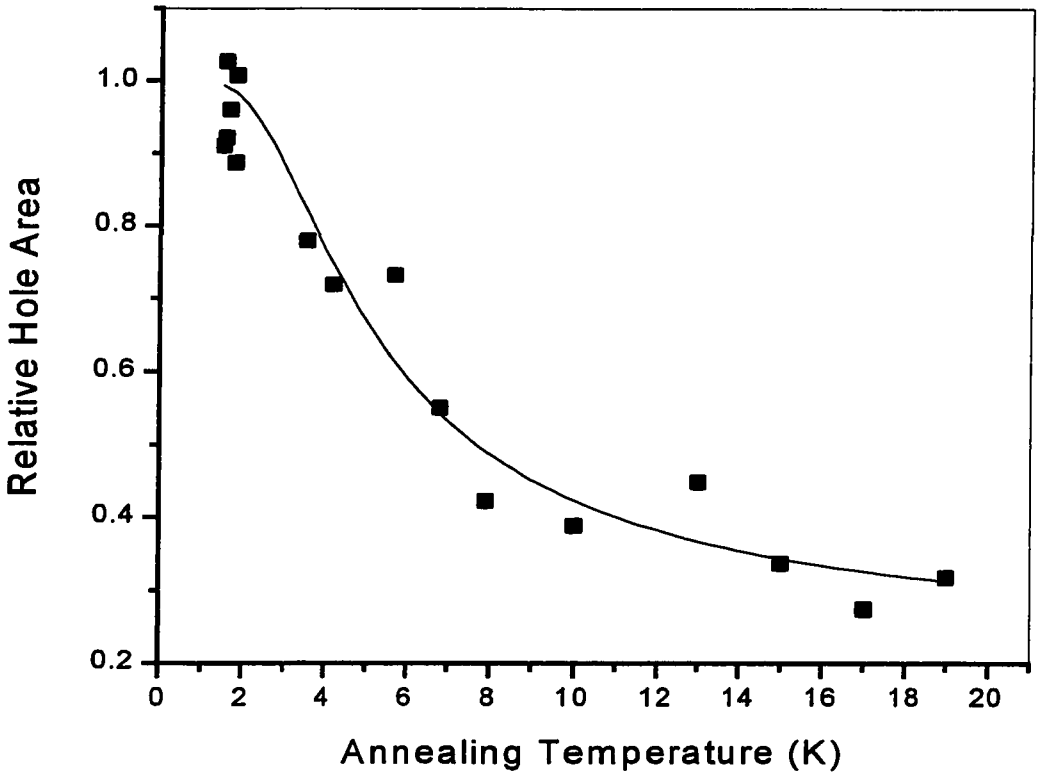

Figure 8.20. Experimental dependence of the relative hole area on annealing temperature in temperature cycling experiment (squares) for $Tm(TTFA)_3$ complex and fitting curve by equation (8.5) (solid line).

spectrum was detected again. At annealing temperature T_A, the ground state of the TLS can undergo a temperature activated barriers crossing or a thermally assisted tunneling from "product" state to initial state. Therefore after temperature cycle, relative spectral hole area, which is proportional to the number of burnt away centers, was expected to decrease. Experimental dependence of the relative hole area on annealing temperature is presented in Fig 8.20. Activation process with reasonable value of attempt frequency failed to describe the observed dependence. Experimental data were fitted by equation derived from thermally assisted tunneling model:

$$\frac{A(T_A)}{A_0} = \exp\left(-\gamma \exp\left(-\frac{\Delta E}{kT}\right)t\right) \qquad (8.5)$$

where $A(T_A)/A_0$ is a relative spectral hole area after temperature cycle with annealing temperature T_A maintained during the time period t. The probability of interwell transition γ and energy splitting ΔE were obtained to be 5×10^{-3} s^{-1} and 9.5 K respectively. A dramatic difference between these parameters related to ground state and parameters obtained from the temperature dependence of quantum efficiency of hole burning indicates that a reversal process in ground state cannot be responsible for the observed decrease in quantum efficiency with temperature. Thus, we have to conclude that a reversal process counteracting hole burning at higher temperatures originates in the TLS excited state or in some unknown intermediate state. The latter possibility appears to be very remote because no other experimental evidences of existence of such state were found.

The obtained conclusion enables us to discriminate between two possible paths of the hole burning reaction (see Fig. 8.16). The Path B can not explain consistently results of temperature cycling experiments and temperature dependence of quantum efficiency and has to be ruled out.

8.5. Conclusion.

The hole burning mechanism can be outlined as follows: at low temperature the hole burning reaction is described by the Path A (Fig. 8.16). At higher temperatures, an efficient thermally assisted reversal tunneling process occurs at the excited state. This process causes dramatic reduction in quantum efficiency of hole burning with temperature. Much weaker similar process in ground state is responsible for refilling of the spectral hole in temperature cycling experiments. Substantially different values of maximal temperature of hole burning T_{HB} (i.e. at temperature T_{HB} hole burning kinetics is not detectable at achieved signal-to-noise ratio better than 0.1%) and maximal annealing temperature T_A (i.e. spectral hole can not be detected after temperature cycle with temperature exceeding T_A) (see Table 8.5) for materials studied can be explained by differences in corresponding tunneling probabilities that strongly depend on TLS parameters such as shape of the energy barrier and resonance conditions between energy levels. Due to random nature of studied substances, these properties can be hardly derived analytically from the chemical structure of samples. Physical nature of the TLS systems involved in PSHB is not discovered in the present time and appears to be related to photoinduced rearrangements of the local environment of the studied complexes. Certain correlation between structure of the complexes and their ability for spectral hole burning is observed: complexes containing bulkier and heavier side groups $Tm(DBM)_3$

and $Tm(TTFA)_3$ show better temperature stability than complexes with relatively small and light sidegroups $Tm(TFD)_3$ and $Tm(PBD)_3$. On the other hand, $Tm(TFD)_3$ and $Tm(PBD)_3$ complexes demonstrate the highest quantum efficiency of the hole burning process. Observed behavior can be understood qualitatively. If we identify a tunneling transition with a reorientation of the sidegroups, we can see that with the lighter sidegroup the processes of reorientation (tunneling) and hole burning are easier. In contrast, the heavier and bulkier sidegroups have lower probability of tunneling that leads to lower efficiency of hole burning and high thermal stability of the spectral holes.

In summary, for the first time, persistent spectral hole burning in Tm^{3+} ion complexes was observed and studied. Extensive spectroscopic investigation of a set of novel materials, Tm^{3+}: ligand complexes in PMMA, has been performed. Major spectroscopic parameters obtained for all samples are presented in Tables 8.2, 8.3, and 8.5. Hole burning mechanism based on TLS model for amorphous media was proposed. Quantum efficiencies of hole burning were obtained and compared for all samples. Gaussian shape of distribution for TLS parameters was proposed and confirmed by the dispersive kinetics of hole burning. Distribution parameters for excited and ground states were obtained and compared for all samples. Temperature dependence of quantum efficiency of hole burning and results of temperature cycling experiments were explained by introduction of reversal thermally assisted tunneling processes in the excited and ground state respectively. Primary parameters of these tunneling processes were obtained.

Parameters	*$Tm(TTFA)_3$*	*$Tm(TFD)_3$*	*$Tm(PBD)_3$*	*$Tm(DBM)_3$*
Tm : % (wt.)	0.21	0.7	0.64	0.4
Tm : % Mole	0.14	0.35	0.32	0.2
n (cm^{-3})	1.2×10^{19}	2.9×10^{19}	2.7×10^{19}	1.8×10^{19}
α (cm^{-1}) at 12 K	0.74	0.25	0.97	0.84
σ_{hom} (cm^2) at 1.4K	1.2×10^{-15}	2.2×10^{-16}	3.8×10^{-16}	1.5×10^{-15}
Γ_{hom} (T)	$T^{1.6\pm0.15}$	$T^{1.3\pm0.15}$	$T^{1.0\pm0.15}$	$T^{1.5\pm0.15}$
$T_{HB,\,max}$ (K)	16	6.5	8	6.5
$T_{A,\,max}$ (K)	20	7	12	30

Table 8.5. Spectroscopic parameters of Tm^{3+}: ligand complexes in PMMA ($^3H_6$ (I) $\leftrightarrow$ $^3H_4$ (I) transition). $T_{HB,\,max}$ and $T_{A,\,max}$ are the maximum hole burning temperatures and maximal annealing temperature respectively.

References for Chapter 8

[1]. W.E. Morerner in: Topics in Current Physics. Persistent spectral hole-burning: science and application, ed. by Morerner (Springer, Berlin, 1987).

[2]. R. M. Macfarlane and R. M. Shelby, in Spectroscopy of Solids Containing Rare Earth Ions, edited by A. A. Kaplyanskii and R. M. Macfarlane (North-Holland, Amsterdam, 1987) p. 51.

[3]. H. Lin, T. Wang, G. A. Wilson, and T. W. Mossberg, *Opt. Lett.* **20** (1995) 91; H. Lin, T. Wang, and T. W. Mossberg, *Opt. Lett.* **20** (1995) 1658; H. Lin, T. Wang, and T. W. Mossberg, Opt. Lett. **21** (1996) 1866.

[4]. R. M. Macfarlane, *Opt. Lett.* **18**, (1993) 829.

[5]. G. Small in: Spectroscopy and excitation dynamics of condensed molecular systems, ed. by A.V. Agranovich and R.M. Horchstrasser, North-Holland, 1983.

[6]. Y. Okamoto, Y. Ueba, F. N. Dzhanibekov, and E. Banks, *Macromolecules*, **14** (1981) 17.

[7]. F. Halverson, J. S. Brinen, and J. R. Leto, *J. Chem. Phys.* **41** (1964) 157.

[8]. B. Henderson and G. F. Imbusch "Optical spectroscopy of inorganic solids" (Clarendon Press, Oxford, 1989).

[9]. J. A. Prins in: Physics of Non-Crystalline Solids, Eds. by J. A. Prins (Wiley, New York, 1965).

[10]. C. Brecher and L. A. Riseberg, Phys. Rev. B, **13** (1976) 81.

[11]. C. Brecher and L. A. Riseberg, Phys. Rev. B, **21** (1980) 2607.

[12]. F. Albert Cotton "Chemical Applications of Group Theory" (John Willey, 1990).

[13]. C. A. Morrison "Angular Momentum Theory Applied to Interactions in Solids" (Springler-Verlag, Lecture Notes in Chemistry, 47)

[14]. G. Koster, J. Dimmock, R. Wheeler, and H. Statz "Properties of the Thirty-Two Point Groups" (MIT Press, Cambridge, 1963)

[15]. W. F. Sager, N. Filipescu and F. A. Serafin, J. Phys. Chem. **69**, no. 4, (1965) 1092.

[16]. C. L. Crofcheck, E. W. Nelson, J. L. Jacobs and A. B. Scranton, Journal of Polymer Science A, **33** (1995) 1735.

[17]. K. C. Joshi and V. N. Pathak, Coord. Chem. Rev. **22** (1977) 37-122, and references therein.

[18]. P. K. Sharma, A. R. van Doorn, A. G. Straring, J. Lum. **62** (1994) 219.

[19]. C. Guery, J. L. Adam, and J. Lucas, *J. Lumin.* **42** (1988) 181.

[20]. W. De, W. Horrocks, Jr., and D. R. Sudnick, *J. Am. Chem. Soc.* **101** (1979) 334.

[21]. S. Uemura, M. Okada, A. Wakamiya, and H. Nakatsuka, Phys. Rev. B, **46** (1992) 10641.

[22]. K. K. Rebane and A. A. Gorokhovskii, *J. Lumin.* **36** (1987) 237 and references therein.

[23]. R. Jankowiak, L. Shu, M.J. Kinney and G.J. Small, J. Lum. **36** (1987) 293.

[24]. R. Jankowiak and G.J. Small, Science **237** (1987) 618.

[25]. A. Elschner, R. Richert and H. Bassler, Proceedings of the Academy of Sciences of the Estonian SSR, **37** (1988) 154.

[26]. I. S. Osad'ko in: Spectroscopy and excitation dynamics of condensed molecular systems, ed. by A.V. Agranovich and R.M. Horchstrasser, North-Holland, 1983.

[27]. A. O. Caldeira and A. J. Laggett, Phys. Rev. Lett. **46** (1981) 211.

[28]. A. J. Bray and M. A. Moore, Phys. Rev. Lett. **49** (1982) 1545.

[29]. A. I. Larkin and Y. N. Ovchinnikov, JETP Lett. **37** (1983) 382.

[30]. K. Fujikawa, S. Iso, M. Sasaki, and H. Suzuki, Phys. Rev. B, **46** (1992) 10295.

Appendix A

Evaluation of vibration generated by closed cycle refrigeration system using optical methods

Introduction.

Low temperatures are required for optical research, in particular for spectroscopic investigation of solids, including laser spectroscopic experiments such as Raman scattering, luminescence line narrowing, spectral hole burning and spectral holography[1]. Our research directed to new materials for high-density frequency domain optical data storage demonstrated the necessity to have simple, dependable low-cost refrigeration systems that provide cryogenic temperatures for a long continuous period of time. Two well-developed low temperature techniques are employed: helium-bath cryostats and closed cycle refrigeration systems. The helium-bath cryostats provide temperatures near 4.2 K; however, they require expensive liquid helium and extensive preparation time. Alternative modern closed cycle refrigeration (CCR) systems are very attractive for temperatures above 8 K due to their immediate advantages of a compact size, operation in any orientation, lack of liquid helium, and ability to achieve low temperatures in relatively short time. The main disadvantage of low priced commercial CCR systems is vibration, which might substantially affect experimental results if not taken into consideration. Only

limited number of experimental data on vibration of commercial CCR systems are available in the literature[2].

In this appendix, we present a simple optical technique for studying mechanical vibration and the application of this technique for investigating the vibration of a commercial CCR system. By analyzing the spectra of vibration of the cold finger, frequencies of the major Fourier components were determined. Reported results can be useful in optical technology that utilizes CCRs.

A.1. Experimental technique

A few sensitive vibrometric methods have been developed in the past. The most common method is based on accelerometry. A regular accelerometer consists of a small mass supported on a force transducer. The force required to accelerate the mass is proportional to the acceleration for nonresonance frequencies. The force is measured by a piezoelectric system: a crystal of quartz or a material such as barium titanate, when stressed, will produce a charge proportional to stress. The crystal may be used in direct compression or in shear. Accelerometry is the dominant method for measuring vibration, however it requires tedious mounting and wiring of sensors[3]. Consequently, it hardly can be applied for evaluation of vibration at places with limited access such as compact vacuumed chamber at cryogenic temperatures. An alternative method is Laser Doppler Vibrometry (LDV), which is used for the detection of vibration without surface contact. LDV measures velocity using the frequency shift of a laser wave caused by motion of a reflecting target. Due to high sensitivity of the LDV, the measured surface does not need to be specially modified or prepared in advance. At the present time, commercially available LDV systems remain too expensive to be cost-effective for occasional

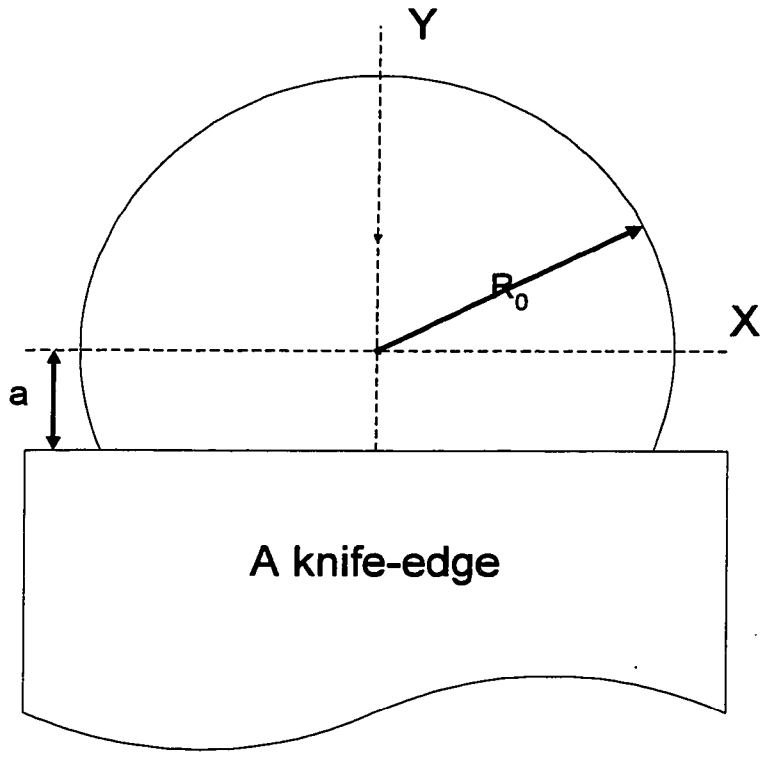

Figure A.1. A cross section of the laser beam in the knife-edge plane is shown. The detected intensity is proportional to the transmitted part of the beam cross section (see text below). *a* is the linear displacement of the knife-edge; R_0 is a radius for the Gaussian laser beam in the knife-edge plane on the level of intensity $1/e^2$.

measurements. Other methods based on laser interferometry use the principle of the standard Michelson interferometer[4]. Interferometric methods provide high sensitivity but require time-consuming alignment. Also, they become particularly complex when instabilities make the measurement object move more than the vibration to be measured.

We propose an optical technique for direct measurement of the displacement based on amplitude modulation of the probe laser beam by the vibrating element. To implement our technique, a sharp knife-edge has to be attached to the vibrating element perpendicular to the axis of a laser beam in such a manner that the laser beam is partially blocked by a knife-edge (see Fig. A.1). Hence, the intensity of the transmitted laser beam depends on the displacement of the knife-edge along Y-axis. The transmitted intensity is measured and analyzed to obtain the amplitude and spectrum of the vibrational motion in the Y-direction.

Due to negligible diffraction of the laser beam on the knife-edge, the intensity modulation of the transmitted beam is considered in terms of geometrical optics. Taking into account Gaussian distribution of intensity across the radius of the laser beam, the variable part of the photosignal is linked to the displacement of the edge by the integral:

$$\Delta I(a) = I_0 \int_0^a \int_0^{\sqrt{R_0^2 - y^2}} \exp\left(-\frac{2(x^2+y^2)}{R_0^2}\right) dx dy \qquad (A.1)$$

where ΔI is a variable part of the photosignal, a stands for a linear displacement of the knife-edge, R_0 is a radius for the Gaussian laser beam in the knife-edge plane on the level of intensity $1/e^2$ and I_0 is a normalization constant (see Fig. A.1).

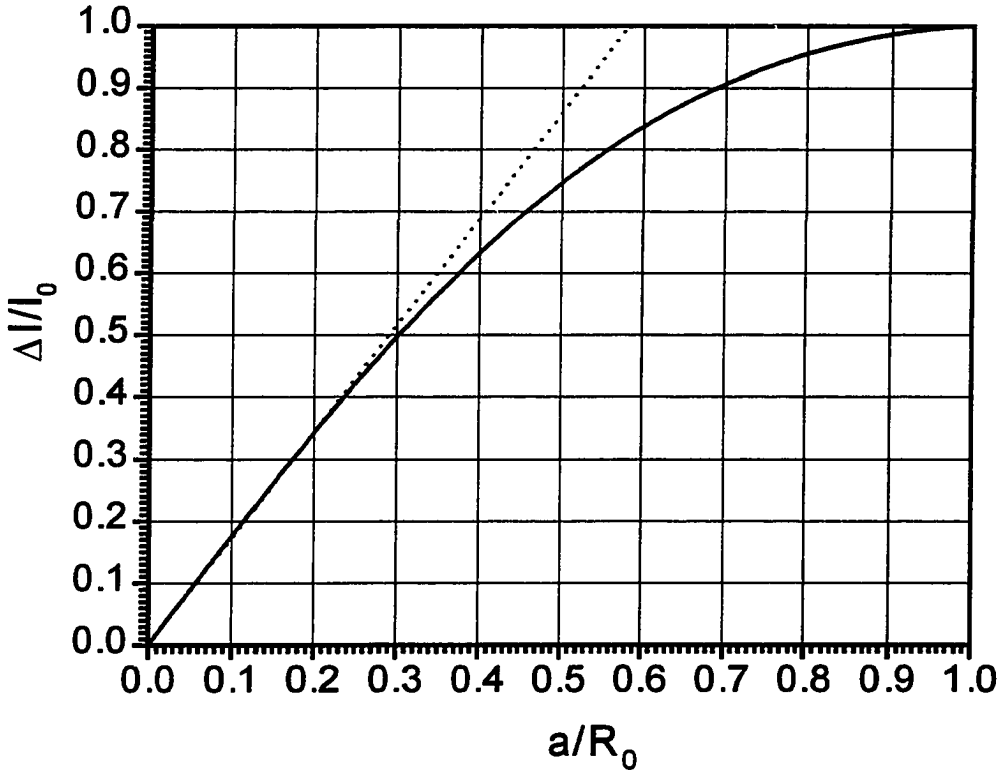

Figure A.2. The calibration curve used to convert the normalized photosignal $\Delta I/I_0$ into displacement amplitude. Solid line represents the numerical calculation of integral (A.1). Dotted line is the linear approximation for the small displacements with $a < R_0/4$.

Analytical solution for the displacement as a function of photosignal is not possible. For small displacement amplitudes, $a < R_0/4$, linear approximation can be used:

$$\frac{a}{R_0} \approx 0.58 \cdot \frac{\Delta I}{I_0} \qquad \left(a < \frac{R_0}{4}\right) \qquad (A.2)$$

A calibration curve based on the numerical integration of (A.1) has been used to convert the detected photosignal to the amplitude of displacement. Using the displacement amplitude normalized to the beam radius in the edge plane, the calibration curve and linear approximation (A.2) are shown in Fig. A.2. Absolute values of amplitude can be easily obtained if the beam diameter in the edge plane is known.

The minimal amplitude of a vibration detectable by the proposed method is proportional to the diameter of the laser beam in the edge plane. Using focusing optics, a laser spot diameter of 10 μm could be easily achieved. Assuming a simple detection system with capability to analyze signals with depth of modulation of 1%, we may estimate measurable displacement as low as 0.1 μm.

A.2. Experimental setup.

A standard green He-Ne laser (output power 4 mW, wavelength of irradiation 543.5 nm) was focused onto a lightweight knife-edge mounted on the sample holder inside the cold head. Initially, without vibration, the position of the edge was adjusted to block half of the input beam. The intensity of the transmitted laser beam was modulated by the vibration of the knife-edge in the perpendicular direction to the beam axis. The transmitted

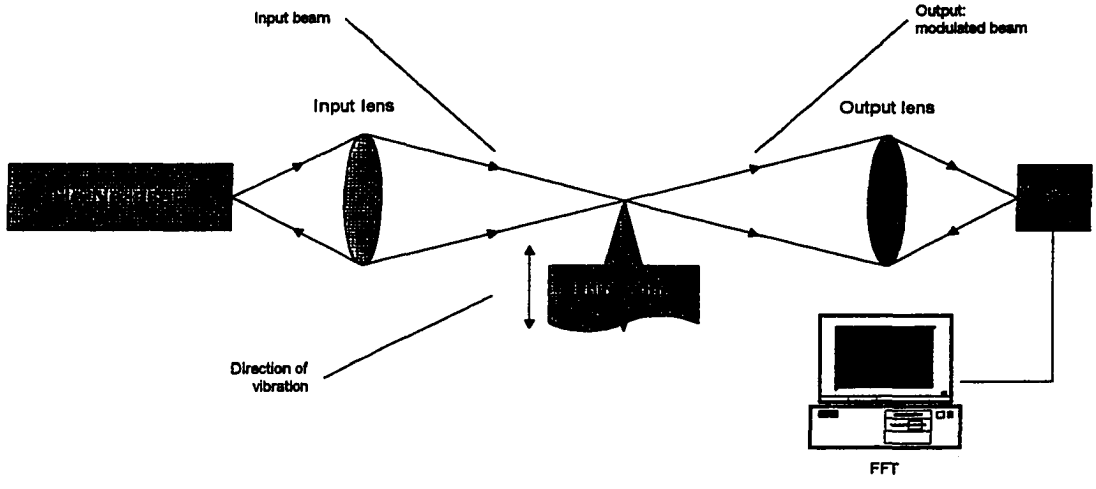

Figure A.3. Optical setup for evaluation of vibration based on the beam modulation by the knife-edge (see text for details).

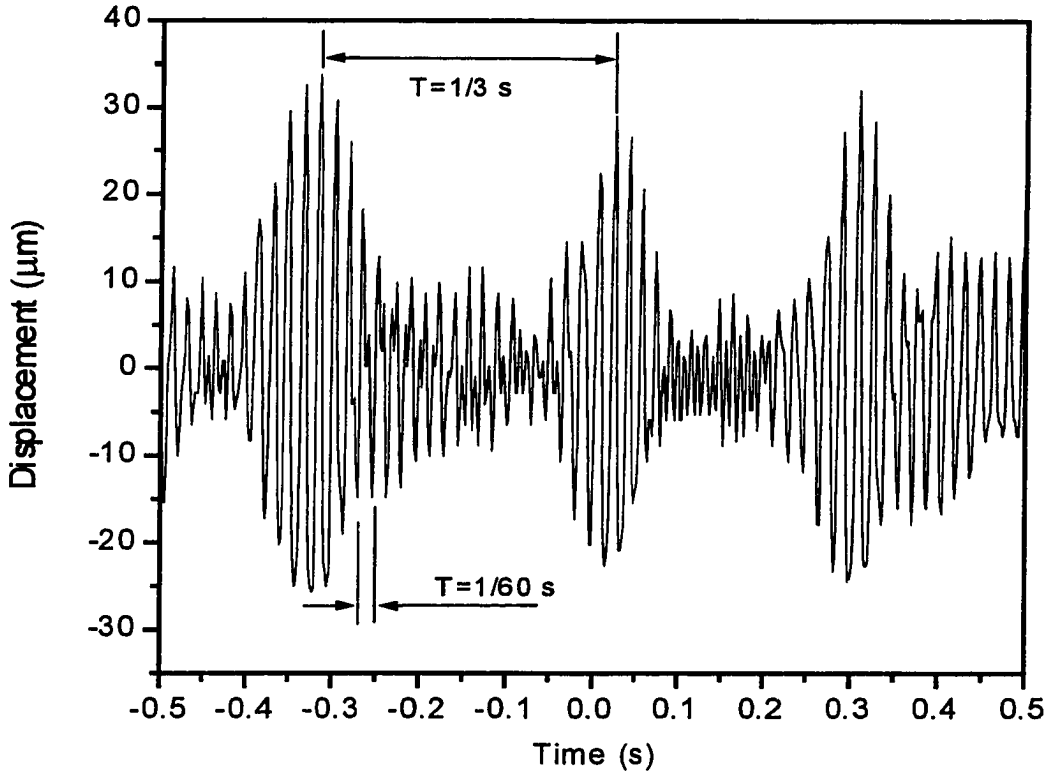

Figure A.4. Representative detected waveform with the cold head fixed into a rigid holder attached to the optical table. The Z-axis was directed vertically (see Fig. A.5). The waveform has been taken at 8 K for vibration in the X-direction and averaged 500 times. The 3 Hz and 60 Hz spectral components can be clearly seen.

light was collected by an output lens and focused onto photodiode PD (see Fig. A.3). An amplified silicon photodiode PD150 (THORLABS) allowed us to measure frequency of vibration up to 50 MHz. All elements were assembled on the optical top supported by six I-2000 vibration isolators. (Newport RS 3000).

To calibrate the photosignal in the units of displacement, we measured the diameter of the laser spot by moving the knife-edge attached to a micrometric table perpendicular to the beam axis and recording the photosignal as a function of displacement. Analyzing obtained curve on the basis of integral (1), a spot diameter of 200 μm has been found. Displacements of 1 μm were easily detectable. Since the measured amplitude of vibration of our CCR system was on the order of 30 μm (see results section below), no attempts to reduce spot diameter and increase sensitivity of detection were made.

The detected photosignal was averaged and analyzed by Tektronix 7248 Digital Storage Oscilloscope. A typical observed signal pattern is presented in Figure 4. Using the oscilloscope's built-in Fast Fourier Transform (FFT) option, the power spectrum of vibration was generated. The analysis of spectral components of the vibration was extremely useful for identifying sources of vibration and designing a custom made holder for reducing the level of vibration.

A.3. Description of the CCR system.

Our study has been conducted for the commercial system CRYO Model 396-022 based on CTI CRYODYNE Model 22 refrigerator. This CRYODYNE system is comprised of a water-cooled compressor unit with oil separation system and refrigerator unit (cold head) located remotely from the compressor. Temperature is controlled by

digital cryogenic temperature controller CONDUCTUS Model LTC-10. Helium gas is used as a refrigerant.

The cold head includes a vacuumed chamber with four quartz windows and a sample holder attached to the cold finger. This allows the CCR system to be used for various optical and spectroscopic measurements. In the present paper, our attention has been concentrated on vibration of the cold finger as the most critical element for optical measurements.

Cool-down and warm-up procedures were performed. The minimal temperature was found to be 8 K. The system was able to reach this temperature in approximately 1.5 hour. Reverse process (with the compressor and the cold head turned off) takes approximately 20 minutes to warm up to 50 K and about 4 hours to reach the initial room temperature.

A.4. Experimental results and discussion.

. Different sets of experiments were performed to measure vibration along the three axes of rectangular coordinates. A schematic representation of the cold head and the system of coordinates are shown in Fig. A.5. Vibration was analyzed for different temperatures of the cold finger, different orientations of the cold head, and two methods for mounting of the cold head's holder.

To check vibration dependence on the orientation of the cold head, the measurements were taken with the cold head held with its Z-axis directed horizontally and vertically. All vibration characteristics measured are independent on the orientation of the cold head. This proves that the investigated CCR system is suitable for mounting in different orientations.

Mounting	Maximum Displacement (microns)		
	X-direction	Y-direction	Z-direction
Holder on the optical table	50	50	22
Holder on the stand	--	30	12

Table A.1. Representative total amplitudes of vibration in different directions and with different mounting apparatus. Temperature at the cold finger was 8 K.

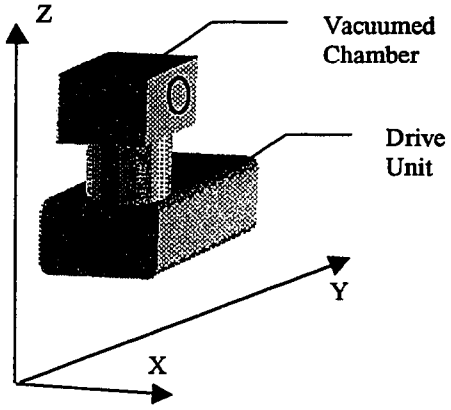

Figure A.5. A schematic picture of the cold head with coordinate system used in Table A.1 and elsewhere in the text.

The temperature range during the course of experiments was 300 - 8 K. The total magnitude of vibration in all three directions appear to be slightly lower with decreasing temperature, i.e. with increasing the operating time. This effect can be attributed to warming up of the equipment.

Two different methods of mounting the cold head have been used. First, the cold head was secured into rigid mechanical holder attached directly to the optical table. However, vibration of the optical table generated by the cold head disrupted operation of the other optical equipment located on the same optical table. To avoid this problem, a second method of mounting of the cold head was tested. The cold head in the same mechanical holder was attached to a special stand placed on the floor in the laboratory. In this case, the cold head was decoupled from the optical top through room floor and vibration isolators of the optical top. Data for both mounting methods in the case of vertical orientation of the Z-axis and temperature at the cold finger 8 K are presented in Table A.1. As we can see, the second mounting method provides, in addition to decoupling of the cold head from the optical table, substantial decrease of magnitude of vibration due to damping in the rigid frame of the stand.

Results of spectral analysis of the vibration are shown in Figure A.6. The spectra consist of a combination of three main components of 3 Hz, 60 Hz and 120 Hz for the holder placed on the optical table. For the holder placed on the stand, some additional components are clearly visible.

Conducted spectral analysis allows to identify sources of the major vibration components. The component at 3 Hz can be attributed to the motion of the displacer (piston) inside the cold head, which occurs with characteristic frequency 3 Hz. Two

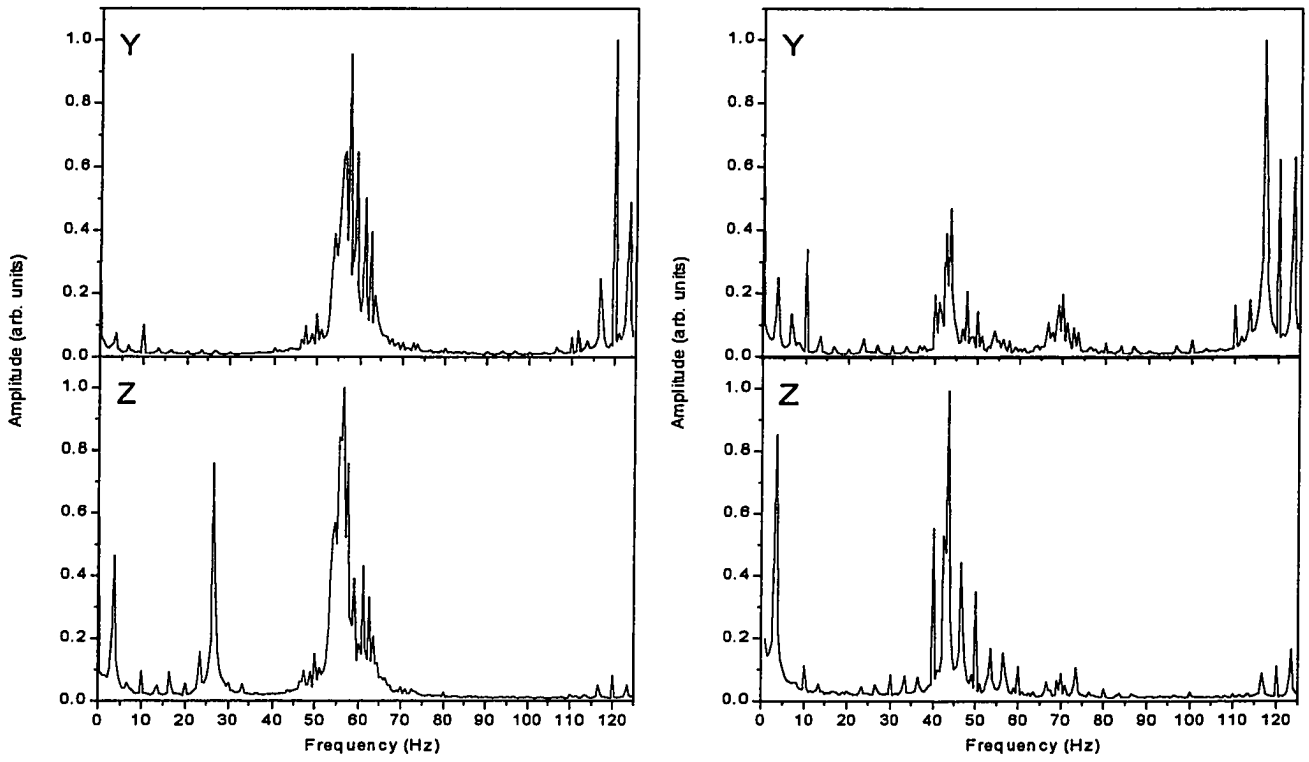

Figure A.6. Normalized spectra of the vibration: (a) the cold head is secured in the mechanical holder attached to the optical table; (b) the mechanical holder attached to separated stand. Spectra taken at 8 K and averaged 500 times.

stronger components at 60 Hz and 120 Hz are caused by the drive motor inside the drive unit of the cold head. The compressor has been eliminated from the possible sources of vibration: no vibration of the cold finger was detected with running compressor while cold head drive unit has been stopped.

A.5. Conclusion.

A simple optical method to evaluate mechanical vibration with sensitivity down to 0.1 μm has been proposed. The developed technique has been applied to investigate the vibration of a closed cycle refrigeration (CCR) system. In all experiments performed, the total amplitude of vibration decreases with warming of the equipment and reaches a stationary level in a hour and a half. The characteristics of vibration do not show any dependence on orientation of the cold head. Using spectral analysis, two major components of vibration at 60 Hz and 120 Hz were found and their origin was ascribed to the drive motor of the cold head. The other significant detected component at 3 Hz was attributed to the motion of the displacer (piston) inside the cold head. Solid mechanical holder in combination with rigid stand decoupled from the optical table suppressed vibration at a level of 30 μm and 12 μm for Y and Z directions respectively.

Conducted experimental study demonstrated that observed high level of vibration requires decoupling of the holder with the cold head from the optical table. Further decrease of vibration requires use of more sophisticated CCR systems with vibration isolating interface between a cold head and a sample holder [5].

References for Appendix A.

[1]. National Media Lab Report (1996) can be obtained at www.nml.org

[2]. A. Fuaret, M. Mualler, H. Tugal "Vibration analyses to reduce particles in sputtering systems" (Solid State Technology, March 1993)

[3]. J. D. Smith "Vibration measurement and analysis" (Butterworths, 1989).

[4]. G. Burdugan, E. Mihailescu, M. Rades "Vibration measurement" (Martin Nijhoff Publishers, 1986).

[5]. E. De Grave, L.H. Bowen, S.W. Hedges "Mossbauer spectroscopy with a microprocessor: a versatile software package" (Nuclear Instruments and Methods 200, 1982, p. 303).

Bibliography.

References for Chapter 1

[1]. W. E. Morerner in: Topics in Current Physics. Persistent spectral hole-burning: science and application, ed. by Morerner (Springer, Berlin, 1987).

[2]. A. M. Stoneham in: Theory of defects in solids Vol. 1,2. Clarendon Press, Oxford, 1975

[3]. A. R. Gutierrez, J. Friedrich, D. Haarer, H. Wolfrum: IBM J. Res. Devel. **26** (1982) 198.

[4]. G. Ashton, Media National Laboratory, Annual Report, 1996.

[5]. Grant proposal by Prof. R.R Alfano and Prof. A. A. Gorokhovsky (1996).

References for Chapter 2

[1]. N. Bloembergen, E. M. Purcell, R. V. Pound: Phys. Rev. **71** (1948) 679.

[2]. A. L. Schawlow: in Advances in Quantum Electronics, (Proc. Second Int. Conf. on Quant. Electr.), Ed. by I.R. Singer, (Columbia Univ., New York 1961), pp. 50-64.

[3]. A. Szabo: Phys. Rev. Lett. **25** (1970) 924.

[4]. R. I. Personov, E. I. Al'shits, L. A. Bykovskaya: Opt. Commun. **6** (1972) 169.

[5]. W. M. Yen, P. M. Selzer (eds.): Laser Spectroscopy of Solids, Springer Topics in Applied Physics, Vol. 49 (Springer, Berlin, Heidelberg 1981).

[6]. A. Szabo: Phys. Rev. B **11** (1975) 4512.

[7]. A. A. Gorokhovskii, R. K. Kaarli, L. A. Rebane: JETP Lett. **20** (1974) 216.

[8]. B. M. Kharlamov, R. I. Personov, L. A. Bykovskaya: Opt. Commun. **12** (1974) 191.

[9]. J. Rubio J. Phys. Chem. Solids **52** (1991) 101.

[10]. J. Zhang, S. Huang and J. Yu, Optics Lett. **17**, no. 16 (1992) 1146.

[11]. R. Menzel and P. Witte, J. Chem. Phys. **87** (1987) 6769.

[12]. K. Hirao, S. Todoroki, D. H. Cho, N. Soga, Optics Lett. **13**, no.19 (1993) 1586.

[13]. I. Sildos, M. Aizergendler, I. Dolindo and I. Renge, Opt. Commun. **73** (1989) 223.

[14]. I. Sildos and A. Osvet, Diamond and Related Materials **3** (1994) 725.

References for Chapter 3

[1]. D. Haarer in: Topics in Current Physics. Persistent spectral hole burning: science and application, ed. by Morerner (Springer, Berlin, 1987).

[2]. K. K. Rebane: Impurity spectra of solids (Plenum Press, New York, 1970).

[3]. J. Friedrich and D. Haarer, Angewandte Chemie, vol. **23**, 2, February 1984, 113-140.

[4]. R. M. Macfarlane and R. M. Shelby in: Spectroscopy of solids containing rare earth ions. (Ed. by A. A. Kaplyanskii and R. M. Macfarlane) Elsevier Science Publishers, 1987.

[5]. D. E. McCumber, M. D. Sturge, J. Appl. Phys. **34** (1963) 1682.

[6]. A. A. Gorokhovskii, R. K. Kaarli, L. A. Rebane: JETP Lett. **20** (1974) 216.

[7]. S. Volker, R. M. Macfarlane, J. H. van der Waals: Chem. Phys. Lett. **53** (1978) 8.

[8]. R. M. Macfarlane, Solid State Physics, RJ IBM **5612** (1987) 56922.

[9]. A. A. Gorokhovskii in: Zero-phonon lines and spectral hole burning in spectroscopy and photochemistry, ed. by O. Sild and K. Haller, Springer-Verlag, 1988.

[10]. K. K. Rebane in: Topics in Current Physics. Persistent spectral hole burning: science and application, ed. by Morerner (Springer, Berlin, 1987).

[11]. M. Drobizhev and M. Sapozhnikov, Chem. Phys. Lett. **236** (1995) 438.

[12]. W. E. Morerner, M. Gehrtz, A. L. Huston, J. Chem. Phys, **88** (1984) 6459-6460.

[13]. L. A. Rebane, A. A. Gorokhovskii, J. V. Kikas, Appl. Phys. B **29** (1982) 235-250.

[14]. R. M. Macfarlane in: Topics in Current Physics. Persistent spectral hole burning: science and application, ed. by Morerner (Springer, Berlin, 1987).

[15]. I. Sildos and A. Osvet, Diamond and Related Materials **3** (1994) 725.

[16]. I. Sildos, M. Aizergendler, I. Dolindo and I. Renge, Opt. Commun. **73** (1989) 223.

[17]. J. Zhang, S. Huang and J. Yu, Optics Lett. **17**, no. 16, (1992) 1146.

[18]. G. Small in: Spectroscopy and excitation dynamics of condensed molecular systems, ed. by A.V. Agranovich and R.M. Horchstrasser, North-Holland, 1983.

[19]. S. K. Lyo, Phys. Rev. Lett. **48**, no. 10, (1982) 688.

[20]. R. M. Macfarlane and R. M. Shelby in: Spectroscopy and excitation dynamics of condensed molecular systems, ed. by A.V. Agranovich and R.M. Horchstrasser, North-Holland, 1983.

[21]. L. R. Narasimhan, D. W. Pack, M. D. Fayer, Chem. Phys. Lett. **152**, no. 4-5, (1988) 287.

[22]. R. Jankowiak, L. Shu, M. J. Kinney and G. J. Small, J. Lum. **36** (1987) 293.

[23]. R. Jankowiak and G. J. Small, Science **237** (1987) 618.

References for Chapter 4

[1]. W. E. Moerner in: Topics in Current Physics. Persistent spectral hole-burning: science and application, ed. by Morerner (Springer, Berlin, 1987).

[2]. M. Kryder in: MRS Bulletin, September 1996, Vol. 21, No. 9.

[3] D. Psaltis, D. Stinson, and G. Kino in: Optics and Photonics News, November 1997 and references therein.

[4]. W. E. Moerner, W. Lenth, and G. C. Bjorklund in: Topics in Current Physics. Persistent spectral hole-burning: science and application, ed. by Morerner (Springer, Berlin, 1987).

[5]. G. Ashton, Media National Laboratory, Annual Report, 1996.

[6]. W. E. Moerner and M. D. Levenson, J. Opt. Soc. Am. B, Vol. **2**, No. 6 (1985) 915.

[7]. W. Lenth and W. E. Moerner, Opt. Commun. **58** (1986) 249.

[8]. N. Murase, K. Horie, M. Terao, and M. Ojima, J. Opt. Soc. Am. B, Vol. **9**, No. 6 (1992) 998.

[9]. W. R. Babbitt and T. W. Mossberg, J. Opt. Soc. Am. B **11** (1994) 1948.

References for Chapter 5

[1]. W. Demtroder, Laser Spectroscopy, Springer, 1996.

[2]. COHERENT documentation for 899-29 Ring-Laser System.

References for Chapter 6

[1]. W. E. Morerner in: Topics in Current Physics. Persistent spectral hole burning: science and application, ed. by Morerner (Springer, Berlin, 1987).

[2]. A. A. Gorokhovsky, Y. V. Kikas, V. V. Palm and L. A. Rebane, Solid State Physics **23** (1981) 1040 (in Russian).

[3]. W.E. Morerner, M. Gehrtz, A. L. Huston, J. Chem. Phys. **88** (1984) 6459-6460.

[4]. J. Friedrich and A. Blumen, Phys. Rev. B **32** (1985) 1434.

[5]. A. Elschner and H. Bassler, Chem. Phys. **123** (1988) 305-315.

[6]. R. Jankowiak, L. Shu, M.J. Kinney and G.J. Small, J. Lum. **36** (1987) 293.

[7]. H. Talon, M. Orrit, and J. Bernard, Chem. Phys. **140** (1990) 177.

[8]. M. Drobizhev and M. Sapozhnikov, Chem. Phys. Lett. **236** (1995) 438.

[9]. W. A. Phillips, J. Low Temp. Phys. 7 (1972) 351.

[10]. W. A. Phillips, Rep. Prog. Phys. **50** (1987) 1657-1708.

[11]. P. W. Anderson, B. I. Haperin and C. M. Varma, Phil. Mag. **25** (1972) 1.

[12]. A. Elschner, R. Richert and H. Bassler, Proceedings of the Academy of Sciences of the Estonian SSR, **37** (1988) 154.

[13]. A. V. Carpenter, A. V. Turukhin, A. A. Gorokhovsky, T. Chu, and Y. Okamoto in: Proceedings of Persistent Spectral Holeburning Workshop, February 14-16, 1997, Bozeman, MT.

[14]. J. Friedrich and D. Haarer, Angew. Chem. Int. Ed. Engl. **23** (1984) 113-140.

[15]. A. A. Gorokhovsky and Ya. V. Kikas, Zhurnal Prikladnoi Spectroskopii, Vol. 28, No. 5, (1978) 566.

[16]. G. Small in: Spectroscopy and excitation dynamics of condensed molecular systems, ed. by A.V. Agranovich and R.M. Horchstrasser, North-Holland, 1983.

[17] K. K. Rebane: Impurity spectra of solids (Plenum Press, New York, 1970).

[18]. R. Richert, Chem. Phys. Lett. **118** (1985) 534.

[19]. M. A. Krivoglaz in: Zero-phonon lines and spectral hole burning in spectroscopy and photochemistry, ed. by O. Sild and K. Haller, Springer-Verlag, 1988.

[20]. R. Richert, J. Chem. Phys. **86** (1987) 1743.

[21]. E. S. Maniloff, F. R. Graf, H. Gygax, S. B. Atner, S. Bernet, A. Renn, U. P. Wild, Chem. Phys. **193** (1995) 173.

[22]. A. V. Turukhin, A. A. Gorokhovsky, T. Chu, Y. Okamoto, C. Moser, I. V. Solomatin and D. Psaltis in: Proceedings of Persistent Spectral Holeburning Workshop, March 7-10, 1999, Bozeman, MT.

References for Chapter 7

[1]. J. Angus and C. Hayman: Science **241**, (1988) 913-921.

[2]. A. M. Zaitsev in: Optical Properties of Diamond, FernUniversitat GHS in Hagen, 1995.

[3]. Grant proposal by Prof. R. R Alfano and Prof. A. A. Gorokhovsky (1996).

[4]. I. Sildos, U. Bogner and A. Osvet in: Pnonon scattering in condensed matter, VII, Eds. M. Meissner and R. O. Pohl, Springer Series in Solid-State Sciences, Vol. **112** (1993) 515.

[5]. R. Bauer, A. Osvet, I. Sildos and U. Bogner: J. Lum. **56** (1993) 57.

[6]. K. Kobashi, K. Nashimura, Y. Kawate, T. Horiuchi: Phys. Rev. B **36** (1988) 4067-4083.

[7]. V. S. Vavilov, A. A. Gippius, A. M. Zaitsev, B. V. Deryagin, B. V. Spitsyn, and A. E. Aleksenko, Sov. Phys. Semicond. **14**, (1980) 1078.

[8]. A. M. Zaitsev, V. S. Vavilov, and A. A. Gippius, Sov. Phys. Lebedev Inst. Rep. **10**, (1981) 15.

[9]. J. Ruan, W. J. Choyke, and W. D. Partlow, Appl. Phys. Lett. **58**, (1990) 295.

[10]. L. Bergman, B. R. Stoner, K.F. Turner, J. T. Glass, and R. J. Nemanich, J. Appl. Phys., **73**, (1993) 3951.

[11]. C. D. Clark, H. Kanda, I. Kiflawi, and G. Sittas, Phys. Rev. B **51**, (1995) 16681.

[12]. H. Sternschulte, K. Thonke, R. Sauer, P. C. Munzinger, and P. Michler, Phys. Rev. B, **50**, (1994) 14554; H. Sternschulte, K. Thonke, J. Gerster, W. Limmer, R. Sauer, J. Spitzer, and P. C. Munzinger, Diamond and Related Materials **4** (1995) 1189-1192.

[13]. T. Feng and D. Schwartz: J. Appl. Phys. **73** (1993) 1415.

[14]. A. T. Collins, L. Allers, C. J. H. Wort, and G. A. Scarsbrook, Diamond and Related Materials, **3**, (1994) 932.

[15]. A. A. Gorokhovsky, A. V. Turukhin, R. R. Alfano, W. Phillips: Appl. Phys. Lett. **66** (1), (1995) 43.

[16]. G. Devies, in *The Optical Properties of Diamond*, in *Chemistry and Physics of Carbon* vol. 13, edited by P. L. Walker, Jr. and P.A. Thrower (Marcel Dekker, New York, Basel, 1977), pp. 1-143.

[17]. A. Szabo, Phys. Rev. Lett. **25**, (1970) 924.

[18]. K. K. Rebane, *Impurity Spectra of Solids*, (Plenum Press, New York, 1970).

[19]. C. A. Klein, T. M. Hartnett, and C. J. Robinson, Phys. Rev. B **45**, (1992) 12854.

[20]. M. Gorman and S. A. Solin, Solid State Commun. **15**, (1974) 761.

[21]. T. N. Kitsopoulos, C. J. Chick, Y. Zhao, and D. M. Neumark, J. Chem. Phys. **95**, (1991) 1441; C. C. Arnold, T. N. Kitsopoulos, and D. M. Neumark, J. Chem. Phys. **99**, (1993) 766.

[22]. A. A. Gorokhovsky and J. Kikas, Opt. Commun. **21**, (1977) 272.

[23]. A. V. Turukhin, C.-H. Liu, A. A. Gorokhovsky, R. R. Alfano, W. Phillips: Phys. Rev. B **54** (23), (1996) 16448.

[24]. L. H. Robins, E. N. Farabaugh, A. Feldman, and L. P. Cook, Phys. Rev. B **43**, (1991) 9102.

[25]. L. Bergman, M. T. McClure, J. T. Glass, and R. J. Nemanich, J. Appl. Phys. **76**, (1994) 3020.

[26]. Y. L. Khong, A. T. Collins, and L. Allers, Diamond and Related Materials, **3**, (1994) 1023.

[27]. T. Dallas, S. Gangopadhyay, S Yi, and M Holtz, in *Applications of Diamond Films and Related Materials: Third International Conference, 1995*, NIST special publication SP 885, p. 449.

[28]. B. Di Bartolo: Optical Interactions in Solids (Wiley, 1989).

[29]. R. A. Street, in *Semiconductors and Semimetals*, edited by J. I. Pankove (Academic, New York, 1984), Vol. 21, p. 197.

[30]. A. T. Collins, and S. C. Lawson, J. Phys. Condens. Matter **1,** (1989) 6929.

[31]. G. Davies, in *The Optical Properties of Diamond*, in *Chemistry and Physics of Carbon* vol. 13, edited by P. L. Walker, Jr. and P. A. Thrower (Marcel Dekker, New York, Basel, 1977), pp. 1-143.

[32]. R. T. Harley, M. J. Henderson, R. M. Macfarlane, J. Phys. C, Solid State Phys. **17**, (1984) L233-L236.

[33]. N. R. S. Reddy, N. B. Manson, and E. R. Krausz: J. Lum. **38**, (1987) 46-47.

[34]. A. Osvet, A. Suisalu and I. Sildos, Proc. Estonian Acad. Sci. Phys. Mater. **41** (1992) 222.

[35]. W. E. Morerner, M. Gehrtz, A. L. Huston, J. Chem. Phys, **88** (1984) 6459-6460.

References for Chapter 8

[1]. W.E. Morerner in: Topics in Current Physics. Persistent spectral hole-burning: science and application, ed. by Morerner (Springer, Berlin, 1987).

[2]. R. M. Macfarlane and R. M. Shelby, in Spectroscopy of Solids Containing Rare Earth Ions, edited by A. A. Kaplyanskii and R. M. Macfarlane (North-Holland, Amsterdam, 1987) p. 51.

[3]. H. Lin, T. Wang, G. A. Wilson, and T. W. Mossberg, *Opt. Lett.* **20** (1995) 91; H. Lin, T. Wang, and T. W. Mossberg, *Opt. Lett.* **20** (1995) 1658; H. Lin, T. Wang, and T. W. Mossberg, Opt. Lett. **21** (1996) 1866.

[4]. R. M. Macfarlane, *Opt. Lett.* **18**, (1993) 829.

[5]. G. Small in: Spectroscopy and excitation dynamics of condensed molecular systems, ed. by A.V. Agranovich and R.M. Horchstrasser, North-Holland, 1983.

[6]. Y. Okamoto, Y. Ueba, F. N. Dzhanibekov, and E. Banks, *Macromolecules*, **14** (1981) 17.

[7]. F. Halverson, J. S. Brinen, and J. R. Leto, *J. Chem. Phys.* **41** (1964) 157.

[8]. B. Henderson and G. F. Imbusch "Optical spectroscopy of inorganic solids" (Clarendon Press, Oxford, 1989).

[9]. J. A. Prins in: Physics of Non-Crystalline Solids, Eds. by J. A. Prins (Wiley, New York, 1965).

[10]. C. Brecher and L. A. Riseberg, Phys. Rev. B, **13** (1976) 81.

[11]. C. Brecher and L. A. Riseberg, Phys. Rev. B, **21** (1980) 2607.

[12]. F. Albert Cotton "Chemical Applications of Group Theory" (John Willey, 1990).

[13]. C. A. Morrison "Angular Momentum Theory Applied to Interactions in Solids" (Springler-Verlag, Lecture Notes in Chemistry, 47)

[14]. G. Koster, J. Dimmock, R. Wheeler, and H. Statz "Properties of the Thirty-Two Point Groups" (MIT Press, Cambridge, 1963)

[15]. W. F. Sager, N. Filipescu and F. A. Serafin, J. Phys. Chem. **69**, no. 4, (1965) 1092.

[16]. C. L. Crofcheck, E. W. Nelson, J. L. Jacobs and A. B. Scranton, Journal of Polymer Science A, **33** (1995) 1735.

[17]. K. C. Joshi and V. N. Pathak, Coord. Chem. Rev. **22** (1977) 37-122, and references therein.

[18]. P. K. Sharma, A. R. van Doorn, A. G. Straring, J. Lum. **62** (1994) 219.

[19]. C. Guery, J. L. Adam, and J. Lucas, *J. Lumin.* **42** (1988) 181.

[20]. W. De, W. Horrocks, Jr., and D. R. Sudnick, *J. Am. Chem. Soc.* **101** (1979) 334.

[21]. S. Uemura, M. Okada, A. Wakamiya, and H. Nakatsuka, Phys. Rev. B, **46** (1992) 10641.

[22]. K. K. Rebane and A. A. Gorokhovskii, *J. Lumin.* **36** (1987) 237 and references therein.

[23]. R. Jankowiak, L. Shu, M.J. Kinney and G.J. Small, J. Lum. **36** (1987) 293.

[24]. R. Jankowiak and G.J. Small, Science **237** (1987) 618.

[25]. A. Elschner, R. Richert and H. Bassler, Proceedings of the Academy of Sciences of the Estonian SSR, **37** (1988) 154.

[26]. I. S. Osad'ko in: Spectroscopy and excitation dynamics of condensed molecular systems, ed. by A.V. Agranovich and R.M. Horchstrasser, North-Holland, 1983.

[27]. A. O. Caldeira and A. J. Laggett, Phys. Rev. Lett. **46** (1981) 211.

[28]. A. J. Bray and M. A. Moore, Phys. Rev. Lett. **49** (1982) 1545.

[29]. A. I. Larkin and Y. N. Ovchinnikov, JETP Lett. **37** (1983) 382.

[30]. K. Fujikawa, S. Iso, M. Sasaki, and H. Suzuki, Phys. Rev. B, **46** (1992) 10295.